

# Single-cell mechanical phenotyping across timescales and cell state transitions

DISSERTATION

zur Erlangung des akademischen Grades

Doctor rerum naturalium

(Dr. rer. nat.)

vorgelegt

der Fakultät Mathematik und Naturwissenschaften  
der Technischen Universität Dresden

von

Marta Urbańska

geboren am 11.12.1988 in Belchatów, Polen

Dresden, Oktober 2021

**Eingereicht am** 12. Oktober 2021

**Tag der Verteidigung** 17. Dezember 2021

**Gutachter**

Prof. Dr. Jochen Guck

Prof. Dr. Timo Betz

Prof. Dr. Stephan Wolfgang Grill

## Abstract

Mechanical properties of cells and their environment have an undeniable impact on physiological and pathological processes such as tissue development or cancer metastasis. Hence, there is a pressing need for establishing and validating methodologies for measuring the mechanical properties of cells, as well as for deciphering the molecular underpinnings that govern the mechanical phenotype. During my doctoral research, I addressed these needs by pushing the boundaries of the field of single-cell mechanics in four projects, two of which were method-oriented and two explored important biological questions. First, I consolidated real-time deformability cytometry as a method for high-throughput single-cell mechanical phenotyping and contributed to its transformation into a versatile image-based cell characterization and sorting platform. Importantly, this platform can be used not only to sort cells based on image-derived parameters, but also to train neural networks to recognize and sort cells of interest based on raw images. Second, I performed a cross-laboratory study comparing three microfluidics-based deformability cytometry approaches operating at different timescales in two standardized assays of osmotic shock and actin disassembly. This study revealed that while all three methods are sensitive to osmotic shock-induced changes in cell deformability, the method operating at the shortest timescale is not suited for detection of actin cytoskeleton changes. Third, I demonstrated changes in cell mechanical phenotype associated with cell fate specification on the example of differentiation and de-differentiation along the neural lineage. In the process of reprogramming to pluripotency, neural precursor cells acquired progressively stiffer phenotype, that was reversed in the process of neural differentiation. The stiff phenotype of induced pluripotent stem cells was equivalent to that of embryonic stem cells, suggesting that mechanical properties of cells are inherent to their developmental stage. Finally, I identified and validated novel target genes involved in the regulation of mechanical properties of cells. The targets were identified using machine learning-based network analysis of transcriptomic profiles associated with mechanical phenotype change, and validated computationally as well as in genetic perturbation experiments. In particular, I showed that the gene with the best *in silico* performance, *CAVI*, changes the mechanical properties of cells when silenced or overexpressed. Identification of novel targets for mechanical phenotype modification is crucial for future explorations of physiological and pathological roles of cell mechanics. Together, this thesis encompasses a collection of contributions at the frontier of single-cell mechanical characterization across timescales and cell state transitions, and lays ground for turning cell mechanics from a correlative phenomenological parameter to a controllable property.



# Kurzfassung

Die mechanischen Eigenschaften von Zellen und ihrer Umgebung haben einen unbestrittenen Einfluss auf physiologische und pathologische Prozesse, wie die Gewebeentwicklung oder die Metastasierung bei Krebs. Daher besteht ein dringender Bedarf Methoden zur Messung der mechanischen Eigenschaften von Zellen zu etablieren und zu validieren, sowie die molekularen Faktoren zu entschlüsseln, die den mechanischen Phänotyp der Zellen bestimmen. In meiner Doktorarbeit wurde dieser Bedarf anhand von vier Projekten adressiert, die die Grenzen des Gebiets der Einzelzellmechanik erweitert haben. Zwei von diesen Projekten waren methodenorientiert und zwei erforschten wichtige biologische Fragestellungen. Zuerst zeigte ich die breite Anwendbarkeit der Echtzeit-Verformungszytometrie für die mechanische Hochdurchsatz-Phänotypisierung einzelner Zellen und trug dazu bei, diese Methode zu einer vielseitigen, bildbasierten Zellcharakterisierungs- und Sortierplattform zu erweitern. Die neuentwickelte Plattform ermöglicht die Sortierung von Zellen sowohl nach bildbasierten Parametern, als auch anhand trainierter neuronaler Netze, die mit Rohbildern arbeiten. Des Weiteren führte ich eine laborübergreifende Studie durch, in der drei auf unterschiedlichen Zeitskalen arbeitende Varianten der mikrofluidischen Verformungszytometrie verglichen wurden. Für den Vergleich wurden zwei standardisierte Analyseverfahren durchgeführt, die auf der Anwendung osmotischer Schocks, beziehungsweise des Aktinabbaus basierten. Diese Studie zeigte, dass alle drei Methoden für die Messung von osmotischen schock-induzierten Veränderungen der Zellverformbarkeit geeignet sind. Es wurde jedoch auch gezeigt, dass die Methode, die im kürzesten Zeitintervall agiert, ungeeignet für den Nachweis von Veränderungen des Aktinzytoskeletts ist. Anschließend zeigte ich, am Beispiel der neuronalen Differenzierung und Dedifferenzierung, wie sich der mechanische Phänotyp von Zellen mit der Bestimmung des Zellschicksals verändert. Während der Reprogrammierung zur Pluripotenz erlangten neurale Vorläuferzellen einen zunehmend steiferen Phänotyp, der sich im Prozess der neuronalen Differenzierung wieder umkehrte. Der steife Phänotyp induzierter pluripotenter Stammzellen entsprach dem von embryonalen Stammzellen, was darauf hindeutet, dass die mechanischen Eigenschaften von Zellen mit ihrem Entwicklungsstadium eng verbunden sind. Abschließend identifizierte und validierte ich neue Zielgene, die an der Regulierung der mechanischen Eigenschaften von Zellen beteiligt sind. Um diese Zielgene zu identifizieren, wurden die transkriptomischen Profile, die mit der Veränderung des mechanischen Phänotyps einhergehen, anhand einer auf maschinellem Lernen basierter Netzanalyse verarbeitet. Die Resultate wurden rechnerisch und durch genetische Manipulationsexperimente validiert. Insbesondere zeigte ich, dass das Zielgen mit der besten *in silico* Leistung, *CAV1*, die mechanischen Eigenschaften von Zellen verändert, wenn es hoch- oder herunterreguliert wird. Die Identifizierung neuer Zielgene zur Modifikation des mechanischen Phänotyps ist entscheidend für zukünftige Untersuchungen der physiologischen und pathologischen Rollen der Zellmechanik. Zusammengefasst beinhaltet diese Dissertation wesentliche Beiträge auf dem Gebiet der mechanischen Einzelzellcharakterisierung über eine Reihe von Zeitskalen und Zellveränderungen und legt den Grundstein für die Transformation der mechanischen Eigenschaften der Zellen von einem korrelativen phänomenologischen hin zu einem kontrollierbaren Parameter.



# List of Publications

The research performed during my PhD has resulted in a number of publications. In particular, the following five first-author publications form the basis of the work presented in this dissertation:

1. M. Urbanska<sup>#</sup>, M. Winzi, K. Neumann, S. Abuhattum, P. Rosendahl, P. Müller, A. Taubenberger, K. Anastassiadis, and J. Guck<sup>#</sup>. (2017). **Single-cell mechanical phenotype is an intrinsic marker of reprogramming and differentiation along the mouse neural lineage**, *Development*, 144(23), pp. 4313–4321.
2. M. Urbanska<sup>\*</sup>, P. Rosendahl<sup>\*</sup>, M. Kräter<sup>\*</sup>, and J. Guck. (2018). **High-throughput single-cell mechanical phenotyping with real-time deformability cytometry**, *Methods in Cell Biology*, 147, pp. 175–198.
3. M. Urbanska<sup>\*</sup>, H.E. Muñoz<sup>\*</sup>, J.S. Bagnall, O. Otto, S.R. Manalis, D. Di Carlo, and J. Guck. (2020). **A comparison of microfluidic methods for high-throughput cell deformability measurements**, *Nature Methods*, 17(6), pp. 587–593.
4. A.A. Nawaz<sup>\*</sup>, M. Urbanska<sup>\*</sup>, M. Herbig<sup>\*</sup>, M. Nötzel, M. Kräter, P. Rosendahl, N. Toepfner, M. Kubánková, R. Goswami, S. Abuhattum, F. Reichel, P. Müller, A. Taubenberger, S. Girardo, A. Jacobi, and J. Guck. (2020). **Intelligent image-based deformation-assisted cell sorting with molecular specificity**, *Nature Methods*, 17(6), pp. 595-599.
5. M. Urbanska<sup>\*</sup>, Y. Ge<sup>\*</sup>, M. Winzi, S. Abuhattum, M. Herbig, M. Kräter, N. Toepfner, J. Durgan, O. Florey, M. Dori, F. Calegari, F.-N. Lolo, M.Á. del Pozo, A. Taubenberger, C.V. Cannistraci, and J. Guck. (2021). **De novo identification of universal cell mechanics regulators**, *bioRxiv*, preprint available at: <https://doi.org/10.1101/2021.04.26.441418> (in revision).

Additionally, I have contributed to several collaborative projects that are not explicitly included in this monograph, but have resulted in the following publications:

6. A. Jacobi, P. Rosendahl, M. Kräter, M. Urbanska, M. Herbig, and J. Guck. (2019). **Analysis of biomechanical properties of hematopoietic stem and progenitor cells using real-time fluorescence and deformability cytometry**, *Methods in Molecular Biology*, 2017, pp. 135-148.
7. L.D.C. Stankevicius, M.R. Shaebani, D. Vesperini, M. Urbanska, D.A.D. Flormann, E. Terriac, A.K.B. Gad, F. Cheng, J.E. Eriksson, F. Lautenschläger. (2020). **Vimentin provides target search efficiency and mechanical resilience for dendritic cell migration**, *bioRxiv*, preprint available at: <https://doi.org/10.1101/2020.12.18.423401>.
8. P. Mohanasundaram, L.S.C. Rato, M. Modi, M. Urbanska, F. Lautenschläger, F. Cheng & J.E. Eriksson. (2021). **Cytoskeletal vimentin regulates cell size and autophagy through mTORC1 signaling**. *bioRxiv*. preprint available at: <https://doi.org/10.1101/2021.04.19.440145>.
9. C. Roffay, G. Molinard, K. Kim, V. Barbarassa, M. Urbanska, V. Mercier, J.G. Calvo, S. Matile, J. Guck, M. Lenz, A. Roux. (2021). **Quantitative coupling of cell volume and membrane tension during osmotic shocks**, *bioRxiv*, preprint available at: <https://doi.org/10.1101/2021.01.22.427801> (accepted in *PNAS*).

<sup>#</sup>co-corresponding authors; <sup>\*</sup>equal contributions





# Contents

<b>Abstract</b>	<b>i</b>
<b>Kurzfassung</b>	<b>iii</b>
<b>List of Publications</b>	<b>v</b>
<b>Contents</b>	<b>vii</b>
<b>Introduction</b>	<b>1</b>
<b>Chapter 1 — Background</b>	<b>5</b>
1.1. Mechanical properties as a marker of cell state in health and disease .....	5
1.2. Functional relevance of single-cell mechanical properties.....	8
1.3. Internal structures determining mechanical properties of cells .....	14
1.4. Cell as a viscoelastic material .....	22
1.5. Methods to measure single-cell mechanical properties .....	29
<b>Aims and scope of this thesis</b>	<b>35</b>
<b>Chapter 2 — RT-DC as a versatile method for image-based cell characterization and sorting</b>	<b>37</b>
2.1. RT-DC for mechanical characterization of cells .....	37
2.1.1. Operation of the RT-DC setup.....	37
2.1.2. Extracting Young's modulus from RT-DC data.....	40
2.2. Additional functionalities implemented to the RT-DC setup.....	41
2.2.1. 1D fluorescence readout in three spectral channels .....	41
2.2.2. SSAW-based active cell sorting.....	43
2.3. Beyond assessment of cell mechanics — emerging applications .....	48
2.3.1. Deformation-assisted population separation and sorting.....	50
2.3.2. Brightness-based identification and sorting of blood cells.....	50
2.3.3. Transferring molecular specificity into label-free cell sorting.....	52
2.4. Discussion.....	54
2.5. Key conclusions .....	57
2.6. Materials and experimental procedures.....	58
2.7. Data analysis .....	63
<b>Chapter 3 — A comparison of three deformability cytometry classes operating at different timescales</b>	<b>67</b>
3.1. Results.....	68
3.1.1. Representatives of the three deformability cytometry classes .....	68
3.1.2. Osmotic shock-induced deformability changes are detectable in all three methods .....	70
3.1.3. Ability to detect actin disassembly is method-dependent.....	73
3.1.4. Strain rate increase decreases the range of deformability response to actin disassembly in sDC..	75
3.2. Discussion.....	76
3.3. Key conclusions .....	81
3.4. Materials and methods .....	82

<b>Chapter 4 — Mechanical journey of neural progenitor cells to pluripotency and back</b>	<b>87</b>
4.1. Results.....	88
4.1.1. fNPCs become progressively stiffer during reprogramming to pluripotency.....	88
4.1.2. Transgene-dependent F-class cells are more compliant than ESC-like iPSCs.....	93
4.1.3. Surface markers unravel mechanical subpopulations at intermediate reprogramming stages .....	93
4.1.4. Neural differentiation of iPSCs mechanically mirrors reprogramming of fNPCs .....	95
4.1.5. The closer to the pluripotency, the higher the cell stiffness .....	97
4.2. Discussion.....	98
4.3. Key conclusions .....	101
4.4. Materials and methods.....	102
<b>Chapter 5 — Data-driven approach for <i>de novo</i> identification of cell mechanics regulators</b>	<b>107</b>
5.1. Results.....	108
5.1.1. An overview of the mechanomics approach .....	108
5.1.2. Model systems characterized by mechanical phenotype changes .....	110
5.1.3. Discriminative network analysis on discovery datasets .....	113
5.1.4. Conserved functional network module comprises five genes .....	117
5.1.5. <i>CAV1</i> performs best at classifying soft and stiff cell states in validation datasets.....	118
5.1.6. Perturbing expression levels of <i>CAV1</i> changes cells stiffness.....	120
5.2. Discussion.....	124
5.3. Key conclusions .....	127
5.4. Materials and methods.....	128
<b>Conclusions and Outlook</b>	<b>137</b>
<b>Appendix A</b>	<b>143</b>
<b>Appendix B</b>	<b>149</b>
Supplementary Tables B.1 – B.2.....	149
Supplementary Figures B.1 – B.9 .....	151
<b>Appendix C</b>	<b>161</b>
Supplementary Tables C.1 – C.2 .....	161
Supplementary Figures C.1 – C.5.....	162
<b>Appendix D</b>	<b>167</b>
Supplementary Tables D.1 – D.6.....	168
Supplementary Figures D.1 – D.7.....	174
<b>List of Figures</b>	<b>179</b>
<b>List of Tables</b>	<b>182</b>
<b>List of Abbreviations</b>	<b>183</b>
<b>List of Symbols</b>	<b>187</b>
<b>References</b>	<b>189</b>
<b>Acknowledgements</b>	<b>211</b>





# Introduction

One of the most basic but very informative medical examinations is palpation — a simple test in which a physician feels for firmness, size, and position of patient’s organs to learn about the state of their health. On a microscopic scale, an analogous test can be performed on the fundamental units of our bodies, the cells. Similar to the way organs change their stiffness in diseases, individual cells become mechanically altered during various physiological and pathological processes, such as cell fate specification<sup>1,2</sup>, immune activation<sup>1,3–6</sup>, or malignant transformation<sup>7–11</sup>. A change in the mechanical property is a global signature of alterations happening in the cell interior that can serve as an inherent, label-free marker for biomedical applications<sup>12–14</sup>.

Examining mechanical properties of cells is, however, not a trivial task, as it requires tools that operate at length and force scales relevant to cells. For reference, human cells measure between 8  $\mu\text{m}$  (red blood cell) and 100  $\mu\text{m}$  (oocyte)<sup>15</sup>, generate forces on the order of several nN<sup>16</sup>, and withstand forces on the order of 1  $\mu\text{N}$  before rupture<sup>17</sup>. To meet these scales, scientists need to devise various types of dedicated apparatus. Over the decades, a variety of methods for single-cell mechanical characterization has been introduced, with classical examples including micropipette aspiration<sup>18</sup> or atomic force microscopy (AFM)-based indentation<sup>19</sup>. Such classical methods suffer from technically demanding and time-consuming procedures that limit the number of measured cells and the uptake of these techniques beyond specialized laboratories. Recently introduced deformability cytometry approaches overcome this bottleneck by offering unprecedented throughputs and comparatively simple handling<sup>20</sup>. Throughout this thesis, I have implemented a variant of deformability cytometry, real-time deformability cytometry (RT-DC)<sup>21</sup>, as a workhorse for mechanical characterization of cells. Detailed operation of RT-DC as well as its extension into a versatile image-based characterization platform with sorting capability are described in **Chapter 2**.

While the high throughput of microfluidics-based methods for mechanical characterization of cells is a great advancement, it comes at a cost of shortening the time in which each cell is measured. The short measurement time is inextricably linked with rapid force application, a factor that can influence the magnitude of assessed mechanical properties — cells typically appear stiffer when probed faster<sup>22–24</sup>. Additionally, at very fast probing rates, the relative magnitude of loss (viscous) and storage (elastic) moduli can be completely reversed<sup>25–27</sup>. The microfluidics-based deformability cytometry methods themselves vary not only in the type of channel geometries, but also in the range of timescales in which they induce cell deformation. In the project presented in **Chapter 3**, I undertook an effort of a direct comparison of three state-of-the-art deformability cytometry methods operating at different timescales in two standardized assays of osmotic shock and actin filament disassembly. This study showed that while all three methods detect osmotic shock-induced changes in cell deformability, the sensitivity to

actin disassembly is method-dependent and no deformability response was observed for the method operating at the highest strain rate.

In living organisms, there are several processes for which the mechanical properties of cells are of critical importance. These processes typically involve direct exposure of cells to forces, as is the case for cells circulating through microvasculature<sup>28</sup> or cells squeezing through narrow spaces within solid tissues during cancer metastasis<sup>29</sup>. Another example of a process to which cell mechanics contributes substantially is morphogenesis<sup>30</sup>, during which cells change shape, divide and relocate to give rise to organs and tissues of an adult body. While studying the mechanical properties of cells during morphogenesis may be challenging *in situ*, it is straightforward to monitor mechanical changes accompanying cell fate transitions in *in vitro* model systems. The knowledge generated with such model systems can be used to predict the behavior of cells in more complex environments. Within the framework of the project presented in **Chapter 4**, I investigated the cell mechanical changes in a model of dedifferentiation of murine fetal neural progenitor cells (fNPCs) to induced pluripotent stem cells (iPSCs), and in a converse process of differentiation along neural lineage. I found that fNPCs become progressively stiffer during reprogramming to pluripotency, and that this stiffening is mirrored by iPSCs becoming more compliant in differentiation towards the neural lineage. Furthermore, I showed that the mechanical phenotype of iPSCs is comparable with that of pluripotent stem cells isolated from mouse embryos, suggesting that mechanical properties of cells are inherent to their developmental stage.

Characterization of the mechanical properties during cell state transitions such as cell differentiation brings valuable biophysical insights into cell function, however, to be able to understand and control the mechanical properties, it is necessary to unravel their molecular origins. Mechanical phenotype of cells is attributed in the biggest part to the cytoskeletal structures<sup>31</sup>, with actin network and its contractility playing the most prominent role<sup>32,33</sup>. Other intracellular features, such as the architecture of the plasma membrane, its attachment to the actin cortex, or cytoplasmic packing, can also contribute to the measured properties<sup>20</sup>. Many of the known contributors to cell mechanics are central to cell homeostasis and their alteration can lead to severe impairment of cell function. Thus, it is important to seek novel molecular targets through which mechanical properties could be tuned in subtle ways. In **Chapter 5**, I introduce a mechanomics approach for *de novo* identification of cell mechanics regulators that tackles this challenge. Mechanomics relies on machine learning-based discriminative network analysis of transcriptomic data associated with mechanical phenotype changes in systems ranging from stem cell development to cancer progression. Based on intersection of networks inferred from two systems, we identified a conserved module of five genes with putative roles in the regulation of mechanical properties. We next validated the power of the individual genes to discriminate between soft and stiff cell states *in silico*, and demonstrate experimentally that the top scoring gene, *CAV1*, changes the mechanical phenotype of cells when silenced or overexpressed. Mechanomics approach has the power of hypothesis-free identification of genes involved in cell mechanics regulation and paves

the way towards engineering cell mechanical properties on demand to explore their impact on physiological and pathological cell functions.

This thesis opens with a background chapter (**Chapter 1**) introducing concepts from the field of cell mechanics and mechanical characterization of cells. It continues with a comprehensive introduction of RT-DC, a versatile method for morphological and mechanical characterization of cells and its recent extension to a sorting platform (**Chapter 2**). Next, the impact of measurement timescale on the mechanical characterization of cells in microfluidics-based systems is revealed by comparing three deformability cytometry methods operating at different timescales (**Chapter 3**). **Chapter 4** presents characterization of cell mechanical phenotype change in cell fate transitions, on the example of (de-)differentiation of murine stem cells along the neural lineage. Finally, **Chapter 5** introduces a method that can be used to identify novel targets involved in the regulation of the mechanical phenotype of cells. The obtained results are discussed and put into the context of the relevant scientific literature within the individual result chapters (**Discussion** sections in **Chapters 2–5**). At the end of the thesis, overarching conclusions and future research directions are presented (**Conclusions and Outlook**). Together, this thesis encompasses a collection of contributions at the frontier of single-cell mechanical characterization across timescale and cell transitions.





# — Chapter 1 —

## Background

### 1.1. Mechanical properties as a marker of cell state in health and disease

Over the years, changes in mechanical properties of cells have been reported to accompany many physiological and pathological processes, such as cancer progression<sup>7–10</sup>, leukocyte activation<sup>1,3–6</sup>, red blood cells (RBCs) pathologies<sup>34,35</sup>, or stem cell differentiation<sup>1,2</sup>. Since measurements of mechanical properties circumvent the need of using extrinsic labels, they constitute an attractive, noninvasive way of cell state identification with an implicated clinical applicability (**Figure 1.1**).

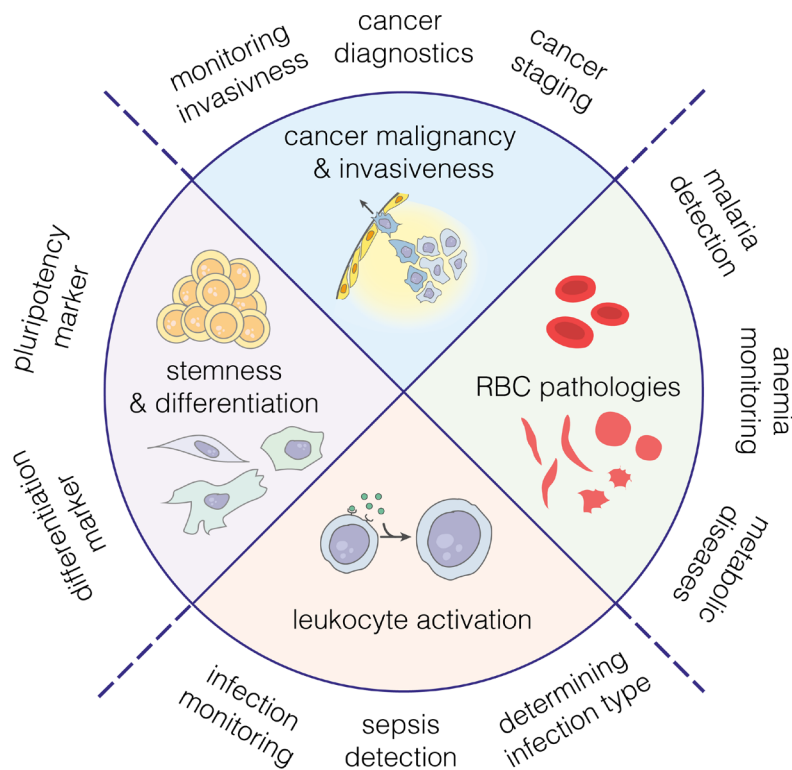


**Figure 1.1 | Mechanical phenotype as a marker of cell state transitions.** The chart provides an overview of several processes that can be identified by looking at the mechanical properties of cells (inner circle) and highlights the biomedical application areas of monitoring the mechanical cell properties (outer region). This figure is modified after Di Carlo<sup>12</sup>.

#### 1.1.1. Malignancy and invasiveness of cancers

Mechanical features of cells and their microenvironment are known to play an important role in carcinogenesis<sup>29,36,37</sup>. While tumorous tissues are typically characterized by increased stiffness<sup>38</sup>, malignant transformation of cells was shown to be correlated with cell softening in overwhelming

majority of studies, and the cancerous cells become softer with increasing invasive potential (see Suresh<sup>39</sup> and Alibert *et al.*<sup>40</sup> for reviews). The decrease in cell stiffness is likely a reflection of the changes in the cytoskeletal organization that are characteristic for malignancy and metastatic progression<sup>39,41–44</sup>, and holds true for cancers originating from different organs, including gastrointestinal tract<sup>41,45</sup>, pancreas<sup>41,46,47</sup>, breast<sup>7,45–48</sup>, mouth<sup>49</sup>, ovaries<sup>8,44,48</sup>, bladder<sup>45,47</sup>, lung<sup>46</sup> and cervix<sup>47</sup>. Exception from this rule constitute leukemias, for which cancerous cells appear stiffer than their healthy counterparts<sup>3,5,50–52</sup>. While many of the aforementioned studies have been performed on cell lines, several attempts of mechanical measurements on cancer cells from patients<sup>5,8,10,46,49</sup> demonstrate that measurements of mechanical properties could be used for cancer diagnostics and staging in clinical settings.

### 1.1.2. Immune cell activation and blood-related diseases

Another process hallmarked by cell mechanical phenotype change is the activation of leukocytes. Leukocytes are the chief actors of the immune system involved in fighting pathogens and inflammatory states in the human body. They are a heterogenous group of cells that consists of granulocytes (neutrophils, eosinophils and basophils), monocytes and lymphocytes, with neutrophils being the most abundant leukocyte type and accounting for 50–70% of all white blood cells<sup>53</sup>. Various biochemical agents, such as cytokines and bacterial products can induce neutrophil activation, during which cells change their inner structure and morphological features in preparation for the immunological function<sup>53</sup>. While several studies have shown that *in vitro* activation of neutrophils is connected with their stiffening within first minutes after the activation<sup>54–57</sup>, other studies reported increased size and deformability of neutrophils on the timescales of 30–60 minutes after exposure to a stimulus<sup>1,58</sup>. These two observations were integrated in recent time-resolved studies of the neutrophil response, which revealed that indeed after the initial phase of stiffening and compaction (first 15 minutes upon stimulation), the cells become larger and more deformable at longer timescales<sup>5,6</sup>. Macrophages and dendritic cells derived from monocytes showed varied deformability responses upon activation, depending on the applied stimulus<sup>4</sup>. In patient-derived samples, neutrophils were observed to have larger size and increased deformability for conditions such as acute lung injury and viral respiratory tract infection<sup>5</sup>, while lymphocytes and monocytes showed more pronounced increase of these two parameters for Epstein-Barr-virus infections<sup>5</sup>. Granulocytes were also shown to have higher deformability in patients with sepsis<sup>59</sup>, and characteristic fingerprints of leukocyte deformability have been associated with various chronic and acute inflammatory conditions<sup>10</sup>. Most recently, it was shown that during COVID19 infection lymphocytes become stiffer, monocytes increase in size, and neutrophils acquire bigger size and higher deformability characteristic for activated state<sup>60</sup>. Interestingly, changes in deformability of leukocytes were also reported in patients with depressive disorder<sup>61</sup>. These studies show that deformability measurements could be used to detect immune cell activation and that the differential responses of the specific immune cell subpopulations could be indicative of the type of infection or inflammatory state.

Beyond mechanical phenotyping of leukocytes, the information about biophysical properties of RBCs is also of potential diagnostic relevance. Firstly, spherocytosis — a condition of spherical rather than biconcave discoidal shape of RBCs characteristic for hemolytic anemias — is characterized by lowered deformation of RBCs<sup>5</sup> and higher Young's modulus<sup>62</sup>. Secondly, the RBCs from sickle cell anemia patients were shown to have an increased elastic modulus, bending modulus and viscosity<sup>63–66</sup>. Furthermore, malaria-infected RBCs are characterized by lowered deformability and increased bending modulus of the membrane<sup>5,67–69</sup>. Altered deformation capacity of RBCs was also shown to accompany conditions not directly related to blood, such as COVID19 infection<sup>60</sup>, persistent depressive disorders<sup>61</sup>, or metabolic disorders such as diabetes and obesity<sup>70</sup>, opening a possibility of screening for non RBC-related diseases by looking at the biophysical phenotype of RBCs.

### **1.1.3. Pluripotency, stemness and cell fate specification**

During embryonic development, pluripotent stem cells differentiate into specialized cell types to give rise to all tissues of the adult body. The transition from undifferentiated to more specialized cell states is underlined by rearrangements in nuclear and cytoskeletal architecture<sup>71,72</sup>, what leads to changes in mechanical properties of cells. Stiffness changes have been shown to be an indicator of early differentiation of murine and human embryonic stem cells (ESCs)<sup>1,70,73</sup>, and cardiac<sup>74</sup> as well as chondrogenic<sup>75</sup> differentiation of human ESCs. Apart from studies on the pluripotent ESCs, mechanical phenotype changes during cell differentiation from multipotent stem cells have been characterized. For example, human mesenchymal stem cells were shown to change their mechanical phenotype during differentiation towards osteogenic<sup>76–78</sup> and adipogenic lineages<sup>77</sup>. Furthermore, the differentiation potential for a given lineage of adipose-derived stem cells (a heterogenous population of mesenchymal stem and stromal cells derived from adipose tissue) was shown to correlate with cell stiffness<sup>79</sup>. Human myeloid precursor cells have been shown to soften during differentiation towards neutrophils and monocytes, but stiffen during differentiation towards macrophages<sup>2,51</sup>. Finally, human hematopoietic stem and progenitor cells<sup>80</sup> and human skeletal stem cells<sup>81</sup> were shown to be distinguishable from other cell types found in bone marrow based on their size and deformability. This shows that mechanical phenotyping has potential for use in distinguishing differentiated cells of specific fates, or separate stem cells from mixed populations. Using the mechanical phenotype as a marker of cell state for cell enrichment is particularly attractive for cases in which surface markers are not well defined, or antibody staining is not desired due to required purity of cells for downstream applications.

## 1.2. Functional relevance of single-cell mechanical properties

Mechanical properties determine how easily cells deform in response to applied forces. Thus, beyond being a valuable marker of cell state transitions, they also influence cellular functions that depend on the ability of cells to change shape. Such functions include circulation through microvasculature, interstitial and transepithelial migration, positioning in multicellular assemblies, cell fate specification as well as proliferation in crowded environments.

### 1.2.1. Circulation through microvasculature

Microcapillaries, the smallest vessels of the cardiovascular system, can have diameters as low as  $2\ \mu\text{m}$ <sup>34,82</sup>, much lower than typical diameters of blood cell ( $8\ \mu\text{m}$  for RBCs<sup>15</sup>, and between  $6$  and  $30\ \mu\text{m}$  for leukocytes<sup>83</sup>). Thus, for efficient circulation through microvasculature, cells need to sufficient deformability<sup>34,82</sup> (**Figure 1.2**). Compromised deformability of blood cells can disturb physiological blood flow and lead to inefficient perfusion of organs, lower oxygen transport and vascular occlusions, all of which have debilitating effects on patient's health<sup>84</sup>. For example, the RBCs stiffened by malaria infection were shown to obstruct small capillaries *in vitro* more readily than the uninfected RBCs<sup>85,86</sup>, and the reduced deformability of RBCs was correlated with fatal disease outcome in patients<sup>87</sup>. Increased occlusions of the capillary system were also observed for less deformable RBCs in sickle cell anemia<sup>88</sup>. Furthermore, stiffened leukocytes characteristic for leukemias<sup>3,50,89,90</sup> and stiffening of leukocytes in response to chemotherapy<sup>91</sup> are associated with leukostasis — a formation of leukocyte plugs in microcapillaries. The accumulation of leukemic cells in the blood vessels of brain or lung can result in sever conditions such as intercranial hemorrhage or respiratory failure<sup>91</sup>. Other conditions in which decreased deformability of leukocytes was reported to contribute to vascular occlusions include acute respiratory distress syndrome<sup>92,93</sup>, sepsis<sup>94</sup> and pneumonia<sup>95</sup>.

Sufficient deformability of cells is also crucial for delivery of stem cells to target organs after intravenous transplantation. Various types of stem cells, including mesenchymal stem cells, hematopoietic stem and progenitor cells as well as other tissue-specific progenitor stem cells, can be transplanted to patients for immunomodulatory or regenerative purposes<sup>96</sup>. When administered intravenously, the cells need to pass through pulmonary capillary beds before arriving to target organs, what carries a risk of substantial sequestration of cells in the lungs and diminished or delayed homing<sup>97–100</sup>. It has recently been demonstrated that expanding mesenchymal stem cells in 3D spheroids rather than in 2D plastic-adherent cultures results in a smaller and more deformable phenotype of cells<sup>28</sup>. This phenotype was connected with faster passage through microfluidic channels mimicking microcirculation, decreased trapping in lung and increased recovery in organs such as liver, heart, spleen or kidney upon transplantation into mice<sup>28</sup>, suggesting that engineering biophysical properties of stem cells could foster their capability to pass microcirculation and enable efficient transplantation.

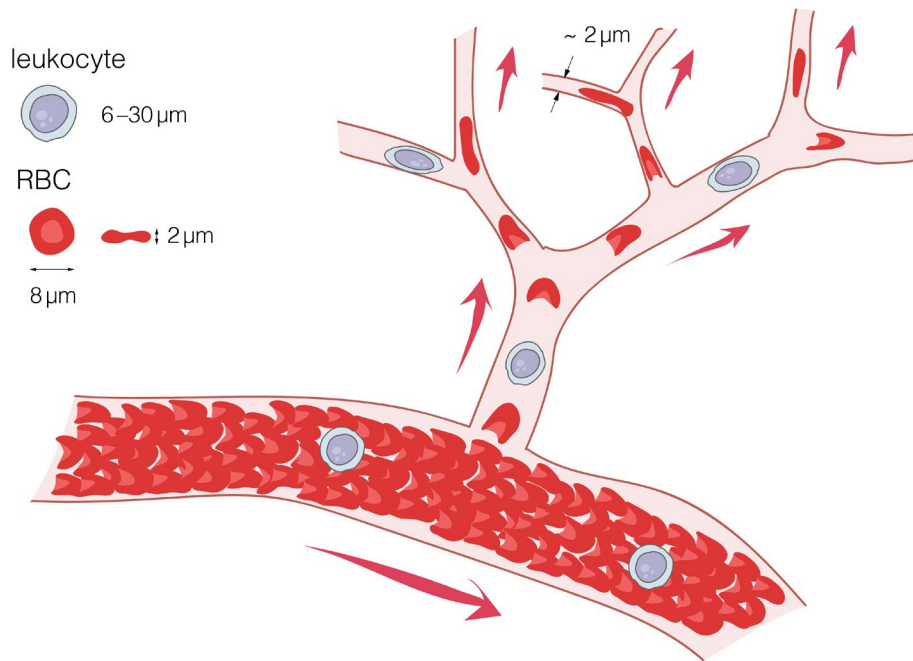


**Figure 1.2 | Circulation through microvasculature requires blood cells to deform.** When circulating through microvasculature, blood cells encounter increasingly narrow capillaries. When the diameter of the vessel becomes smaller than the cell diameter, cells need to deform to pass it. Reference dimensions of undeformed RBCs and leukocytes are provided in the figure.

### 1.2.2. Invasion and migration in cancer metastasis

Another important cellular function influenced by mechanical properties of cells is invasion and migration in the context of cancer malignancy. Metastasis, a sequence of events that leads to development of secondary tumors, is the major cause of cancer-related deaths<sup>101</sup>. Metastatic progression is a multistep process that includes detachment of the cells from primary tumor, migration through surrounding tissues, two events of crossing the epithelium during entering and exiting the blood vessels, as well as colonization and secondary tumor formation<sup>102</sup> (**Figure 1.3**).

Softer phenotype of cancer cells, frequently associated with cancer invasion and metastasis, has been hypothesized to facilitate squeezing of cells through narrow spaces<sup>7,44,103</sup>, and there is some direct evidence that cell stiffness plays a role at various stages of the metastatic cascade. For example, during detachment from primary tumor, cells undergo epithelial to mesenchymal transition (EMT), a process in which epithelial, polarized cells undergo cytoskeletal remodeling and reduction of intracellular adhesion to acquire mesenchymal, motile phenotype<sup>104</sup>. EMT was shown to reduce cellular stiffness and promote invasion<sup>105</sup>, and softening of cells during their detachment and migration from breast cancer spheroids was directly observed<sup>106,107</sup>. Recently, it has also been demonstrated that cancer cells soften while entering narrow constrictions<sup>108</sup>, suggesting that they adapt their mechanical properties to the encountered migratory challenges. Interestingly, while interphase cells become softer during EMT, the mitotic cells increase their cortical stiffness, what could have implications for successful cell division in crowded environments<sup>109</sup>. The ability of cells to deform is also crucial for transendothelial migration

during intra- and extravasation<sup>110</sup>, and the deformability of cell nucleus is rate-limiting for passing through narrow pores<sup>111–113</sup>, both when crossing epithelial barriers and invading the tissues. While cell softening is generally thought to promote migration, stiffer cells may have advantage for resisting cell damage during exposure to forces, for example in circulation. Thus, it is likely that for successful metastasis cancer cells need to adapt their mechanical properties throughout the process<sup>29</sup>. Since cell softening and mechanical adaptability of the cells appear crucial for successful metastasis, mechanical properties of cancer could be targeted for preventing cancer spreading, a perspective that is actively explored<sup>114,115</sup>.

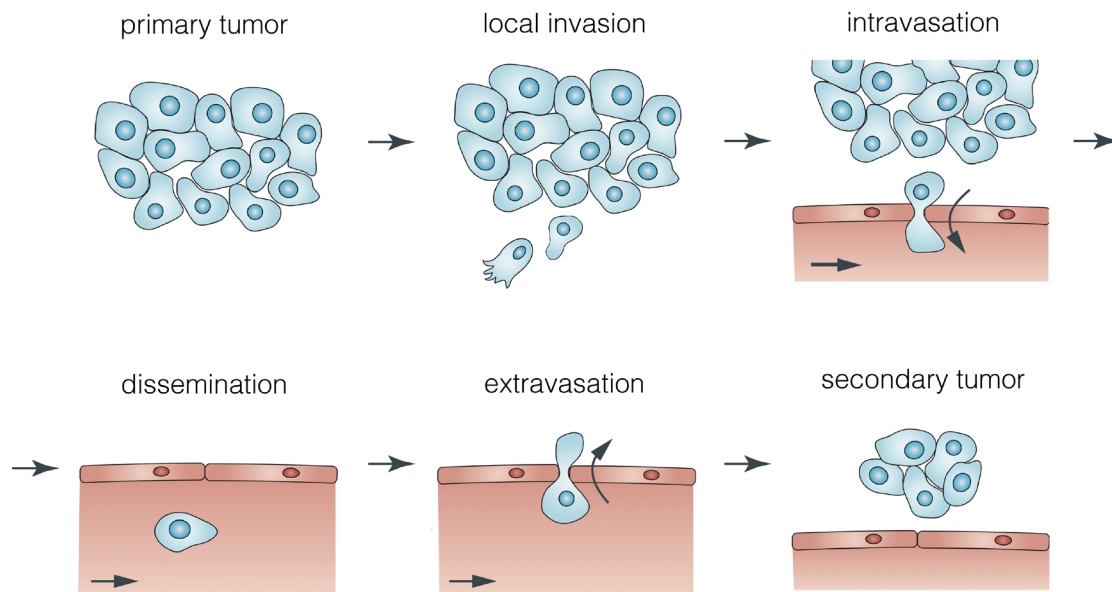


**Figure 1.3 | Stages of cancer metastasis.** In distant metastasis cancer cells are disseminated to new sites via bloodstream to form secondary tumors. First, cells detach from the primary tumor and explore the surrounding tissue (local invasion). The detached cells enter nearby blood vessels (intravasation) and are carried with the bloodstream (dissemination). Some of the circulating cells exit the blood vessels (extravasation), migrate through local tissue, proliferate and form a secondary tumor. This figure is modified from Wirtz *et al.*<sup>116</sup>.

### 1.2.3. Migratory capability of immune cells

Another type of cells that undergo extensive migration are immune cells. Immune cells extravasate and migrate through tissues to reach the sites of infection or inflammation within the body<sup>117,118</sup>. For example, in innate immunity response, neutrophils and macrophages are recruited to infection sites to eliminate pathogens from the body<sup>119</sup> (**Figure 1.4**). Neutrophils circulate in the blood stream and extravasate into tissues when captured by adhesion molecules displayed by activated endothelium<sup>120</sup>. Macrophages are either recruited locally from the population residing in the tissues or are differentiated from monocytes recruited from the blood stream<sup>117,121</sup>.

Differentiation of myeloid precursor cells towards neutrophils is accompanied by increase in cell deformability and decrease in viscosity, both of which facilitate migration<sup>2,51,122</sup>. High deformability of neutrophils was also shown to facilitate their adhesion to blood vessels essential for extravasation<sup>123</sup>. Neutrophils show increase in deformability during activation<sup>58,124,125</sup>, what could further promote their

migratory capability. Same as for cancer cells, the migration of neutrophils through narrow spaces was shown to be limited by the deformation of their nucleus<sup>126</sup>, and the whole cells become transiently softer when entering constrictions<sup>127</sup>. Contrary to neutrophils, macrophages appear less compliant than their precursor cells on short timescales, however, they do show decreased viscosity and increased compliance at longer timescales<sup>2</sup>. Since macrophages do not circulate through vasculature, they may not require high deformability at short timescales, and their long timescale properties likely support tissue infiltration<sup>2</sup>. On the other hand, high elasticity of macrophages (measured on short timescales) was reported to facilitate phagocytosis and increase with activation of macrophages<sup>128</sup>. Other immune cells that migrate into tissues, such as lymphocytes B and T, natural killer cells, or dendritic cells, experience similar obstacles and their successful trafficking is likely also influenced by their mechanical properties.

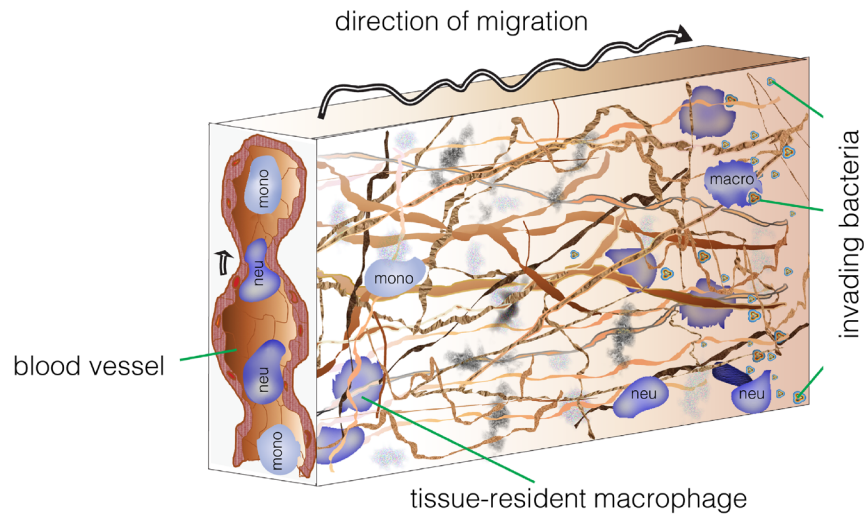


**Figure 1.4 | Migration of neutrophils and macrophages to bacterial infection site.** In case of bacterial infection, neutrophils and monocytes circulating in the blood vessels extravasate and migrate towards the infection site. After leaving the blood stream, monocytes differentiate into macrophages. Other macrophages that already reside in the tissues, the so-called tissue-resident macrophages, are also recruited towards the infection site. mono – monocyte, macro – macrophage, neu – neutrophil. This figure is modified from Ekpenyong *et al.*<sup>2</sup>.

#### 1.2.4. Cell fate specification and morphogenesis

Cell mechanics has been shown to play a role in cell fate specification and development, starting from the earliest embryonic stages (see **Figure 1.5** for an overview of early embryonic development in mice). The compaction of the 8-cell-stage mouse embryo, crucial for progression of development, is driven by pulses in cortical tension generated by actomyosin contractility of the outside-facing cell surfaces<sup>129</sup>. Subsequent lineage specification of outer-facing trophectoderm (TE) and inner cell mass (ICM) is triggered by differences in cell mechanical properties: cells with lower cortical tension tend to engulf other cells and position outwards, whereas cells with high cortical tension are internalized<sup>129,130</sup>. The specification towards TE and ICM is supported by the Hippo/YAP mechanosensitive pathway<sup>131–133</sup>. The loss of naïve pluripotency of ESCs, isolated from ICM of early blastocyst (E3.5, **Figure 1.5**), and

their differentiation towards primed state has been demonstrated *in vitro* to require membrane tension decrease<sup>134,135</sup>.

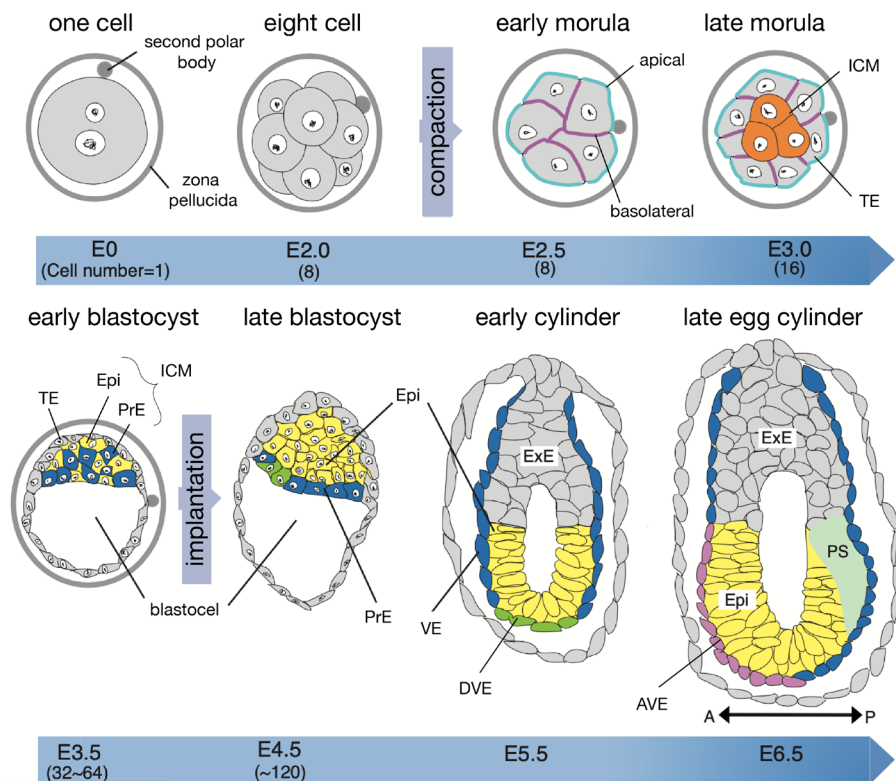


**Figure 1.5 | An overview of early development of a mouse embryo.** Schematic illustrates main morphological changes and cell fate specification events that take place from fertilization to gastrulation in the mouse embryo. The time of development is indicated at the bottom axes; E, embryonic day. Cell types are color coded. AVE, anterior visceral endoderm; DVE, distal visceral endoderm; Epi, epiblast; Exe, extra-embryonic ectoderm; ICM, inner cell mass; PrE, primitive ectoderm; PS, primitive streak; TE, trophoblast; VE, visceral endoderm; symmetry axis in E6.5: A, anterior; P, posterior. This figure is adapted from Takaoka and Hamada<sup>136</sup>.

At later stages of embryonic development where EMT is involved, such as primitive streak formation, gastrulation (**Figure 1.6**) and neural crest cells formation, the cells acquiring mesenchymal phenotype, by analogy to EMT in cancer, are expected to soften what would support their migratory capabilities. It has been shown in our group that inducing EMT in epiblast stem cells (EpiSCs; isolated from E4.5 epiblast) makes cells more deformable (Dr. Maria Winzi, unpublished data) and that differentiation of ESCs towards mesoderm and ectoderm decreases cell stiffness<sup>137</sup>. During gastrulation in zebrafish embryo, the three generated cell lineages were shown to acquire distinct mechanical phenotypes with ectoderm cells exhibiting highest cortical tension, mesoderm intermediate one, and endoderm being the softest<sup>138</sup>. This differences in cortical tension are sufficient to guide cell sorting in multicellular assemblies, with stiffest ectoderm cells being sorted towards aggregate center when mixed with mesoderm cells<sup>138</sup>. Apart from enabling cell migration or sorting, mechanical properties of individual cells can contribute to stiffness of local microenvironment and through that influence behavior of



neighboring cells. A prominent example constitutes migration of neural crest cells in *Xenopus laevis* embryos, which is driven by myosin-dependent stiffening of underlying mesoderm cells<sup>139,140</sup>.

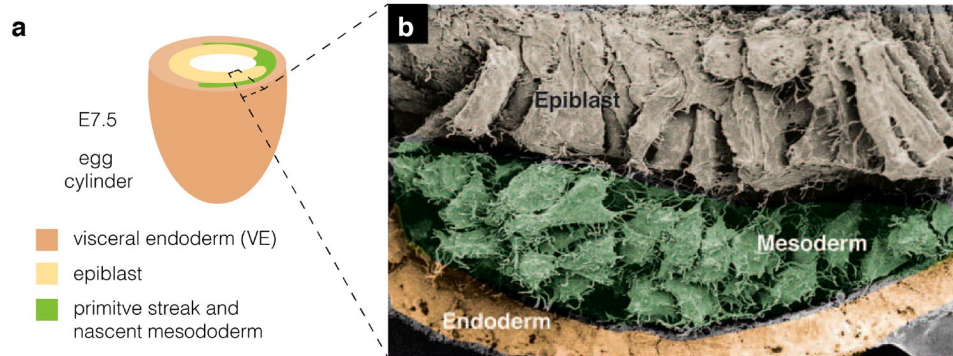


**Figure 1.6 | Epithelial and mesenchymal cell phenotype in gastrulating mouse embryo.** **a**, Diagram of a E7.5 gastrulating mouse embryo. **b**, Scanning electron micrograph of a transverse section through a E7.5 mouse embryo. Epiblast, mesoderm and endoderm are color coded as in **a**. Note that epiblast has an epithelial structure with closely packed cells, while mesoderm corresponds to loosely packed mesenchymal phenotype. Mesoderm emerges from epiblast during EMT. This figure was modified from Ferrer-Vaquero *et al.*<sup>141</sup>.

All of the above examples of functional relevance of mechanical properties were focused on whole-cell stiffness or deformability of cells. Undoubtedly, this is a simplified view, as in many of the discussed processes the mechanical properties of the microenvironment and the interactions between the cells play an equally important role<sup>37,142,143</sup>. Furthermore, often not the static whole-cell mechanical properties, but their local anisotropies or actively-driven dynamic evolution over time are the drivers of cellular functions<sup>30</sup>. These aspects are, however, beyond the scope of this thesis.

The processes discussed in this section illustrate that mechanical properties of cells are of crucial importance for cellular functions. To be able to influence mechanics-dependent cell functions, it is necessary to understand structural and molecular determinants of single-cell mechanical properties.

### 1.3. Internal structures determining mechanical properties of cells

Most animal cells — including human and mouse cells characterized in this thesis — are enclosed by a plasma membrane and contain membrane-bound organelles as well as membrane-less compartments and macromolecular assemblies<sup>144</sup>, an overview of which is presented in **Figure 1.7**. All of these constituents are embedded in a semi-fluid, gel-like cytoplasm, that is characterized by a high degree of macromolecular crowding<sup>145</sup>. Membrane-bound organelles include cell nucleus, Golgi apparatus, endoplasmic reticulum, lysosomes and other vesicles, such as peroxisomes or endosomes. The functional cell elements not surrounded by membranes include ribosomes, centrosome, nucleolus and macromolecular assemblies such as the cytoskeleton filaments. In the following sections, cellular constituents that are known to contribute to the mechanical properties of cells are discussed in detail.

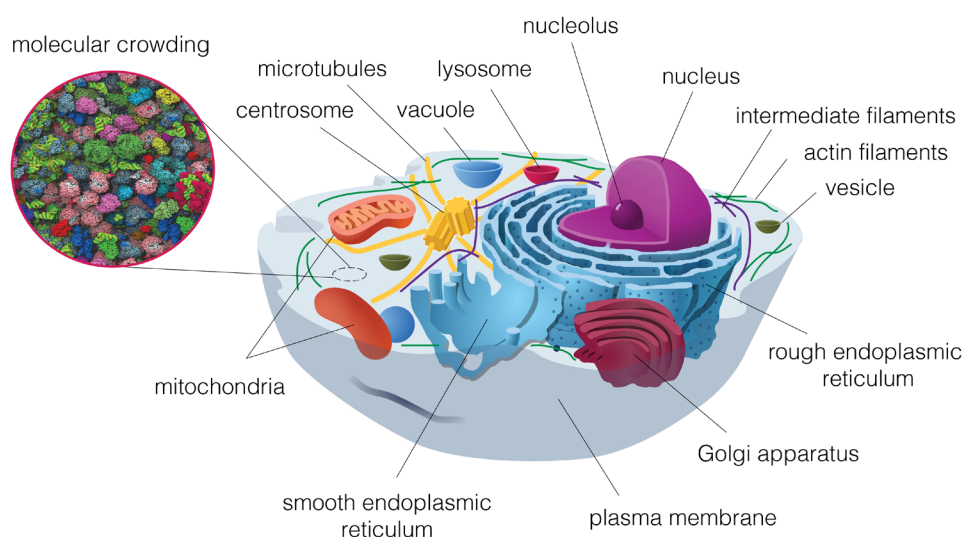


**Figure 1.7 | Schematic diagram of an animal cell.** The diagram presents simplified cell architecture with an overview of main cell structural and functional components. In reality, the cell is much more crowded with organelles and macromolecules. The inset on the left shows a model of the molecular crowding in the bacterial cytoplasm. The cell image is adapted from Wikimedia Commons<sup>146</sup>, the inset depicting cytoplasmic crowding is adapted from McGuffee *et al.*<sup>147</sup>.

#### 1.3.1. Cytoskeleton

The cytoskeleton, an interconnected network of filamentous proteins, gives structural stability to the cell and is one of the major contributors to mechanical properties of the cell<sup>31</sup>. The three major types of cytoskeletal networks present in eucaryotic cells are actin, intermediate filaments, and microtubules. Each of these networks has a distinct supramolecular architecture, mechanical characteristics and distribution within the cell (**Figure 1.8**).

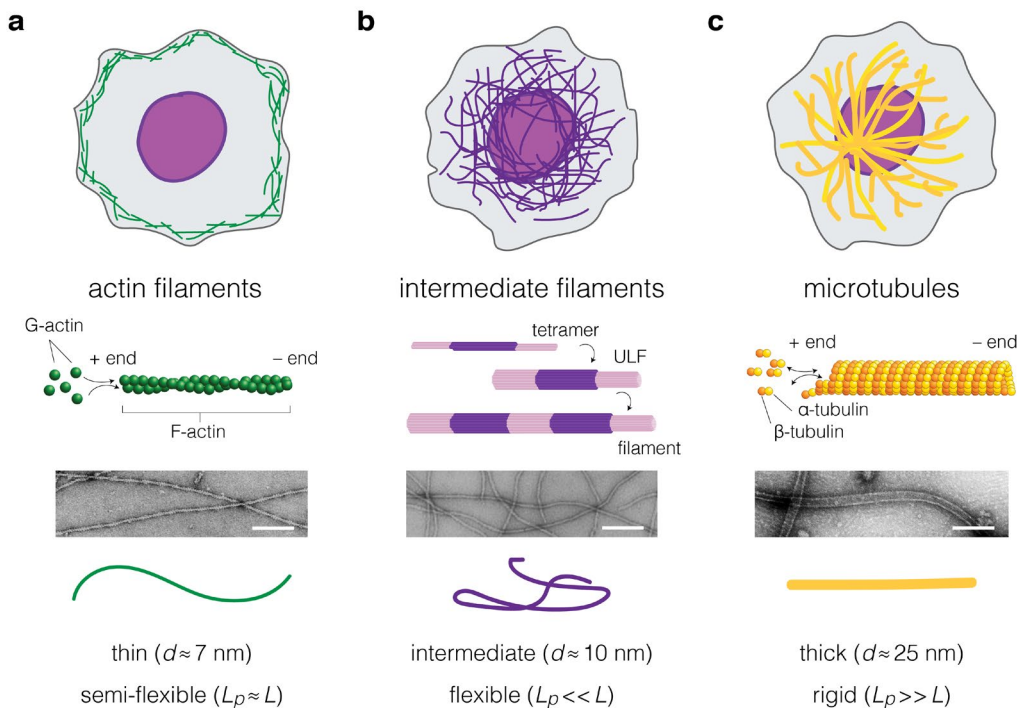


**Figure 1.8 | The three major types of cytoskeletal networks.** a, Actin filaments. b, Intermediate filaments. c, Microtubules. From top to bottom, the panels depict the typical distribution of respective filamentous networks within a cell, the structure of the filaments, the morphology of the respective filaments reconstituted *in vitro* and imaged with transmission electron microscopy, and the visualization of the relative flexibility of the filaments. ULF – unit-length filament. The electron micrographs are adapted from Hermann *et al.*<sup>148</sup>, scale bars: 100 nm.

Actin filaments are helices of two intertwined monomer strands, with faster growing plus end, and slower growing minus end. Their persistence length  $L_p$ , a length over which the directionality of a filament is preserved, amounts to several micrometers<sup>149–152</sup>. This means that the actin filaments show limited bending over their typical lengths  $L$  ( $L_p \approx L$ ) and are considered semi-flexible<sup>153</sup>. In suspended cells, actin filaments organise predominantly into an actin cortex — a thin, crosslinked network underpinning the plasma membrane<sup>32</sup> (**Figure 1.8a**). In adherent cells, apart from the cortical mesh, actin filaments also form bundled cables spanning longer distances called stress fibers<sup>154</sup>. Importantly, actin filaments do not form an inert network, but are under tension generated by the contractility of myosin motors, mainly non-muscle myosin II. Myosin motors slide antiparallel actin filaments relative to each other using energy produced by ATP hydrolysis. The contractile capability of the actin network is influenced by its architecture, which is governed by the following actin accessory proteins: (i) passive actin cross-linkers (e.g.,  $\alpha$ -actinin and formin), (ii) actin nucleators that initiate polymerization (formins) and branching (Arp2/3), and (iii) actin-membrane linkers that connect the actin cortex to the plasma membrane (ERM (ezrin, moesin and radixin) or myosin I protein families)<sup>155,156</sup> (**Figure 1.9**). On the regulatory level, actomyosin contractility is primarily governed by the signaling cascades mediated by a Rho GTPase RhoA and its downstream effector Rho-protein kinase ROCK<sup>33</sup> (**Figure 1.10**). Actin cytoskeleton modulates cell shape and participates in many active cellular processes in which generation of force is required, such as cell migration or cytokinesis.

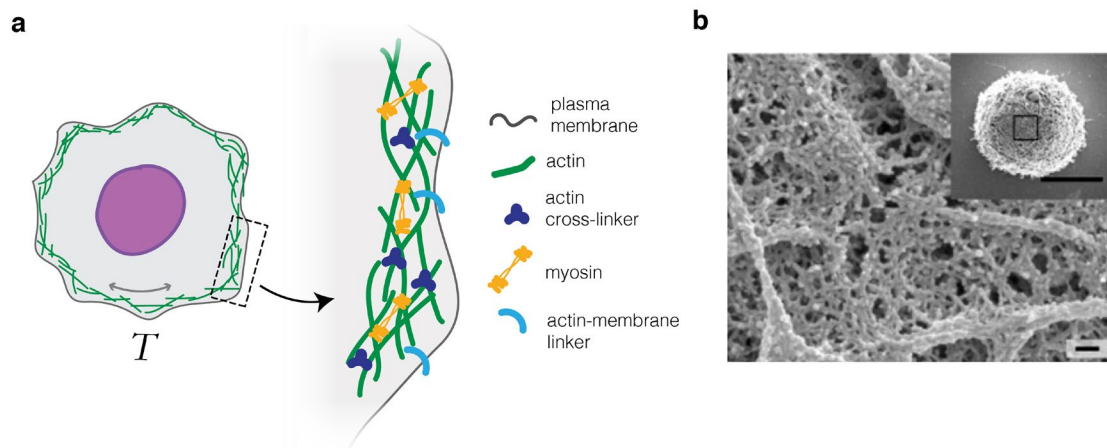


**Figure 1.9 | Actin cortex underlies the plasma membrane and determines the mechanical properties of the cell surface.** **a**, The actin cortex directly underlies the plasma membrane and is under tension,  $T$ , due to contractility generated by myosin motors. Zoom-in: the actin filaments in the cortex are cross-linked by myosin and passive actin cross-linkers, the cortex is anchored to the plasma membrane via actin-membrane linkers such as ezrin, radixin and moesin (ERM). **b**, Scanning electron micrograph showing the actin cortex meshwork of a membrane-extracted interphase HeLa cell. Scale bars: 10  $\mu\text{m}$  in the overview image, 100 nm in the magnified image. The electron micrograph is adapted from Chugh *et al.*<sup>157</sup>.

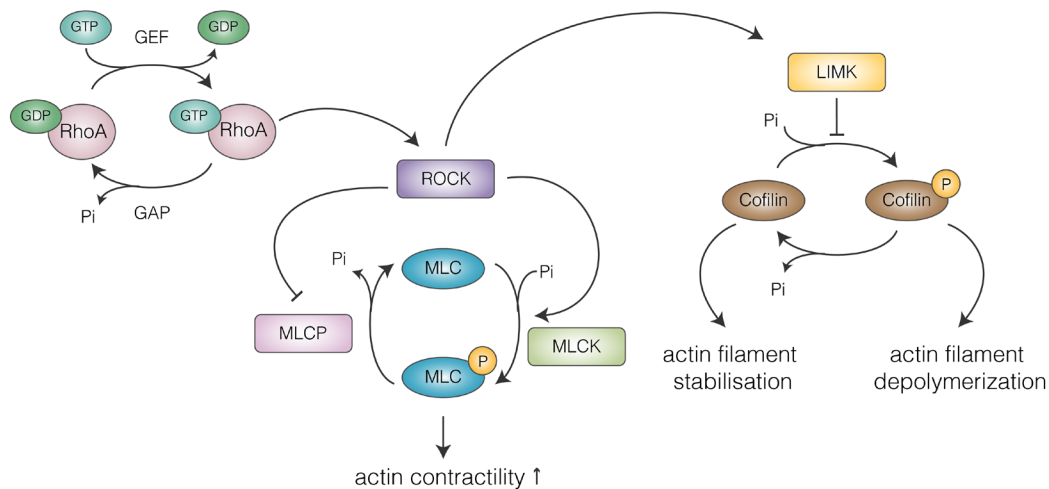


**Figure 1.10 | The contractility of the actin cytoskeleton is regulated by RhoA signalling pathway.** RhoA is a small GTPase that is active when associated with GTP. Its cycling between the active and inactive state is facilitated by the regulatory proteins: guanine nucleotide exchange factors (GEFs) and GTPase-activating proteins (GAPs). Through its effector protein ROCK, RhoA increases the phosphorylation of myosin light chain (MLC) in dual way: by directly phosphorylating MLC, in parallel with MLC kinases (MLCK), and by inhibiting MLC phosphatases (MLCP). Increased MLC phosphorylation results in increases actin contractility. ROCK additionally contributes to stabilization of actin filaments by activating LIM domain-containing protein kinase (LIMK) that inhibits cofilin dephosphorylation. The scheme is based on the information in references<sup>158,159</sup>.

Intermediate filaments are the most heterogeneous family of the cytoskeletal filaments, that includes members such as vimentin, keratin, or desmin filaments<sup>148</sup>. The basic structural units of the intermediate filaments are elongated dimers that combine in pairs to form tetramer rods. Eight tetramers associate radially into unit-length filaments before assembling longitudinally into 10 nm wide apolar filaments (**Figure 1.8b**). With a persistence length on the order of 1  $\mu\text{m}$  ( $L_p \ll L$ ), intermediate filaments are the most flexible cytoskeletal filaments<sup>160,161</sup>. Typically, they form a dense meshwork located deeper inside the cytoplasm than the actin cortex. This meshwork surrounds the cell nucleus and spreads towards the cell periphery<sup>148</sup>. It gives mechanical stability to the cells and has been shown to protect the genetic material contained within the nucleus from damage during passage through narrow constrictions<sup>162</sup>. Apart from the cytoplasmic intermediate filaments, a special class of intermediate filaments called lamins, comprised of A-type and B-type lamins, is involved in the formation of the nuclear lamina that underlays the nuclear envelope<sup>163</sup>. The nuclear lamina is connected to the cytoskeleton via the linker of nucleoskeleton and cytoskeleton (LINC) complex (**Figure 1.11**).

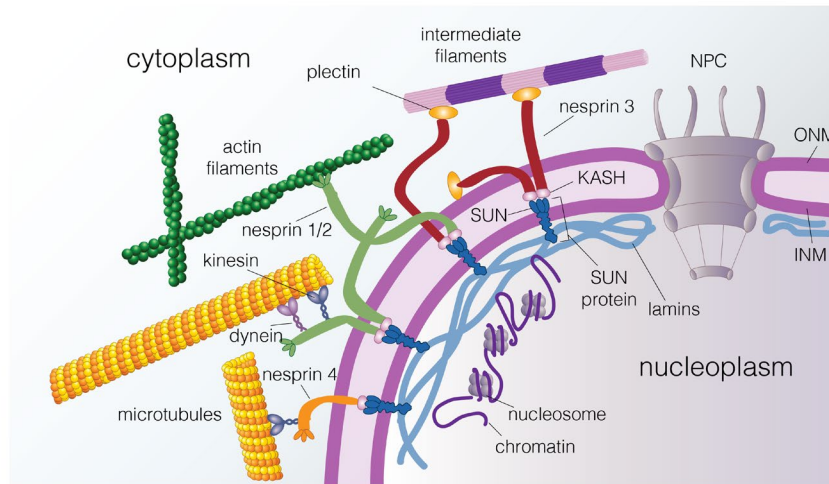


**Figure 1.11 | Nucleus is interconnected with the cytoskeletal networks.** The nucleoskeleton is formed from lamin fibers that underline the inner membrane of the nuclear envelope. The LINC complex connects nucleoskeleton with the cytoskeleton and is comprised of SUN proteins that span the inner nuclear membrane (INM) and nesprins that span the outer nuclear membrane (ONM). SUN proteins bind to the nuclear lamina and chromatin on the nucleoplasm side, and nesprins bind to all three cytoskeletal networks directly (actin) or via adaptor proteins such as dyneins, kinesins (microtubules) and plectins (intermediate filaments). Nesprins have a C-terminal KASH domain that faces the perinuclear space and interacts with SUN domain of the SUN proteins. Nuclear pore complexes (NPCs) span the nuclear envelope and provide for selective transport in and outside of the nucleus. The schematics is based on the information from refs<sup>164–166</sup>.

The third type of cytoskeletal filaments, microtubules, are hollow cylinders with 25 nm outer diameter (**Figure 1.8c**). They are formed by the polymerization of  $\alpha/\beta$ -tubulin heterodimers that align horizontally to form protofilaments, 13 of which come together laterally to form a hollow tube. Similar to actin filaments, microtubules have plus and minus ends, i.e., they are polar, what is important to their function as molecular tracks for the transportation of cargo within cells. Microtubules undergo alternating phases of rapid polymerization and disassembly, referred to as dynamic instability, that allows the filaments to explore space and execute cellular functions<sup>167,168</sup>. Their stability and

functionality can be modified by posttranslational modifications and by microtubule-associated proteins, that include motor proteins (kinesins and dyneins), enzymes that depolymerize (e.g., MCAK) or sever the filaments (spastin, katanin), filament nucleators (e.g., XMAP215), end-binding proteins (e.g., EB1) and structural MAPs such as tau or MAP2<sup>168,169</sup>. The persistence length of microtubules is the highest from all cytoskeletal components and reaches several millimeters ( $L_p \gg L$ )<sup>149,152</sup> — they behave like straight, rigid rods. Apart from the function as filamentous tracks for molecular motors, microtubules assemble the mitotic spindle to execute segregation of genetic material during cell division. In cells, microtubules grow out of the microtubule organizing centers (MTOCs), such as the centrosome, located in the proximity of the nucleus, and spread radially towards the cell edge<sup>168</sup>. Microtubules withstand compressive forces generated by actomyosin contractility and the environment, and show characteristic buckling under load<sup>170</sup>.

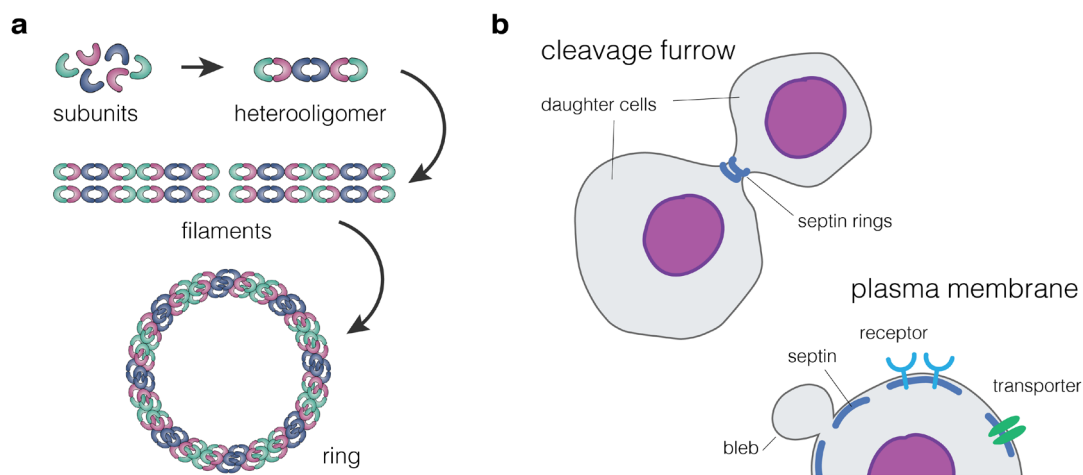


**Figure 1.12 | Septin cytoskeleton assembly and localization within cells.** **a**, Septin subunits from various septin groups (indicated by colors) come together to form heterooligomeric complexes. Such complexes join end-to-end to form non-polar filaments. Septin filaments associate laterally to form bundles and higher-order structures such as rings. Modified from Mostowy *et al.*<sup>171</sup>. **b**, Two typical localizations of septins within cells. During cell division septins form rings in the cleavage furrow to facilitate cytokinesis. In non-dividing cells, septin assembles under the plasma membrane and acts as a scaffold that restrains diffusion of receptors and transporters, and takes part in membrane retraction after bleb formation.

Beyond the three canonical networks discussed above, septins are increasingly recognized as the fourth cytoskeletal component<sup>171</sup>. Septins form rod-like heterooligomeric complexes (typically hexa- or octameric), that can come together to form filaments and higher-order structures such as rings and meshworks<sup>171,172</sup> (**Figure 1.12a**). During cell division, septin rings facilitate cleavage furrow formation<sup>173</sup>. In non-dividing cells septins form filamentous network at the cell cortex. This network is involved in functions such as bleb retraction and lateral compartmentalization of plasma membrane<sup>171,174,175</sup> (**Figure 1.12b**). Septins are known to interact with membranes and other cytoskeletal networks<sup>172</sup>, and have an implicated role in maintaining cell shape and cortical rigidity<sup>176</sup>.

Among all cytoskeletal networks, the actin network, and its contractility regulated via Rho signaling, is recognized as the most prominent contributor to the global mechanical phenotype<sup>33</sup>. Destabilization

of the actin cytoskeleton with chemical agents, such as cytochalasins or latrunculins, drastically reduces cell stiffness, both in adherent and suspended cells<sup>17,177–181</sup>. Similarly, the inhibition of actomyosin contractility with myosin inhibitors, such as Blebbistatin, and ROCK inhibitors, such as Y27632, results in decrease of cell stiffness and surface tension<sup>182–184</sup>. Newly developed optogenetic tools for activation of RhoA can be leveraged to locally control actin contractility<sup>185</sup>. So far, these tools have been exploited to study the influence of contractility on process such as cell migration<sup>186,187</sup>, traction force generation<sup>186,188</sup>, cleavage furrow formation<sup>189</sup> and control of morphogenetic processes<sup>190,191</sup>. Their implementation for the study of mechanical properties of cells remains to be explored. Intermediate filaments, in particular vimentin and keratins, have also been demonstrated to contribute to mechanical responses of cells, especially in measurements at high strains<sup>162,192–195</sup>. Actin and microtubules networks reconstituted *in vitro* break under 20% and 50% strains, respectively. On the contrary, intermediate filament networks withstand very high strains and show strain-stiffening<sup>196,197</sup>. These properties support the notion that intermediate filaments have a load-bearing function at high cell deformation. Although there is some evidence of the contribution of microtubules to cell stiffness at high strains<sup>198</sup>, their role has been difficult to address directly, since drug-induced microtubule disassembly evokes reinforcement of actin cytoskeleton and cell contractility<sup>199</sup>. Depletion of septins has been shown to reduce cell stiffness in cultured cells<sup>200</sup>, more extensive insights on their role in cell mechanics are yet to be established. There is a growing evidence suggesting that the cytoskeletal networks interact more universally with one another via both direct physical links, as well as at the regulatory level<sup>172,201,202</sup>, thus, more holistic approach in studies of the impact of cytoskeleton on cell mechanics is desirable.

### 1.3.2. Plasma membrane structures

When considering the deformation of the cell surface it is important to discuss not only the contribution of the cytoskeleton, but also the contribution of the plasma membrane. The plasma membrane is an asymmetric lipid bilayer comprising inner and outer leaflets, each composed of a fluid mosaic of lipids (phospholipids, glycolipids and sterols) and proteins<sup>203</sup>. Reconstituted lipid bilayers are easy to bend (their bending modulus is on the order of  $10^{-19}$  N m<sup>-1</sup>) but very difficult to stretch (their area expansion modulus ranges from 0.1 to 1 N m<sup>-1</sup>), and typically rupture at 2–4% lateral extension<sup>204,205</sup>. The plasma membrane is, however, not a flat lipid bilayer, but an extensively wrinkled surface with actively maintained topological features such as membrane folds, caveolae, clathrin-coated pits, blebs, microvilli and membrane ruffles<sup>206,207</sup> (**Figure 1.13**). The membrane excess gathered in these superstructures can buffer increase in the membrane tension and account for up to five-fold volumetric expansion of cells (two-fold surface area expansion), with further membrane reservoirs up to a total of >10-fold volume increase available for recruitment from the intracellular membranes via exocytosis<sup>208</sup>. In particular, caveolae, characteristic cup-shaped invaginations formed by membrane proteins caveolins and cytoplasmatic cavins, have been shown to react robustly to membrane tension increase and act as a first responder when cells are subjected to stress<sup>209</sup>. Noteworthy, the functions of caveolae, and

caveolins in particular, are multifaceted as apart from structuring the membrane, they also engage in signaling functions and cross-talk with cytoskeletal networks<sup>210,211</sup>.

The effective tension of the plasma membrane in unstressed cells ranges from 0.03 to 0.3 mN m<sup>-1</sup>, and is dictated by an interplay between in-plane tension in the lipid bilayer and the contributions from the connections between the membrane and the underlying cytoskeleton, and the intracellular pressure<sup>206</sup>. Plasma membrane tension is important for regulating process such as vesicular trafficking and signaling connected to it<sup>206</sup>. However, with respect to the global mechanical properties of the cell surface, plasma membrane tension is considered to be dominated by the cortical tension<sup>183,212</sup>.

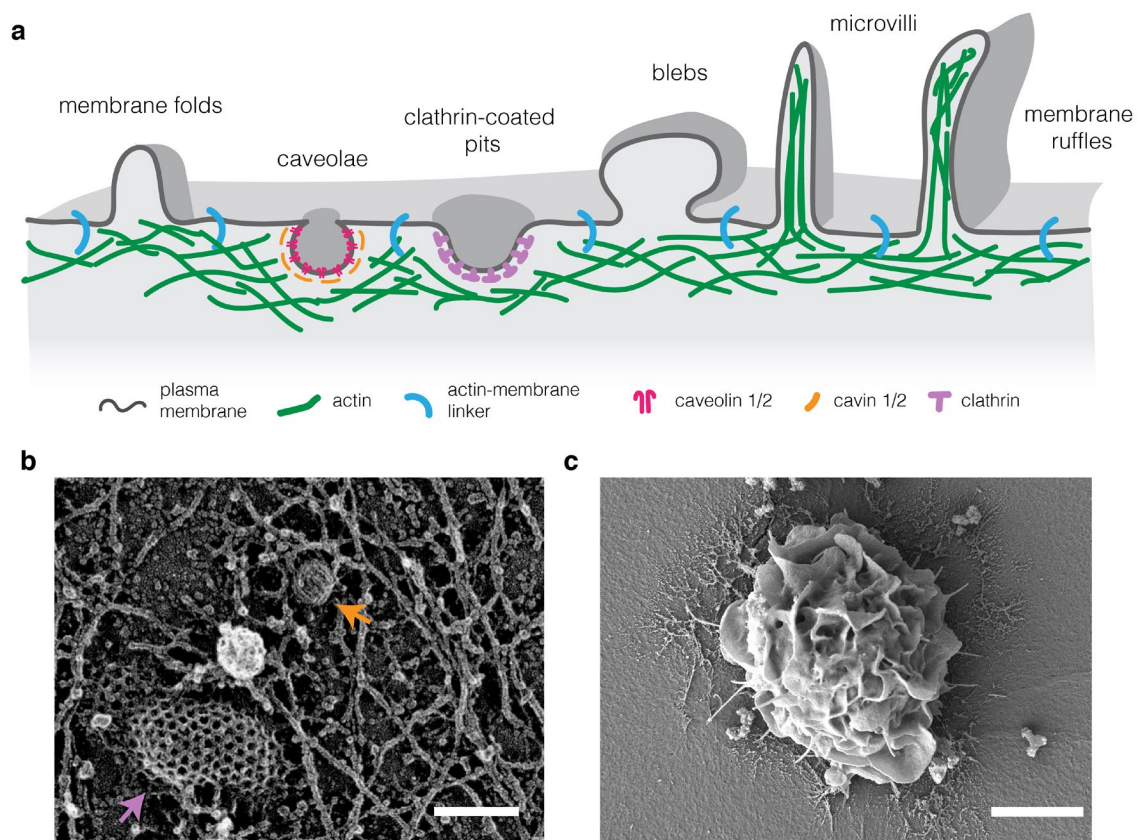


**Figure 1.13 | Cells maintain membrane reservoirs in topological superstructures.** **a**, Schematic overview of membrane superstructures maintained at the cell surface. Schematics is based on refs<sup>206,213</sup>. **b**, Scanning electron micrograph showing the cytoplasmic surface of the plasma membrane with underlying actin cortex from fetal rat skin keratinocytes. Apart from actin meshwork, there is a clearly discernable caveolar bud (orange arrow) and a clathrin-coated pit (purple arrow). Scale bar: 100 nm. Adapted from Morone *et al.*<sup>214</sup>. **c**, Scanning electron micrograph of a macrophage showing numerous membrane ruffles on its surface. Scale bar: 5  $\mu$ m. Adapted from Escolano *et al.*<sup>215</sup>.

### 1.3.3. Contribution of the nucleus

Apart from the structures located close to the cell surface, the organelles laying deeper inside the cytoplasm, in particular the cell nucleus, can contribute to the measured mechanical responses. The relative stiffness of the nucleus with respect to the stiffness of the whole cell is controversial. Based on the early reports, the nucleus is considered to be stiffer than the whole cell<sup>216–218</sup>. However, the



properties of the nucleus are typically either inferred from the behavior of the nucleus within the cell<sup>216,217</sup> or assessed in the isolated nuclei<sup>217,218</sup>. These conditions are non-ideal, as when embedded in the cell, the nucleus is surrounded and supported by the cytoskeleton (see **Figure 1.8** and **Figure 1.11**), and in the case of chemical or mechanical extraction, the properties of the nucleus can be compromised. Several recent reports challenge the notion of the nucleus being stiffer than the whole cell<sup>219–222</sup>. Firstly, AFM indentation measurements conducted on the nucleus within cells, but exposed apically, yielded Young's modulus values lower than the ones obtained for whole cells<sup>219</sup>. Secondly, theoretical modelling of the nuclear contributions in the micropipette aspiration<sup>220</sup> and AFM indentation experiments<sup>221</sup> points towards low nuclear stiffness. Finally, probing of enucleated cells with AFM showed that removing the nucleus did not lower the cell stiffness<sup>222</sup>. Nonetheless, there is clear evidence suggesting that modification of the mechanical properties of the nucleus — either by manipulation of the nuclear lamina<sup>223–226</sup> or by changing the compaction of the chromatin<sup>227</sup> — can lead to changes in the mechanical properties of the whole cell. This indicates that the nucleus is an important structural element within the cell that contributes to cell mechanics either directly or by influencing other cellular components.

#### **1.3.4. Macromolecular crowding**

Finally, the properties of the cytoplasm itself can have an impact on the overall cell stiffness. Cytoplasm is a crowded environment filled to near capacity with macromolecules<sup>145</sup>. The level of molecular crowding in the cell can be increased either by water efflux<sup>228–232</sup> or by overexpression of proteins that account for big fraction of the cellular volume such as ribosomes<sup>233</sup>. The increase in the volume fraction occupied by macromolecules leads to a steep increase in the stiffness of the cytoplasm and concomitant decrease of diffusivity<sup>230,233</sup>, analogous to the glass transition observed in colloidal mixtures<sup>230</sup>. This increase in cytoplasmic stiffness leads, in turn, to decrease in whole-cell deformability and affects most of the global mechanical measurements of the cell<sup>228–232</sup>.

## 1.4. Cell as a viscoelastic material

To be able to compare mechanical properties of different cells, it is necessary to parametrize them. Most of the biological materials, including cells, are viscoelastic, i.e., they exhibit both fluid-like time-dependent viscous responses and solid-like elastic ones. Therefore, a combination of concepts from the theory of elasticity and fluid mechanics — integrated in a discipline called rheology — is necessary to describe mechanical responses of cells<sup>234</sup>. In a typical rheological experiment, a relationship between strain  $\varepsilon$  (relative displacement of the material) and stress  $\sigma$  (force per unit area) is established and used to deduce the mechanical properties of the material. In practice, either constant stress is applied to the material and the strain is monitored over time (creep test), or constant strain is applied and the ensuing stress is recorded (stress-relaxation test)<sup>234,235</sup>. In the examples below, I will focus on the former type of testing.

### 1.4.1. Elastic solid and viscous fluid

Before discussing the behavior of cell-like viscoelastic materials, it is useful to introduce the characteristics of purely elastic solids and purely viscous fluids. A linear elastic solid exposed to uniaxial stretch behaves like a Hookean spring — the induced strain is linearly dependent on the applied stress with a proportionality constant called Young's modulus  $E$ <sup>236</sup>:

$$\sigma = E\varepsilon. \tag{1.1}$$

Young's modulus defines how much stress is necessary to deform an object to a certain degree and is a measure of material's resistance to deformation, i.e., its stiffness — the higher the Young's modulus, the stiffer the material. An elastic solid, represented in one-dimensional rheological models as a spring, responds instantaneously to imposed loads and recovers to its initial shape immediately after the load is released (**Figure 1.14a–b**). On the contrary, the response of a viscous fluid is not instantaneous, but evolves over time with a rate determined by the fluid viscosity  $\eta$ <sup>234</sup>:

$$\sigma = \eta \frac{d\varepsilon}{dt}. \tag{1.2}$$

The fluids that behave according to the above equation, i.e., for which the relation between stress and strain rate  $\frac{d\varepsilon}{dt}$  is linear, are called Newtonian fluids. The mechanical element used to represent a viscous fluid is called a dashpot. Dashpots not only show time-dependent evolution of strain, but also, contrary to elastic solids, do not restore their initial shape after removal of applied loads (**Figure 1.14c**).

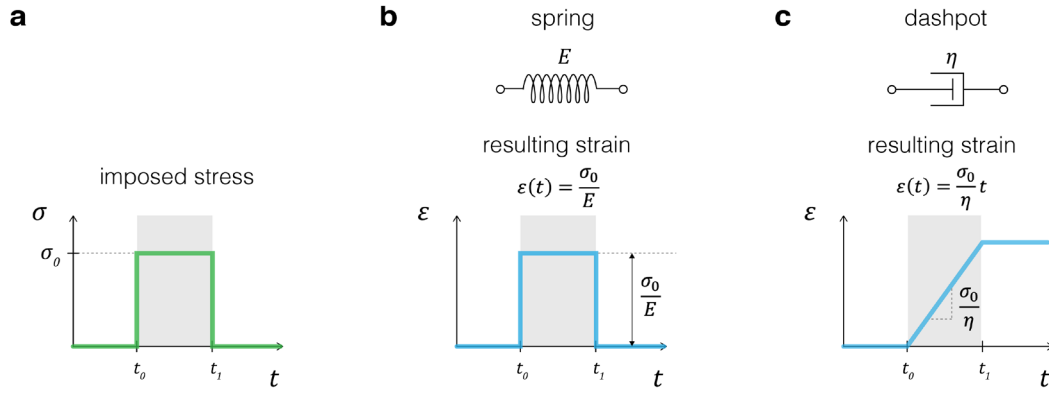


**Figure 1.14 | Response of purely elastic and purely viscous mechanical elements to stress.** **a**, Time course of the step stress of magnitude  $\sigma_0$  applied to the mechanical elements between time  $t_0$  and  $t_1$ . **b**, Strain response of a purely elastic spring to the step stress shown in **a**. **c**, Strain response of a purely viscous dashpot to the step stress shown in **a**. In **b** and **c**, the equation of strain during stress application (creep response, highlighted in gray) is given above the graphs.

### 1.4.2. Spring-dashpot models of viscoelastic materials

The mechanical elements representing elastic (springs) and viscous (dashpots) components can be combined into circuits to model viscoelastic materials<sup>235</sup>. By analogy to electronic circuits, the mechanical elements can be connected either in series or in parallel<sup>237</sup>. In the case of connection in series, all elements experience the same amount of stress, and the total amount of strain is equal to the sum of strains of individual element:

$$\begin{aligned}\sigma_{series} &= \sigma_1 = \dots = \sigma_n \\ \epsilon_{series} &= \epsilon_1 + \dots + \epsilon_n\end{aligned}\tag{1.3}$$

For the elements connected in parallel, the total stress is equal to the sum of stresses of individual elements, and every element experience the same strain:

$$\begin{aligned}\sigma_{parallel} &= \sigma_1 + \dots + \sigma_n \\ \epsilon_{parallel} &= \epsilon_1 = \dots = \epsilon_n\end{aligned}\tag{1.4}$$

These rules, together with **Equations 1.1** and **1.2**, can be used to derive the responses of composite mechanical circuits. The simplest models of viscoelastic materials include the Maxwell model (**Figure 1.15a**), in which one dashpot and one spring are connected in series, and the Kelvin-Voigt model, in which one dashpot and one spring are connected in parallel (**Figure 1.15b**). Three-element models, such as the standard linear solid (SLS, also called Zener model; **Figure 1.15c**) and the standard linear fluid (SLF, also called Jeffreys model; **Figure 1.15d**), exhibit more complex mechanical responses, closer to the ones observed in real materials. SLS consist of a Maxwell model connected in parallel with an additional spring. It is considered to represent a solid, since it shows an instantaneous elastic-like component in its response, and recovers fully to its initial shape upon unloading (**Figure 1.15c**). SLF, in turn, consists of a Maxwell model connected in parallel with an additional

dashpot. SLF is considered to model a viscoelastic fluid, because rather than reaching an equilibrium value it continuously deforms under constant stress. Additionally, it does not show full shape recovery after the load is released (**Figure 1.15d**).

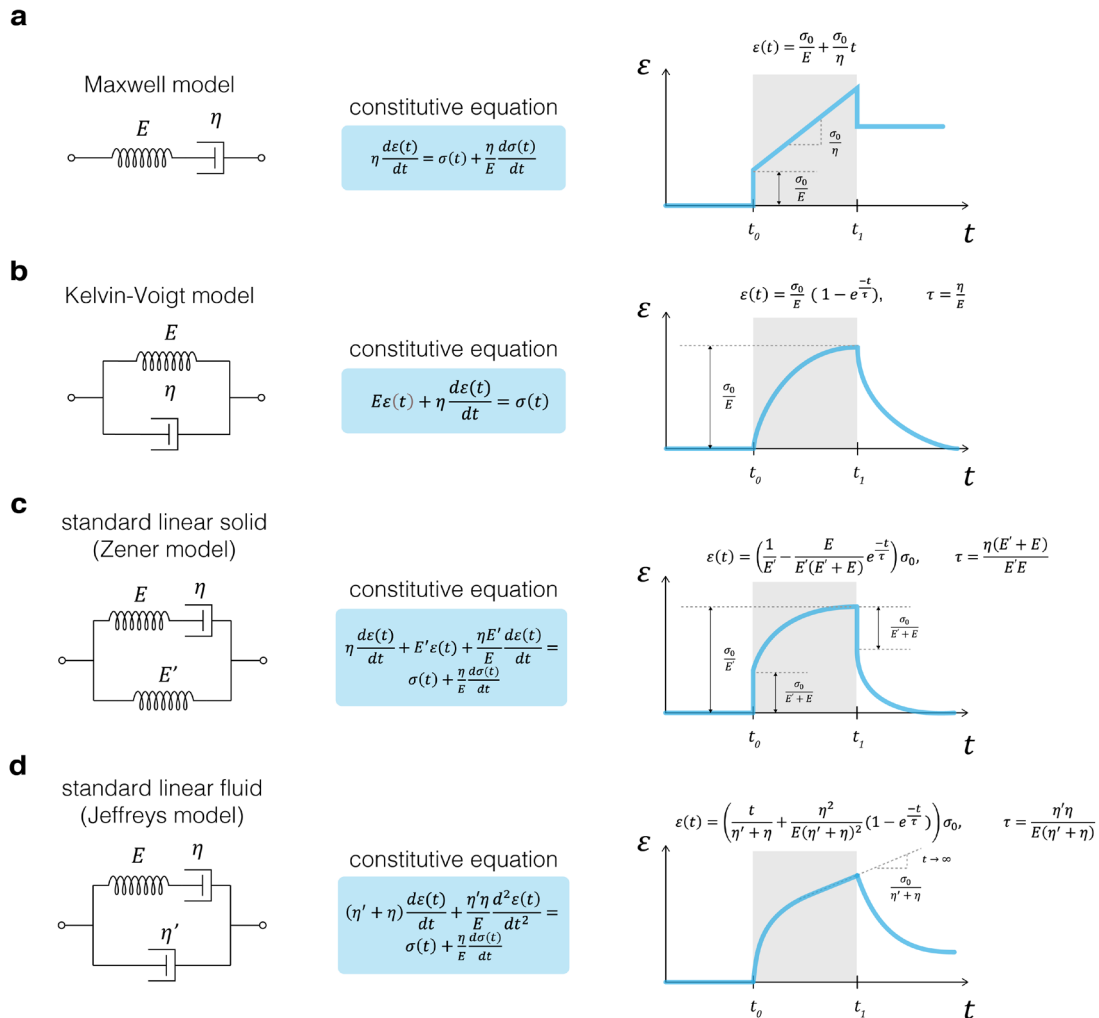


**Figure 1.15 | Two- and three-element spring-dashpot models of viscoelastic materials.** **a**, Maxwell model. **b**, Kelvin-Voigt model. **c**, Standard linear solid (Zener model). **d**, Standard linear fluid (Jeffreys model). From left to right, each panel includes a spring-dashpot representation, constitutive equation governing stress-strain relationship for a given model, and a strain response to a step-stress of magnitude applied between time  $t_0$  and  $t_1$ , as depicted in **Figure 1.14a**. The corresponding equations of strain during stress application (creep response, highlighted in gray) are given above each graph, with  $\tau$  denoting the retardation time. The equations and graphs are based on refs<sup>238–241</sup>.

In the models presented in **Figure 1.15b–d**, the buildup of strain is proportional to a negative exponential of time divided by the retardation time  $\tau$ :  $\varepsilon(t) \propto e^{-\frac{t}{\tau}}$ . The retardation time is a function of viscosities and Young’s moduli of the constituent mechanical elements and is a useful indicator of the timescale in which the material responds. Adding further elements to the spring-dashpot models can introduce multiple response timescales to the material. In a generalized Maxwell model (Wiechert model), consisting of a spring connected in parallel with a freely chosen number of Maxwell elements, an arbitrary number of timescales can be introduced<sup>235</sup>. The growing number of elements, however,

makes it challenging to solve such models analytically and the individual fit parameters become hard to interpret.

### 1.4.3. Power law and springpot representation

An alternative approach to the modelling using spring-dashpot approximations, is to capture the response of the viscoelastic material with an empirical single-exponent power law<sup>242</sup>. The creep response of a power-law material is characterized by the following proportionality:

$$\varepsilon(t) \propto (t)^\beta \sigma_0, \quad 1.5$$

with power exponent  $\beta$  that takes values between zero and one characterizing the fluidity of the material. Power law describes a material with a continuous distribution of timescales. For  $\beta = 0$ , the material behaves as a solid (**Equation 1.5** becomes equivalent to the creep response of a spring, see **Figure 1.14b**), and for  $\beta = 1$ , the material behaves as a fluid (**Equation 1.5** becomes equivalent to the creep response of a dashpot, see **Figure 1.14c**)<sup>242</sup>.

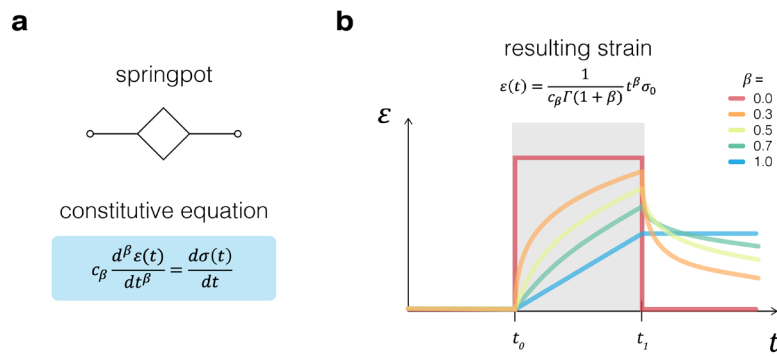


**Figure 1.16 | Springpot as a versatile viscoelastic element.** **a**, Symbolic representation and the constitutive equation of a springpot. **b**, Response of springpots with different exponents  $\beta$  to a step stress of magnitude  $\sigma_0$  applied between time  $t_0$  and  $t_1$ . The equation for strain during creep (section highlighted in gray) is given above the graph.  $c_\beta$  and  $\beta$  are coefficients obtained by fitting either creep or stress-relaxation response,  $\Gamma$  denotes the gamma function. Panel **b** is modified from Bonfanti *et al.*<sup>241</sup>.

Recently, a mechanical element that captures the power-law behavior called springpot was introduced<sup>241,243</sup>. Its constitutive equation was derived based on the empirical power-law relaxation behavior of materials using fractional calculus<sup>243</sup> (**Figure 1.16a**). Springpots are versatile viscoelastic elements that can behave, depending on the value of the exponent  $\beta$ , as either springs or dashpots or in between (**Figure 1.16b**). Thus, they are proposed as unified mechanical models of cells and cellular components<sup>33,244</sup>.

### 1.4.4. Modes of mechanical loading

So far, we have only considered the responses to load of idealized one-dimensional materials. In actual experiments, apart from the magnitude of applied forces, it is also important to consider the mode of

loading and potential load-induced volume change. The two most frequently implemented loading modes are uniaxial extension/compression and shearing<sup>234,238</sup> (**Figure 1.17**).

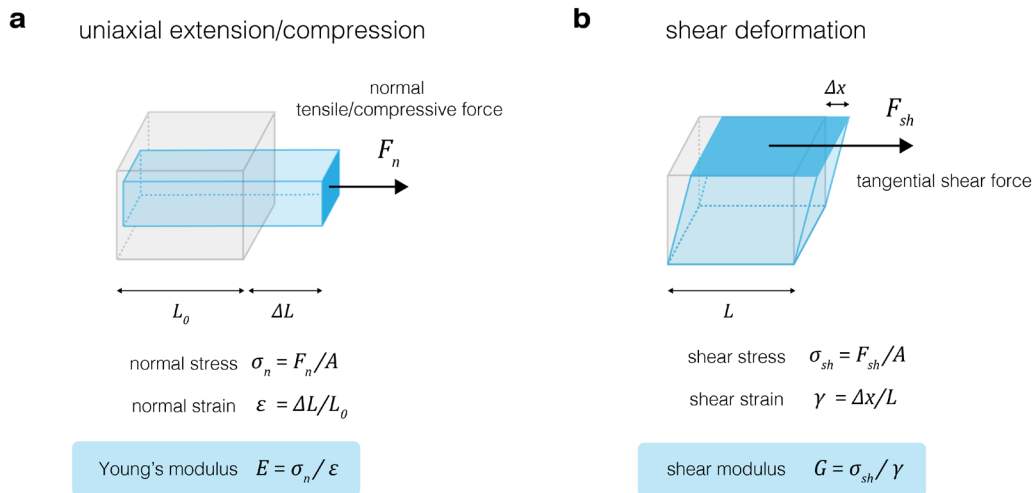


**Figure 1.17 | Two common modes of mechanical loading and the related elastic moduli.** **a**, Uniaxial extension/compression. **b**, Shear deformation. In **a** and **b**, the directionality of the applied force is indicated with the arrow, and the surface to which the force is applied is indicated with opaque blue.

In a uniaxial extension/compression experiment the force is applied perpendicular to one of the sides of a material block, causing elongation along the force application axis and compression along the perpendicular axis in extension experiment, the opposite is true in the case of compression (**Figure 1.17a**). Uniaxial extension/compression is a three-dimensional equivalent of loading considered for the one-dimensional spring-dashpot models. The elastic modulus that describes the proportionality between the normal stress and normal strain is Young's modulus  $E$ , analogous to the one introduced in **Equation 1.1**. During shearing deformation, the shear force is applied along one surface of a material what causes a change in material's shape without changing its length. The type of elastic modulus that connects the applied shear stress to induced shear strain is called shear modulus  $G$  (**Figure 1.17b**). The extent to which a material changes its volume during uniaxial extension or compression is determined by Poisson's ratio,  $\nu$ , which is a ratio of the transverse strain to the axial strain:

$$\nu = \frac{\varepsilon_{trans}}{\varepsilon_{axial}} \tag{1.6}$$

Most biological materials consist to a high degree of nearly incompressible water. Hence, they are typically assigned Poisson's ratio of an incompressible material equal to 0.5<sup>234</sup>. Knowing the Poisson's ratio of a material, its shear and Young's moduli can be converted into one another using the following relation:

$$G = \frac{E}{2(1 + \nu)} \tag{1.7}$$

### 1.4.5. Oscillatory probing

Apart from the application of static, step-like stresses or strains, rheological probing of viscoelastic materials can be performed in a dynamic fashion using an oscillatory test signal.

In an oscillatory experiment, typically a sinusoidal shear strain  $\gamma$  of a small amplitude  $\gamma_0$  is applied to the material with an angular frequency  $\omega$ :

$$\gamma(t) = \gamma_0 \sin(\omega t). \quad 1.8$$

The resulting stress  $\sigma$  oscillates in time with an amplitude  $\sigma_0$  and is delayed with respect to strain by a phase shift  $\theta$  (**Figure 1.18**):

$$\sigma(t) = \sigma_0 \sin(\omega t + \theta). \quad 1.9$$

The phase shift is a dimensionless measure of viscoelastic damping in the material. It takes values from  $0^\circ$  to  $90^\circ$ , with  $0^\circ$  corresponding to an ideal elastic solid,  $90^\circ$  to a Newtonian liquid, and the values in between to a viscoelastic material<sup>234</sup>. The resulting stress can be expressed as a sum of elastic and viscous contributions:

$$\sigma(t) = \gamma_0(G' \sin(\omega t) + G'' \cos(\omega t)), \quad 1.10$$

with  $G'$  denoting the storage shear modulus that corresponds to the elastic contributions and the  $G''$  denoting the loss shear modulus, corresponding to the viscous contributions to the material response. Storage and loss moduli constitute, respectively, the real and imaginary parts of the complex shear modulus  $G^*$  obtained in the oscillatory rheological measurements:

$$G^*(\omega) = G'(\omega) + iG''(\omega). \quad 1.11$$

The one-dimensional rheological models presented in this chapter can help us get some intuition on how viscoelastic materials respond to loads and extract mechanical properties of the cells for comparative purposes. However, even when extended to a three-dimension description, they still constitute only a crude approximation of the viscoelastic materials encountered in biology. Contrary to conventional materials, biological materials are heterogenous, non-isotropic and show a high degree of nonlinearity<sup>245</sup>. Thus, it is important to realize that the mechanical properties obtained from experimental testing will depend on the assumed material model and on the testing parameters characteristic for a selected measurement method.

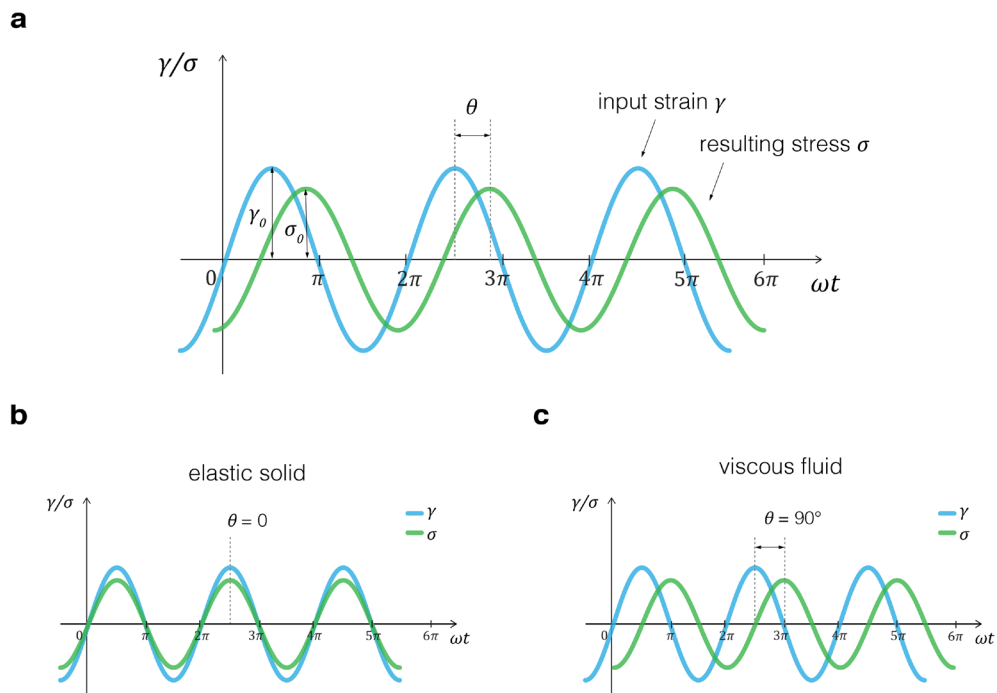


**Figure 1.18 | Dynamic response of a viscoelastic material to a sinusoidal probing signal.** **a**, A sinusoidal strain of magnitude  $\gamma_0$  and angular frequency  $\omega$  is applied over time in an oscillatory fashion (blue curve). The resulting stress (green curve) oscillates with a magnitude  $\sigma_0$  and same frequency, but is shifted with respect to strain by a phase shift  $\theta$ . **b**, A response of an elastic solid is characterized by no phase lag. **c**, Response of a viscous fluid is characterized by a phase shift of  $90^\circ$ .



## 1.5. Methods to measure single-cell mechanical properties

Over the past few decades, a rich variety of methods for probing mechanical properties of single cells has been established<sup>246</sup>. These methods can be categorized based on several criteria, such as whether they probe the mechanical properties globally or locally, whether adherent or suspended cells are measured, and whether a step or oscillatory test signal is applied to the cells. An overview of most widespread techniques is presented in **Table 1.1** and **Figure 1.19**, and a description of their operation is presented in the subsections below.

**Table 1.1 | Summary of methods for single-cell mechanical characterization.** The applied force and throughput estimates are based on the values provided in Hao *et al.*<sup>246</sup>, unless indicated otherwise. adh. – adherent, susp. – suspended, osc. – oscillatory.

	scale		cell state		applied mechanical signal			applied force	throughput
	global	local	adh.	susp.	step	osc.	no		
micropipette aspiration	×	×	×	×	×			pN – $\mu$ N	$\leq 10$ cells h <sup>-1</sup>
AFM	× <sup>§</sup>	×	×	× <sup>§</sup>	× <sup>#</sup>	× <sup>†</sup>		pN – $\mu$ N	$\leq 40$ cells h <sup>-1</sup> <sup>§</sup>
optical stretcher	×			×	×	×		pN – nN	1 – 100 cells h <sup>-1</sup>
parallel-plate rheometry	×		×	×	×	×		nN – $\mu$ N	$\leq 10$ cells h <sup>-1</sup>
magnetic twisting cytometry		×	×			×		pN – 100 nN <sup>153</sup>	$\sim 100$ cells h <sup>-1</sup>
particle tracking microrheology		×	×				×	none	$\sim 30$ cells h <sup>-1</sup>
optical tweezers	×			×	×	×		fN – 500 pN <sup>153</sup>	$\leq 10$ cells h <sup>-1</sup>
deformability cytometry	×			×	×			pN – $\mu$ N	1 – 1000 cells s <sup>-1</sup>
Brillouin microscopy		×	×	×			×	none	10 – 200 cells h <sup>-1</sup> &
acoustic microscopy		×	×	×			×	none	$\sim 10$ cells h <sup>-1</sup>

<sup>§</sup>wedged cantilever, <sup>#</sup>indentation, <sup>†</sup>microrheology, <sup>§</sup>based on own experimental experience, &lower bound corresponds to conventional implementation, upper bound to a line-scanning variant integrated with microfluidic sample delivery (Zhang *et al.*<sup>247</sup>)

### 1.5.1. Micropipette aspiration

In one of the earliest attempts, elasticity of cells was measured by sucking a part of a sea urchin egg cell into a narrow capillary in a micropipette aspiration assay<sup>248,249</sup> (**Figure 1.19a**), a method that quickly gained popularity and was adapted for mechanical characterization of various eucaryotic cell types<sup>18</sup>. In micropipette aspiration experiments, the aspirated cell extension and the pipette geometry can be related to the suction pressure using Laplace law to derive cell surface tension. Further mechanical

properties such as viscosity and Young's modulus can be derived from time-resolved micropipette aspiration measurements using continuum models for a liquid drop or a solid sphere<sup>18</sup>. Depending on the size of the capillary and whether the whole cell is aspirated into the pipette, either local or global cell properties can be assessed.

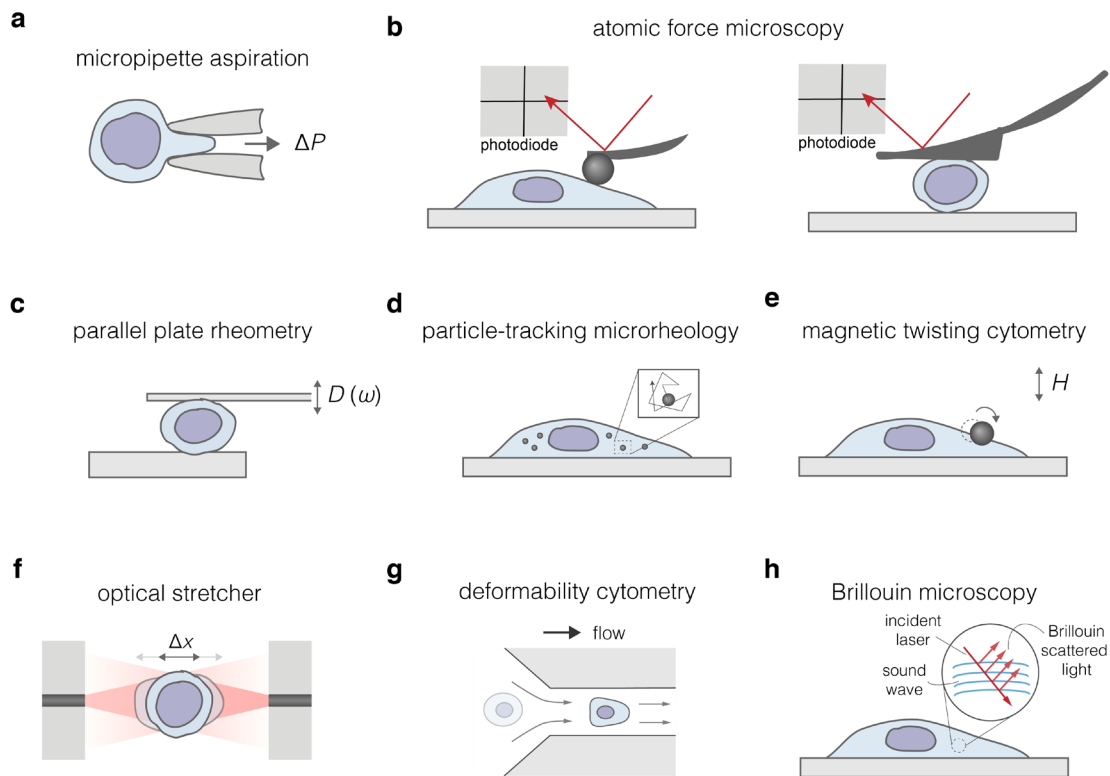


**Figure 1.19 | An overview of selected methods for the measurements of single-cell mechanical properties.** **a**, Micropipette aspiration,  $\Delta P$  – applied pressure difference. **b**, Atomic force microscopy measurements can be conducted on adherent cells (left-hand side) using a variety of cantilever tip geometries (here pyramidal tip is depicted) or on rounded cells (right-hand side). **c**, Optical stretcher,  $\Delta x$  – cell extension in  $x$  direction. **d**, Parallel plate rheometry,  $D(\omega)$  – oscillating displacement. **e**, Magnetic twisting cytometry,  $H$  – magnetic field. **f**, Particle-tracking microrheology. **g**, Deformability cytometry, **h**, Brillouin microscopy.

### 1.5.2. Indentation and parallel plate compression

Other early approaches to measuring cell mechanics, such as parallel plate compression<sup>250–253</sup> and cell indentation using a cell poker<sup>177,254,255</sup>, relied on pushing into the cells rather than pulling on them. The parallel plate compression of single cells was first conducted using home-devised setups with a pair of glass plates, one fixed to a stiff support and one to a flexible arm that acts as a bending balance<sup>250–253</sup>. Concurrently, similar apparatus called cell poker was developed for the localized indentation experiments<sup>177,254,255</sup>. Rather than using a plate, cell poker utilized a blunt indenter with 2  $\mu\text{m}$  diameter fixed to a flexible horizontal beam that was lowered onto a cell with an aid of an electromagnet<sup>254</sup> or a piezoelectric motor<sup>177,255</sup>. The depth of the indentation was related to the applied force and used to extract viscoelastic properties from the measurements<sup>256</sup>. Shortly after its introduction, cell poker was

succeeded by AFM<sup>257,258</sup> for the indentation measurements on cells (**Figure 1.19b** and **Figure 1.20**), a method that to date is considered a gold standard of the mechanical measurements on cells.

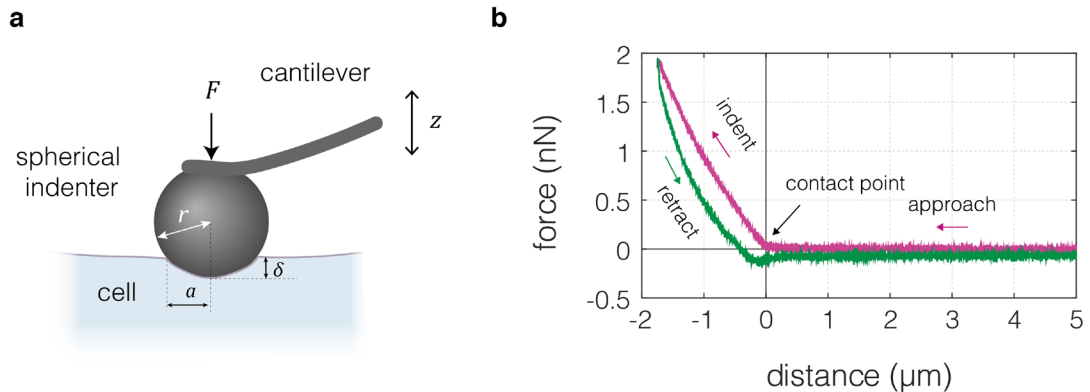


**Figure 1.20 | AFM-based indentation experiment.** **a**, A schematic of a spherical indenter of a radius  $r$  attached to the AFM cantilever that is being pushed into the cell surface with a force  $F$  to an indentation depth  $\delta$ . The  $z$ -movement of the cantilever is actuated by a piezoelectric motor.  $a$  indicates the radius of the contact area between the cantilever tip and the cell. **b**, A representative force–distance curve acquired during an AFM indentation experiment. In magenta the approach phase is presented, with cantilever first being lowered towards the cell surface, then coming into contact with it and finally performing the indentation. In green the retraction phase of the experiment is presented.

Similar to the cell pocker, AFM uses a horizontal probe — the cantilever — that is equipped with a tip pointing towards the sample and is actuated by a piezoelectric motor<sup>19</sup>. The vertical position of the cantilever is tracked based on the extension of the piezoelectric element. The cantilever deflects upon contact with the measured object, and the level of this deflection is detected by tracking the position of a laser beam reflected from the cantilever surface and directed onto the position-sensitive photodiode (**Figure 1.19b**). The force acting on the sample surface (derived based on the cantilever deflection and the cantilever spring constant) is analyzed as a function of the deflection-corrected separation between the sample surface and the indenter (**Figure 1.20**) to derive Young’s modulus of the cell using Hertz model<sup>259</sup>. Further probing modes, such as stress-relaxation<sup>260</sup> or oscillatory probing<sup>25</sup>, can be implemented in the AFM measurements to obtain both viscous and elastic characteristics of the sample. The tip of the AFM cantilever can be a sharply-pointed pyramid that enables measurements with high spatial resolution, or a microsphere glued to a tipless cantilever that performs indentation over a bigger area (**Figure 1.19b**, **Figure 1.20a**). Alternatively, flat cantilevers (such as the wedged cantilever depicted in **Figure 1.19b**, right panel) can be employed to perform parallel plate compression of whole cells<sup>261</sup>, making it straightforward to probe not only adherent, but also suspended cells. Apart from AFM, parallel plate compression is often performed using a piezoelectric micromanipulator called parallel plate rheometer<sup>4,217,262–264</sup> (**Figure 1.19c**). Using such a micromanipulator, cells can be compressed<sup>217,262</sup>, extended (when adhered to the plates)<sup>262–264</sup>, and probed using an oscillatory signal<sup>4,262,264</sup>.

### 1.5.3. Microrheology

Another class of methods that allow for measuring of the local viscoelastic properties of the cells is called microrheology<sup>265</sup>. Methods from this class rely on following tracer microparticles localized either within the cytoplasm or on the cell surface. In the latter case, the particles are typically coated with RGD peptides and attached to the cells via focal adhesions. The motion of the tracer particles can be passively or actively induced, what defines the two subtypes of passive and active microrheology. In passive microrheology, also referred to as particle tracking microrheology, mean square displacement of the spontaneous, thermally driven motion of the tracer particles is measured over time and used to extract the complex shear modulus of the sample<sup>102,266</sup> (**Figure 1.19d**). Typically, synthetic microspheres are injected into the cells for tracing<sup>102</sup>. An elegant alternative constitute genetically encoded multimeric nanoparticles that can be expressed directly within the cells<sup>233</sup>. In active microrheology, the motion of the tracer particles is actuated by external forces generated by magnetic<sup>22,267–271</sup>, electromagnetic<sup>272–274</sup> or acoustic fields<sup>275,276</sup>, applied in a step-wise or oscillatory fashion. Magnetic twisting cytometry (**Figure 1.19e**), a variant of magnetically-actuated microrheology in which the magnetic beads are first magnetized and then translocated and rotated by a magnetic field, has become particularly widespread<sup>22,270,271</sup>. The oscillatory mode of AFM measurements can also be classified as an active microrheology method and is often referred to as AFM microrheology<sup>4,262,264</sup>.

### 1.5.4. Optical traps-based methods

Optical traps, first introduced by Arthur Ashkin<sup>277,278</sup>, have a long history of application in the biological sciences for measuring and applying forces on structures ranging from single molecules to tissues<sup>279–281</sup>. The single-beam laser traps, also called optical tweezers, use a highly focused laser beam that generates a steep gradient of the electromagnetic fields pushing the trapped objects towards the beam center. In the context of cell mechanical measurements, optical tweezers can be used to monitor<sup>282</sup> or actuate<sup>272–274</sup> the displacement of microparticles in microrheological experiments discussed above. Additionally, optical tweezers have been adopted to stretch red blood cells by pulling on a bead attached to the cell surface<sup>283–287</sup>. However, due to the comparatively low maximal forces obtained with the optical tweezers (see **Table 1.1**), this method found little application in probing of other, less deformable cell types. On the contrary, a dual-beam laser trap called optical stretcher<sup>288,289</sup> was successfully applied to stretching of cells of various origin<sup>2,7,49,51,290,291</sup>. Optical stretchers use two divergent, counterpropagating laser beams to trap and, at increased laser intensities, deform the cells (**Figure 1.19f**). The deformation takes place due to the outward facing force generated by the transfer of light momentum onto the cell surface<sup>288</sup>. With the efforts to automatize sample delivery by integration with microfluidic delivery systems<sup>292,293</sup>, optical stretcher can reach measurement rates of up to 100 cells per hour. Compared to the techniques discussed so far, that typically allow for measurements of up to tens of cells per hour (see **Table 1.1**), this is an impressive improvement. However, for obtaining good statistics and through characterization of heterogenous cell populations

higher throughputs are desirable. This is particularly important for clinical applications, for example in diagnostics<sup>13,294</sup>.

### 1.5.5. Microfluidics-based deformability cytometry approaches

The bottleneck of the throughput in mechanical characterization of cells was overcome by the microfluidics-based deformability cytometry (DC) approaches, offering measurement rates of up to thousands cells per second<sup>20,294</sup> — an improvement of a factor of 100,000 compared to 1 cell per minute in most of the conventional techniques (**Figure 1.19g**, **Table 1.1**). Numerous DC approaches, using a variety of channel geometries, detection modes and flow regimes, have been developed since the early 2000s. They can be divided into three major classes: (i) constriction-based deformability cytometry (cDC), (ii) shear flow deformability cytometry (sDC) and (iii) extensional flow deformability cytometry (xDC). In cDC, cells are deformed in a constriction smaller than cell diameter, i.e., cells come in contact with the channel walls during deformation. Cell deformability is typically assessed based on the time the cell requires to enter or pass through the constriction, though in some variants the cell deformation is evaluated based on the bright-field images of the cells<sup>180,295</sup>. The translocation of cells through the constriction is detected by means of optical imaging<sup>3,180,295</sup>, electrical resistance measurements<sup>296,297</sup>, or mechanical frequency changes of a suspended microchannel resonator (SMR)<sup>9</sup>. In sDC and xDC, cells are deformed by hydrodynamic flow in a contactless manner, and cell deformation is derived from images acquired at high speed. sDC and xDC differ in the channel geometry used, the timescale of deforming the cells and the flow regime in which they operate. In sDC, cells are driven through a funnel-like constriction into a microfluidic channel where they are deformed by shear forces and pressure gradients into a bullet-like shape within few milliseconds<sup>21,298</sup>. sDC operates at a flow regime dominated by viscous forces called Stokes flow. A prominent example of this class is real-time deformability cytometry (RT-DC)<sup>21</sup> — a method extensively used and further developed in this thesis (introduced in detail in **Chapter 2**). xDC, in turn, operates at an intermediate flow regime called inertial flow, in which inertial forces cannot be neglected and can lead to useful effects such as cell focusing<sup>299</sup>. Typical channel geometry for xDC is a cross junction in which cells are deformed by an extensional flow within a few microseconds. The prototype for this class of methods was developed in the Di Carlo group and was called deformability cytometry (DC)<sup>1</sup>. Another variant of deformability cytometry that is related to xDC is inertial cell stretcher. In inertial stretcher, cells are delivered at high speeds into a T-junction and their deformation is induced by collision with the channel wall<sup>300,301</sup>. Representatives of the three different deformability cytometry classes are discussed in more detail in **Chapter 3** featuring a highly-standardized cross-laboratory study comparing their performance.

### 1.5.6. Imaging-based elastography techniques

Mechanical properties of single cells can also be evaluated in a non-invasive way using imaging-based elastography techniques. In particular, Brillouin microscopy is emerging as a promising tool for

mapping mechanical properties of living samples<sup>302</sup>. Classical elastography techniques such as optical coherence elastography or magnetic resonance elastography have found implementation for viscoelastic characterization of tissues<sup>303</sup>. These techniques allow for acquisitions of relatively big fields of view; however, they do not offer enough spatial resolution to monitor properties of individual cells. On the contrary, Brillouin microscopy allows for the characterization of local mechanical properties at a sub-cellular resolution in the gigahertz frequency range<sup>304,305</sup>. In Brillouin microscopy, the light scattered on the acoustic phonons (intrinsically present in the material due to thermal vibrations) is used to deduce viscoelastic properties of the measured sample (**Figure 1.19h**). The shift in frequency of Brillouin-scattered light carries the information about longitudinal modulus of the material, and the linewidth of the scattered light contains the information about the material's viscosity<sup>304</sup>. Brillouin microscopy enables mechanical characterization of single cells not only in suspension or in monolayers, but also within multicellular structures and living organisms<sup>306,307</sup>, which is a unique characteristic of the method and its particularly interesting application area<sup>302</sup>. Another, somewhat less widespread method for non-invasive mechanical imaging of cells is acoustic microscopy that relies on measuring the attenuation of acoustic waves within the cell interior<sup>308–310</sup>.

Due to different probing modalities and operation parameters, individual methods for measuring cell mechanics deliver results that differ both in magnitude and nature of measured properties. This issue was illustrated in a recent study comparing elastic and viscous moduli measured with an array of methods (AFM indentation, magnetic twisting cytometry, particle tracking microrheology, parallel-plate rheometry, and optical stretching) for the same cell line maintained in standardized conditions<sup>311</sup>. The obtained values showed a spread over two orders of magnitude for elastic modulus and three orders of magnitude for viscous modulus. The discrepancies were attributed to the differences in the magnitude of applied stress and strain rate, size of the probe, probing length scale, and whether the cells were attached or in suspension. It is therefore important to understand the peculiarities and limitations of individual methods, and, ideally, apply methods that are relevant to the time and length scales of studied processes. For providing a unified understanding of properties measured with different methods, further validation and comparison studies are required.

## Aims and scope of this thesis

Integrating biophysical perspective into the current, biochemically-oriented description of cellular behaviors fosters comprehensive understanding of physiological and pathological processes. In particular, single-cell mechanical properties, such as whole-cell stiffness or deformability, are a marker of cell state transitions with relevance for cell function. To gain a thorough understanding of the role of single-cell mechanical phenotype in physiology, several developments are necessary. Firstly, it is necessary to establish and validate methods that allow for robust assessment of mechanical properties. Secondly, it is important to explore changes in mechanical phenotype of cells during physiologically relevant processes. Finally, it is necessary to uncover ways of tuning mechanical properties of cells on demand to enable exploring their function. The work performed during this thesis was aimed at addressing these demands and was split into four projects with the following specific aims:

- consolidate real-time deformability cytometry as a robust method for high-throughput single-cell mechanical phenotyping and support its integration with a sorting modality,
- cross-validate three classes of microfluidics-based deformability cytometry operating at different timescale to enable interpretation of deformability measurements performed across platforms,
- explore the relationship between mechanical phenotype and cell fate during reprogramming of fetal neural precursor cells to pluripotency and differentiation of pluripotent stem cells along neural lineage,
- establish a method for identification of novel cell mechanics regulators from transcriptomic data associated with mechanical phenotype changes; perform validation of selected target genes in perturbation experiments.

Chapter 2 is based on and contains materials adapted from the following publications:

M. Urbanska\*, P. Rosendahl\*, M. Kräter\*, and J. Guck. (2018). **High-throughput single-cell mechanical phenotyping with real-time deformability cytometry**, *Methods in Cell Biology*, 147, pp. 175–198.

DOI: 10.1016/bs.mcb.2018.06.009

Own contributions: investigation, visualization, writing – original draft preparation, writing – review and editing

A.A. Nawaz\*, M. Urbanska\*, M. Herbig\*, M. Nötzel, M. Kräter, P. Rosendahl, N. Toepfner, M. Kubánková, R. Goswami, S. Abuhattum, F. Reichel, P. Müller, A. Taubenberger, S. Girardo, A. Jacobi, and J. Guck. (2020). **Intelligent image-based deformation-assisted cell sorting with molecular specificity**, *Nature Methods*, 17(6), pp. 595-599.

DOI: 10.1038/s41592-020-0831-y

Own contributions: investigation (partial contribution), data curation, formal analysis, visualization, writing – original draft preparation, writing – review and editing

\*equal contributions



## — Chapter 2 —

# RT-DC as a versatile method for image-based cell characterization and sorting

RT-DC is a microfluidics-based deformability cytometry platform, originally introduced for on-the-fly evaluation of mechanical properties of single cells in suspension at high throughput. It relies on high-speed imaging of cells passing through a narrow constriction in a microfluidic channel. The method was developed in the group of Prof. Guck and first published in 2015<sup>21</sup>. Since then, its functionality has been expanded by integrating a flow cytometry-like capability of measuring 1D fluorescence signal in three spectral channels<sup>312</sup>, and a sorting capability that allows for separation of cells with selected properties downstream of analysis<sup>313</sup>. The images acquired in RT-DC can be used not only to evaluate mechanical properties of cells, but also to extract many other parameters such as cell brightness, contour roughness, or texture features, all of which can be exploited for label-free, multidimensional identification of cells. Moreover, both the extracted features<sup>314</sup> and raw cell images<sup>313,315</sup> can be used to train artificial intelligence (AI) algorithms to classify different cell types — an aspect that is only beginning to be explored and will likely become more central for the method’s use in the future.

RT-DC was used throughout this thesis as a workhorse for measurements of cell mechanics. I have made substantial contributions to developing standard operating procedures and optimizing its use for cultured cells. I have also been actively involved in the implementation of the sorting capability to the RT-DC setup. The purpose of this chapter is to introduce RT-DC and all its modalities, describe experimental procedures connect to its use, and showcase several applications of the method beyond the mechanical phenotyping of cells.

### 2.1. RT-DC for mechanical characterization of cells

RT-DC relies on flowing cells through a constriction in a microfluidic channel in which they are deformed in a contactless manner by hydrodynamic stresses (**Figure 2.1a,b**). The deformation of cells is evaluated based on bright-field images and used, together with cell area, to extract mechanical properties of measured cells (**Figure 2.1c,d**).

#### 2.1.1. Operation of the RT-DC setup

An RT-DC setup is assembled on a standard inverted microscope (such as Axiovert 200M or Axio Observer Z1, Zeiss, Germany), and consists of a high-precision syringe pump (two modules neMESyS 290N, NeMESyS, Cetoni, Germany), a high-speed CMOS camera (MC1365, Mikrotron, Germany),

an LED lamp for stroboscopic illumination that is synchronized with the camera (AcCellerator L1, Zellmechanik Dresden, Germany), and a stage with a customized holder on which a microfluidic chip is installed during the measurements (**Figure 2.1a**). The setup operation is controlled by a user interface (*ShapeIn*, Zellmechanik Dresden) on a standard personal computer.

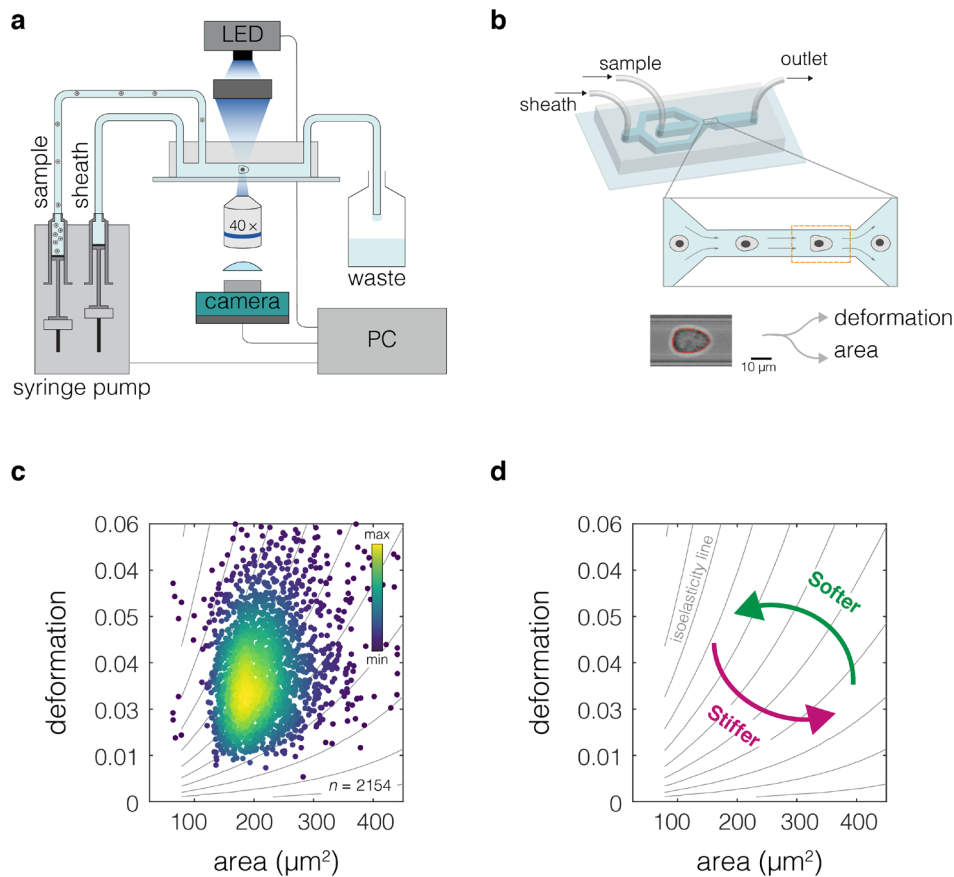


**Figure 2.1 | Operation principle of RT-DC for mechanical characterization of cells.** **a**, Schematic overview of the RT-DC setup consisting of syringe pumps, LED-based stroboscopic illumination source and a CMOS camera, installed on an inverted microscope and controlled by a personal computer (PC). **b**, 3D illustration of the RT-DC chip, close-up depicts the constriction of the channel in which cells are deformed, the imaged region of interest is indicated by an orange dashed line. At the bottom, an exemplary cell image is shown with fitted contour (red line). **c**, A representative deformation vs. cell area scatter plot obtained during an RT-DC measurement. Each dot represents a single cell, the color scale indicates event density. The measurement was performed using ECC4 carcinoma cell line. **d**, Isoelasticity lines derived from numerical simulations aid in identifying cells of corresponding mechanical properties in a deformation vs. area plot. In **c** and **d**, plots correspond to a measurement using 30 μm channel and a total flow rate of 0.16 μl s<sup>-1</sup>.

The microfluidic chip accommodates sample inlet, through which a cell suspension is introduced, and sheath fluid inlet, for the introduction of the fluid used for the focusing of cells (**Figure 2.2**). The measurement buffer, used for both cell resuspension and as a sheath fluid, has an increased viscosity to provide for sizeable cell deformation and prevent cell sedimentation during measurements (see **Section 2.6.2** for more details).

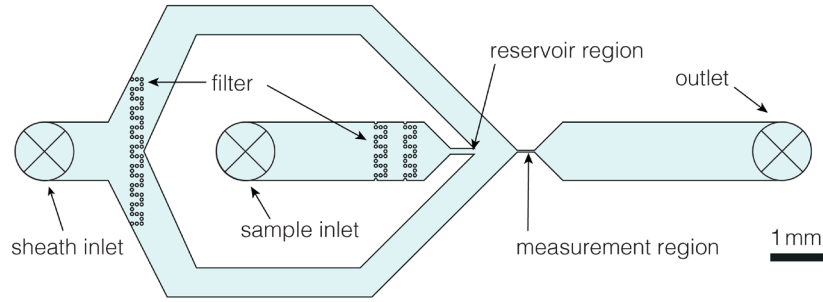


**Figure 2.2 | Layout of the RT-DC chip.** Sheath fluid enters the chip via the sheath inlet on the left, and splits into two branches before combining with the sample flow after the reservoir region. Both sheath and sample fluids pass through micro-pillar filter structures right after entering the chip. In the channel constriction of the measurement region, hydrodynamic stresses deform the cells. After the measurement, the fluid leaves the chip through the outlet on the right. This figure is modified from Urbanska, Rosendahl, Kräter *et al.*<sup>316</sup>.

Sample and sheath flows are driven into the microfluidic chip by a computer-controlled syringe pump at a 1:3 ratio that has proven to provide the best focusing of cells. Focused cells enter the channel constriction where they are deformed by shear and normal stresses<sup>298,317</sup>. The shear stresses are caused by the parabolic flow velocity distribution, and the normal stresses are caused by the pressure gradient. Together, they lead to cell deformation into a characteristic bullet-like shape as depicted in **Figure 2.1b**.

During the measurements, cell images are acquired using a high-speed CMOS camera and a synchronized stroboscopic LED illumination. Stroboscopic illumination is necessary to prevent motion blurring. For example, at a flow rate of  $0.16 \mu\text{l s}^{-1}$  in a  $30 \mu\text{m}$  channel, cells reach a velocity of about  $0.18 \text{ m s}^{-1}$ . Thus, to keep motion blurring below the resolution of the microscope (ca.  $0.5 \mu\text{m}$ ), the exposure time needs to be adjusted to values as low as  $2 \mu\text{s}$ . A high-power LED (CBT-90, Luminus Devices, CA, USA) with a custom driver circuit provides the necessary illumination intensities and an adjustable pulse length between  $1 \mu\text{s}$  and  $10 \mu\text{s}$ . The imaging is typically performed with a  $40\times$  objective (EC-Plan-Neofluar,  $40\times/0.75$ , Zeiss). The resulting images are directly processed by a personal computer (PC) with a custom-written C++ software, which is now available commercially from Zellmechanik Dresden under the name *ShapeIn*. The image processing consists of the following steps: (i) background subtraction, (ii) threshold filtering, (iii) contour finding, and (iv) contour processing for the estimation of cell size, position, deformation, and brightness, among others. For mechanical characterization, the parameter deformation defined as  $1 - \text{circularity}$  is of primary interest:

$$\text{deformation} = 1 - \text{circularity} = 1 - \frac{2\sqrt{\pi A}}{P}, \quad 2.1$$

where  $A$  is the cross-section area of the contour, and  $P$  the perimeter of the contour.

In a typical RT-DC measurement, thousands of cells are measured and displayed on an area-deformation scatter plot for inspection (**Figure 2.1c**). Since larger cells experience higher stresses in the constriction, the deformation is not a direct measure of cell mechanical properties — a similarly stiff, but larger cell necessarily deforms more. An analytical model<sup>298</sup> as well as numerical simulations<sup>317</sup>

have been developed to provide reference isoelasticity lines for finding cells of different sizes with corresponding stiffness (**Figure 2.1d**) and to assign Young's modulus for each cell as explained in detail in the next section.

### 2.1.2. Extracting Young's modulus from RT-DC data

To be able to draw conclusion about mechanical properties of cells with different sizes, it is necessary to estimate the Young's modulus of the cells. This can be done using either analytical<sup>298</sup> or numerical approaches<sup>317</sup>, and requires making assumptions about the nature of the material that the cell is made of. While some attempts have been made to use more complex models of cells, such as neo-Hookean hyperelastic bulk or elastic shell models<sup>298,317</sup>, the simple model of cell as an isotropic elastic sphere with linear properties is the one that is, so far, broadly applied. Regardless of its simplicity, it provides a convenient approximation of cell mechanical properties for comparative purposes.

In practice, a lookup table, graphically presented in **Figure 2.3a**, is used to assign Young's modulus to the area and deformation values obtained for each cell in the RT-DC measurement. Importantly, the currently available lookup table was corrected for the shear-thinning of the measurement buffer (MB) that contains methylcellulose (MC) and image pixilation effects discussed in more detail elsewhere<sup>318</sup>.

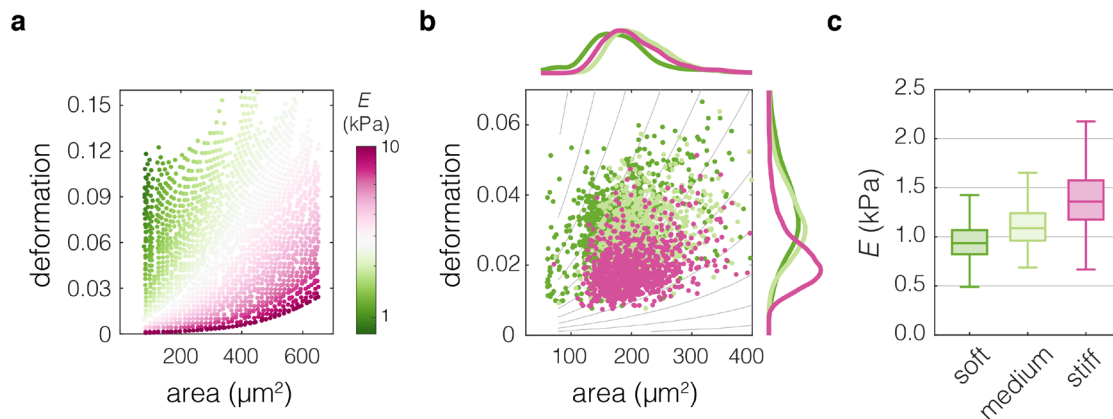


**Figure 2.3 | Determination of Young's modulus from RT-DC data.** **a**, A lookup table based on the simulation is used to assign Young's modulus values for given area and deformation. The colored region indicates the area covered by the simulations. The color map indicates the Young's modulus values. **b**, An overlay of area-deformation scatter plots for three separately measured cell lines of different mechanical properties (magenta – A549, stiff; bright green – EBC1, medium; dark green – Wa-hT, soft). **c**, Box plot of apparent Young's modulus,  $E$ , estimated based on deformation and area in (b). The cell population with same area but higher deformation has lower  $E$  (bright green compared to magenta). For cells with similar deformation, the one with smaller area has lower  $E$  (dark green compared to bright green). The box plots in **d** spread from 25th to 75th percentiles with a line at the median, whiskers span  $1.5 \times$  interquartile range (IQR).

Young's modulus extraction for three cell lines with different mechanical properties: Wa-hT, EBC-1, and A549 is illustrated in **Figure 2.3b–c**. The population of EBC-1 cells has higher deformation values as compared to the population of A549 cells, and both populations are similar in area (**Figure 2.3b**). Consequently, A549 cells have higher Young's modulus than EBC-1 (**Figure 2.3c**). On the other hand,

Wa-hT and EBC-1 cell populations have similar deformation values but different areas (**Figure 2.3b**), and thus the two cell lines differ in their mechanical properties (**Figure 2.3c**).

It is important to bear in mind that the computations on which the lookup table is based are performed for initially spherical cells and the Young's modulus extraction should not be performed for cells that show non-spherical, pre-deformed shapes beforehand. This can be checked by assessing cell deformation in the reservoir region of the channel, in which cells should show only negligible deformation values. Additionally, since the lookup table covers limited area in the deformation-area space, evaluating samples that lie close to the boundaries of this area may result in discarding significant percentage of data and result in introducing artifacts.

## 2.2. Additional functionalities implemented to the RT-DC setup

### 2.2.1. 1D fluorescence readout in three spectral channels

RT-DC was extended to include flow cytometry-like fluorescence readout in the RT-FDC variant developed by Rosendahl *et al.*<sup>312</sup>. The RT-FDC setup, apart from the LED illumination source and a camera, also features an array of lasers and detectors for the characterization of cell fluorescence (**Figure 2.4**).

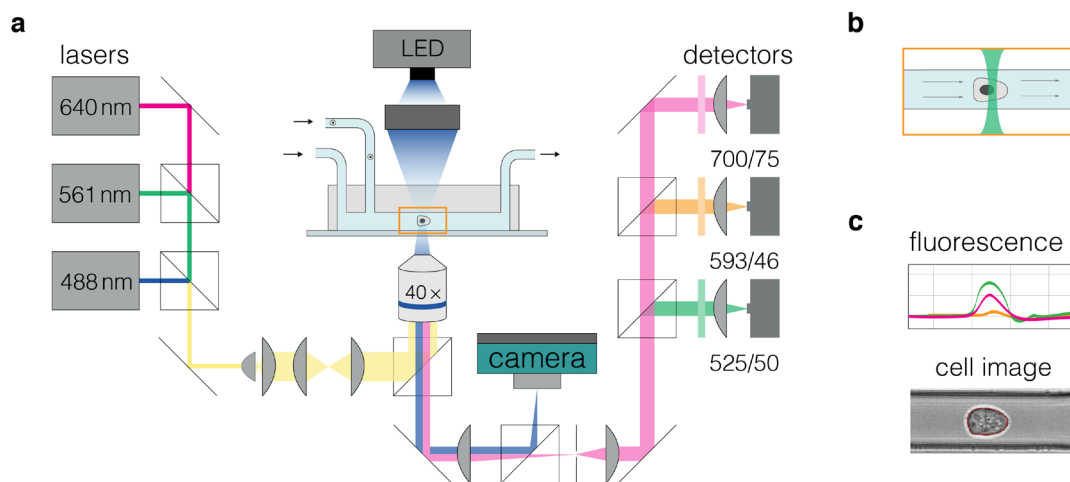


**Figure 2.4 | RT-DC setup with fluorescence measurement functionality.** **a**, Schematic overview of a real time fluorescence and deformability cytometry (RT-FDC) setup. The setup includes LED-based illumination source and camera necessary for bright-field imaging of cells, as well as three laser sources (488 nm, 561 nm, and 488 nm) and an array of detectors with dichroic beam splitters and filters in three spectral ranges (525/50, 593/46, and 700/75) that enable 1D detection of fluorescence signal in three spectral channels. **b**, A light sheet is created from the laser light perpendicular to the channel axis. **c**, When a cell passes the light sheet, a temporal peak of fluorescence signal from each channel is recorded, and assigned to the cell image.

In particular, three solid-state lasers with wavelengths of 488 nm, 561 nm and 640 nm are implemented onto the setup (OBIS 488-nm LS 60 mW; OBIS 561-nm LS 50 mW; OBIS 640-nm LX 40 mW; Coherent GmbH, Germany). The laser beams are combined, thanks to a cylindrical lens

(LJ1695RM-A; Thorlabs), form a light sheet that illuminates cells passing through the microfluidic channel constriction (**Figure 2.4b**). Using dichroic beam splitters and filters with distinct spectral specifications, the light emitted by the sample is split into three fluorescence channels: FL1 (FF555-Di03, FF03-525/50; Semrock), FL2 (zt 633 RDC, Chroma Technology Corp; FF01-593/46, Semrock), and FL3 (700/75 ET; Chroma Technology Corp) and detected using avalanche photodiodes (MiniSM10035; SensL Corporate). As a result, 1D fluorescent signals are acquired over time in three spectral channels in parallel with cell images (**Figure 2.4c**). Several parameters of the fluorescence peaks can be extracted, such as maximum height of the peak (fl-max) and area under the peak that carry information about fluorescence intensity in the cells, or peak width, that carries information about the size of the fluorescence signal and can be used to deduce localization of the signal within the cell, for example the nuclear versus cytoplasmic localization<sup>312</sup>.

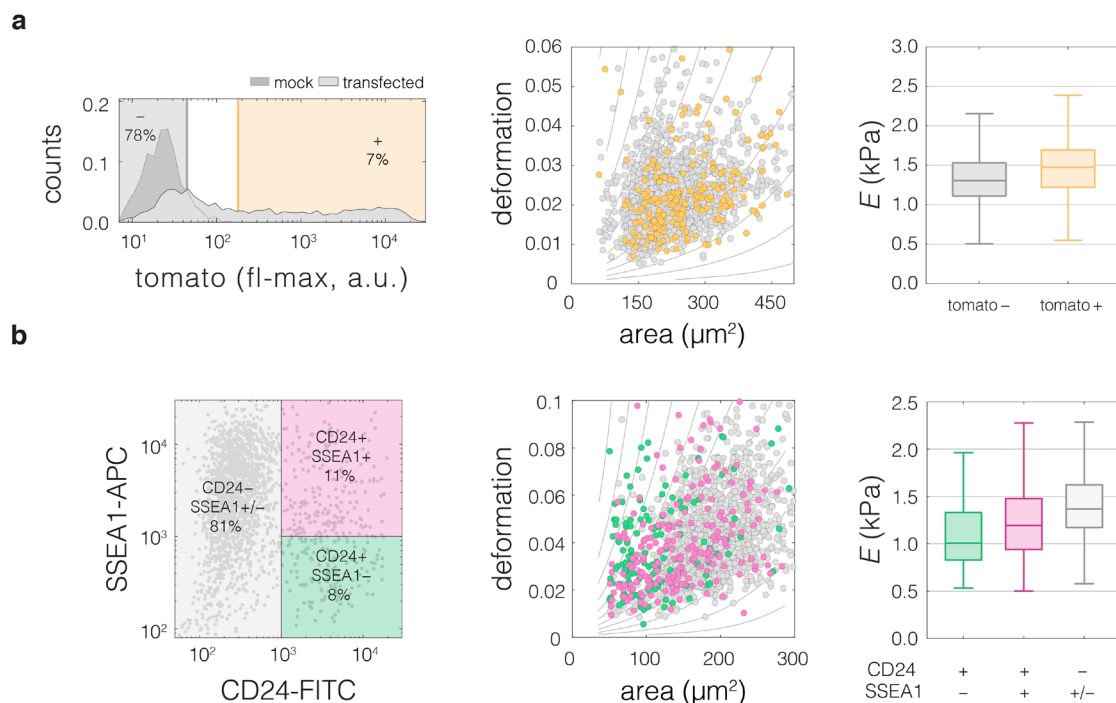


**Figure 2.5 | Examples of fluorescence-based gating of RT-FDC data.** **a**, Fluorescent gating based on one spectral channel (FL2) of TGBC18TKB cells expressing tomato marker together with caveolin-1. **b**, Fluorescent gating based on two spectral channels of iPSCs at 23rd day of reprogramming stained with antibodies against SSEA1 and CD24. The fluorescence gating (leftmost column) can be used to visualize cells of interest in the space of parameters extracted from standard RT-DC measurement such as area and deformation (middle column) or to compare values of a property of interest, for example Young's modulus  $E$ , for cells from different populations (rightmost column).

The access to the fluorescence measurements expands the repertoire of RT-DC applications and enables selective analysis of cells of interest in mixed populations. For example, in the case of transient transfections with a transgene carrying a fluorescent marker, the transfected cells can be identified on-the-fly and gated for to extract their characteristics and compare them with non-transfected controls. In **Figure 2.5a**, an example is shown, in which TGBC18TKB adenocarcinoma cells were transiently transfected with plasmid expressing caveolin-1 with tomato under independent ribosomal entry site

(IRES) as a fluorescence marker (see **Chapter 5** for more details). The fluorescence signal can be used to identify cells expressing the tomato marker, and by extension caveolin-1. Furthermore, staining of cells with antibodies targeting specific surface markers can be used for identification of cells of interest. In **Figure 2.5b** an example is shown, in which induced pluripotent stem cells (iPSCs) are stained with two surface markers: SSEA1 and CD24, labelled with APC (SSEA1) and FITC (CD24) fluorochromes that can be detected in FL3 and FL1, respectively. These markers allow for distinguishing between bone-fide iPSCs (SSEA1+/-, CD24-), transgene-dependent iPSCs (SSEA1+, CD24+), and non-pluripotent cells (SSEA1-, CD24+) in mixed populations at the intermediate stages of reprogramming towards pluripotency (see **Chapter 4** for mor details). The gating of cells using one- (as in **Figure 2.5a**) and two-dimensional (as in **Figure 2.5b**) fluorescence gates is a procedure widely used in the flow cytometry community<sup>319</sup>, and many surface markers are established for identification of cell types in populations of various origins, for example for identification of leukocyte populations in blood samples<sup>320</sup>.

### 2.2.2. SSAW-based active cell sorting

To harness the real-time analysis potential of RT-FDC for active sorting based on characterized cell properties, a SSAW-based deflection mechanism was introduced to the RT-FDC setup (**Figure 2.6a**). Downstream of the analysis region, SSAW are generated by two opposing interdigital transducers (IDTs) flanking the channel and propagate on the lithium niobate substrate (**Figure 2.6a–b**). This allows for pushing the cells of interest into the target outlet.

The chromium-gold IDTs are actuated at their resonance frequency,  $f$ , given by:

$$f = \frac{v}{\lambda}, \quad 2.2$$

where  $v$  is the velocity of sound in the lithium niobate substrate ( $1890 \text{ m s}^{-1}$ ) and  $\lambda$  is the acoustic wavelength, defined by the distance between adjacent IDT fingers. The distance between the two IDTs is a multiple of  $\lambda$ , which results in constructive interference of counter-propagating waves and emergence of standing waves. The SSAW are tuned to have one pressure node, positioned in front of the target channel, towards which cells are deflected when SSAW are triggered. SSAW generate an acoustic radiation force,  $F_r$ , that pushes cells towards the pressure node and directed them into the target outlet.  $F_r$  is given by the following formula<sup>321</sup>:

$$F_r = -\left(\frac{\pi p_0^2 V_p \beta_f}{2\lambda}\right) \phi(\beta, \rho) \sin(2kx), \quad 2.3$$

where  $p_0$  is the acoustic pressure,  $\lambda$  is the acoustic wavelength,  $V_p$  is the volume of the particle,  $\beta$  is compressibility,  $\rho$  is density, and  $\phi$  is the acoustic contrast factor that defines if the particle will translate to the pressure node ( $\phi > 0$ ) or the pressure antinode ( $\phi < 0$ ) defined as:

$$\phi(\beta, \rho) = \frac{5\rho_p - 2\rho_f}{2\rho_p + \rho_f} - \frac{\beta_p}{\beta_f}. \quad 2.4$$

The subscripts  $p$  and  $f$  stand for particle and fluid, respectively.

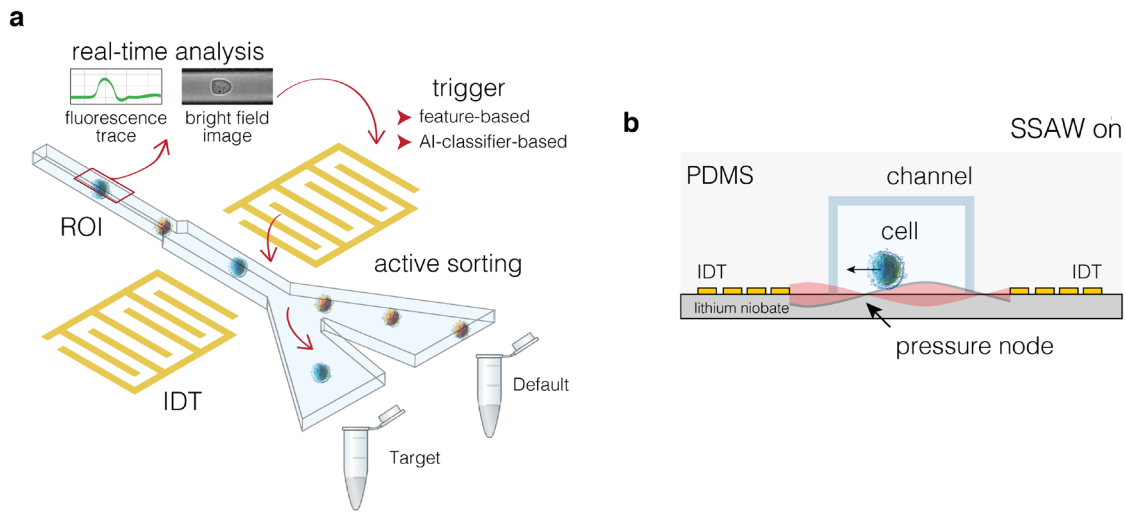


**Figure 2.6 | Operation principle of sorting real-time fluorescence and deformability cytometry (soRT-FDC).** **a**, A schematic representation of the sorting principle. Downstream of the analysis ROI (marked with red box), a sorting region is introduced, in which cells are pushed towards the target outlet by SSAW generated by the IDTs placed at both sides of the channel. A trigger for SSAW is induced only for cells matching the sorting criteria. **b**, A cross-section view of the sorting region of the microfluidic channel. SSAW are generated by the IDTs and propagate on the lithium niobate substrate, the chip is designed so that only one pressure node is present within the channel width. Cells are pushed towards the pressure node placed in front of the target outlet. This figure is modified from Nawaz, Urbanska, Herbig *et al.*<sup>313</sup>.

To accommodate the sorting functionality, the design of the standard RT-DC chip (**Figure 2.2**) was updated to the one shown in **Figure 2.7a**. The length of the narrow channel in which cells are deformed was extended from 300 to 880  $\mu\text{m}$ . Afterwards, the 20 or 30  $\mu\text{m}$  channel broadens to 50  $\mu\text{m}$  to allow space for SSAW-induced cell deflection, before it bifurcates into default and target outlets. The bifurcation point is placed 5  $\mu\text{m}$  off-center, so that all cells are collected in the default outlet when SSAW is switched off. Additionally, a syringe operated in withdrawal mode is mounted to the default outlet to ensure no accidental slipping of cells to the target. Typically, sorting experiments are conducted using flow rates of 0.01, 0.03 and ca.  $-0.027 \mu\text{l s}^{-1}$  for the sample, sheath, and default outlet modules, respectively (20  $\mu\text{m}$  chip), or 0.02, 0.06, and ca.  $-0.05 \mu\text{l s}^{-1}$  (30  $\mu\text{m}$  chip), and 0.6% methylcellulose buffer. A serpentine channel was introduced close to the sample inlet region to aid in cell focusing and longitudinal ordering<sup>322</sup> (**Figure 2.7a**). Cells are exposed to SSAW for about 2 ms in the 50  $\mu\text{m}$  wide and 200  $\mu\text{m}$  long sorting region, what allows for sufficient displacement (**Figure 2.7b**).

A digital output (TTL) is generated based on the real-time assessment of high-speed microscopy images or fluorescence signals from the three available fluorescence channels (for full list of parameters computed in real-time that are available for sorting see **Table 2.1**), and triggers SSAW actuation with a dedicated generator (BSG F20, BelektronikG, Germany). The delay induced by image processing is



on average 225  $\mu\text{s}$ , and the total delay between image exposure and sorting trigger is below 1 ms. Thus, the analysis ROI is placed 120–180  $\mu\text{m}$  before the end of the deformation channel (depending on flow rate and channel size) to allow for timely generation of the output signal. The image acquisition, analysis and signal processing are executed by a custom C++ program running on a standard desktop computer. To allow for inspection of a bigger region during sorting, the experiments are typically performed using a 20 $\times$  objective (Plan-Apochromat, 20 $\times$ /0.8; #440640-9903, Zeiss). Additionally, a polarizer (Polarizer D, 90° rotatable, removable; #427706-0000-000, Zeiss) is introduced between the illumination light and the chip to cancel out the double refraction caused by the birefringent lithium niobate substrate.

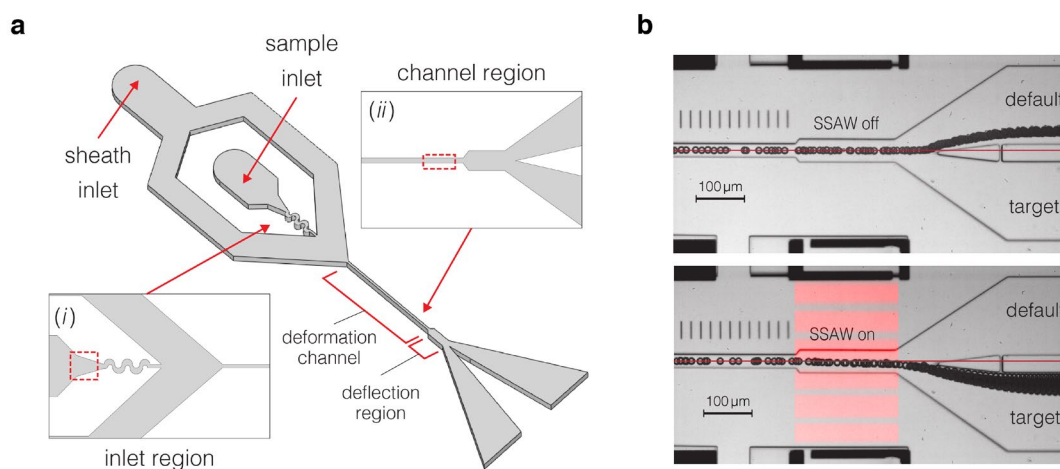


**Figure 2.7 | Overview of the microfluidic chip used for sorting.** **a**, A schematic of the sorting chip layout, with zoom-in insets depicting the areas around the sample inlet (*i*) and analysis channel (*ii*). **b**, Images visualizing bead trajectories in the sorting chip in the presence (upper image) and absence (lower image) of SSAW actuation. The images were created by a minimum intensity projection of 700 frames taken over 350 ms. The red line indicates the center of the channel and serves as a guide for the eye to demonstrate the off-center position of the bifurcation point. This figure is modified from Nawaz, Urbanska, Herbig *et al.*<sup>313</sup>.

The sorting efficacy of the soRT-FDC setup was validated using heterogeneous mixtures of polymer beads. First, fluorescence-activated sorting was demonstrated by separating AlexaFluor488-labeled from unlabeled polyacrylamide (PAAm) beads with a 4.7-fold enrichment (**Figure 2.8a**). Next, we validated the efficiency of sorting for image-derived parameters such as area and deformation. For area-based sorting, we used a mixture of commercially-available monodisperse polymer beads of two different sizes (SiO<sub>2</sub>-F-L3519-1, 13.79  $\pm$  0.59  $\mu\text{m}$  diameter and PMMA-F-B1423, 17.23  $\pm$  0.24  $\mu\text{m}$  diameter; Microparticles, Germany), and observed a 5.7-fold enrichment (from 16.9% to 96.3% purity) when sorting for the bigger beads (**Figure 2.8b**). For deformation-based sorting, we mixed two PAAm bead populations of different stiffness. Using a combined gating for area and deformation, we obtained an increase of targeted beads from 16.2% in the initial mixture (prepared in a 1:6 ratio), to 83.7% in the target sample, amounting to 5.2-fold enrichment. The PAAm beads used for experiments presented in **Figure 2.8a,c** were produced in house according to previously established procedures<sup>323</sup>.

Table 2.1 | Features analysed in real-time during RT DC measurement.

image-derived features	
<b>position x</b>	position along channel axis
<b>position y</b>	position lateral in the channel ( $\mu\text{m}$ )
<b>bounding box size x (a)</b>	size of the object in the direction parallel to the flow ( $\mu\text{m}$ )
<b>bounding box size y (b)</b>	size of the object in the direction perpendicular to the flow ( $\mu\text{m}$ )
<b>aspect ratio (a/b)</b>	ratio between object's length and height
<b>area raw</b>	area enclosed by the contour fitted to the object (pixel)
<b>area</b>	area enclosed by the convex hull of the contour fitted to the object (pixel & $\mu\text{m}$ )
<b>area ratio</b>	ratio between area raw and area
<b>deformation</b>	$1 - \frac{2\sqrt{\pi \text{ area}}}{\text{perimeter}}$ $\frac{I_{yy}}{I_{xx}}$
<b>inertia ratio</b>	$I_{yy}$ - second moment of contour area calculated for $y$ -direction
<b>(convex or raw contour)</b>	$I_{xx}$ - second moment of contour area calculated for $x$ -direction
	$I_{yy} = \iint_A y^2 dx dy, I_{xx} = \iint_A x^2 dx dy$ <p><math>x</math> and <math>y</math> represent Cartesian coordinates</p>
<b>Young's modulus</b>	mechanical property that quantifies cell stiffness derived from numerical simulations <sup>317</sup> , in real-time obtained from a look-up table based on object size and deformation (Pa)
<b>brightness</b>	average brightness of pixels enclosed by the contour fitted to the object (a.u.)
<b>s.d. brightness</b>	standard deviation of the brightness of pixels enclosed by the contour fitted to the object (a.u.)
fluorescence trace-derived features	
<b>FL1 intensity</b>	maximum fluorescence intensity (fl-max) recorded in channel 1 (a.u.); excitation wavelength 488 nm, emission filter 525/50
<b>FL2 intensity</b>	maximum fluorescence intensity (fl-max) recorded in channel 2 (a.u.); excitation wavelength 561 nm, emission filter 593/46
<b>FL3 intensity</b>	maximum fluorescence intensity (fl-max) recorded in channel 3 (a.u.); excitation wavelength 640 nm, emission filter 700/75

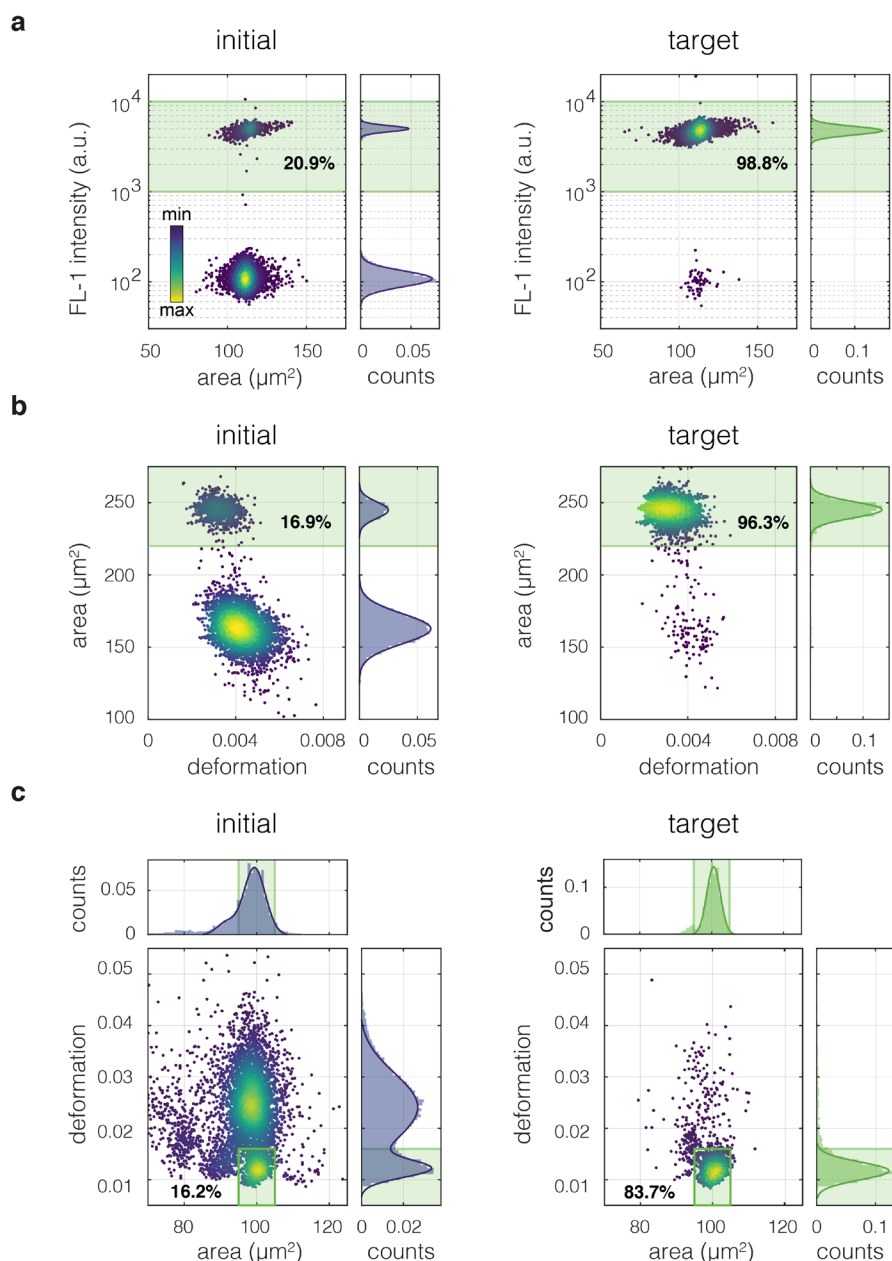


**Figure 2.8 | Fluorescence and feature-based sorting of beads with SORT-FDC.** **a**, Fluorescence-based sorting from a mixture of fluorescent and non-fluorescent PAAm beads. **b**, Area-based sorting from a mixture of beads of two different sizes. **c**, Sorting with a double gate for area and deformation from a mixture of PAAm beads with different stiffness. The scatter plots for initial samples are shown on the left-hand side of each panel, and the plots for samples collected in the target outlet are shown on the right. The color map represents event density. The histograms accompanying scatter plots were fit with a superposition of Gaussian functions (solid lines). The gates used for sorting are outlined in green. Percentages on scatter plots indicate the fraction of beads in the sorting gate. Data for this figure was acquired by Dr. Ahmad A. Nawaz, the figure is modified from Nawaz, Urbanska, Herbig *et al.*<sup>313</sup>.

Cells are known to be more difficult to translocate using SSAW than polymer beads due to their lower acoustic contrast factor<sup>324</sup> that determines the radiation force (see **Equation 2.3**). Hence, we next tested area and deformation-based sorting of living cells. Specifically, we sorted Kc167 drosophila cells from their 1:4 mixture with human promyelocytic leukemia cells (HL60/S4) with a 4-fold enrichment

and 88.2% purity (**Figure 2.9a**), and a sub-fraction of red blood cells (RBCs) with high deformation from diluted whole blood with a 3-fold enrichment and 91.3% purity (**Figure 2.9b**).

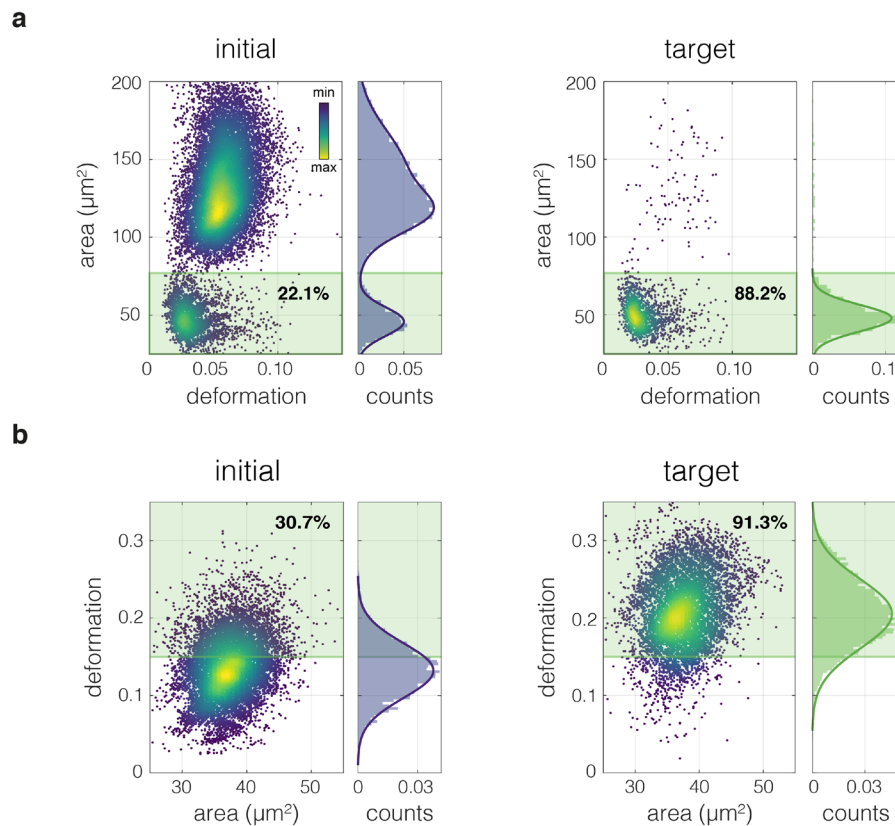


**Figure 2.9 | Feature-based sorting of cells with soRT-FDC. a,** Area-based sorting of a mixture of Kc167 cells (smaller size) and HL60/S4 cells (bigger size). **b,** Deformation-based sorting of red blood cells from whole diluted blood. The scatter plots for initial samples are shown on the left-hand side of each panel, and the plots for samples collected in the target outlet are shown on the right. The color map represents event density. The histograms accompanying scatter plots were fit with a superposition of Gaussian functions (solid lines). The gates used for sorting are outlined in green. Percentages on scatter plots indicate the fraction of cells in the sorting gate. Data for this figure was acquired by Dr. Ahmad A. Nawaz, the figure is modified from Nawaz, Urbanska, Herbig *et al.*<sup>313</sup>.

### 2.3. Beyond assessment of cell mechanics — emerging applications

Even though RT-DC was originally introduced for the deformation-based evaluation of the mechanical properties of cells, it can be utilized to perform multifaceted morphological characterization and sorting of cells. This section presents examples of three application of RT-DC beyond evaluation of cell mechanics. First of all, the parameter deformation does not only aid in evaluation of mechanical properties, but also in discriminating different cell types in heterogenous population that would be obscured otherwise. An example of this is distinguishing of the main cell types in the whole blood samples (**Section 2.3.1**). Secondly, further parameters such as cell brightness can be deduced from the acquired images and serve as an additional dimension for further cell separation. In blood, this allows for distinguishing of sub-fractions of myeloid cells<sup>5</sup>, which can then be sorted in a label-free way as

shown on the example of neutrophils (Section 2.3.2). A wealth of image-derived morphological and texture parameters (a selection of which is summarized in Table 2.1 and Table 2.5) can be derived for each cell and used in a way analogous to brightness to perform image-based cell classification. Finally, thanks to the access to thousands of images of cells labelled for identity using fluorescence markers, neural networks (NNets) can be trained to recognize cells of interest based on images alone. We demonstrated this possibility on the examples of NNet-based sorting of neutrophils from blood (Section 2.3.3).

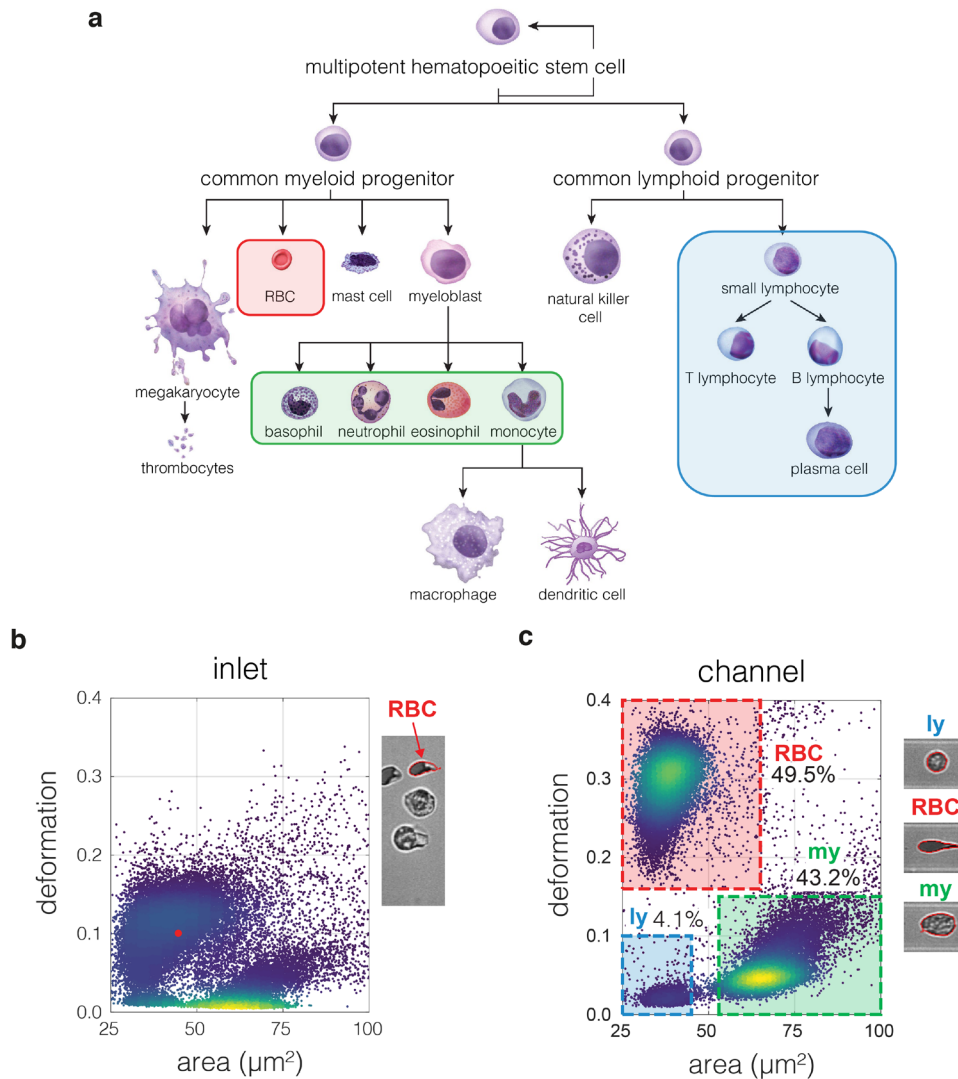


**Figure 2.10 | Deformation-assisted discrimination of three major cell types in blood samples.** **a**, An overview of hematopoietic lineages. The cells identified as RBC, myeloid cells and lymphocytes in RT-DC measurements are outlined with red, green, and blue frames, respectively. **b**, Deformation-size scatter plot of RBC-depleted blood sample measured in the inlet region. **c**, Deformation-size scatter plot of RBC-depleted blood measured in the channel region as shown. The clearly distinguishable cell populations include: red blood cell (RBC) lymphocytes (ly) and myeloid cells (my). The percentages of respective cell types are indicated in the plot. The typical images of cells from each population are shown on the right. Panel **a** is adapted from *Openstax Anatomy and Physiology* textbook<sup>325</sup>, under *CC BY 4.0* license<sup>326</sup>. Data for **b** and **c** was acquired by Dr. Ahmad A. Nawaz, these panels are adapted from Nawaz, Urbanska, Herbig *et al.*<sup>313</sup>.

### 2.3.1. Deformation-assisted population separation and sorting

Flow-induced deformation of cells, together with their alignment along the major channel axis, enhances the separation of cell subpopulations in blood samples, and allows for distinguishing of three major blood cell types: RBCs, myeloid cells and lymphoid cells (indicated with shaded squares in **Figure 2.10a**). When characterized in the inlet region of the chip (**Figure 2.7a**, inset *i*), where cells experience negligible hydrodynamic forces and are randomly oriented, the three blood cell populations show an overlap in the area-deformation scatter plots (**Figure 2.10b**). Measuring the same sample in the deformation channel (**Figure 2.7a**, inset *ii*), where cells are deformed and aligned with the channel major axis, results in a clear separation of blood cell subtypes (**Figure 2.10c**), what is used for their identification<sup>5,21</sup>. Specifically, the RBC population with high deformation values moves further away from the two remaining cell subtypes on the deformation axis. Thanks to the clear separation of the subpopulations, sorting using area-deformation gates is possible. We were able to sort for the three cell populations and obtained a purity of 96.6% for RBCs (**Figure 2.11a**), 89.1% for lymphocytes (**Figure 2.11b**), and 94.7% for myeloid cells (**Figure 2.11c**), with an enrichment factor of 1.95, 21.7 and 2.0, respectively (the percentages of cells in the respective gate before sorting are indicated in **Figure 2.10c**).

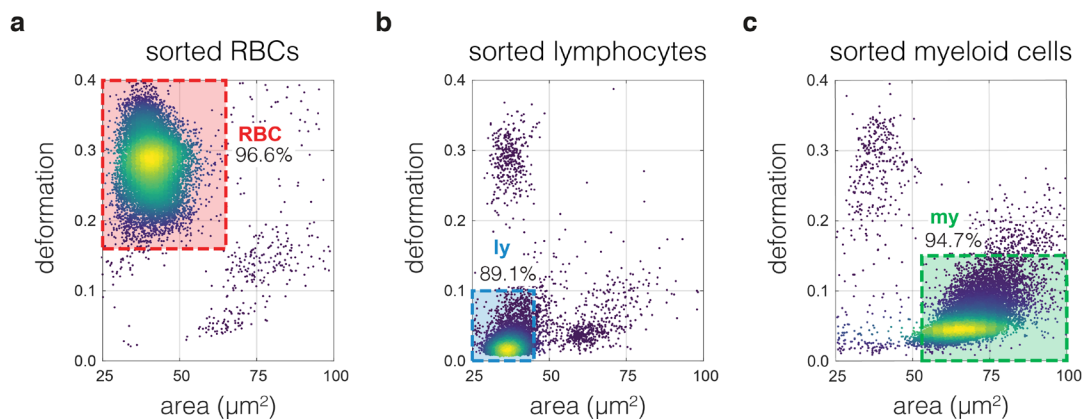


**Figure 2.11 | Deformation-assisted sorting for three major blood cell types.** **a–c**, Analysis of cells collected in the target when sorting for RBCs (**a**; area: 25–65 μm<sup>2</sup>, deformation: 0.16–0.40), lymphocytes (**b**; area: 25–45 μm<sup>2</sup>, deformation: 0–0.10) and myeloid cells (**c**; area: 53–120 μm<sup>2</sup>, deformation: 0–0.15) from RBC-depleted blood using gates indicated in the plot. Cells were sorted from the initial sample presented in **Figure 2.10c**. Percentages indicate purity. All sorting experiments were conducted with an additional gate for area ratio 1.0–1.1. Data for this figure was acquired by Dr. Ahmad A. Nawaz, the figure is modified from Nawaz, Urbanska, Herbig *et al.*<sup>313</sup>.

### 2.3.2. Brightness-based identification and sorting of blood cells

The myeloid cell fraction defined with the area-deformation gate above comprises several distinct cell types: basophils, neutrophils, eosinophils and monocytes (see **Figure 2.10a**). Adding an additional parameter, the average brightness within the cell contour, enables distinguishing of these cell types<sup>5</sup> (**Figure 2.12a**). Since brightness is a parameter calculated in real-time by the analysis software, it can be utilized for sorting of the specified myeloid blood subtypes.

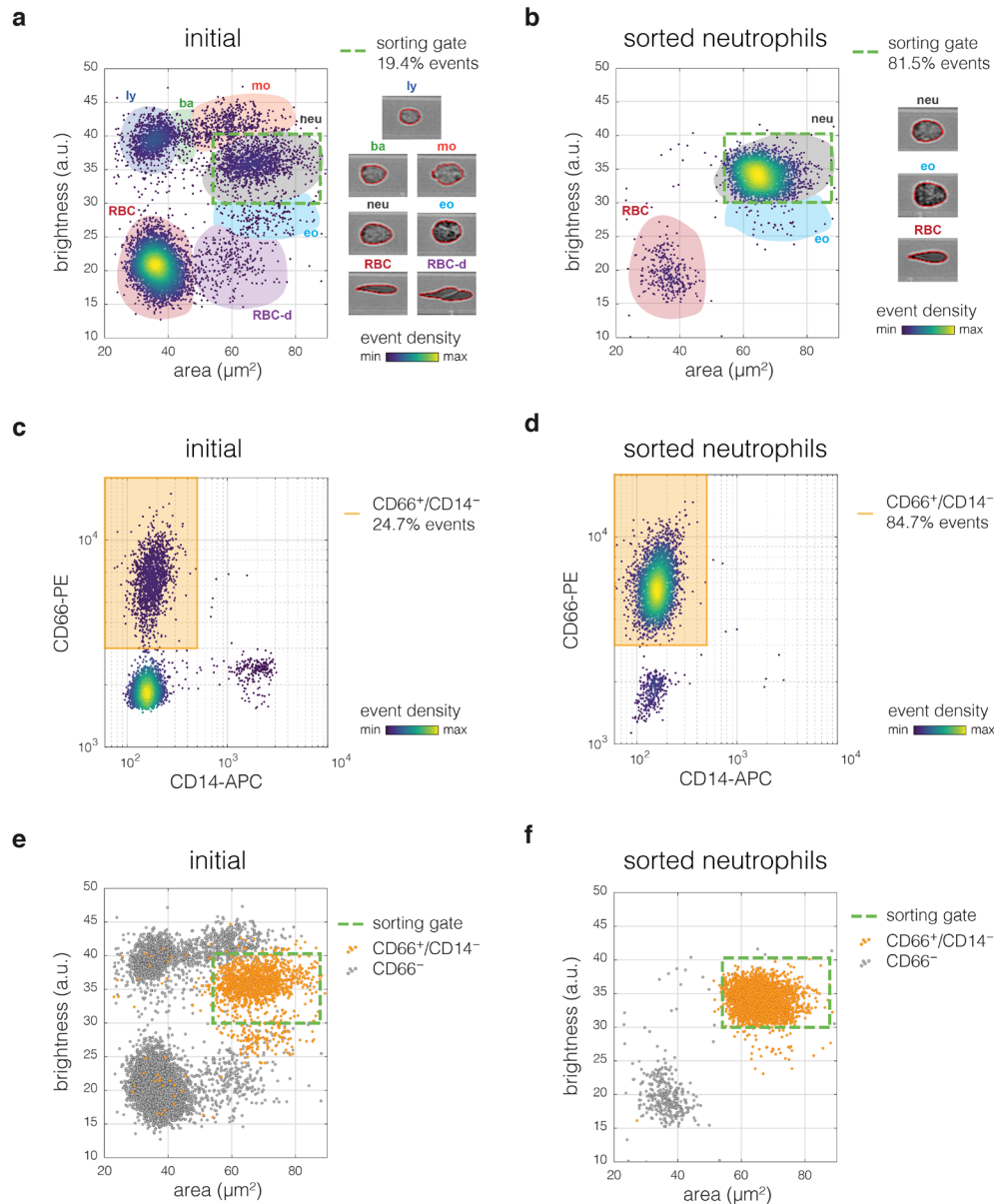


**Figure 2.12 | Brightness-based neutrophils sorting from RBC-depleted blood.** **a,b**, Brightness-area scatter plots of RBC-depleted blood for initial (**a**) and target (**b**) samples. Color-coded patches delineate subpopulations of different cell types. Sorting gate is indicated with dashed green line. Typical cell images of respective subpopulations are displayed next to the scatter plots. The subpopulations include: lymphocytes (ly), basophils (ba), monocytes (mo), neutrophils (neu), eosinophils (eo), red blood cells (RBC) and red blood cell doublets (RBC-d). **c,d**, CD66 and CD14 surface marker expression for initial (**c**) and target (**d**) samples measured with RT-FDC. **e,f**, Brightness-cell size scatter plots as in **a** and **b** with CD66<sup>+</sup>/CD14<sup>-</sup> cells (putative neutrophils) indicated in orange. Data for this figure was acquired by Dr. Ahmad A. Nawaz, the figure is modified from Nawaz, Urbanska, Herbig *et al.*<sup>313</sup>.

To demonstrate this possibility, we used a combination of area (50–100  $\mu\text{m}^2$ ) and brightness (30–40 a.u.) gates to perform label-free sorting of neutrophils from RBC-depleted blood. The percentage of events in the sorting gate increased from 19.4% in the initial sample to 81.5% in the target sample (**Figure 2.12a,b**), amounting to 4.2-fold enrichment. The identity of sorted cells was validated after sorting via staining with a mixture of APC-conjugated anti-human CD14 (dilution 1:20, #17-0149-42,

eBioscience, CA, USA) and PE-conjugated anti-human CD66a/c/e (dilution 1:40, #34303, BioLegend, CA, USA) and analysis with RT-FDC. The CD66<sup>+</sup>/CD14<sup>-</sup> cells, corresponding to neutrophils<sup>320</sup>, constituted 24.7%, in the initial and 84.7% in the target samples (**Figure 2.12c,d**). This corresponds well with the fractions contained in the size-brightness gate set for neutrophils (**Figure 2.12a,b**). 74.4% of all CD66<sup>+</sup>/CD14<sup>-</sup> events in the initial sample fell into the size-brightness gate specified for vital, resting, single neutrophils<sup>6</sup> (**Figure 2.12e**). The remaining 25.6% of CD66<sup>+</sup>/CD14<sup>-</sup> events appear to belong to other blood cell type populations (**Figure 2.12e**), implicating occurrence of false positive neutrophil classification when using molecular labels. This observation points towards an important advantage of using physical parameters, such as size and brightness, for cell identification — the circumvention of the false positives observed in the fluorescent staining.

### 2.3.3. Transferring molecular specificity into label-free cell sorting

The image-derived parameters exploited for sorting in the aforementioned examples, including area, deformation, and brightness, are far from being exhaustive. Apart from the parameters listed in **Table 2.1** and **Table 2.5**, more elaborate features such as Haralick texture features, scale-invariant feature transforms, local binary patterns, or threshold adjacency statistics<sup>327–330</sup> can be extracted from the images and used for cell classification. However, the extraction of such parameters is typically too computationally expensive to allow for their real-time evaluation. Another approach is to take advantage of information contained within all pixels of the raw image, and use a neural network (NNet) to classify cells of interest in a featureless way (**Figure 2.13a**). NNet training generally requires a sufficiently large labelled dataset training. Using the RT-FDC platform, thousands of cell images can be acquired within seconds and their labelling can be achieved by connecting them with the expression of surface markers. Such labelled datasets are ideal for NNet training, and the NNet classifiers can be used thereafter to replace the fluorescent markers for a given classification task. The NNet-based classification can be performed in real-time and used for sorting. In this way, the molecular specificity of the fluorescent labels can be transferred into label-free NNet-based cell classification and sorting.

As an example, we trained a NNet for the identification and sorting of neutrophils based on bright-field images alone. To this aim, we have employed a dedicated *AIDeveloper* software developed in house by Dr. Maik Herbig<sup>315</sup>. First, we have chosen a type of network called multilayer perceptron (MLP) with an architecture that was identified to offer a good trade-off between maximum validation accuracy (MVA = 85.9 %) and inference time (183.7  $\mu$ s) for hand-labelled blood datasets<sup>313,331</sup> (**Figure 2.13b**). This architecture was then trained on a dataset of 34,206 blood cell images correlated with CD66/CD14 staining, in which CD66<sup>+</sup>/CD14<sup>-</sup> events were labelled as neutrophils. Next, we applied the trained MLP on a validation dataset (5,925 cells), and observed a classification accuracy of 95.5% using fluorescent labels as ground truth (**Figure 2.13c**). Finally, the MLP was applied to sort neutrophils from RBC-depleted blood based on images alone. The post-analysis of the target and initial samples



was performed using RT-FDC, with CD14/CD66 staining as validation of cell identity. We obtained a 89.7% purity and an 10-fold enrichment of CD66<sup>+</sup>/CD14<sup>-</sup> cells after image-based sorting using cell images and the trained NNet (**Figure 2.13d,e**). This demonstrates the feasibility of transferring molecular specificity conferred in fluorescent markers into label-free image-based sorting using soRT-FDC. Label-free sorting is of particular relevance for applications in which introducing fluorescent labels is undesirable, for example in transplantation. Specific examples of where label-free sorting for transplantation could be of interest include hematopoietic stem cells<sup>332,333</sup> or retinal precursor cells<sup>334,335</sup>.

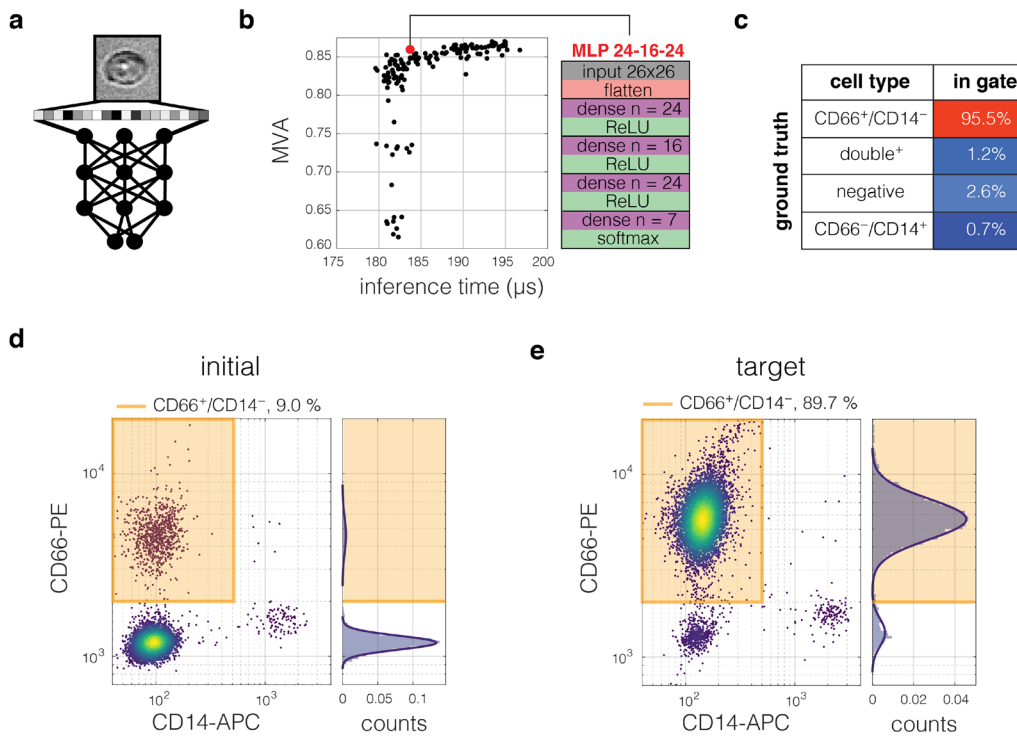


**Figure 2.13 | NNet-based sorting of neutrophils from RBC-depleted blood.** **a**, Schematic representation of NNet-based image analysis. **b**, Maximum validation accuracy (MVA) versus inference time for 162 tested differently complex MLPs. The MLP selected for sorting (MLP 24-16-24) is indicated in red; its architecture details are summarized on the right. **c**, Percentage of different cell types classified as neutrophils by NNet. Calculation based on fluorescent staining: CD66<sup>+</sup>/CD14<sup>-</sup> cells correspond to neutrophils, CD66<sup>-</sup>/CD14<sup>+</sup> to monocytes, double negative cells to RBCs and double positive are staining errors or cell doublets. **d,e**, Post-analysis of the initial (**d**) and the target (**e**) samples using RT-FDC and CD14/CD66 staining. Data for this figure was acquired by Dr. Maik Herbig, the figure is reprinted from Nawaz, Urbanska, Herbig *et al.*<sup>313</sup>.

## 2.4. Discussion

RT-DC is a robust method for rapid and continuous mechanical characterization of large populations of suspended cells. Cell images acquired during the measurements can be utilized to extract not only cell deformation that carries information about mechanical properties, but also further image-derived parameters such as cell size and brightness. Various combinations of the extracted parameters can be utilized for identification of cell types in heterogeneous populations, as discussed in **Sections 2.3.1** and **2.3.2** on the example of blood. The combination of RT-DC with fluorescence detection in three spectral channels<sup>312</sup> (**Section 2.2.1**) and SSAW-based sorting<sup>313</sup> (**Section 2.2.2**) has transformed the original RT-DC setup into a versatile soRT-FDC platform for fluorescence- and image-based single cell analysis and sorting. Noteworthy, the thousands of bright-field cell images generated with RT-DC can be labelled for cell identity using fluorescent markers and leveraged for training of NNets, that ultimately enable AI-assisted, image-based classification and separation of cells (**Section 2.3.3**).

In terms of mechanical characterization, an invaluable asset of RT-DC is the availability of the analytical model<sup>298</sup> and numerical simulations<sup>317</sup> that allow for mapping of cell area and deformation to Young's modulus (**Section 2.1.2**). This is of particular importance when comparing cells of different sizes, as in such cases the deformation information alone could be misleading (see **Figure 2.3**). Furthermore, the extracted Young's moduli can be used to compare RT-DC results with the mechanical characterization using other methods. It is important to remember that several assumptions underlie both of the theoretical approaches, namely, that cells are homogenous and isotropic elastic bodies and that they are spherical before entering the channel<sup>298,317</sup>. These assumptions may not faithfully reflect heterogeneous nature of cell structure and shape, however, similar simplifications underlie the Hertz model<sup>259</sup>, customarily used for extracting Young's modulus from AFM indentation curves. Regardless, the assigned Young's moduli fulfill their purpose as an effective parameter describing cell stiffness and facilitate mechanical comparison of different cell populations.

Apart from characterization of Young's modulus from a snapshot of steady-state cell deformation, RT-DC can be exploited to derive time-dependent properties of cells such as viscosity. For this purpose, the evolution of cell deformation has to be measured over extended period covering cell entry or passage through the channel. A challenge for modelling the deformation response is posed by the complex nature of the stresses applied to cells during their entry into the channel constriction. In the bottleneck region preceding the constriction, cells experience increasing extensional stress arising from the acceleration of the fluid around the cell, and after entry to the channel, cells experience the shear forces arising from the parabolic flow profile<sup>336,337</sup>. These two sources of stress are superimposed and hard to disentangle. An elegant solution to this problem, proposed by Fregin *et al.*<sup>336</sup>, is to decompose the cell shape into a sum of shape modes that are symmetric around the flow axis (even modes, reflecting the deformation induced by the extensional flow), and a sum of shape modes that are asymmetric around the flow axis (odd modes, reflecting the bullet-like cell shape induced inside

the channel) using Fourier decomposition. That way the relaxation inside the channel, traced by the deformation of reconstituted odd shape modes, can be considered a creep compliance experiment and modeled using a selected material model, e.g., a Kelvin-Voigt, to extract cell viscosity<sup>336</sup>. As tested by fitting the curves obtained via numerical simulations of viscoelastic spheres of given viscosity, using squared inertia ratio can give even better estimate of the viscosity than fitting the deformation curves obtained for the contours reconstituted from odd coefficients of the Fourier modes<sup>337</sup>. Future direction in extracting time-dependent properties of cells in RT-DC include exploring model-free approaches for derivation of frequency-dependent viscoelastic moduli based on Fourier transform, so far implemented for AFM step-strain<sup>338,339</sup> and step-stress experiments<sup>340</sup>, as well as devising microfluidic channel geometries that ensure a simpler stress profile.

The main limitation of RT-DC in terms of mechanical characterization of cells is performing the measurements on suspended cells. For adherent cell lines, organoids, or tissue sections, single cell suspensions need to be generated prior to the experiments, what may affect the properties of the cells that rely on cell-cell and cell-substrate attachment. For example, it has previously been demonstrated for mesenchymal stem cells that harvesting the cells from the substrate and keeping them in suspended state may cause cell stiffening over time<sup>341</sup>. Thus, it is crucial to control the time between cell detachment and the measurements, and to bear in mind that mechanical differences observed for adherent cells may not always be maintained in the suspended state.

RT-DC is characterized by straightforward operation, automated data acquisition and low sample volume required for analysis, what makes it an attractive method not only for basic research but also for clinical applications. RT-DC has been successfully implemented for identification of several medically relevant pathological conditions based on the properties of blood cells. Examples include exposure of RBCs to *Plasmodium falciparum*<sup>5,69</sup>, spherocytosis<sup>5</sup>, leukocyte activation<sup>5,6,124</sup>, as well as acute myeloid and lymphatic leukemias<sup>5</sup>. Most recently, it has been demonstrated using RT-DC that during infection with COVID19 the physical properties of blood cells are altered, and do not recover to previous levels long after the infection is over<sup>60</sup>, what may play a role in persisting long-term symptoms referred to as long COVID. Analysis of blood in RT-DC is particularly straightforward as blood cells are naturally in the suspended state. Expanding RT-DC characterization to cells extracted from solid tissue biopsies, in particular for potential usage in cancer diagnostics and staging, will require implementation of a robust method for sample dissociation, such as TissueGrinder<sup>342</sup>— a mechanical dissociation method that allows for generation of highly viable cell suspensions from tissues within several minutes.

High measurement throughput and low sample processing time render RT-DC particularly well suited for performing screening experiments. Such screens, aimed at discovering regulators of mechanical properties or other morphological features of cells, can be performed using dedicated libraries, such as RNA interference (RNAi)<sup>343</sup>, CRISPR<sup>344</sup>, or chemical compound libraries. So far several attempts at

RNAi screens have been performed in the group: (i) a pilot screen for regulators of mitotic cell mechanics in *Drosophila* cell line Kc167 using 42 pre-selected genes<sup>312</sup>, (ii) its expansion with >200 kinases/phosphatases (project of Dr. Katarzyna Plak, unpublished data), and (iii) a screen of genes involved in cell softening during epithelial to mesenchymal transition in epiblast stem cells (EpiSCs) using 50 pre-selected genes (project of Dr. Maria Winzi, unpublished data). Such screens, with treatments typically performed in triplicate, are still limited in scale hugely due to the sample preparation and loading times. Future developments aimed at automatization of sample pre-processing and measurement handling, for example by integrating a robot harvesting cells directly from a multi-well plate, autonomously loading the sample and running the measurements, will enable performing of such screens at a much broader scale.

The sorting modality introduced in the soRT-FDC setup is a first demonstration of active sorting for cell mechanics with practically useful throughput. Previous attempts of active sorting based on mechanical properties using optical stretcher were limited in throughput to <100 cells per hour. For comparison, soRT-FDC enables sorting at rates of up to 100 cells per second. Typically, depending on abundance of cells of interest in the sample, several thousands of cells can be sorted in the timespan of an hour. Passive methods for mechanics-based sorting, such as deterministic lateral displacement<sup>345,346</sup>, inertial microfluidics<sup>347</sup>, acoustophoresis<sup>348,349</sup>, or filtration-based approaches<sup>350,351</sup> provide high throughput; however, they often convolve cell deformability with size — small stiff cells are sorted with large soft ones — and, since the sorting parameters are hard-wired into the device design, they do not offer flexibility in choosing sorting parameters on demand. soRT-FDC, in turn, is well suited for freely and flexibly combining sorting for mechanics and other available parameters, such as cell size, fluorescence, or brightness. Label-free sorting of cells enabled by soRT-FDC, including feature-based as well as featureless AI-based sorting, is of high interest for downstream applications for which lack of extrinsic labels is of crucial importance. Such applications include sorting, for example of hematopoietic stem cells<sup>332,333</sup> or retinal precursor cells<sup>334,335</sup> enrichment, for use in transplantation.

With thousands of cells characterized in every experiment, RT-DC is poised for integration with machine learning for applications such as cell and sample classification. As presented in **Section 2.3.3** on example of neutrophils, raw images labelled for cellular identity using fluorescent markers can be used for training of NNets for image-based recognition of cells of interest. Similarly, image-based discrimination of B- and T-cells in whole blood samples can be achieved using NNets trained on CD3/CD19 and CD3/CD56-stained samples<sup>315</sup>. Another example of machine learning-assisted classification of cell types is discrimination of mature RBCs from reticulocytes using a combination of parameters extracted from images<sup>314</sup>. Further examples of label-free image-based classification of cell can be found in the literature concerning conventional as well as microfluidics-based imaging flow cytometry (reviewed in Luo *et al.*<sup>352</sup>), and include classification of cells based on their cell cycle stages<sup>353</sup> or discrimination of platelets aggregates<sup>354</sup>. Apart from classification of cell subpopulations within

a given sample, machine learning-based approaches can be utilized to compare parameter distribution patterns between different samples for sample classification purposes, for example, in diagnostics.

So far, RT-FDC combines bright-field imaging and fluorescence acquisition for a multiparametric characterization of cell phenotypes. In the future, further modalities could be added to RT-FDC to expand obtained biophysical parameters. For example, the integration of Raman spectroscopy, already demonstrated for flow-through configuration<sup>355,356</sup>, would enable label-free chemical characterization of cells. Thanks to the integration of quantitative phase imaging onto the platform, parameters such as refractive index and cell mass could be characterized<sup>357</sup>. Finally, addition of Brillouin line-scanning microscopy would enable characterization of longitudinal modulus<sup>247,358</sup>.

Taken together, the combination of RT-FDC and SSAW-based cell sorting in conjunction with NNet classification provides for a flexible sorting platform, soRT-FDC, capable of not only parameter-based sorting, but also of AI-assisted, image-based separation of cells. The latter provides the opportunity to transfer molecular specificity into label-free cell sorting and to identify new cell types, the distinction of which is not possible on the basis of known features. Further developments of the platforms, in particular automation of sample handling and integration with machine learning-based data analysis, will accelerate RT-DC-driven discoveries and contribute to the understanding of the role of cell mechanics and morphology in health and disease.

## 2.5. Key conclusions

- RT-DC is a versatile method for single-cell mechanical phenotyping that can be utilized to characterize various suspended and adherent cell types.
- Thanks to its integration with SSAW-based deflection mechanism, RT-DC can be used for image-activated cell sorting according to parameters such as cell deformation, size, and brightness.
- Combining two or more parameters (e.g., deformation, size, and brightness for blood cell types) enables efficient classification of cell types within heterogenous populations.
- The images generated during RT-DC experiments can be used not only to extract parameters, but also to train neural networks to classify and sort cells based on raw images.
- Using fluorescent markers for cell labelling in training datasets enables transferring of molecular specificity into label-free image-based cell sorting.

## 2.6. Materials and experimental procedures

### 2.6.1. Microfluidic chips

RT-DC chips were made from polydimethylsiloxane (PDMS, SYLGARD, 188 Dow, Corning Inc., NY, USA) using soft lithography techniques. A mixture of PDMS and curing agent (10:1, w/w) was poured over a silicon wafer master and cured as described in detail elsewhere<sup>359</sup>. The holes for connecting the sheath and sample tubing are punched through the PDMS replica (**Figure 2.2**) with the channel imprint using a 1.5 mm puncher (e.g., Biopsy Punch #49115, Pfm Medical AG, Germany). The PDMS replica were covalently bound to a microscopy-suited cover glass (40 × 24 mm<sup>2</sup>, Assistent, Germany) and sealed by plasma activation (50 W, 30 s, Plasma Cleaner Atto, Diener Electronic, Germany). The width of the channel used for given application should be selected in correspondence to the cell size. For optimal performance, cell diameters should cover 20–90% of the channel width. Commonly used channel widths range from 15 to 40 μm.

For sorting chips, the PDMS replicas (with channel design presented in **Figure 2.7a**) were bonded to a 128° Y-cut lithium niobate (LiNbO<sub>3</sub>, Roditi International, UK) substrate instead of the glass coverslip. Prior to bonding, thin layers of chromium and gold (Cr/Au, 10 nm/70 nm, respectively; Kurt J. Lesker, UK) were deposited on top of the substrate to form the IDTs flanking the sorting channel region (see **Figure 2.6a**). Each IDT had 40 electrode pairs, an aperture of 200 μm, and an inter-finger distance of 70 μm, resulting in an excitation frequency of 55.23 MHz. Additionally, a 100 nm layer of SiO<sub>2</sub> was deposited on top of the substrate to improve bonding to PDMS. The sorting chips were prepared by Dr. Ahmad A. Nawaz.

### 2.6.2. Measurement buffer

The measurement buffer (MB), used for both cell suspension and as a sheath fluid during the RT-DC measurements, contains methylcellulose for achieving an increased buffer viscosity. High MB viscosity allows for appreciable cell deformations at moderate flow rates and reduces cell sedimentation during the measurements.

MB was prepared by dissolving 0.5% (w/v) methylcellulose (MC, 4000 cPs #36718, Alfa Aesar, Germany) in a physiological buffer, such as PBS or the cell culture medium. After prolonged mixing of about 24 h on a rotary mixed to fully dissolve the MC powder, the buffer was filtered through a vacuum filter unit (Stericup-GP, 0.22 μm, Merc Millipore, Germany), and its viscosity was adjusted to 15 mPa s at 23 °C using a falling drop viscometer (HAAKE, Thermo Fisher Scientific, MA, USA). For blood measurements and sorting MB with final viscosity of 25 mPa s, prepared by dissolving 0.6% (w/v) MC in PBS, was used. The osmolarity of the MB was adjusted to 320 ± 20 mOsm to accommodate for the physiological osmolarities of most eucaryotic cell lines. For reference, RPMI-based media have an osmolarity of approximately 300 mOsm, which roughly corresponds to

the osmolality of human blood plasma<sup>360</sup>. DMEM-based media, depending on exact composition and provider, have an osmolality ranging from 310 and 360 mOsm, and the osmolality of PBS solutions usually falls between 285 and 325 mOsm.

### 2.6.3. Consumables

Commercially available consumables necessary for conducting RT-DC measurements are listed in **Table 2.2**.

**Table 2.2 | Consumables necessary for setting up an RT-DC experiment.** This table is adapted from Urbanska, Rosendahl, Kräter *et al.*<sup>316</sup>.

Article	Product Name; Company	Order No.
<b>FEP tubing</b>	FEP Tubing 1/16" OD, 0.030" ID; Postnova Analytics, Germany	1520XL
<b>syringe connector part 1</b>	PEEK Union for 1/16" OD Tubing; Postnova Analytics, Germany	P-702
<b>syringe connector part 2</b>	F Luer to 1/4-28 FB, F; Postnova Analytics, Germany	P-658
<b>sheath /sample syringe</b>	BD Luer-Lok™ 1-mL syringe; BD Biosciences, NJ, USA	613-4971
<b>syringe for tubing cleaning</b>	BD Disposable Luer-Lok™ tip 5-mL syringe; Henke Sass Wolf, Germany	613-2043
<b>syringe needle</b>	Blunt Fill Needle 18G; BD Biosciences, NJ, USA	BDAM305180
<b>syringe filter unit</b>	Millex-GV, 0.22 um, PVDF; Merck Millipore, Germany	SLGV004SL

### 2.6.4. Sample preparation

A variety of cell sources can be used in RT-DC experiments. Within the framework of this thesis, experiments on non-adherent cells grown in suspension, adherent cell lines, as well as on blood were performed using variations of the general protocols outlined below. It is further possible to use samples such as solid tissues or cells cultured in 3D, providing that a dissociation is performed in advance as briefly described below.

#### *Non-adherent cells*

To collect semi-adherent cells or cells growing in suspension, the desired culture volume was centrifuged according to standard procedures (e.g., 5 min at 150 g). After pelleting the cells, supernatant was carefully removed to prevent dilution of MB. The cell pellet was resuspended thoroughly by pipetting up and down several times in 20–1000 µl of MB (20 µl is the minimal sample volume required

for filling the channel and running a measurement at one flow rate; 1000  $\mu\text{l}$  is the maximal sample volume that can be aspirated into the 1 ml syringe typically used). The cell suspensions used for measurements had concentrations of  $3\text{--}5 \times 10^6$  cells  $\text{ml}^{-1}$ .

#### *Adherent cells*

Adherent cells need to be detached from the substrate prior to generating single-cell suspension. To this end, a PBS washing step, followed by an incubation with a dissociation agent (e.g., trypsin, accutase, collagenase, or EDTA) was performed. After dissociation, cells were suspended in a buffer quenching the activity of the dissociation agent (e.g., serum-containing buffer in case of trypsin) or diluting it. The detached cells were then centrifuged and resuspended in MB as described above.

For adherent cells, the transition from cell-surface contact to a single cell state often leads to remodeling of actin cytoskeleton, and consequent change in mechanical properties over time<sup>341</sup>. This adaptation is differently pronounced depending on the cell type and should ideally be tested prior to performing experiments of interest by following the mechanical phenotype of cells over time after harvesting. When substantial change in stiffness is observed over initial time after detachment, it is advisable to preincubate cells in suspension before performing the measurements.

#### *Blood*

For whole-blood RT-DC measurements, 50  $\mu\text{l}$  of anti-coagulated blood was diluted in 950  $\mu\text{l}$  MB and mixed gently by manual rotation of the sample tube<sup>5</sup>. Depending on the cell population of interest, the ratio of blood to MB may be adjusted. For example, for effective measurements of the very abundant red blood cells, it is sufficient to dilute 5  $\mu\text{l}$  blood in 995  $\mu\text{l}$  MB. For the sorting experiments, the blood samples were depleted from RBCs to increase the relative content of lymphocytes and myeloid cells. To this end, anti-coagulated whole blood was drawn into 10 ml sodium-citrate tubes and mixed with the dextran solution (6% dextran in 0.9% sodium chloride solution) in a 4:1 ratio. RBCs were allowed to sediment for 30 min, forming a red pellet. RBC-depleted supernatant was then collected and centrifuged for 10 min at 120 g. Finally, the cell pellet was resuspended in MB (0.6% MC).

#### *3D cell cultures and solid tissue sections*

3D cell cultures, such as organoids or spheroids, as well as solid tissue sections can be prepared for RT-DC measurements using standard dissociation protocols based on enzymatic (e.g., incubation in a mixture of collagenase and DNase) or mechanical dissociation (using tools such as tissue grinder). Since such preparations may generate a lot of debris, it is recommended to perform washing steps with PBS. Additionally, the prepared cell suspension can be filtered through a strainer with a mesh size of 40  $\mu\text{m}$  (EASYstrainer™ #542 040; Greiner Bio-One, Germany; #431750, Corning Inc., NY, USA; FlowMi #H136800040, Belart, NJ, USA or alike). This procedure reduces amount of cell clusters and debris with big diameter that may clog the RT-DC channel entry during the measurements.



### 2.6.5. Setup preparation

The two following subsections contain general instructions and are written in the present tense.

Two 1 ml luer-lock syringes are filled with previously filtered MB (using a 0.22- $\mu\text{m}$  syringe filter unit) with an aid of blunt-end needles. The sheath fluid syringe is filled up to 1 ml, the sample syringe is filled to ca 0.2-0.5 ml to allow for later sample aspiration. FEP tubing (ca. 25 cm long, cleaned by flushing with 70% ethanol and distilled water and blow-dry with compressed air before using) is connected to the pre-filled syringes using dedicated luer-lock connectors (see **Table 2.2**), and the tubing is filled with MB by manually pushing the liquid through. The syringes are mounted onto the syringe pump and adjusted tightly. After connecting the sheath fluid tubing to the sheath inlet of the microfluidic chip (see **Figure 2.2**), the chip is filled with MB by setting the sheath flow to  $1 \mu\text{l s}^{-1}$ . After the sheath fluid has filled the whole chip (observe in ‘Prepare’ mode in the *ShapeIn2* software) and a drop has appeared in the sample inlet, reduce the sheath flow rate to  $0.01 \mu\text{l s}^{-1}$ . Next, cell suspension (prepared as described in **Section 2.6.4**) is aspirated into the sample syringe using a negative flow rate of  $-1 \mu\text{l s}^{-1}$ , the sample tubing is connected to the sample inlet (see **Figure 2.2**) and the sample flow is started at  $\sim 0.1 \mu\text{l s}^{-1}$ . When first cells appear in the field of view, the flowrate of both sheath and sample syringes is adjusted to the one used in the measurement (see **Table 2.3** and **Table 2.4** for measurement flow rates typically used for respective channel sizes). Finally, when the drop of liquids appears in the outlet, the tubing is fitted and its free end is placed into a waste container. Manufacturers and ordering number of consumables necessary for the described procedure are listed in **Table 2.2**.

**Table 2.3 | Flow rates used for the RT-DC measurements with 0.5% MC medium.** Table adapted from Urbanska, Rosendahl, Kräter *et al.*<sup>316</sup>.

channel width	total flow rate	sample flow rate	sheath flow rate
10 $\mu\text{m}$	$0.004 \mu\text{l s}^{-1}$	$0.001 \mu\text{l s}^{-1}$	$0.003 \mu\text{l s}^{-1}$
	$0.008 \mu\text{l s}^{-1}$	$0.002 \mu\text{l s}^{-1}$	$0.006 \mu\text{l s}^{-1}$
	$0.016 \mu\text{l s}^{-1}$	$0.004 \mu\text{l s}^{-1}$	$0.012 \mu\text{l s}^{-1}$
20 $\mu\text{m}$	$0.04 \mu\text{l s}^{-1}$	$0.01 \mu\text{l s}^{-1}$	$0.03 \mu\text{l s}^{-1}$
	$0.08 \mu\text{l s}^{-1}$	$0.02 \mu\text{l s}^{-1}$	$0.06 \mu\text{l s}^{-1}$
	$0.12 \mu\text{l s}^{-1}$	$0.03 \mu\text{l s}^{-1}$	$0.09 \mu\text{l s}^{-1}$
30 $\mu\text{m}$	$0.16 \mu\text{l s}^{-1}$	$0.04 \mu\text{l s}^{-1}$	$0.12 \mu\text{l s}^{-1}$
	$0.24 \mu\text{l s}^{-1}$	$0.06 \mu\text{l s}^{-1}$	$0.18 \mu\text{l s}^{-1}$
	$0.32 \mu\text{l s}^{-1}$	$0.08 \mu\text{l s}^{-1}$	$0.24 \mu\text{l s}^{-1}$
40 $\mu\text{m}$	$0.32 \mu\text{l s}^{-1}$	$0.08 \mu\text{l s}^{-1}$	$0.24 \mu\text{l s}^{-1}$
	$0.64 \mu\text{l s}^{-1}$	$0.16 \mu\text{l s}^{-1}$	$0.48 \mu\text{l s}^{-1}$
	$0.96 \mu\text{l s}^{-1}$	$0.24 \mu\text{l s}^{-1}$	$0.72 \mu\text{l s}^{-1}$

**Table 2.4 | Flow rates used for the RT-DC measurements with 0.6% MC medium.** Table adapted from Jacobi *et al.*<sup>80</sup>.

channel width	total flow rate	sample flow rate	sheath flow rate
20 $\mu\text{m}$	0.02 $\mu\text{l s}^{-1}$	0.005 $\mu\text{l s}^{-1}$	0.015 $\mu\text{l s}^{-1}$
	0.06 $\mu\text{l s}^{-1}$	0.015 $\mu\text{l s}^{-1}$	0.045 $\mu\text{l s}^{-1}$
	0.18 $\mu\text{l s}^{-1}$	0.045 $\mu\text{l s}^{-1}$	0.135 $\mu\text{l s}^{-1}$
30 $\mu\text{m}$	0.16 $\mu\text{l s}^{-1}$	0.04 $\mu\text{l s}^{-1}$	0.12 $\mu\text{l s}^{-1}$
	0.24 $\mu\text{l s}^{-1}$	0.06 $\mu\text{l s}^{-1}$	0.18 $\mu\text{l s}^{-1}$
	0.32 $\mu\text{l s}^{-1}$	0.08 $\mu\text{l s}^{-1}$	0.24 $\mu\text{l s}^{-1}$

### 2.6.6. Measurement procedure

Before the measurement, it is useful to set ‘hard’ gates for cell size and aspect ratio to avoid recording superfluous data. Gating out objects with very small size is recommended to prevent recording debris, and gating out particles of large size and large aspect ratio is helpful for discarding cell clusters. A standard setting for a 20  $\mu\text{m}$  channel is a minimum height and length of 3  $\mu\text{m}$ , a maximum height of 20  $\mu\text{m}$ , and a maximum length of 80  $\mu\text{m}$ . The maximum aspect ratio is typically set to 2. Additionally, ‘soft’ gates can be set, for which data outside of the gate is recorded but not included in the online event count or online plots.

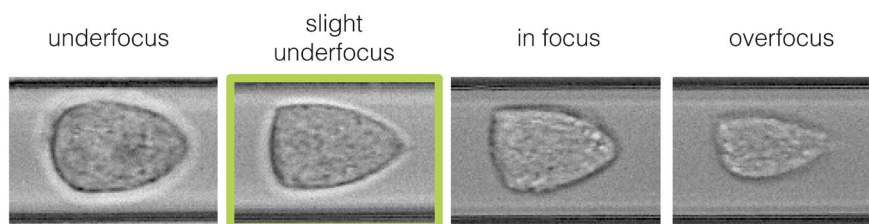


**Figure 2.14 | Setting focus for the RT-DC measurements.** For accurate image thresholding and contour fitting, the cells should be in slight underfocus (second image from the left, indicated with green box), i.e., the cell should appear darker than the background, with a bright halo around its edge. This figure is modified from Urbanska, Rosendahl, Kräter *et al.*<sup>316</sup>.

After the chip has been filled with sheath and sample fluids (**Section 2.6.5**), and the flow rate adjusted to the desired measurement value, it is necessary to wait  $>1$  min for the flow to equilibrate. In the meantime, the focus of the cells is adjusted to slight underfocus (**Figure 2.14**), what is necessary for accurate fitting of the cell contours. Next, a measurement is started and the desired number of events is acquired. Even though mostly only data from one flow rate is used for final analysis, it is recommended to record measurement at three flowrates as specified in **Table 2.3** and **Table 2.4**, as it provides an internal control if the measurement was setup correctly — the deformation of the cells should increase with the increasing flow rate. Finally, a recording in the 100  $\mu\text{m}$  wide reservoir region is performed (see **Figure 2.2**). In this region, cells do not experience significant loads and thus should be spherical. Any deviation from a spherical shape in this region indicates a pre-deformation that is not caused by the forces in the constriction channel.

## 2.7. Data analysis

The analysis of the RT-DC results is similar to the one performed for the flow cytometry data, with the added possibility of inspecting individual events by looking at their images. Routinely performed data analysis steps include gating, calculation of parameters of interest not computed online (e.g., Young’s modulus values), and application of statistical methods such as linear mixed-effects models for comparison of results obtained for different samples. A dedicated open-source software called *Shape-Out* (*Shape-Out2*; available at <https://github.com/ZELLMECHANIK-DRESDEN>) is recommended for analyzing the RT-DC data as it supports loading of the native ‘.rtdc’ files and reads settings recorded with during the measurements. Moreover, *Shape-Out* provides tools for filtering, parameter calculations, and plotting. The raw or processed data can be exported from *Shape-Out* in ‘.csv’ or ‘.fcs’ formats, which can be used for analysis in other programs such as Excel (Microsoft, WA, USA), MatLab (MathWorks, MA, USA), Origin (OriginLab, MA, USA) or FlowJo (FlowJo LCC, OR, USA).

### 2.7.1. Data filtering

Cell parameters computed in real-time, such as area, deformation, aspect ratio and area ratio (see **Table 2.1** for full list), as well as many more parameters computed from the images and fluorescent trace offline (**Table 2.5**) can be used for filtering during data post-processing steps. The filters typically set before the measurement are discussed in **Section 2.6.6**. Below the filtering strategies using three parameters — area, area ratio, and aspect ratio — are discussed. Additional gating can be applied to select cell types of interest in heterogeneous samples.

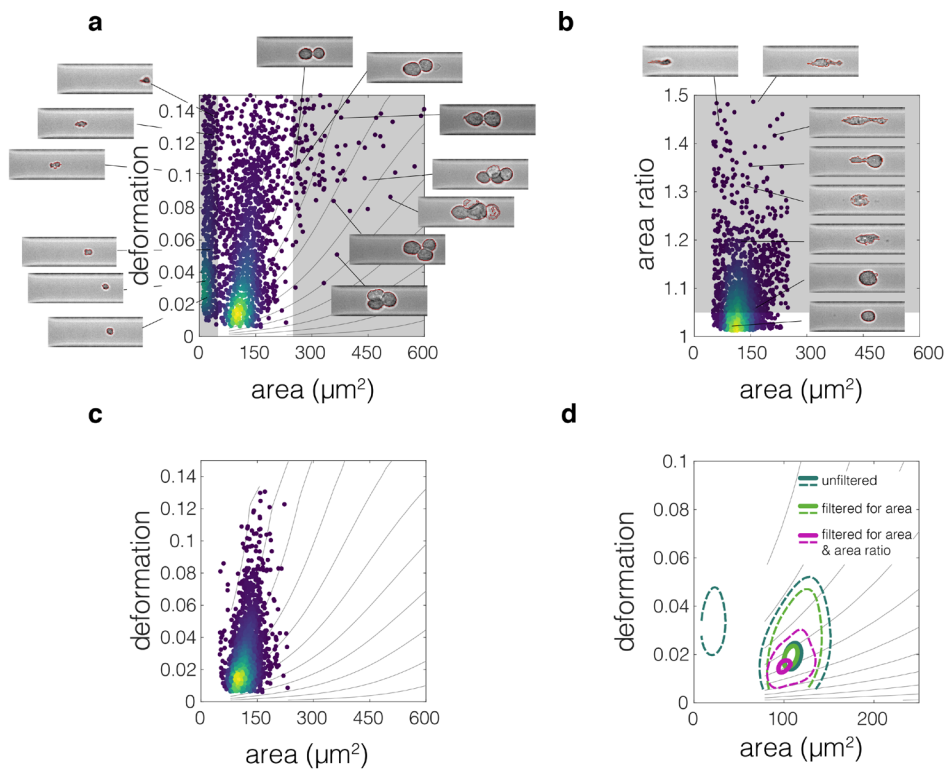
**Table 2.5 | Additional features available during post-processing in *Shape-Out*.**

image-derived features	
<b>absolute tilt of raw contour</b>	angle between the object’s major axis and the axis parallel to the flow direction
<b>principal inertia ratio of raw contour</b>	maximum inertia ratio that can be computed (rotation-invariant)
<b>volume</b>	object’s volume calculated by rotation of its contour around the rotation axis parallel to the flow direction <sup>361</sup> ( $\mu\text{m}^3$ )
fluorescence trace-derived features*	
<b>FL area of the peak</b>	area under the peak(a.u.)
<b>FL position of peak</b>	position of the peak maximum along the x axis ( $\mu\text{s}$ ) <sup>§</sup>
<b>FL width</b>	full width at half maximum of the peak ( $\mu\text{s}$ ) <sup>§</sup>
<b>FL number of peaks</b>	number of detected signal maxima in a given frame
<b>FL distance between two first peaks</b>	The distance between detected peak maxima ( $\mu\text{s}$ ) <sup>§</sup>

\*available for all three spectral channels (FL1, FL2 and FL3)

§derived from the temporal signature of the signal, thus estimated in  $\mu\text{s}$

*Area.* Cell cross-section area, which serves as a measure of cell size, can be used to excluded events that are smaller (e.g. cell debris) or bigger (e.g. cell doublets or aggregates) than the cells of interests. The appropriate values of the filters can be determined by inspecting area-deformation scatter plots. It is typically easy to distinguish by eye the population of small debris from the population of cells, and from the population of bigger outliers (**Figure 2.15a**). Additionally, images of individual events can be inspected in *Shape-Out* by selecting a data point of interest on the deformation vs area scatter plot, what further aids in the selection of filter boundaries (**Figure 2.15a**).



**Figure 2.15 | An example of RT-DC data filtering using area and area ratio.** **a**, Area filter. Area–deformation scatter plot of unfiltered data from an exemplary measurement of ECC4 carcinoma cells ( $n = 5,095$ ). Filters for area are shaded in gray and exemplary pictures of the events being filtered out are shown alongside the plot. **b**, Area ratio filter. Area ratio–deformation scatter plot of data filtered for size ( $n = 3,500$ ) with the filtered area ratio values shaded in gray. Exemplary pictures of cells with different area ratio values are shown in the plot. Bottom picture represents an event with acceptable area ratio value (1.02). **c**, Area–deformation scatter plot of data filtered for both area and area ratio ( $n = 2,433$ ). **d**, Contour plots of unfiltered data, data filtered for area, and data filtered for both area and area ratio. Solid lines indicated 95% density contour, and dashed lines indicate 50% density contour.

*Area ratio.* Cells with protrusions and cells whose contours are not tracked correctly often have overestimated deformation values, what may lead to wrong conclusions about their mechanical properties. To avoid this, events should be filtered using the area ratio parameter (**Figure 2.15b–c**). Area ratio is defined as the ratio between area of the convex hull of the detected contour and the area of raw contour (**Figure 2.16a,b**). The more protrusions and concave sections are present in the contour, the higher the area ratio value (**Figure 2.16c**). Strongly deformed cells with smooth surface will have low area ratio, thus, filtering for this parameter does not bias the mechanical measurement. The area ratio takes values  $\geq 1$ , and is usually set for values below 1.05–1.10, depending on the sample.

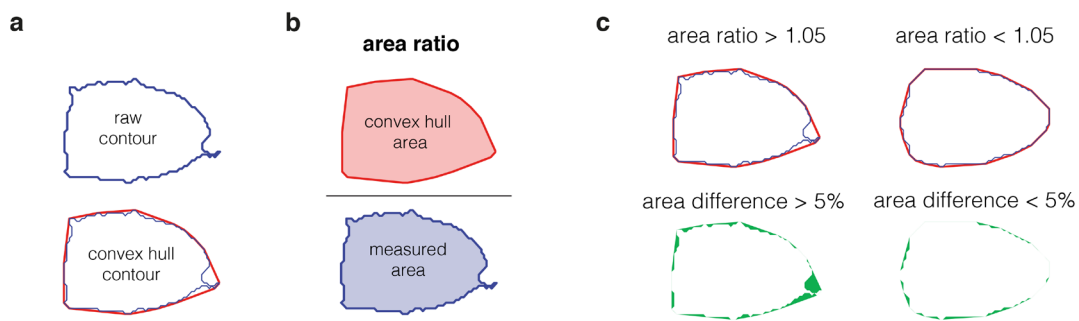


**Figure 2.16 | Graphical representation of the area ratio parameter.** **a**, An exemplary raw cell contour as detected by the thresholding algorithm (top) and the same contour encircled by its convex hull (bottom). **b**, Graphical representation of the area ratio parameter, which is defined as the ratio between the convex hull and measured area. **c**, Example of contours with area ratio above 1.05 (left), typically excluded from analysis, and with area ratio below 1.05 (right). The area shaded in green in the bottom row corresponds to the area difference between convex hull and measured area. This figure is modified from Urbanska, Rosendahl, Kräter *et al.*<sup>316</sup>.

*Aspect ratio.* Aspect ratio is defined as the ratio between the length and the height of the cell contour's bounding box (size  $x$  to size  $y$ ). It is useful for excluding elongated objects, and particularly well suited for filtering out red blood cells (RBCs) in analysis of whole blood samples. RBCs are present in the whole blood  $\sim 1,000$  times excess with respect to white blood cells (WBCs), thus, when analyzing WBCs is of interest, it is recommended to gate out RBCs during the measurement to avoid recording of excessive amount of data. Due to their shape and their softness, RBCs have much larger aspect ratio values compared to other cells, and setting the aspect ratio to values between 0.5 and 2 effectively excludes RBCs from the measurement<sup>5</sup>. Aspect ratio can also assist in filtering out cell doublets and cell aggregates, those however, are also discarded using area and area ratio filters as described above.

### 2.7.2. Statistical analysis

Large cell numbers evaluated in RT-DC measurements lead to low standard errors of the analyzed parameters and, as a consequence, overestimated significance in standard statistical tests such as Student's  $t$ -test or Mann-Whitney  $U$  test<sup>361</sup>. Thus, rather than comparing the cell populations measured in the individual experiments or pooled from many experiments, it is more appropriate to test the reproducibility of the observed differences among several replicates. A statistical approach that enables replicate-based analysis that has proven to be well suited for the RT-DC data analysis is the implementation of linear mixed-effects models with random intercept and random slope. Such models set the random variation caused by experimental noise and day-to-day variation into relation with the difference that might be induced by the treatment/sample type, and estimates a meaningful  $p$ -value. The linear mixed-effects model analysis can be used in *Shape-Out*, and is based on the lme4 package<sup>362</sup> for R (R Core Team; <http://www.r-project.org/>). Its implementation for RT-DC data analysis is discussed in detail elsewhere<sup>361</sup>.

Chapter 3 is based on and contains materials adapted from the following peer-reviewed publication:

M. Urbanska\*, H.E. Muñoz\*, J.S. Bagnall, O. Otto, S.R. Manalis, D. Di Carlo, and J. Guck. (2020). **A comparison of microfluidic methods for high-throughput cell deformability measurements**, *Nature Methods*, 17(6), 587–593.

DOI: 10.1038/s41592-020-0818-8

Own contributions: investigation, project administration, formal analysis, visualization, writing – original draft preparation, writing – review and editing

\*equal contributions

## — Chapter 3 —

### A comparison of three deformability cytometry classes operating at different timescales

Deformability cytometry encompasses a class of microfluidics-based approaches for mechanical characterization of single cells at throughputs orders of magnitude higher than classical methods (see **Table 1.1**). Such microfluidic approaches allow for robust assessment of the ability of cells to change shape under applied forces — their deformability — and enable comprehensive characterization of homogenous and heterogenous cell populations in short time. The high throughput of the deformability cytometry methods, together with the ease of the instrument handling and the high automatization potential, render these approaches suitable for applications not only in basic research but also in clinical settings<sup>294</sup>.

The three major deformability cytometry classes, introduced in **Section 1.5.5**, include constriction-based deformability cytometry (cDC), shear flow deformability cytometry (sDC) and extensional flow deformability cytometry (xDC). These classes differ in type and magnitude of applied stress, the rate at which cells are deformed, and the way deformability is parametrized. Thus, it is not straightforward to draw conclusions about the results obtained with different methods. The variability in types of analyzed samples and preparation conditions in the published datasets additionally limit the possibility to directly compare the performance of the methods using previous results. Despite many demonstrated applications of the respective methods and substantial work on identifying cellular structures that contribute to deformability changes within the individual methods, a direct comparison of their performance is still missing.

To address this gap, we performed a highly-standardized cross-laboratory study comparing representatives of the three deformability cytometry classes: *(i)* an SMR-based cDC variant<sup>9</sup>, *(ii)* RT-DC<sup>21</sup> as an example of sDC, and *(iii)* DC<sup>1</sup> as an example of xDC. With these methods, we evaluated deformability of human promyelocytic leukemia (HL60) cells — from the same source and passage number — in two standardized assays, subjecting the cells to osmotic changes and to latrunculin B (LatB)-induced actin disassembly. I have performed the RT-DC measurements and coordinated the project. The cDC measurements were performed by Josephine Shaw Bagnall in the group of Prof. Scott R. Manalis at Massachusetts Institute of Technology, Cambridge, MA, USA, and the xDC measurements were performed by Hector E. Muñoz in the group of Prof. Dino Di Carlo at University of California, Los Angeles, CA, USA. The comparative analysis was performed by myself in collaboration with Hector E. Muñoz.

## 3.1. Results

### 3.1.1. Representatives of the three deformability cytometry classes

As a cDC representative, we used an SMR-based variant utilizing a silicon microcantilever with an embedded microfluidic channel<sup>9</sup>. The microchannel features a constriction smaller than the cell size (6  $\mu\text{m}$  wide, 15  $\mu\text{m}$  high, and 50  $\mu\text{m}$  long; **Figure 3.1a**) close to the cantilever tip. The cell suspension is driven through the channel by a constant pressure of 1 kPa, and the cells are in contact with the channel wall when passing the constriction. The time taken by the cell to enter and pass through the constriction is assessed using changes in the resonance frequency of the SMR (**Figure 3.1a**). For cDC, cell deformability  $D$  is defined as the inverse of cell passage time (**Figure 3.1a**). The method operates with a throughput of a few cells per second and a strain rate of 0.04 kHz.

In sDC and xDC — here represented by RT-DC<sup>21</sup> and DC<sup>1</sup>, respectively — cells are deformed in a contactless manner by hydrodynamic forces, and the assessment of cell deformability is based on high-speed imaging. Yet, these two methods differ in the type of channel geometries used, and more importantly, in the probing timescales and Reynolds numbers characterizing their operation (see **Table 3.1**). The dimensionless Reynolds number ( $\text{Re} = \frac{\rho v L}{\eta}$ , where  $\rho$  is the fluid density,  $v$  the mean flow velocity,  $L$  the characteristic length of the flow system, and  $\eta$  the dynamic viscosity of the fluid) expresses the relative importance of inertial and viscous forces at given flow conditions. For the experimental parameters used in this study,  $\text{Re}$  is equal to 0.4 for sDC and 150 for xDC. The very low  $\text{Re}$  in case of sDC ( $\ll 1$ ) indicates a dominance of viscous forces, characteristic for the type of laminar flow called Stokes flow. xDC, in turn, operates in an inertial flow regime, where inertial forces cannot be neglected and can lead to useful effects such as cell focusing<sup>299</sup>.

The operation of sDC is described in great detail in **Chapter 2**. In brief, cells are driven through a funnel-like constriction into a narrow microfluidic channel where they are deformed by shear forces and pressure gradients into a bullet-like shape<sup>21,298</sup> (**Figure 3.1b**). The steady-state cell deformation evaluated at the end of the 300- $\mu\text{m}$  long channel, defined as  $1 - \text{circularity}$  (**Figure 3.1b**), constitutes the measure of cell deformability. It takes a few milliseconds for each cell to translocate through the deformation channel, which gives an estimate of the strain rate of 0.2 kHz. Typically, over 100 cells per second can be analyzed. For HL60 cells, chips with a 20  $\mu\text{m} \times 20 \mu\text{m}$  channel were used; which, together with hydrodynamic focusing implemented upstream of the deformation channel, assures that cells are not in contact with the channel walls. The stress acting on the cells during the deformation in the 20- $\mu\text{m}$  channel and 0.04  $\mu\text{l s}^{-1}$  flow rate reaches values close to 1 kPa (see **Supplementary Figure A.3**).

In xDC, cells are deformed into ellipsoids by an extensional flow at a cross-junction of a microfluidic chip (**Figure 3.1c**). The cells arrive at the cross-junction with a speed of several meters per second, from which they are fully decelerated and deformed via inertial forces within a few microseconds.



In that way, over 1,000 cells per second can be analyzed. Cell size is determined from images recorded before the cell extension, and deformability,  $D$ , is defined as the maximal aspect ratio observed in the extensional flow region. The channels forming the junction have a rectangular cross-section of  $60 \mu\text{m} \times 30 \mu\text{m}$ . Before entry to the analysis region, cells are aligned via inertial focusing in serpentine channels, and do not interact with the channel walls. Compared to sDC and cDC, xDC applies several times higher stress, and reaches a strain rate of 20 kHz (see **Table 3.1** and **Appendix A**).

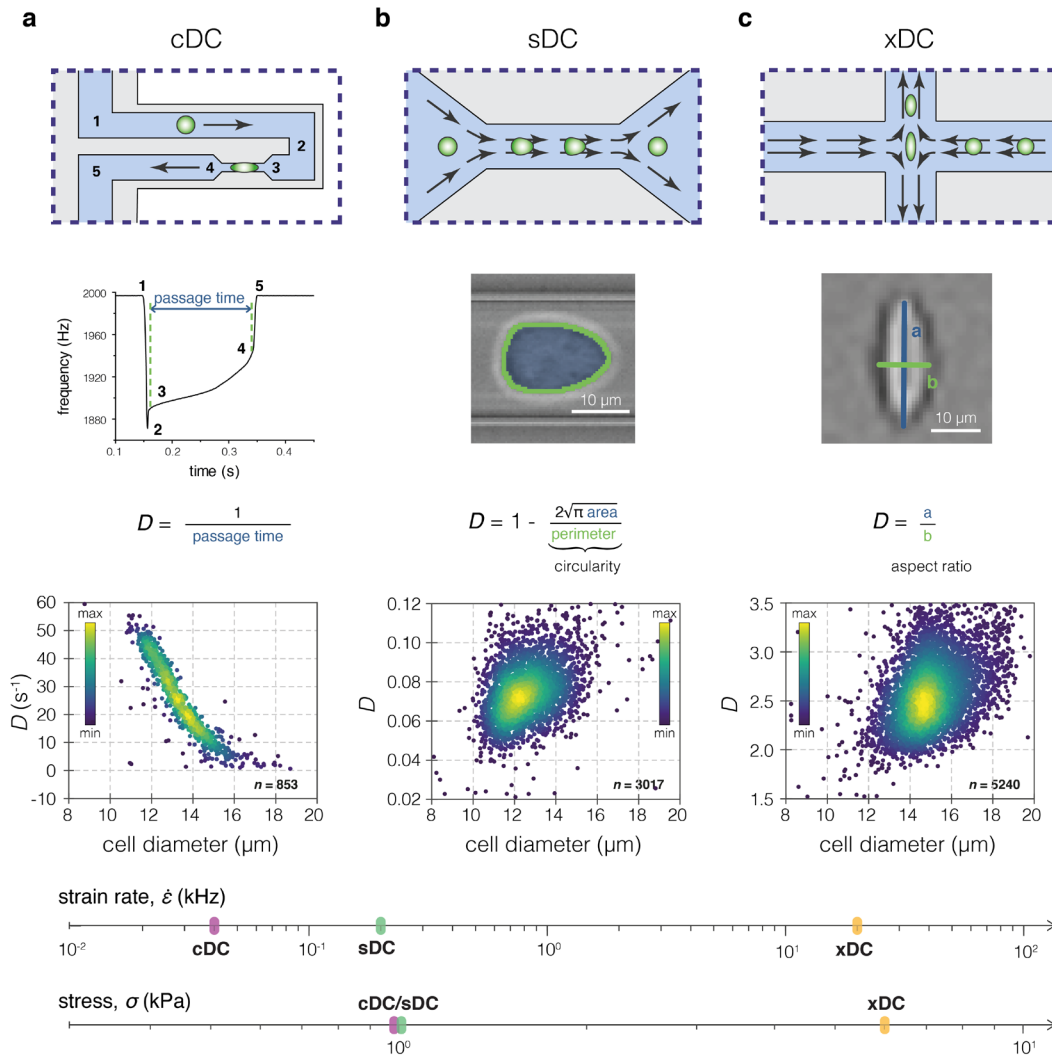


**Figure 3.1 | Representatives of the three deformability cytometry classes used in this study.** a–c, Operation principle of cDC (a), sDC (b) and xDC (c). Each panel includes a schematic of chip geometry (upper row), the definition of deformability  $D$  (middle row), and a typical scatter plot of  $D$  versus cell diameter (lower row). Color maps in scatter plots correspond to event density. The numbers 1–5 in the plot of frequency vs. time correspond to the cell positions in the cDC microchannel indicated in the scheme above. The strain rates and stresses applied to the cells in the respective methods are indicated on the axes at the bottom. This figure is reprinted from Urbanska, Muñoz *et al.*<sup>363</sup>.

The cell size and deformability data obtained during the measurements are typically displayed on scatter plots (**Figure 3.1**). Hallmark parameters of the three deformability cytometry classes are summarized in **Table 3.1**. The estimation of applied stresses and induced strains for the respective methods is outlined in **Appendix A**.

**Table 3.1 | Characteristic operation parameters of cDC, sDC, and xDC.** This table is adapted from Urbanska, Muñoz *et al.*<sup>363</sup>

	cDC	sDC	xDC
deformability measure	passage time <sup>-1</sup>	1-circularity	aspect ratio
detection	frequency shift	imaging	imaging
analysis	offline	real-time	offline
throughput (cells s <sup>-1</sup> )	1	100	1,000
timescale of cell deformation, $\tau$ (ms)	10	1	0.01
cell contact with channel walls	yes	no	no
channel width $\times$ height ( $\mu\text{m}$ )	$6 \times 15$	$20 \times 20$	$60 \times 30$
mean flow velocity, $v$ (m s <sup>-1</sup> )	0.01	0.1	3.5
viscosity of measuring buffer, $\eta$ (mPa s)	1	5.7	1
Re in the measuring channel	0.1	0.4	150
mean absolute strain, $\bar{\epsilon}$	37%	17%	24%
strain rate, $\dot{\epsilon}$ (kHz)	0.04	0.2	20
applied stress, $\sigma$ (kPa)	$\sim 1$	$\sim 1$	$\sim 6$

### 3.1.2. Osmotic shock-induced deformability changes are detectable in all three methods

To compare cDC, sDC, and xDC side-by-side, we first performed a series of hyper- and hypo-osmotic shock experiments on HL60 cells. In hyperosmotic shock, in which the buffer osmolarity exceeds physiological one, water is driven out of cells to compensate for the difference in osmolyte concentrations between the cell interior and the exterior<sup>364</sup> (**Figure 3.2**). This leads to decreased cell size and increased molecular crowding inside the cell, what has been linked to elevated cell stiffness<sup>228,229,231,232</sup>. On other hand, in hypo-osmotic conditions water is driven into the cell to compensate for the higher osmolyte concentration in the cell interior<sup>364</sup>. This causes cell swelling and dilution of intracellular material (**Figure 3.2**). Hypo-osmotic swelling has been shown to cause a decrease in cell stiffness<sup>228,229,231</sup>.

To induce an osmotic shock response, the buffer's osmolarity was altered with respect to the physiological osmolarity of HL60 cells (300 mOsm). Hyperosmotic solutions with osmolarities ranging from 400 to 700 mOsm were prepared by adding mannitol to the measurement buffer. Hypo-osmotic solutions with osmolarities of 250 and 200 mOsm were prepared by diluting osmolytes in the respective measurement buffer in water. To minimize biological batch-to-batch variability in cell properties, we utilized a fast-growing HL60 cell subline (HL60/S4) shared between the three participating laboratories at the same passage number and used within 10 passages. Cells were exposed to altered osmolarity 10 minutes prior to the measurements. Consistently across the methods, cell size and deformability

were decreased in the hypertonic conditions, while increase of both parameters was observed in moderate hypo-osmotic challenge (**Figure 3.3, Supplementary Figure B.1 and B.2**).

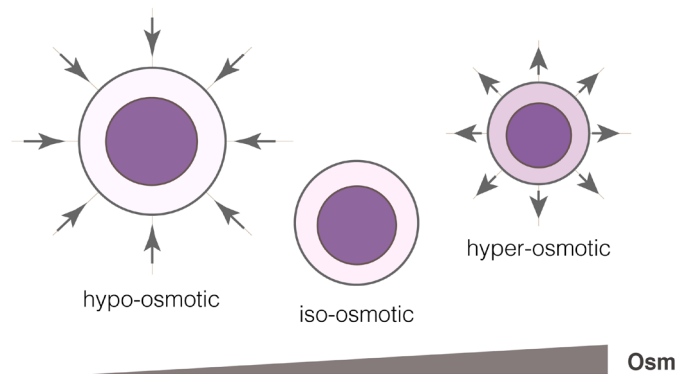


**Figure 3.2 | Schematic representation of the osmotic shock assay.** Decreased extracellular osmolarity (hypo-osmotic condition, left-hand side) with respect to the iso-osmotic condition (middle) causes cell swelling and dilution of intracellular material. Elevated extracellular osmolarity (hypertonic condition, right-hand side) causes cell shrinkage and an increase in macromolecular crowding inside the cell. Arrows indicate the direction of water flow. This figure is modified from Urbanska, Muñoz *et al.*<sup>363</sup>.

The response of cells to an osmotic shock is a dynamic process and, after initial cell swelling or shrinking, cells are known to undergo a regulatory volume response<sup>364</sup>. Using sDC, we observed that, while in the hypertonic conditions deformability response saturated quickly, in the hypo-osmotic conditions the response showed non-monotonic evolution over time (**Supplementary Figure B.3**), with peak appearing at different times after exposure for different conditions. Thus, to avoid uncertainty whether or not at the fixed measurement time we captured the magnitude of the response accurately, we excluded the hypo-osmotic conditions from data fitting.

Since deformability is parametrized differently in the respective methods and takes values in different ranges, we introduced a normalized value called relative deformability  $RD$  calculated with respect to the control condition (see **Materials and methods** and **Supplementary Figure B.2**).

For each method, the relationships between  $RD$  and the normalized extracellular osmolarity in the hyperosmotic shock were fit with an exponential curve (**Figure 3.3d, Supplementary Table B.1**) of a following formula:

$$RD = e^{\lambda(1 - Osm/Osm_{iso})}, \quad 3.1$$

where  $\lambda$  is the decay constant that describes the sensitivity of  $RD$  to the change in the osmolarity,  $Osm$ , normalized to the isosmotic condition,  $Osm_{iso}$ . We decided to perform the exponential fit because, compared to linear and power law fits, it provided the best description of the obtained results across methods (**Supplementary Figure B.4**).

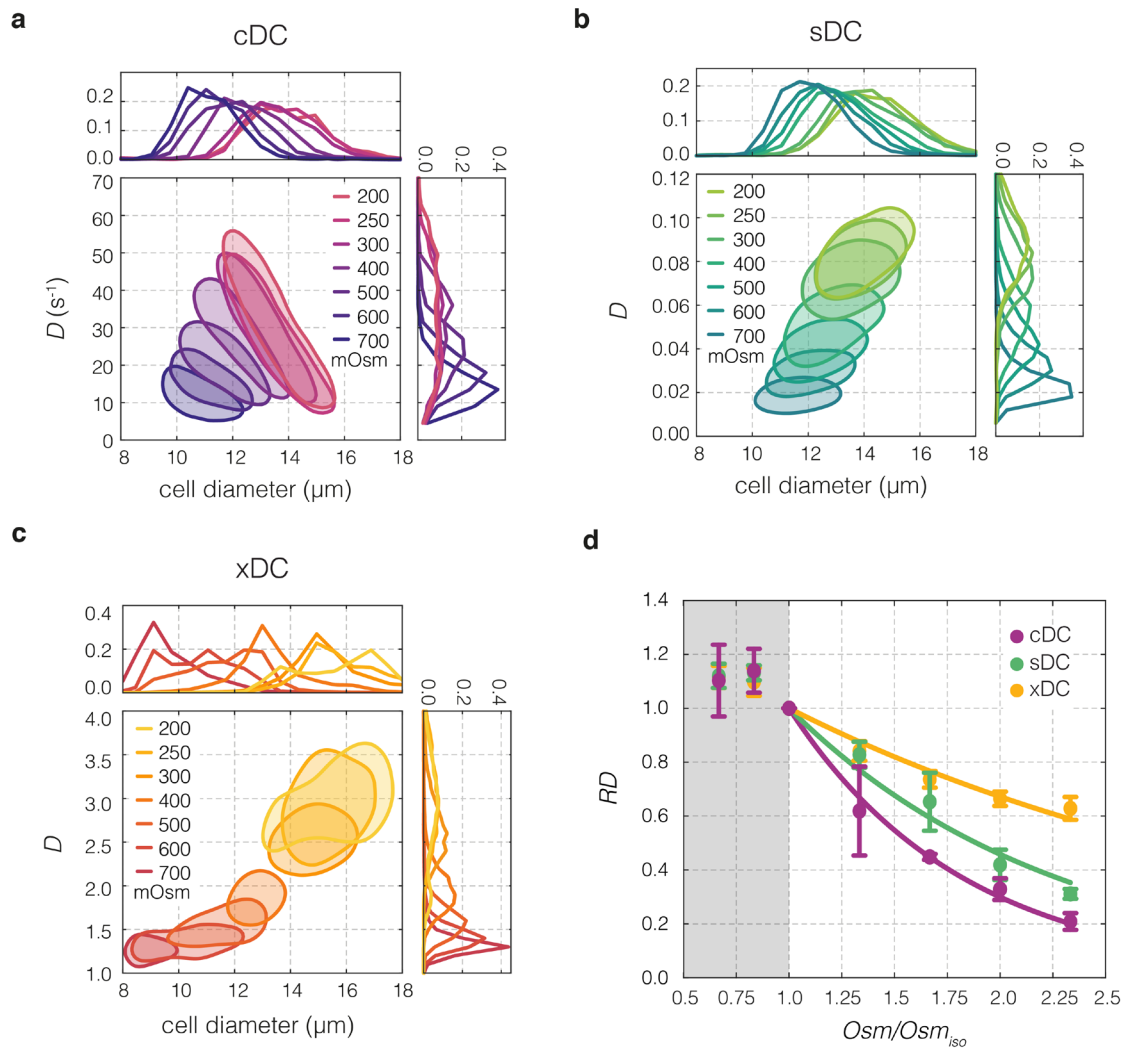


**Figure 3.3 | Effects of osmolarity changes on cell deformability.** **a–c**, Plots of deformability  $D$  vs cell diameter for HL60 cells exposed to different osmolarity in an exemplary cDC (**a**), sDC (**b**) and xDC (**c**) experiment. Contours delineate 50% density and are accompanied by deformability and cell diameter histograms. The osmolarity values are color-coded as indicated in the respective legends. **d**, Relative deformability,  $RD$ , as a function of normalized osmolarity,  $Osm/Osm_{iso}$ , for cDC (purple), sDC (green) and xDC (yellow) measurements. Data points represent means of medians of multiple experimental replicates ( $n = 3, 4$ , and  $4$ , for cDC, sDC, and xDC, respectively), and error bars represent standard deviation. Lines represent exponential fits to data. Hypoosmotic shock data excluded from the fitting procedure is shaded in gray. This figure is modified from Urbanska, Muñoz *et al.*<sup>363</sup>.

We observed the same trend of decreasing  $RD$  with increasing osmolarity in all three methods, however, the decay constants  $\lambda$ , describing the sensitivity of  $RD$  to the osmolarity changes, differed between the methods. The pairwise  $F$ -tests on the pairs of curves showed that there is a significant difference between the cDC and xDC curves ( $F_{2,33} = 167.893$ ,  $p < 0.001$ ), cDC and sDC curves ( $F_{2,33} = 26.856$ ,  $p < 0.001$ ), as well as between sDC and xDC curves ( $F_{3,33} = 17.839$ ,  $p < 0.001$ ). The sensitivity of the exponential decay was the highest for cDC, reaching values 1.5 and 3 times higher than the ones obtained for sDC and xDC, respectively (**Supplementary Table B.1**).

### 3.1.3. Ability to detect actin disassembly is method-dependent

The comparability of the deformability measurements in cDC, sDC, and xDC, was further tested in a LatB-induced actin disassembly assay. As described in **Section 1.3.1**, actin cytoskeleton is a major contributor to the mechanical properties of cells, and its destabilisation with chemical agents causes a decrease in cell stiffness<sup>17,178–180</sup>. In suspended cells such as HL60, actin filaments are organised predominantly into an actin cortex—a thin, crosslinked filament network underlying the inner leaflet of the plasma membrane<sup>32</sup>. The marine toxin LatB binds free actin monomers thereby hindering actin polymerization and destabilizing actin filaments in a dose-dependent manner<sup>365,366</sup> (**Figure 3.4**).

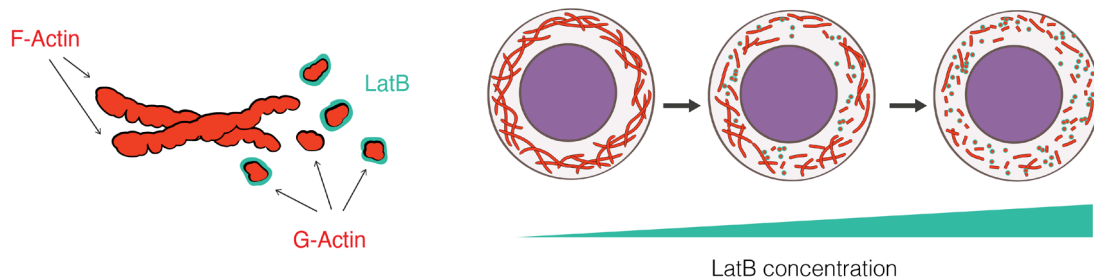


**Figure 3.4 | Schematic representation of the actin disassembly assay.** LatB binds to globular actin monomers (G-actin) and prevents their polymerization into filamentous actin (F-actin), what leads to dose-dependent disassembly of actin cytoskeleton. This figure is modified from Urbanska, Muñoz *et al.*<sup>363</sup>.

HL60 cells were treated with a range of LatB concentrations (1–100 ng ml<sup>-1</sup>, corresponding to 2.53–253 nM) and DMSO as a vehicle control, and measured using the three respective methods (**Figure 3.5**). Analysis of variance showed that the increasing concentration of LatB had a significant effect on the deformability of the cells as measured with cDC ( $F_{6,16} = 17.2, p = 3.6 \times 10^{-6}$ ) and sDC ( $F_{6,28} = 34.3, p = 1.2 \times 10^{-11}$ ), however, the deformability measured with xDC did not show significant changes upon LatB treatment ( $F_{6,21} = 0.38, p = 0.89$ ). Though, in xDC a slight decrease in deformability was observable for the highest LatB dose (**Figure 3.5c–d, Supplementary Figure B.5**). Of note, treatment with LatB concentrations beyond 100 ng ml<sup>-1</sup> resulted in lowering of measured deformabilities in cDC and xDC (**Supplementary Figure B.6**). Such high LatB concentrations are related to drug-induced substrate detachment observed for adherent cells<sup>1,365</sup>, and thus may be connected to more extensive changes within the actin structure leading to changes in cell integrity. The measured cell size remained constant for low LatB concentrations, and decreased slightly for LatB concentrations of 50 ng ml<sup>-1</sup> (in cDC) and 100 ng ml<sup>-1</sup> (in all three methods) (**Supplementary Figure B.7**).

To parametrize the sigmoidal dose-response of  $RD$  to LatB treatment, we have used a four-parameter log-logistic regression model<sup>367</sup> of the following formula:

$$RD([\text{LatB}], (b, c, d, e)) = c + \frac{d-c}{1+\exp(b(\log([\text{LatB}])-\log(e)))} \quad 3.2$$

where [LatB] is the concentration of the drug, and  $b$ ,  $c$ ,  $d$ ,  $e$  are the fit parameters, corresponding to:  $b$  – the steepness of the dose-response curve,  $c$ ,  $d$  – the lower and upper limits of the  $RD$  response, and  $e$  – the effective  $EC_{50}$  dose at which half-maximum response is obtained. This model yielded a significant fit for the cDC and sDC data, which was not the case for the xDC results (Figure 3.5d, Supplementary Table B.2).

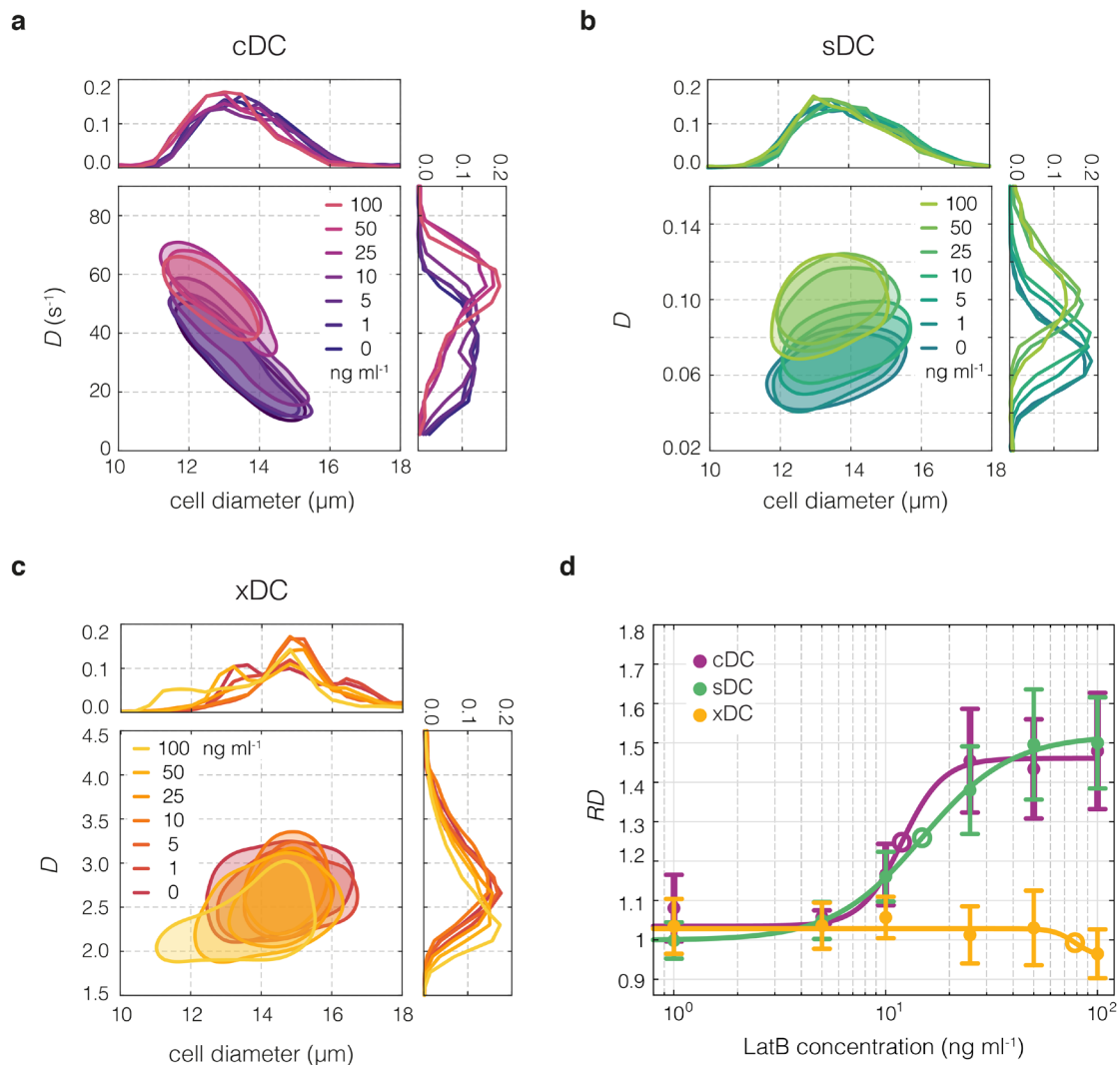


**Figure 3.5 | Effects of LatB-induced disassembly of actin cytoskeleton on cell deformability.** a–c, Plots of deformability  $D$  vs cell diameter for HL60 cells treated with increasing concentrations of LatB in an exemplary cDC (a), sDC (b) and xDC (c) experiment. Contours delineate 50% density and are accompanied by deformability and cell diameter histograms. The LatB concentrations are color-coded as indicated in the respective legends. d, Relative deformability,  $RD$ , as a function of LatB concentration for cDC (purple), sDC (green) and xDC (yellow) measurements. Data points represent means of medians of multiple experimental replicates ( $n = 3, 5$ , and  $4$ , for cDC, sDC, and xDC, respectively), and error bars represent standard deviation. Lines represent four-parameter log-logistic fits, open circles indicate  $EC_{50}$  values. This figure is modified from Urbanska, Muñoz *et al.*<sup>363</sup>.

The  $EC_{50}$  reached similar values for cDC and sDC:  $11.9 \text{ ng ml}^{-1}$  (95% CI [6.8, 17.0]) and  $15.2 \text{ ng ml}^{-1}$  (95% CI [9.9, 20.4]), respectively. cDC and sDC also showed comparable magnitude of the maximum  $RD$  response, as illustrated by the upper limit of the sigmoidal curve yielding 1.5 (95% CI [1.4, 1.5]) for

cDC and 1.6 (95% CI [1.5, 1.7]) for sDC. The fits obtained for sDC and cDC did not show significant difference in a pairwise  $F$ -test ( $F_{4,50} = 0.6$ ,  $p = 0.69$ ), whereas cDC and xDC curves ( $F_{4,43} = 44.3$ ,  $p = 1.0 \times 10^{-14}$ ), as well as sDC and xDC curves ( $F_{4,55} = 63.7$ ,  $p = 5.3 \times 10^{-20}$ ) were significantly different.

### 3.1.4. Strain rate increase decreases the range of deformability response to actin disassembly in sDC

Each of the three deformability cytometry classes employed in this study has an optimal flow rate range at which it operates, thus, achieving corresponding strain rates or stress rate in the respective methods is not feasible. Notwithstanding, we decided to test whether increasing the flow rate in sDC measurements (within the range conventionally used in this method) would influence the magnitude of the measured deformability response to LatB treatment. We assessed the LatB dose-response curves, for both deformability and relative deformability, at three different flow rates (fr1 = 2.4  $\mu\text{l min}^{-1}$ , fr2 = 4.8  $\mu\text{l min}^{-1}$ , and fr3 = 7.2  $\mu\text{l min}^{-1}$ ), and observed that the responses decreased in range with increasing flow rate (**Figure 3.6**). To confirm this observation quantitatively we calculated the response range ( $\Delta D$ ,  $\Delta RD$ ) as a difference between the upper ( $e$ ) and lower limits ( $d$ ) of the log-logistic regression fit (**Equation 3.2**). The obtained response ranges are summarized in **Table 3.2**. We further compared the relative deformability response curves using a pairwise  $F$ -test and could confirm that the curves for fr1 and fr2 ( $F_{4,62} = 3.1$ ,  $p = 0.02$ ), fr2 and fr3 ( $F_{4,62} = 3.6$ ,  $p = 0.01$ ), as well as fr1 and fr3 ( $F_{4,62} = 15.8$ ,  $p = 5.6 \times 10^{-9}$ ) significantly differ from one another.

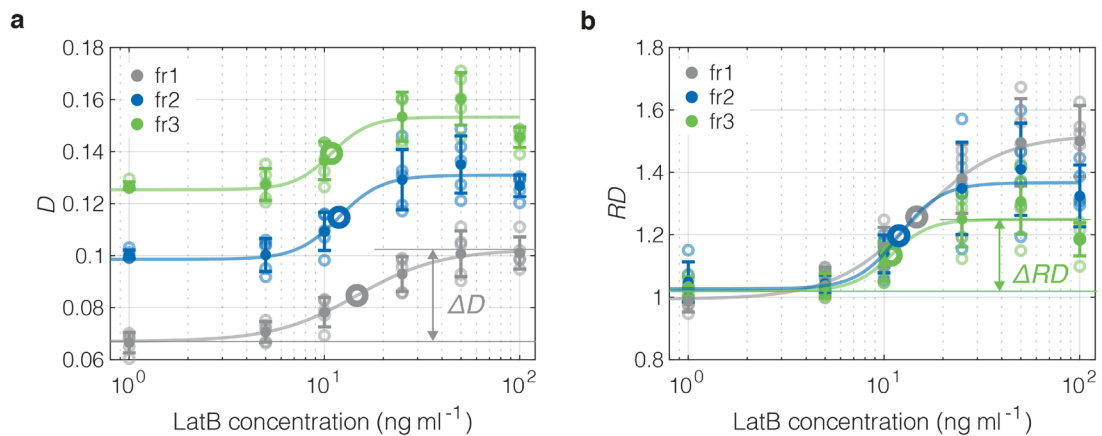


**Figure 3.6 | Increasing the flow rate in sDC impacts the magnitude of deformability response to LatB treatment.** **a–b**, Deformability,  $D$  (**a**), and relative deformability,  $RD$  (**b**), as a function of LatB concentration at three different flowrates (fr1 = 2.4  $\mu\text{l min}^{-1}$ , fr2 = 4.8  $\mu\text{l min}^{-1}$ , and fr3 = 7.2  $\mu\text{l min}^{-1}$ ). The different flowrates are color-coded as indicated in the figure legend (fr1 – gray, fr2 – blue, fr3 – green). Bold open circles indicate EC50, faint open circles indicate medians of individual measurements, lines connect means of measurement replicates for each flowrate ( $n = 5$ ), error bars correspond to standard deviation of the mean distributions. Bin-selected data was used. This figure is modified from Urbanska, Muñoz *et al.*<sup>363</sup>.

**Table 3.2 | Ranges of response to LatB treatment at different flowrates in sDC.** The response range of deformability ( $\Delta D$ ) and relative deformability ( $\Delta RD$ ) was determined as the difference between the upper and lower limit. The lower and upper limits of the four-parameter log-logistic model fit are reported together with their 95% confidence intervals.

	deformability			relative deformability		
	lower limit	upper limit	$\Delta D$	lower limit	upper limit	$\Delta RD$
<b>fr1</b>	0.067 [0.063, 0.071]	0.1024 [0.097, 1.108]	0.035	0.99 [0.94, 1.05]	1.52 [1.44, 1.60]	0.53
<b>fr2</b>	0.099 [0.094, 0.103]	0.131 [0.126, 0.136]	0.032	1.03 [0.97, 1.08]	1.37 [1.30, 1.43]	0.34
<b>fr3</b>	0.124 [0.121, 0.130]	0.153 [0.149, 0.158]	0.029	1.02 [0.98, 1.06]	1.25 [1.21, 1.29]	0.22

## 3.2. Discussion

Establishment and validation of techniques that allow for reliable measurements of mechanical properties of cells is crucial for advancing the field of cell mechanics<sup>294</sup>. A recent comparison across a broad range of techniques revealed that the mechanical properties measured for the same cell line varied by three order of magnitudes when measured with different methods<sup>311</sup>. This comparison included a set of methods (AFM, magnetic twisting cytometry, particle tracking microrheology, parallel-plate rheometry, and optical stretching) that operate at different magnitude of stress and strain rate, use different probe size, probing length scale, and measure cells in either suspended or adherent states. Here we performed a similar comparison, but focused on microfluidics-based deformability cytometry methods for high-throughput mechanical phenotyping. All deformability cytometry classes probe whole-cell mechanical properties in suspended cells, what greatly reduces the potential sources of the variability compared to the previous study. However, the different methods vary in the magnitude of applied stress and the measurement timescale, which defines stress and strain rates (**Table 3.1**). We tested the performance of the three widely-used microfluidic deformability cytometry variants, cDC, sDC, and xDC, in two standardized assays of osmotic shock and actin disassembly. In total, half a million cells were measured in this study — a number impossible to achieved with traditional, low-throughput methods.

An exponential decrease of deformability with increasing osmolarity was observed with all three deformability cytometry methods, though, each method showed a distinct sensitivity of the exponential decay (see **Figure 3.3** and **Supplementary Table B.1**). Exposure to osmotic shocks leads to multifaceted changes in the cell interior, and influences not only the internal structure and molecular crowding within the cytoplasm, but also in the cell nucleus<sup>368,369</sup>. Furthermore, it was previously reported that the osmotic shock can elicit changes in the relative F-actin content<sup>122</sup> and actin cytoskeleton structure<sup>228</sup>. The overall changes in mechanical properties were, however, shown to be



actin-independent and attributed to macromolecular crowding inside the cell<sup>230</sup>. Thus, we can conclude that all three methods are well suited for detecting changes in intracellular packing.

LatB-induced actin disassembly resulted in dose-dependent increase of deformability in cDC and sDC measurements, while xDC measurements did not show deformability change upon treatment. The differences in the ability to detect actin cytoskeleton disassembly between cDC/sDC and xDC can likely be attributed to the different strain rates at which the methods are operating. cDC and sDC induce strain at the rate of 0.04 and 0.2 kHz, respectively, and show an almost identical change in the measured deformabilities upon LatB treatment, as demonstrated by comparable EC<sub>50</sub> and maximum deformation values at high LatB concentrations (see **Figure 3.5d** and **Supplementary Table B.2**). The measured EC<sub>50</sub> values of 15.2 ng ml<sup>-1</sup> (38.5 nM) for sDC and 11.9 ng ml<sup>-1</sup> (30.1 nM) for cDC correspond roughly to the 68 nM EC<sub>50</sub> value reported for a stiffness-based dose-response relationship measured for LatB in adherent cells<sup>178</sup>. xDC, on the other hand, applies strain at a rate of 20 kHz, 100 times faster than sDC and 500 times faster than cDC, and has been previously reported to not measure significant responses to actin cytoskeletal perturbations<sup>1</sup>. This is presumably due to fluidization observed for actin networks at high strains magnitudes and strain rates<sup>196,370</sup>. Increasing the flow rate — and through that the strain rate — decreases the range of deformability response in sDC measurements, what further supports the idea of strain rate-dependence of measured response to LatB (**Figure 3.6**). In addition, recent studies have demonstrated that adapting cross-slot xDC to operate at lower strain rates enables detection of deformability changes upon disruption of actin cytoskeleton<sup>17,181</sup>. Similarly, using another variant of xDC that relies on cells colliding with a channel wall at a T-junction, it was shown that deformation increase after actin disruption is measurable only at low flow rates<sup>301</sup>. Cell stiffness decrease in response to actin disassembly was shown to vanish at high probing frequencies also in AFM microrheology<sup>27</sup>. In particular, at frequencies exceeding 1 kHz, latrunculin-treated cells did not show decrease in their storage modulus upon treatment. AFM microrheology uses a very different probing modality (oscillatory measurements) and represents a local rather than whole-cell measurement. Nonetheless, it is interesting to note that the frequency at which the response to actin disassembly subsides lies between the probing frequencies of cDC/sDC and xDC.

Even though it would be desirable to compare the tested methods when adjusted to operate at comparable strain rates, such adjustment is not feasible due to technical limitations. For example, in SMR-based cDC, the dynamic range of the measurements on easily deformable cells (such as HL60) is diminished at high flow rates, and the differences between treatments becomes hard to capture. With the 2- $\mu$ s illumination time and up to 5,000 fps imaging rate enabled by current hardware in sDC, increasing the mean flow velocity beyond 30 cm s<sup>-1</sup> would diminish the quality of acquired images by motion blurring. Additionally, increasing the flow rate would drive the system away from Stokes flow regime and challenge the real-time analysis. Decreasing the flow rate in sDC would require adjusting the imaging to avoid capturing the same cell twice and, for many cell types, no measurable deformation would be induced. In xDC, in turn, advantage is taken of inertial effects that can be achieved only at

Re exceeding 20-30<sup>299</sup>, and optimal focusing of cells is achieved at flow rates exceeding 700  $\mu\text{l min}^{-1}$  (mean flow velocity of 6.5  $\text{m s}^{-1}$ )<sup>1</sup>. Thus, in their standard operation, the measurement timescales of cDC, sDC, and xDC cannot be made equal.

Beyond measuring cell deformability, every presented method offers an additional set of unique functionalities. In SMR-based cDC, additional parameters describing cell passage through the constriction such as entry and transit velocity can be obtained. More importantly, this method also provides a highly sensitive readout of cell buoyant mass<sup>9,371</sup>. Furthermore, since in cDC cells are in contact with channel walls, the measurements of passage dynamics can provide information about surface friction experienced by cells that can be relevant to processes such as cancer metastasis<sup>9</sup>. A unique feature of sDC is the real-time processing of acquired images that enables active sorting downstream of deformability analysis<sup>313</sup>. sDC also enables measurements of 1D fluorescence signal in three spectral channels in parallel with deformability characterization in a specialized setup<sup>312</sup>, and offers the possibility to extract Young's moduli from deformability data<sup>298,317</sup>. Last but not least, a recent extension of the sDC method, dynamic RT-DC, enables assignment of viscosity to measured cells by analysing the time evolution of cell deformation over the channel length<sup>336</sup>. xDC offers a throughput one order of magnitude higher than sDC, and two orders of magnitudes higher than cDC, and is thus best suited for characterization of big cell populations and screening for rare cells. Finally, the bright-field cell images recorded during sDC and xDC measurements can be used for extraction of additional image-based features for cell characterisation, or for AI training.

**Table 3.3 | Demonstrated applications of the different deformability cytometry classes.** Summary of studies employing different types of deformability cytometry to investigate various processes in cell lines and in primary tissue samples. This table is adapted from Urbanska, Muñoz *et al.*<sup>363</sup>.

method	demonstrated biological applications
cDC	cytoskeleton perturbations <sup>3,9,180,295,296,372</sup> , chromatin reorganization <sup>295</sup> , nuclear envelope alteration <sup>295,373</sup> , inflammation mediation <sup>3</sup> , leukostasis <sup>3</sup> , cancer cell discrimination <sup>48,180</sup> , cancer cell invasion potential <sup>48</sup> , endothelial-mesenchymal transition <sup>374</sup> , osmotic stress <sup>372</sup> , protein synthesis inhibition <sup>372</sup> , cell cycle progression <sup>372</sup> , neutrophil differentiation <sup>373</sup> , oxidative damage of erythrocytes <sup>375</sup> , circulating tumor cells and blood cells discrimination <sup>374,376</sup>
sDC	cytoskeleton perturbations <sup>21,179,377</sup> , cell cycle progression <sup>21,312</sup> , blood cell type discrimination <sup>5,21,336</sup> , cancer malignancy <sup>11,377</sup> , erythrocyte pathologies <sup>5,69</sup> , leukocyte activation <sup>5,6,124</sup> , leukemia subtypes discrimination <sup>5</sup> , stem cell differentiation <sup>81,378,379</sup> , yeast dormancy <sup>380</sup> , viral infection of a human cell line <sup>381</sup> , ability to pass through microcirculation <sup>28</sup>
xDC	cytoskeleton perturbation (at low probing rates) <sup>17,181</sup> , chromatin reorganization <sup>382</sup> , nuclear envelope alteration <sup>382</sup> , stem cell differentiation <sup>1,382,383</sup> , characterization of blood cells <sup>374</sup> and cells in pleural fluids <sup>1,10</sup> , cancer malignancy <sup>10</sup> , leukocyte activation <sup>1,59</sup> , heat-treated erythrocytes <sup>384</sup>

The standardised comparison of the three microfluidic-based deformability methods presented in this study furthers our understanding of the dominant features responsible for measured deformations across different platforms, and can provide a guideline for choosing a method suitable for the specific scientific questions to be addressed. While all methods provide a good readout of stiffness changes induced by alterations in macromolecular crowding; cDC and sDC, but not xDC operated at high strain rates, are suitable for measuring actin cytoskeleton disassembly. xDC, however, was previously shown to provide a good readout of changes in structures localised deeper in the cells, such as the nucleus<sup>1,382</sup>. For further reference regarding suitability of individual methods for various applications, a comprehensive overview of up-to-date studies using the three different deformability cytometry classes is presented in **Table 3.3**.

Given the ease of implementation and the different cell mechanics contributors probed, the two assays of osmotic compression and actin disassembly presented here, together with relative deformability as a normalized deformability metric, could be used as a benchmark validation protocol for microfluidic-based deformability methods developed in other laboratories. Noteworthy, despite the variability in deformability measures used in the individual methods, the relative deformability changes enabled universal observation of trends and precise extraction of response parameters, such as shared EC<sub>50</sub> values between cDC and sDC for LatB dose-response experiments.

In the future, this comparison study could be extended by including additional treatments targeting further cellular components. For example, the mechanical properties of the nucleus could be targeted by modulating chromatin condensation using drugs such as trichostatin A<sup>227,385</sup>, or by modulating the levels of lamins<sup>223–226</sup>. To further foster cross-method standardization, engineered particles that mechanically mimic cells could be utilized. Hydrogel beads made of polyacrylamide, with size and elastic properties similar to those of mammalian cells, are readily available<sup>323,386</sup>. Several bead batches with a range of Young's moduli could be used to compare the ranges of deformability responses across the different platforms. Additionally, a production of gels with independently tunable storage and loss moduli (representing elastic and viscous component of the mechanical response) was recently demonstrated<sup>387</sup>. These gels were prepared by entrapping linear polyacrylamide in a permanently crosslinked polyacrylamide network. Using a similar approach, beads of comparable storage moduli, but varying loss moduli, could be manufactured and used to test how the viscous component of a viscoelastic material affects measured deformability at different measurement timescales.

In sum, this validation study provides a context for interpreting deformability measurements across the various deformability cytometry platforms, highlights strengths and limitations of the respective methodologies, and fosters cell deformability as a powerful metric for mechanical assessment of single cells at high throughputs.

In the subsequent chapters of this thesis (**Chapters 4 and 5**), I performed AFM measurements to validate the mechanical differences observed with RT-DC for some of the cell lines probed in the respective chapters. The AFM measurements included both indentation experiments and oscillatory probing that covered further ranges of timescales (**Figure 3.7**). The AFM indentation was performed on a 0.2 s timescale (extension speed of  $5 \mu\text{m s}^{-1}$  and indentation depth of approximately  $1 \mu\text{m}$ ), and the probing in AFM microrheology was performed on the timescale of 5 ms (200 Hz)–0.3 s (3 Hz). The results obtained with the different methods are compared in **Chapters 4 and 5**.

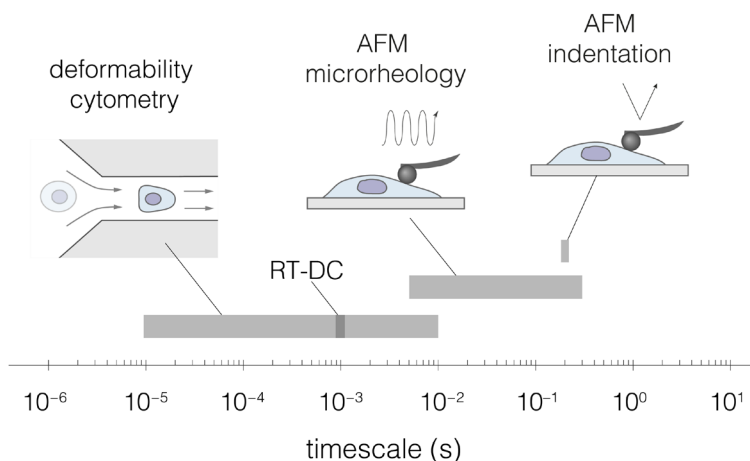


**Figure 3.7 | Comparison of timescales used in deformability cytometry and AFM-based probing techniques implemented in this thesis.** The different deformability cytometry methods cover timescales of several  $\mu\text{s}$  to several ms, the 1-ms timescale characteristic for RT-DC is marked with darker shading; AFM microrheology was used with 3–200 Hz frequencies that cover 5 ms–0.3 s timescale; AFM indentation experiments were performed on a timescale of 0.2 s.

It is important to note that apart from the measurement timescales, there are further differences between deformability cytometry and AFM measurements: (i) while whole-cell deformability is measured in deformability cytometry, AFM performs local measurements (here with  $5\text{-}\mu\text{m}$  bead), (ii) in deformability cytometry cells are always measured in the suspended state, whereas in AFM cells are typically measured on a substrate in either adherent or rounded state, (iii) in deformability cytometry a mean absolute strain of 17% is applied (**Table 3.1**), what for  $13\text{-}\mu\text{m}$  cell corresponds to roughly  $2 \mu\text{m}$  change in cell diameter, in AFM indentation a deformation of ca.  $1 \mu\text{m}$  is induced, and in AFM microrheology the magnitude of cantilever oscillations was set to 10 nm (**Table 3.4**).

**Table 3.4 | Characteristic operation parameters of AFM as compared to RT-DC.**

	RT-DC	AFM microrheology	AFM indentation
<b>cell state</b>	suspended	adherent   rounded	adherent   rounded
<b>deformation scale</b>	whole-cell	local ( $5 \mu\text{m}$ bead)	local ( $5 \mu\text{m}$ bead)
<b>timescale</b>	1 ms	5 ms (200 Hz)–0.3 s (3 Hz)	0.2 s
<b>induced strain</b>	$2 \mu\text{m}$	10 nm	$1 \mu\text{m}$
<b>strain rate</b>	$2 \text{mm s}^{-1}$	$0.03\text{--}2 \mu\text{m s}^{-1}$	$5 \mu\text{m s}^{-1}$

### 3.3. Key conclusions

- Three microfluidics-based deformability cytometry classes operating at different timescales and stress magnitudes — cDC, sDC, and xDC — were compared in two standardized assays of osmotic shock and actin disassembly.
- All three methods detected exponential decrease in deformability with increasing hyperosmotic shock, though, they varied in the sensitivity of the response, which was higher for longer deformation timescales.
- cDC and sDC, but not xDC operating at the highest strain rate, detected deformability increase upon actin disassembly.
- Increasing strain rate in sDC decreased the range of the deformability response to actin disassembly.
- These results suggest that at fast probing timescales ( $\tau \ll 1$  ms) cellular elements other than actin cytoskeleton dominate the response.

### 3.4. Materials and methods

#### 3.4.1. Cell culture and treatments

##### *Cell culture*

Stocks of HL60/S4 cell line (RRID: CVCL\_II77; a kind gift from Donald E. Olins and Ada L. Olins, Department of Biology, Bowdoin College, Brunswick, Maine, 04101, USA) were shared between the three participating laboratories at the same initial passage number and were used within 10 passages. Cells were cultured in ATCC-modified RPMI 1640 medium (Gibco) supplemented with 1% penicillin/streptomycin (Gibco) and 10% heat-inactivated FBS (Gibco) at 37°C, with 5% CO<sub>2</sub>. Subculturing was performed every second day by spinning down the desired number of cells and resuspension in fresh medium, the cell concentration in culture was maintain between 10<sup>5</sup> and 10<sup>6</sup> cells ml<sup>-1</sup>.

##### *Osmotic shock*

The isosmotic media (cell culture media and measurement buffers) had osmolarity of 300 mOsm as measured by freezing point osmomemeter (Fiske 210 Micro-Sample Osmometer, Advanced Instruments, MA, USA). Hyperosmotic media were prepared by adding 18.22, 36.43, 54.65, and 72.86 mg of D-Mannitol (MW: 182.172 g mol<sup>-1</sup>, Sigma Aldrich, St. Louis, MO) per 10 ml of the measurement buffer to obtain solutions of 400, 500, 600, and 700 mOsm, respectively. Hypoosmotic media were prepared by adding deionized water to the measurement buffer in 1:2 or 1:5 ratio to obtain solutions with osmolarity of 200 and 250 mOsm, respectively. HL60/S4 cells at a culture density between 0.5–1.0 × 10<sup>6</sup> ml<sup>-1</sup> were harvested for measurements by centrifugation at 180 × g for 5 minutes. The cell pellet was resuspended in osmolarity-adjusted measurement buffer and the resuspended cells were incubated for 10 minutes at 37°C, 5% CO<sub>2</sub> before the measurement. The measurements of cell deformability were performed at room temperature (22–24°C).

##### *LatB treatment*

Latrunculin B (MW 395.5 g mol<sup>-1</sup>, Sigma Aldrich) was dissolved in DMSO at a concentration of 1 mg ml<sup>-1</sup> to prepare the stock solution, which was then shared between the participating laboratories. The stock solution was pre-diluted in DMSO to 10,000 × the desired concentration, so that upon final dilution equal DMSO concentration was present in all treatments (0.01 % v/v) (see **Table 3.5**). Subsequently, LatB was diluted 10,000× in the appropriate measurement buffer to final LatB concentrations of 1, 5, 10, 25, 50 and 100 ng ml<sup>-1</sup>. HL60/S4 cells at a density between 0.5 and 1.0 × 10<sup>6</sup> ml<sup>-1</sup> were harvested by centrifugation at 180 × g for 5 minutes, resuspended in LatB-containing solution, and incubated for 30 minutes at 37°C, 5% CO<sub>2</sub> prior to the measurements. The subsequent deformability measurements were conducted at room temperature (22–24°C).

**Table 3.5 | Summary of mass and molar concentrations of LatB.**

	mass concentration	molar concentration	total dilution factor	pre-dilution in DMSO
<b>DMSO</b>	0.01 % (v/v)	-	10,000 ×	-
<b>LatB stock</b>	1 mg ml <sup>-1</sup>	2.53 mM	-	-
	0.001 µg ml <sup>-1</sup>	2.53 nM	1 mln ×	100 ×
	0.005 µg ml <sup>-1</sup>	12.65 nM	200,000 ×	20 ×
<b>LatB treatment</b>	0.01 µg ml <sup>-1</sup>	25.3 nM	100,000 ×	10 ×
	0.25 µg ml <sup>-1</sup>	63.25 nM	40,000 ×	4 ×
	0.05 µg ml <sup>-1</sup>	126.5 nM	20,000 ×	2 ×
	0.1 µg ml <sup>-1</sup>	253 nM	10,000 ×	-

### 3.4.2. Deformability cytometry measurements

#### *cDC measurements*

All the cDC measurements were performed by Josephine Shaw Bagnall in the group of Prof. Scott R. Manalis at the Massachusetts Institute of Technology, Cambridge, MA, USA. The SMR device, with overall design and fabrication procedures similar to the previously published ones<sup>9</sup>, featured a fluidic channel with a 6 µm wide, 50 µm long, and 15 µm deep constriction. Similar to more recent SMRs<sup>388,389</sup>, the device used in this study (fabricated by CEA-Leti, France) was operated via piezoceramic actuation and had a piezoresistive readout system to monitor cantilever vibration frequency. To avoid unspecific adhesion to the channel walls, the device interior was passivated with 1 mg ml<sup>-1</sup> polyethylene glycol (PLL(20)-g[3.5]-PEG(2), SuSoS, Switzerland). A constant pressure of 1.0 kPa was applied throughout the experiment to drive cells through the fluidic channel. Single cell buoyant mass and passage time were determined from changes in the resonant frequency of the microcantilever. Individual cell diameters were estimated from cell volume obtained by combining SMR buoyant mass measurements with Coulter counter volume measurements (Multisizer 4, Beckman Coulter, CA, USA) as described previously<sup>9</sup>.

#### *sDC measurements*

The chip fabrication and experimental procedures connected to sDC measurements are described in detail in **Chapter 2**. In brief, cells were suspended in a viscosity-adjusted measurement buffer (0.5% methylcellulose in PBS) and introduced to the microfluidic chip via a syringe pump. The overall flow rate during the experiments was set to 0.04 µl s<sup>-1</sup> (0.01 µl s<sup>-1</sup> sample flow and 0.03 µl s<sup>-1</sup> sheath flow) unless indicated otherwise. The imaging was performed at the end of a ~300 µm long channel with a 20 µm × 20 µm square cross-section with a high-speed camera. The cell area and deformation were determined from cell contours in real-time by an image processing algorithm developed in house<sup>21</sup>. Cell diameter was calculated during offline analysis from measured surface area and defined as

for a circle with an equivalent surface area. To discard events with rough or incomplete contours, the results were filtered for an area ratio between 1.00 and 1.05.

#### *xDC measurements*

All the cDC measurements were performed by Hector E. Muñoz in the group of Prof. Dino Di Carlo at the University of California, Los Angeles, CA, USA. Soft lithography was used to fabricate the xDC PDMS devices, which were then bonded to glass slides, according to procedures described in detail elsewhere<sup>1</sup>. Cell suspensions were injected into the microfluidic chip using a syringe pump set to 750  $\mu\text{l min}^{-1}$ . The dimensions of microfluidic channels close to the cross-junction were equal to 60  $\mu\text{m} \times 30 \mu\text{m}$ . The region of interest was imaged with a high-speed camera at approximately 500,000 frames  $\text{s}^{-1}$ , with sub-microsecond exposure time. Videos were analyzed by a MATLAB program in an automatized manner. Cell diameter was measured on the undeformed cells before the arrival at the junction, and cell aspect ratio was assessed during cell deformation at the junction. Cell diameter is estimated as a minimum value of diameters assessed at  $\pm 30^\circ$  with respect to the direction perpendicular to the flow.

### 3.4.3. Data analysis

#### *Relative deformability calculation*

Relative deformability,  $RD$ , was calculated by dividing the deformability of the treated cells,  $D_t$ , by the median deformability of control cells from a given experimental set,  $\tilde{D}_{ctrl}$ :  $RD = \frac{D_t}{\tilde{D}_{ctrl}}$ . The measured deformability is influenced the cell size. To reduce the measurement bias for changing cell size across conditions, the  $RD$  calculations were based only on deformability values of cells contained with a 1- $\mu\text{m}$  wide diameter bin that was most represented among all treatment and control samples for a given experimental set (see **Supplementary Figure B.2** and **B.5**). To visualize the influence of the bin selection on the observed trends,  $RD$  response for data with no bin, 3- $\mu\text{m}$  bin and 1- $\mu\text{m}$  bin is presented in **Supplementary Figure B.8** and **B.9**.

#### *Osmolarity data curve fitting*

Due to concerns about non-monotonic nature of  $RD$  response over time in hypo-osmotic conditions, only hypertonic conditions were used for curve fitting. To best describe  $RD$  as a function of  $Osm/Osm_{iso}$  we tested fitting three functions: (i) exponential, (ii) power law, and (iii) linear, constrained to pass through a fixed point (1,1) representing control measurement at the  $Osm_{iso}$  (**Supplementary Figure B.4a–c**). The fitting was performed using the nonlinear least-square *nls* function from the *stats* package in R (R Development Core Team). The goodness of the three respective fits was assessed by evaluating their mean absolute residuals and Bayesian information criterion, BIC (*BIC* function in *stats* package in R). Exponential functions gave best fitting results across the three methods (**Supplementary Figure B.4d,e**). For statistical analysis, exponential fit curves were compared in pairs



via the  $F$ -test in R<sup>390</sup>. To account for multiple pairwise comparison across the three datasets, Bonferroni adjusted  $p$ -values were calculated by multiplying  $p$ -values by three<sup>391</sup>.

*LatB dose–response curve fitting*

$RD$  values were calculated with respect to DMSO vehicle control.  $RD$  response to LatB concentration was fit with a four-parameter log-logistic regression curve with the formula presented in **Equation 3.2**<sup>367</sup>. The fitting was performed using *drm* function in *drc* package<sup>367</sup> in R. Curves were compared in pairs via the  $F$ -test in R<sup>390</sup>. To account for multiple pairwise comparison across the three datasets, Bonferroni adjusted  $p$ -values were calculated by multiplying  $p$ -values by three<sup>391</sup>.

*Data and code availability.*

Dataset containing numerical values from all deformability measurements supporting findings of this study are publicly available on figshare under the following identifier: doi:10.6084/m9.figshare.11704119. MATLAB and R codes used to perform statistical analysis and generate data representations shown in this chapter are available on GitHub at <https://github.com/dicarolo-lab/metadeformability>.

Chapter 4 is based on and contains materials adapted from the following peer-reviewed publication:

M. Urbanska<sup>\*</sup>, M. Winzi, K. Neumann, S. Abuhattum, P. Rosendahl, P. Müller, A. Taubenberger, K. Anastasiadis, and J. Guck<sup>\*</sup>. (2017). **Single-cell mechanical phenotype is an intrinsic marker of reprogramming and differentiation along the mouse neural lineage**, *Development*, 144(23), pp. 4313–4321.

DOI: 10.1242/dev.155218

available under:

<https://journals.biologists.com/dev/article/144/23/4313/19252/Single-cell-mechanical-phenotype-is-an-intrinsic>

Own contributions: conceptualization, investigation, project administration, formal analysis, visualization, writing – original draft preparation, writing – review and editing

<sup>\*</sup>co-corresponding authors

## — Chapter 4 —

# Mechanical journey of neural progenitor cells to pluripotency and back

Early embryonic development is a fascinating process in which a blueprint of a body plan emerges from a single cell through a series of cell divisions, differentiation, and cellular rearrangements<sup>136,392–394</sup> (see **Section 1.2.4**). During this process, cells undergo fate transitions that are characterized not only by activation of specific gene expression programs, but also by remodeling of cellular architecture. The changes in cellular architecture are, in turn, inherently related to changes in cell morphology and mechanical properties, both of which can affect successful progression of embryogenesis<sup>392,394</sup>.

Developmental cell fate transitions can be studied *in vitro* using pluripotent stem cells (PSCs) as a model system. PSCs have the unlimited ability to self-renew in culture and can develop into cells of all three primary germ layers — ectoderm, endoderm, and mesoderm — and therefore into all cells of an adult body, but cannot form extraembryonic tissues such as placenta<sup>395,396</sup>. Two types of PSCs can be established from mouse embryos: naïve embryonic stem cells (ESCs) derived from inner cell mass of preimplantation blastocyst (E3.5–4.5) and primed pluripotent epiblast stem cells (EpiSCs) derived from epiblast of post-implantation embryo (E5.5–7.5)<sup>396,397</sup>. Apart from isolation from the embryo, PSCs can be also obtained by dedifferentiation of (semi-)specialized cells back to the pluripotent state in a process called cellular reprogramming. Takahashi and Yamanaka showed in 2006 that it is sufficient to express four transcriptional factors: Oct4, Sox2, Klf4, and cMyc (OSKM) to rewire the transcriptional network of cells and generate induced pluripotent stem cells (iPSCs)<sup>398</sup>. Remarkably, ESCs and iPSCs can contribute to normal development when injected back into embryo and generate so-called chimeras<sup>395</sup>. iPSCs reprogramming is a dynamic remodeling process which has been widely characterized in terms of changes in gene expression patterns<sup>399–404</sup>, epigenetic landscape<sup>405,406</sup> or cytoskeletal organization<sup>71,407</sup>. Yet, little is known about how cell mechanical properties change during that process.

In the study presented in this chapter, I explored reprogramming to pluripotency and differentiation along neural lineage as a model to study mechanical phenotype changes in cell fate transitions. In particular, I characterized mechanical properties of murine fetal neural progenitor cells (fNPCs) isolated from E15.5 embryos during reprogramming towards iPSCs, and the mechanical properties of iPSC during differentiation towards the neural lineage. I further characterized mechanically an alternative pluripotent state called F-class and, using surface markers, identified mechanical subpopulation of cells at intermediate reprogramming stages. Finally, I compared the mechanical phenotype of iPSCs with

that of ESCs isolated from E3.5 embryo, to which iPSCs correspond in their potency. Together, the cell types characterized in this study span 12 days of murine development (**Figure 4.1**).

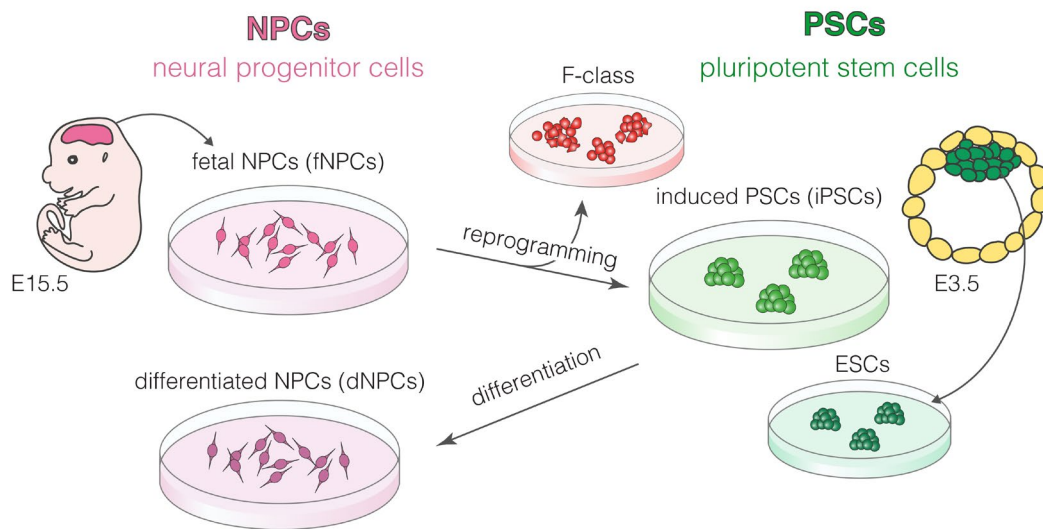


**Figure 4.1 | Stem cell model of developmental transition from neural precursor cells to pluripotent stem cells.** Cellular reprogramming and differentiation along neural axis were studied *in vitro*. fNPCs isolated from E15.5 mouse embryos were reprogrammed to iPSCs. iPSCs correspond in their potency to ESCs derived from the inner cell mass of E3.5 embryos. F-class is an alternative pluripotent state that is a by-product of transgene-induced reprogramming. iPSCs were differentiated back to NPCs to study the process reverse to reprogramming.

## 4.1. Results

### 4.1.1. fNPCs become progressively stiffer during reprogramming to pluripotency

fNPCs with an integrated cassette for doxycycline (dox)-inducible expression of the OSKM factors were used to follow mechanical phenotype changes during transition of specialized cells towards pluripotency. The timeline of the reprogramming is summarized in **Figure 4.2a**. On day 0, OSKM expression was initiated by addition of dox to the fNPCs culture. Dox was supplemented daily until day 19, and removed afterwards to stabilize cells in a transgene-independent state. To guide the cells towards the ground state of pluripotency, starting on day 14 the medium was additionally supplemented with two inhibitors: PD0325901 and CHIR99021 (2i), targeting MEK1/2 and GSK3 $\alpha/\beta$ , respectively<sup>408,409</sup>. From day 7 onwards formation of round, dome-like colonies characteristic of pluripotent stem cells was observed (**Figure 4.2a**). On the days indicated in **Figure 4.2a**, cells were harvested and characterized using RT-DC. Area-deformation scatter plots for four reference stages (day 0, 7, 14, and 28) along the reprogramming process are presented in **Figure 4.2b**. As visualized by the contour plots in area-deformation space (**Figure 4.2c**), the fNPCs increased in size and cross multiple isoelasticity lines towards the stiffer phenotype over the reprogramming process. The observed stiffening is further visualized by comparing the distributions of Young's moduli extracted from the area-deformation data (**Figure 4.2d**, see also **Supplementary Figure C.1** and **C.2**).

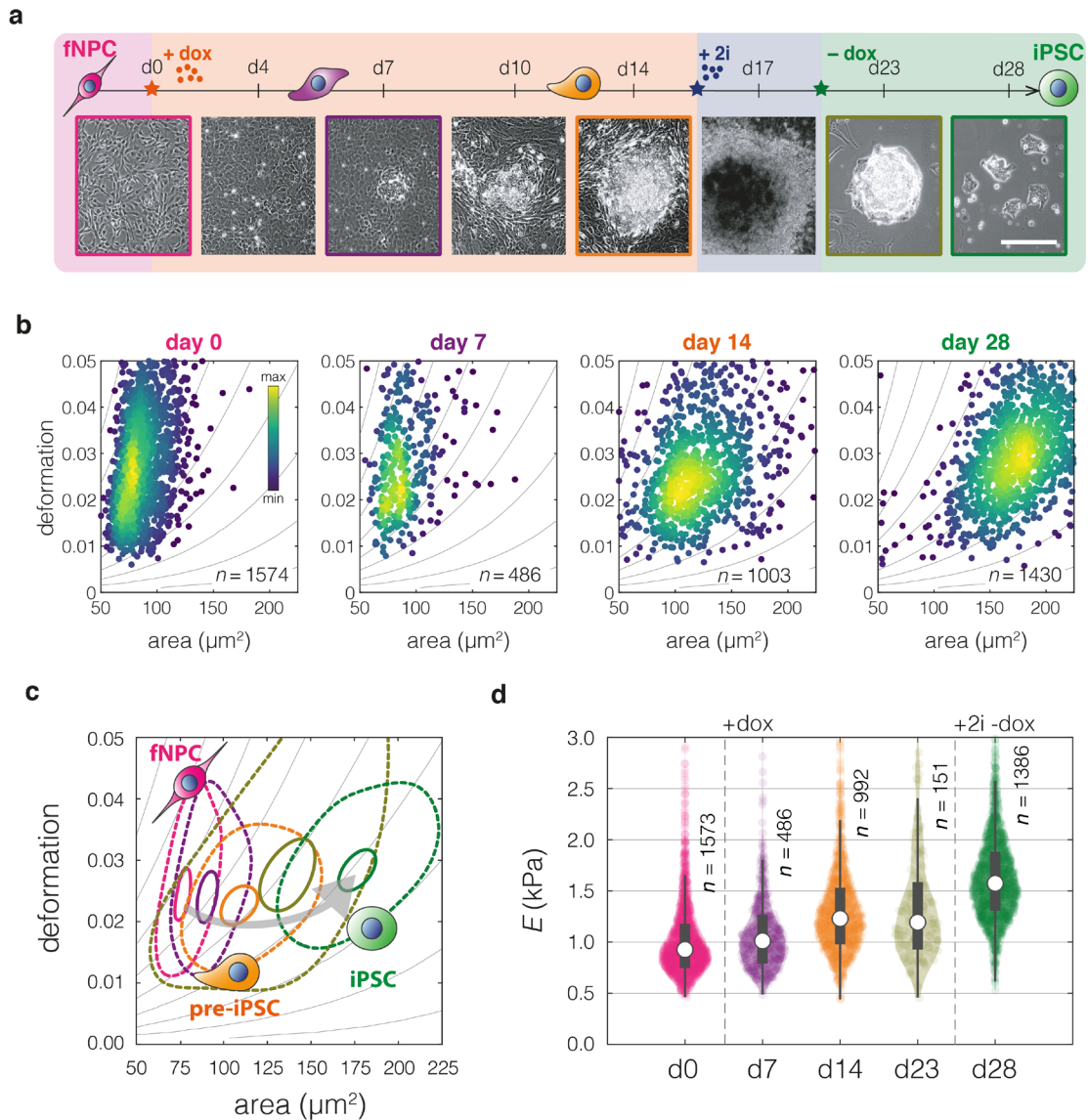


**Figure 4.2 | fNPCs become progressively stiffer during reprogramming to pluripotency.** **a**, Time course of reprogramming of fNPCs towards pluripotency. Bright field images show representative cell morphologies. Scale bar corresponds to 200  $\mu\text{m}$ . **b**, Deformation–area scatter plots of cell populations characterized by RT-DC on reprogramming days 0, 7, 14, and 28. Color map indicates event density. **c**, Contour plots of cell populations from reprogramming days 0, 7, 14, 23, and 28. Solid lines delineate 95% density and dashed lines 50% density. The populations are color-coded as in **a**. **d**, Young’s moduli extracted for cell populations in **c**. Boxes on top of violins extend from 25th to 75th percentiles, with a dot at the median, whiskers indicate  $1.5 \times \text{IQR}$ . This figure is modified from Urbanska *et al.*<sup>378</sup>.

To validate that fNPCs were successfully reprogrammed to iPSCs, changes in expression of neural markers and pluripotency-related genes were assessed at the final stage of reprogramming (after day 28) compared to the initial population of fNPCs. The qRT-PCR analysis showed upregulation of pluripotency genes (*Nanog*, endogenous *Oct4* (*Oct4\**), and *E-cadherin* (*Ecad*)) and downregulation of neural markers (*Sox1*, *Nestin*, *Vimentin* (*Vim*) or *N-cadherin* (*Ncad*)), confirming the acquisition of pluripotent state (**Figure 4.3**).

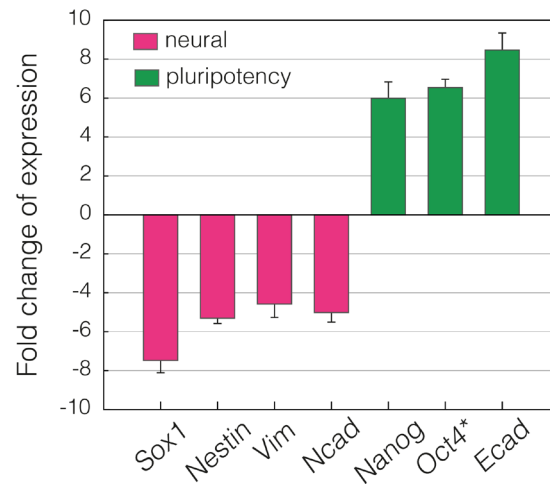


**Figure 4.3 | Expression signature of neural and pluripotency markers confirms successful reprogramming.** Fold change of expression of selected neural markers (magenta) and pluripotency markers (green) assessed in fully reprogrammed iPSCs as compared to fNPCs using qRT-PCR. Bars represent means and error bars represent standard deviation for  $n = 3$  biological replicates. This figure is adapted from Urbanska *et al.*<sup>378</sup>.

Since iPSCs are pluripotent cells that morphologically, transcriptionally and functionally resemble ESCs, I wondered whether the mechanical phenotype of iPSCs is comparable to that of ESCs. To test that, I performed several measurement replicates on ESCs and compared the obtained results with that obtained for iPSCs. As illustrated in **Figure 4.4**, there is no significant difference between the Young's moduli obtained for ESCs and iPSCs.

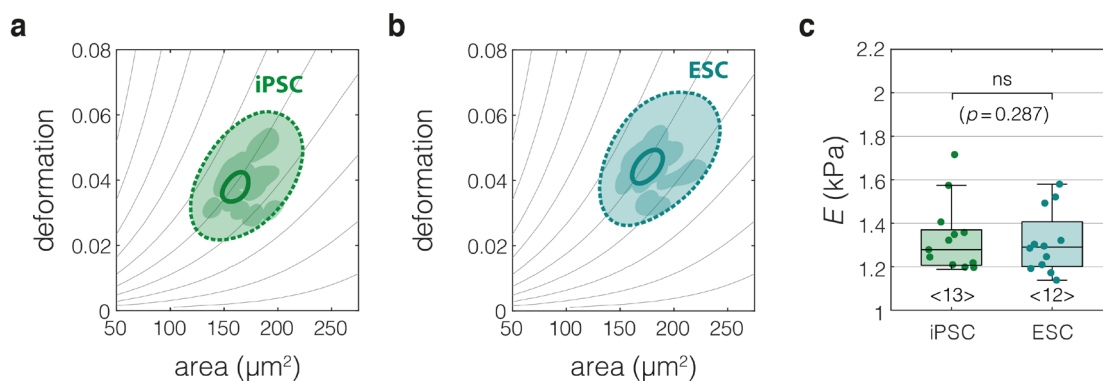


**Figure 4.4 | Mechanical phenotype of iPSCs is equivalent to that of ESCs.** **a–b**, Area–deformation contour plots for multiple RT-DC measurements performed on iPSCs (**a**) and ESCs (**b**). Dark solid line outlines 95%-density contour and dashed line outlines 50%-density contour of data pooled from all experiments. Shaded regions cover 95%-density areas for populations from individual experiments. **c**, Young's moduli derived for iPSC and ESC. Data points represent medians of individual RT-DC measurements from **a** and **b**. Boxes extend from the 25th to 75th percentiles, with a line at the median, whiskers indicate  $1.5 \times \text{IQR}$ . Statistical analysis was performed using a linear mixed-effects model on all measurement replicates. This figure is modified from Urbanska *et al.*<sup>378</sup>.

Next, I sought to confirm the mechanical phenotype difference between the terminal states of reprogramming using another established mechanical characterization technique, namely, AFM. iPSCs had higher stiffness than fNPCs as measured by AFM indentation on rounded cells (**Figure 4.5b**),

qualitatively reproducing the RT-DC results (**Figure 4.5a**). In terms of absolute values, the Young's moduli of both fNPCs and iPSCs were higher when measured with RT-DC (**Figure 4.5; Supplementary Table C.1**). While AFM measurements on rounded cells settled on the substrate are more comparable with the suspended cell state measured in RT-DC, additional AFM measurements on adherent cells were performed to check if observed differences are influenced by substrate attachment (see **Figure 4.5d–f** for exemplary images of measured cells). Also in the adherent state, higher Young's modulus values were observed for iPSCs than for fNPCs (**Figure 4.5c**). The summary of median Young's moduli corresponding to **Figure 4.5a–c** is presented in **Supplementary Table C.1**. Together, the collected data show that iPSCs are stiffer than fNPCs across different methods and independent of measuring suspended or adhered cells.

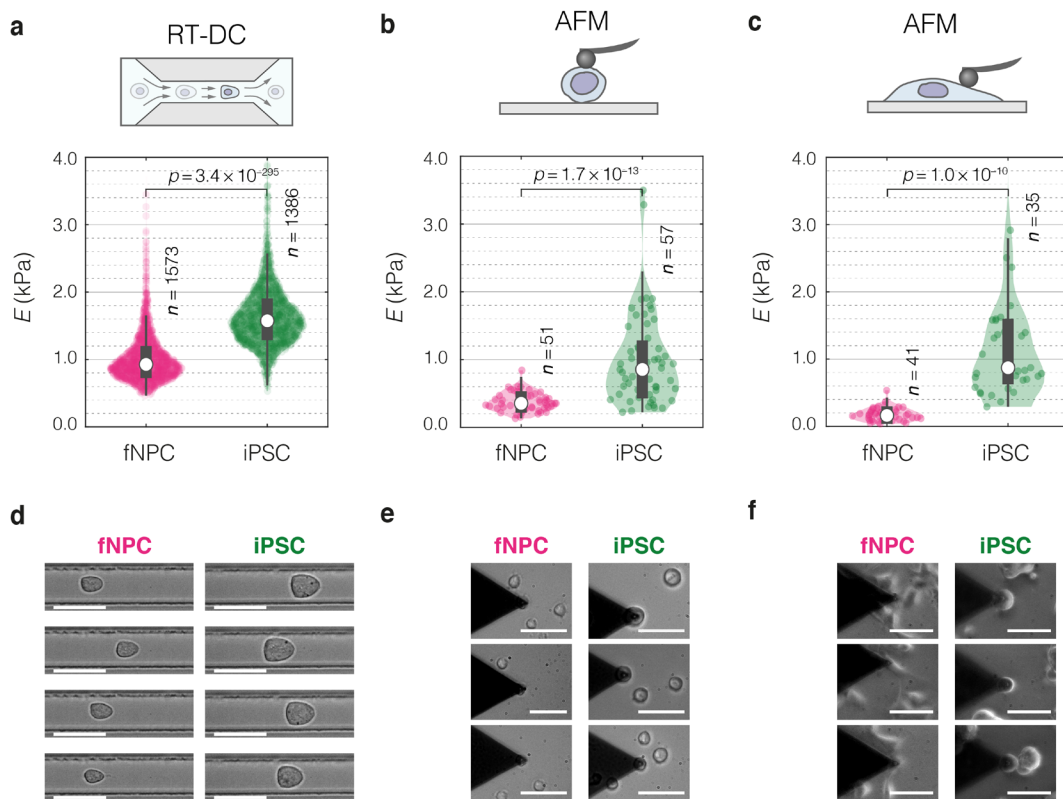


**Figure 4.5 | iPSCs are stiffer than fNPCs in RT-DC measurements as well as in AFM measurements on rounded and adherent cells.** **a–c**, Young's moduli of fNPCs and iPSCs obtained in an RT-DC measurement (**a**), in an AFM measurement on rounded cells (**b**), and in an AFM measurement on adherent cells (**c**). **d–f**, Representative bright field images of fNPCs and iPSCs measured in suspension in RT-DC (**d**), measured in rounded state with AFM (**e**), and measured while adhering to the substrate in AFM (**f**). The dark triangle visible in the images in **e** and **f** is the AFM cantilever. Scale bars represent 40, 50, and 50  $\mu\text{m}$  for **d**, **e**, and **f**, respectively. In **a–c**, boxes on top of the violins extend from 25th to 75th percentiles, with a dot at the median, whiskers indicate  $1.5 \times \text{IQR}$ . Data points indicate individual cells. Statistical analysis was performed using two-sided Wilcoxon rank sum test. This figure is modified from Urbanska *et al.*<sup>378</sup>.

Interestingly, iPSCs, that show round cell morphology also when attached to the substrate (**Figure 4.5f**), had similar Young's modulus independent of measuring in suspended

( $0.853 \pm 0.489$  kPa, median  $\pm$  MAD; **Figure 4.5b**) or adherent state ( $0.871 \pm 0.599$  kPa, median  $\pm$  MAD; **Figure 4.5c**) ( $p = 0.25$ ; two-sided Wilcoxon rank sum test). fNPCs, in turn, showed a change in morphology from spindle-shaped to rounded when detached from the substrate (**Figure 4.5e,f**), and accompanying increase in Young's modulus in rounded ( $0.354 \pm 0.109$  kPa, median  $\pm$  MAD; **Figure 4.5b**) as compared to adherent state ( $0.163 \pm 0.075$  kPa, median  $\pm$  MAD; **Figure 4.5c**) ( $p = 1.45 \times 10^{-10}$ ; two-sided Wilcoxon rank sum test).

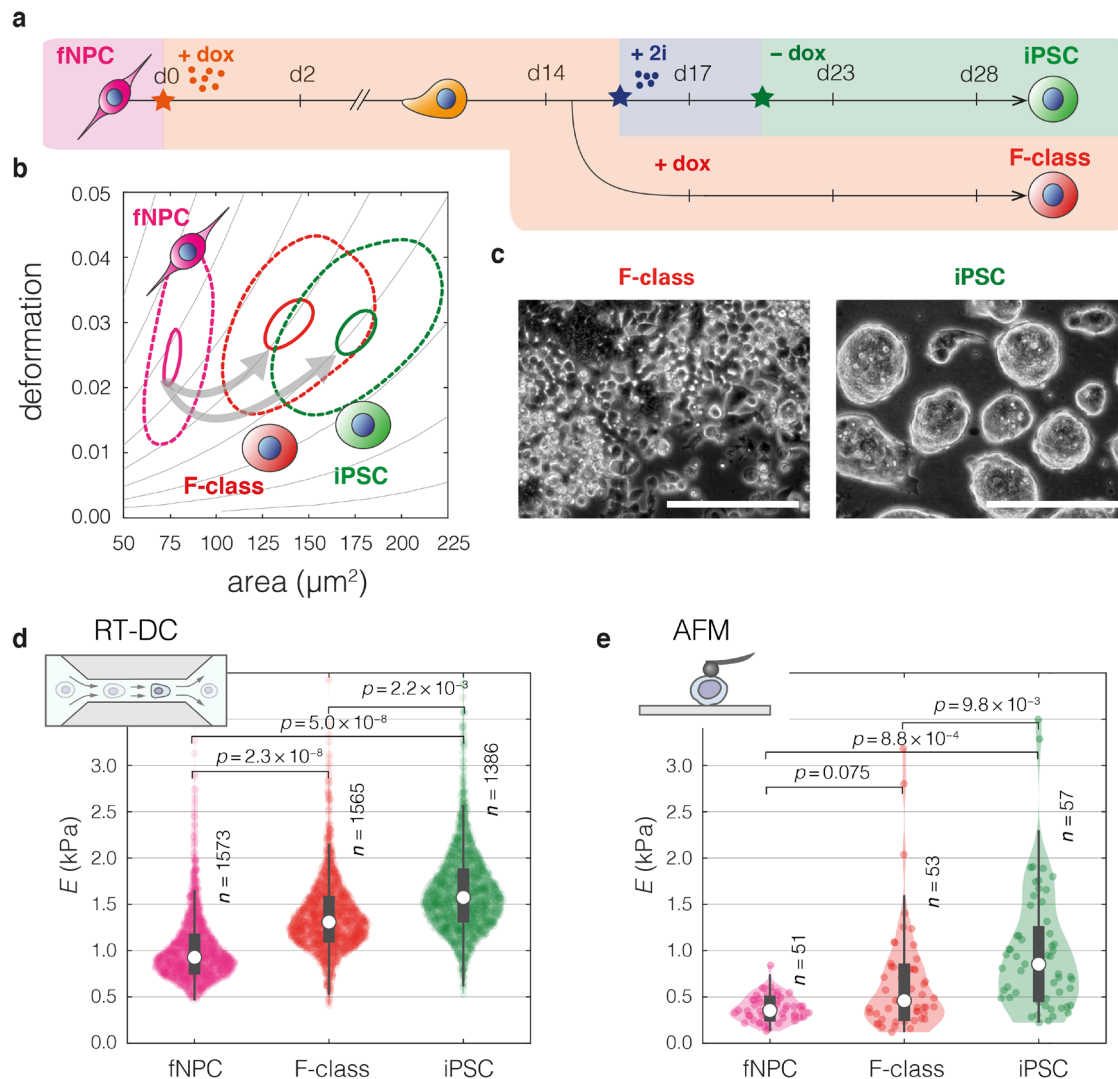


**Figure 4.6 | F-class cells are more compliant than transgene-independent iPSCs.** **a**, Time course of fNPCs reprogramming with two different routes leading to transgene-independent iPSCs (upper route) and transgene-dependent F-class cells (lower route). **b**, Contour plots of fNPCs on reprogramming day 0, and F-class cells as well as iPSCs at the end of reprogramming. Solid lines delineate 95% density and dashed lines 50% density. **c**, Phase-contrast images of cultures of F-class cells (fuzzy colonies, left panel) and iPSCs (compact colonies, right panel). Scale bars represent 200  $\mu\text{m}$ . **d**, Young's moduli estimated for fNPCs, F-class cells, and iPSCs from a representative RT-DC experiment. **e**, Young's moduli estimated for fNPCs, F-class cells, and ESC-like iPSCs from a representative AFM indentation experiment on rounded cells. In **d** and **e**, boxes on top of violins extend from 25th to 75th percentiles, with a dot at the median, whiskers indicate  $1.5 \times \text{IQR}$ , data points indicate individual cells. Statistical analysis was performed using linear mixed-effects models on multiple measurement replicates (see **Supplementary Figure C.3** and **Supplementary Table C.2**). This figure is modified from Urbanska *et al.*<sup>378</sup>.



#### 4.1.2. Transgene-dependent F-class cells are more compliant than ESC-like iPSCs

If dox is not removed from culture towards the end of reprogramming, the cells can stabilize in an alternative pluripotent state called F-class<sup>410</sup> (**Figure 4.6a**). F-class cells depend on the ectopic expression of the OSKM factors, are highly proliferative, and grow in cell-contact independent manner. They form fuzzy colonies as opposed to compact, dome-like colonies characteristic for the dox-independent ESC-like iPSCs, also referred to as C-class<sup>410</sup> (**Figure 4.6c**). I tested whether F-class cells show a different mechanical phenotype compared to the standard iPSCs and observed that F-class cells are more compliant than iPSCs, but less compliant than fNPCs in both RT-DC measurements (**Figure 4.6b,d**) and AFM indentation experiments on rounded cells (**Figure 4.6e**). Thus, the distinct pluripotent F-class cell state is not only characterized by different growth dynamics, but also by a distinct mechanical phenotype.

Of note, even though the directionality of mechanical phenotype changes between the respective cell types was the same in AFM and RT-DC, the Young's modulus values obtained from the RT-DC measurements were approximately twice as high as those obtained from the AFM indentation measurements on rounded cells (**Figure 4.6d,e, Supplementary Table C.2**).

#### 4.1.3. Surface markers unravel mechanical subpopulations at intermediate reprogramming stages

Even though the emergence of pluripotent cells is asynchronous, i.e., at the intermediate reprogramming stages there is a mixture of flat adherent cells and pluripotent stem cell-like colonies (**Figure 4.2a, d7–d23**), clearly distinct mechanical subpopulations were not observed (**Figure 4.2b,d, Supplementary Figure C.1 and C.2**). To investigate whether more and less advanced cells present at the intermediate stages of reprogramming differ mechanically, I used SSEA1/CD24 surface marker staining and took advantage of RT-FDC<sup>312</sup> to track cell identity and cell mechanics simultaneously. SSEA1 is a known pluripotency marker<sup>400,402,411</sup>, and CD24 was previously shown to be present in F-class cells but absent in iPSCs<sup>412</sup>.

On day 0, fNPCs were positive for CD24 (CD24+) and negative for SSEA1 (SSEA1-) (**a, day 0**). As reprogramming progressed, an increasing number of CD24 +/SSEA1+ cells emerged (**Figure 4.7a, day 2–10, Figure 4.7b**). With continuous dox supplementation, F-class cells stabilized in a CD24+/SSEA1+ state, whereas upon dox withdrawal, the iPSCs stabilized in a CD24- state with moderate expression of SSEA1 (**Figure 4.7a, day 28**). The mechanical characterization of cells corresponding to the marker expression presented in **Figure 4.7** is presented in **Supplementary Figure C.2**.

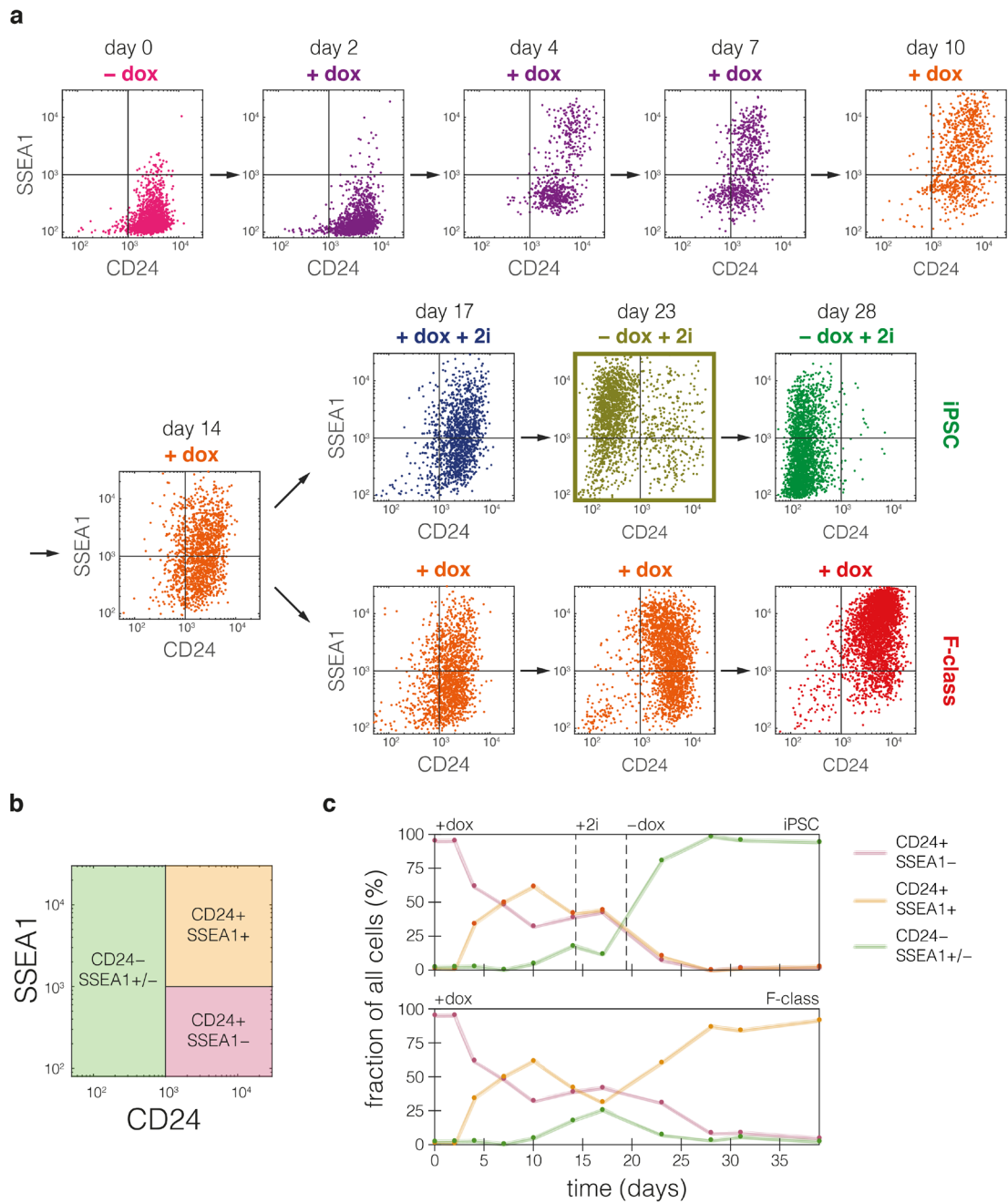


**Figure 4.7 | The evolution of CD24/SSEA1 expression during fNPC reprogramming towards two pluripotency routes. a,** Scatters of CD24 vs SSEA1 surface marker expression along the time course of reprogramming towards F-class and iPSCs. The signals of SSEA1-APC and CD24-FITC represent maximum fluorescence intensity recorded with fluorescence channels 1 and 3, respectively, of the RT-FDC setup. **b,** Graphical representation of gating for CD24+/SSEA1-, CD24+/SSEA1+ and CD24-/SSEA1+/- cells. **c,** Evolution of relative content of the respective populations gated as shown in **b** on days 0 to 28 of reprogramming towards iPSCs (top panel) and F-class cells (bottom panel). This figure is adapted from Urbanska *et al.*<sup>378</sup>.

Interestingly, on day 23, shortly after dox withdrawal, cells were distributed among all three marker-based phenotypes: CD24+/SSEA1- cells corresponding to the start of reprogramming, CD24+/SSEA1+ cells corresponding to intermediate reprogramming stage and F-class cells, and CD24- cells with moderate expression of SSEA1 that correspond to the ESC-like iPSCs (**Figure 4.7a**,

day 23). The mechanical phenotype of the measured cell population on this day showed a seemingly unimodal distribution (**Figure 4.8a**; **Supplementary Figure C.2**, day 23). However, when cells were classified into groups according to the CD24/SSEA1 expression, it became apparent that the respective cell populations differ in their mechanical properties. CD24+/SSEA1- cells were the most compliant ones, with phenotype similar to that of fNPCs, CD24+/SSEA1+ cells corresponding to F-class cells had intermediate stiffness and highest spread, and CD24- cells, corresponding to fully reprogrammed iPSCs were the stiffest (**Figure 4.8b,c**). The relative stiffness of the three cell groups roughly corresponds to the three terminal states of reprogramming (see **Figure 4.6**). It can be thus concluded that even though it is not apparent without surface marker-assisted classification, the distinct mechanical subpopulations of cells are present at the intermediate stages of reprogramming.

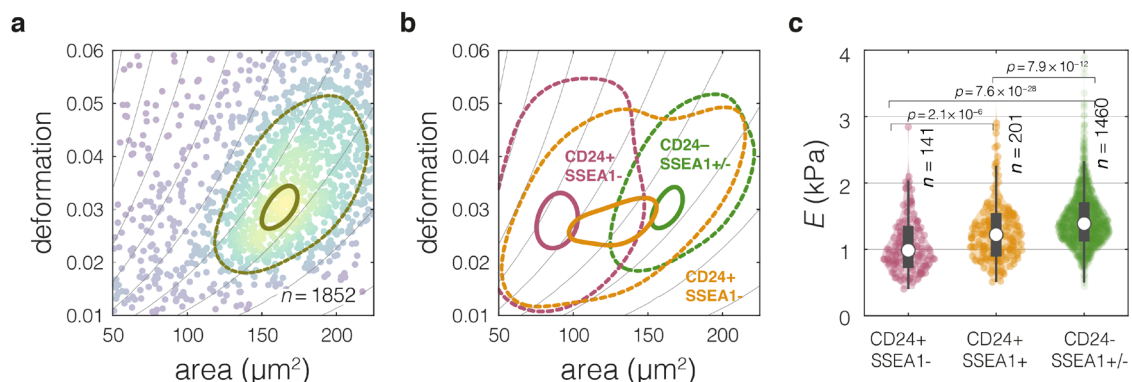


**Figure 4.8 | CD24/SSEA1-based gating reveals mechanical subpopulations on reprogramming day 23.**  
**a**, Area-deformation plot of cell population on reprogramming day 23 (-dox +2i) with delineated 95%-density (solid line) and 50%-density (dashed line) contours. **b**, Color-coded 95%-density (solid lines) and 50%-density (dashed lines) contour plots of deformation versus cell area for the cell population from **a** subdivided into three groups based on the expression of CD24 and SSEA1 markers (see **Figure 4.7b** for the definition of gates). **c**, Distributions of Young's moduli estimated for CD24+/SSEA1-, CD24+/SSEA1+, and CD24-/SSEA1+/- cells. Boxes on top of the violins extend from 25th to 75th percentiles, with a dot at the median, whiskers indicate  $1.5 \times \text{IQR}$ , data points indicate individual cells. Statistical analysis was performed using two-sided Wilcoxon rank sum test. This figure is modified after Urbanska *et al.*<sup>378</sup>.

#### 4.1.4. Neural differentiation of iPSCs mechanically mirrors reprogramming of fNPCs

Next, I asked whether the mechanical phenotype of iPSCs could be reversed to that of fNPCs in the process of differentiation towards the neural lineage. Neural differentiation was induced by seeding cells at low density and culturing them in N2B27 medium. In the absence of Lif and 2i, pluripotent cells are known to spontaneously differentiate towards the neural lineage<sup>413</sup>. To further facilitate the commitment towards neural progenitors, the growth medium was supplemented with epidermal growth factor (EGF) and fibroblast growth factor 2 (FGF2) on differentiation day 7, when neural rosettes began to form (**Figure 4.9a**). Mechanical characterization with RT-DC revealed that, inversely to fNPC reprogramming, iPSCs became smaller and more compliant during the time course of differentiation towards the neural lineage (**Figure 4.9b-d**, **Supplementary Figure C.4** and **C.5**).

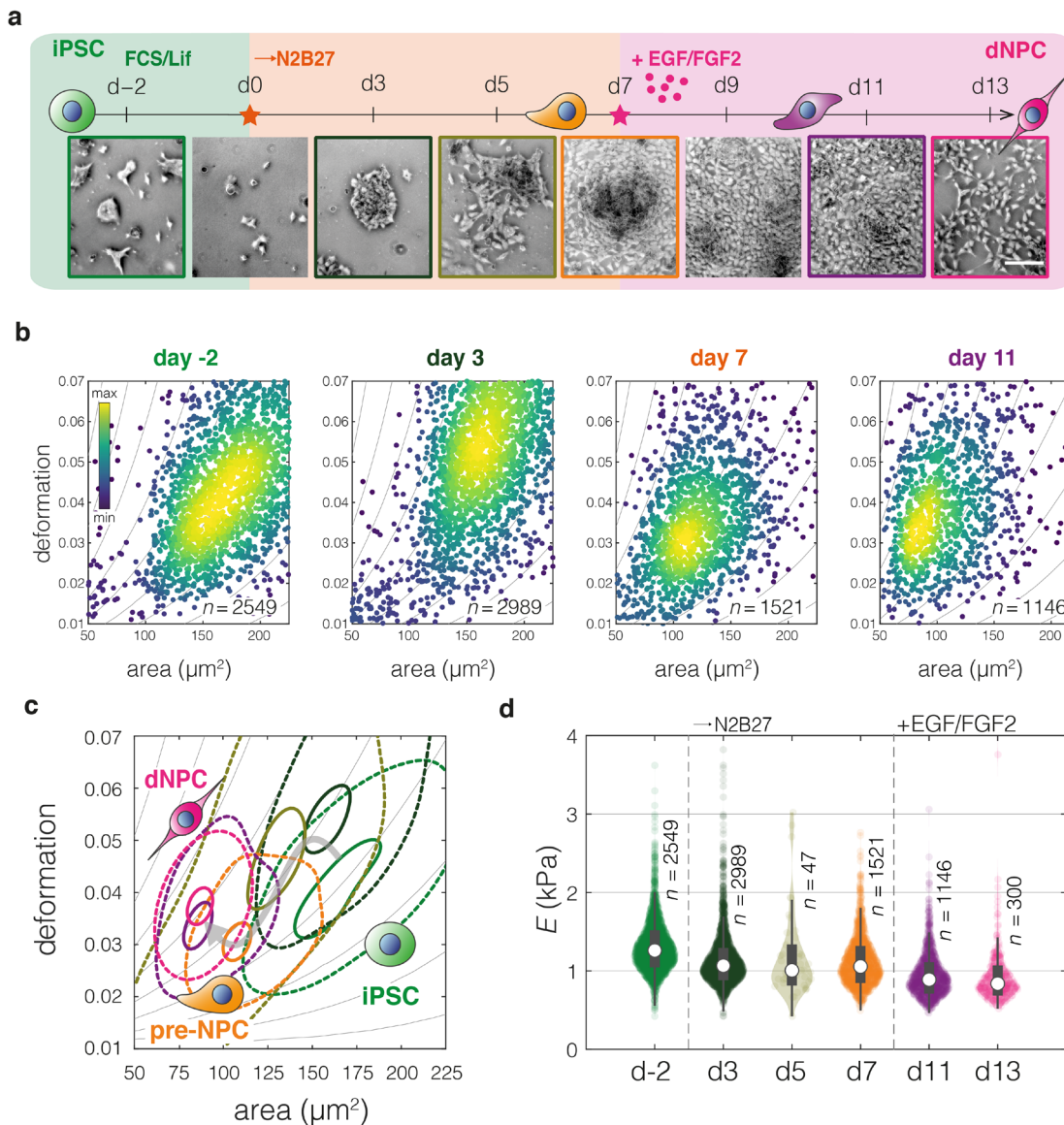


**Figure 4.9 | iPSCs become progressively softer during differentiation towards neural lineage.** **a**, Time course of neural differentiation of iPSCs. Phase contrast images show representative cell morphologies. Scale bar represents  $200 \mu\text{m}$ . **b**, Deformation–area scatter plots of cell populations characterized by RT-DC on differentiation days -2, 3, 7, and 11. Color map indicates event density. **c**, Contour plots of cell populations characterized on differentiation days -2, 3, 5, 7, 11, and 13. Solid lines delineate 95% density and dashed lines 50% density. The populations are color-coded as in **a**. **d**, Violin plots of Young's moduli extracted for cell populations in **c**. Boxes on top of the violins extend from 25th to 75th percentiles, with a dot at the median, whiskers indicate  $1.5 \times \text{IQR}$ . This figure is modified from Urbanska *et al.*<sup>378</sup>.

The successful differentiation towards neural precursors was confirmed by verifying the expression of Nanog, Sox2, and Pax6 via immunofluorescence. dNPCs showed loss of pluripotency marker Nanog, maintained expression of Sox2 characteristic of the pluripotent state as well as neural fate, and acquired expression of neural transcription factor Pax6 (**Figure 4.10**). This combination of markers confirms successful guiding towards the neural lineage during differentiation. The comparison of the mechanical phenotype of terminal states of fNPCs reprogramming and neural differentiation of iPSCs illustrates that the two processes mirror each other mechanically (**Figure 4.11a**).

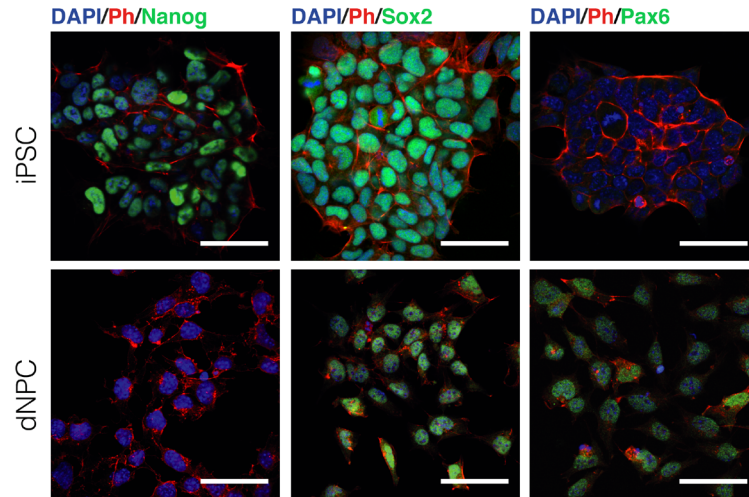


**Figure 4.10 | The differentiated NPCs lose Nanog, maintain Sox2, and acquire Pax6 expression.** Immunofluorescence staining for Nanog, Sox2 and Pax6 at the beginning (iPSC) and end (dNPC) of the differentiation. Ph, Phalloidin. Scale bars represent 50  $\mu\text{m}$ . This figure is adapted from Urbanska *et al.*<sup>378</sup>.

#### 4.1.5. The closer to the pluripotency, the higher the cell stiffness

Finally, I collected the mechanical characterization results obtained for various cell states spanning developmental stages from naïve pluripotency (represented by ESCs and iPSCs, and corresponding to E3.5) to early neural commitment (represented by fNPCs and dNPCs corresponding to E15.5) in mouse. Ordering cell states according to their decreasing commitment along neural lineage and increasing pluripotency revealed that measured cell stiffness increases with increasingly pluripotent character of cells (**Figure 4.11b**).

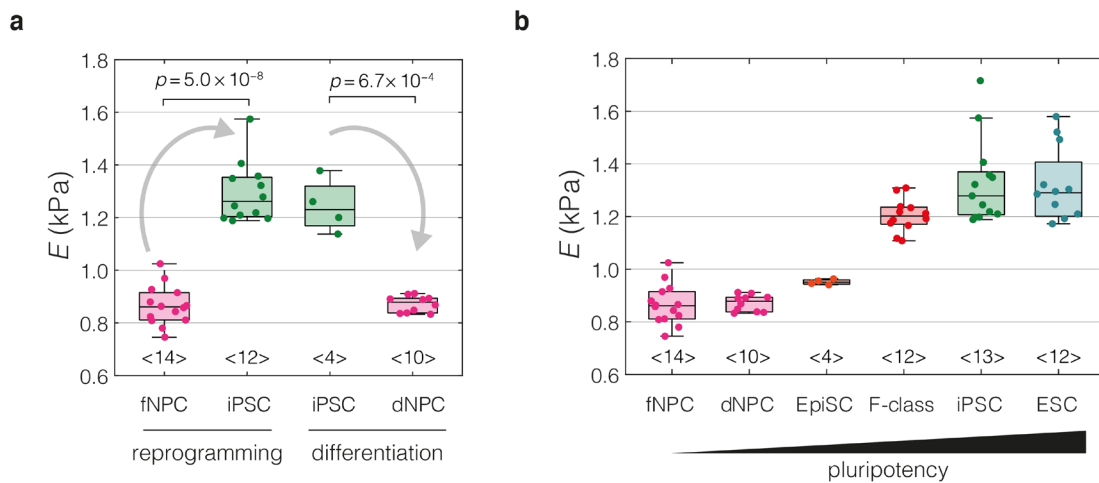


**Figure 4.11 | Mechanical phenotype along the neural progenitors-pluripotency axis.** **a**, Young's moduli derived from multiple RT-DC experiments for the terminal stages of reprogramming and differentiation. **b**, Young's moduli derived from multiple RT-DC measurements for cells representing different developmental stages from early neural commitment to pluripotency. Data points represent medians of individual RT-DC measurements, the numbers of measurements are indicated at the bottom of the plots. Boxes extend from the 25th to 75th percentiles, with a line at the median, whiskers indicate  $1.5 \times \text{IQR}$ . Statistical analysis was performed using linear mixed-effects models. This figure is modified from Urbanska *et al.*<sup>378</sup>.

## 4.2. Discussion

Intrinsic and extrinsic mechanical cues are gaining recognition as prominent contributors to cell and tissue morphogenesis<sup>142,414–416</sup>. To deepen our understanding of the relationship between cell mechanics and cell fate and of the impact of cell mechanics on development, detailed studies on biomechanical aspects of cell identity changes are indispensable. To this end, I performed population-scale mechanical characterization of cells during cell fate transitions from early neural commitment to pluripotency in an *in vitro* setting. I found that fNPCs acquire stiffer phenotype while being reprogrammed towards iPSCs (**Figure 4.2**), and, conversely, iPSCs become more compliant and retrieve the fNPC phenotype during neural differentiation (**Figure 4.9**). I further showed that mechanically different subpopulations are present at intermediate reprogramming stages, and that transgene-dependent F-class cells are softer than ESC-like iPSCs (**Figure 4.6**). The majority of mechanical measurements were performed on suspended cells using RT-DC, however, the stiffer phenotype of iPSCs as compared to fNPCs was confirmed by AFM indentation measurements on rounded as well as adherent cells (**Figure 4.5**). By comparing a spectrum of cell types along the neural commitment — from the most specified fNPCs through EpiSCs and F-class cells to the pluripotent iPSCs and ESCs — we identified that the closer the cells are to the pluripotent state, the stiffer their phenotype (**Figure 4.11b**).

Contrary to the observations presented here, murine ESCs have been reported to become stiffer during differentiation in several previous studies<sup>1,70,73</sup>. In contrast to differentiation towards neural lineage performed here, Pillarisetti *et al.*<sup>70</sup> induced mesodermal differentiation, whereas Chowdhury *et al.*<sup>73</sup> and Gossett *et al.*<sup>1</sup> investigated heterogeneous population of differentiated progeny consigning, most likely, of cells from all three germ layers. Furthermore, the authors employed different methods for probing cell stiffness. Chowdhury *et al.*<sup>73</sup> used optical magnetic twisting cytometry that relies on twisting magnetic beads anchored to the cytoskeleton via focal adhesions. Such probing modality characterizes local rather than global cell mechanical properties, and can be influenced by the differences in focal adhesion formation between measured cell types. Pillarisetti *et al.*<sup>70</sup> employed AFM to probe mechanical changes in differentiated cells in adherent cell exclusively. Gossett *et al.*<sup>1</sup> performed measurements with DC, which, same as RT-DC, relies on measuring single cells in suspension, but operates at much faster timescales and applies higher stress. These operation characteristics decrease the sensitivity of the method to cytoskeletal contributions, while potentially increasing chances of capturing nuclear contributions (see **Chapter 3**). Cell stiffening during differentiation observed by DC could therefore stem from previously reported increase in nuclear stiffness during differentiation<sup>417</sup>.

Some other reports, however, point towards softening of PSCs in early differentiation. Two recent studies showed that membrane tension drop, concomitant with decreased RhoA activity and reduced membrane-to-cortex attachment, is necessary for early differentiation of ESCs<sup>134,135</sup>. Even though the authors did not measure whole-cell stiffness directly, the drop in membrane tension and, even more so, the drop in RhoA activity, are indicative of decreased cell stiffness — active RhoA promotes

actomyosin contractility that increases cortical tension and overall cell stiffness<sup>33</sup>. Furthermore, other studies performed in parallel in our group revealed that early differentiation of PSCs can lead to decrease in cell stiffness. Firstly, ESC differentiation towards mesoderm and ectoderm was characterized in RT-DC using T-Brachyury and Sox1 reporters, respectively. Both lineages acquired softer phenotype during differentiation, with ectodermal fate — corresponding to neural differentiation — being associated to softer cell phenotype than mesodermal fate<sup>137</sup>. Secondly, induction of EMT in EpiSCs, that corresponds to differentiation of pluripotent EpiSCs towards mesoderm, was shown to result in decreased Young's modulus of cells (Dr. Maria Winzi, unpublished data).

The direction of stiffness change during differentiation is likely influenced by the specific fate towards which a cell differentiates. Mechanical properties of tissues as well as individual cells are connected with their origin. For example, load-bearing tissues such as bone, cartilage or skeletal muscle are characterized by high Young's moduli, while other tissues such as breast or brain have relatively low stiffness<sup>418</sup>. On the level of single cells, osteocytes were shown to be much stiffer than chondrocytes or adipocytes<sup>77,419</sup>, and glial and neuron cells are much more compliant than other eucaryotic cells<sup>420</sup>. We hypothesize that cells from the early embryo exhibit high stiffness that provides for robustness and resistance to mechanical forces that promotes survival. The differentiating cells at gastrulation-stage embryo need to reorganize and migrate to new locations, for which cell softening could be of benefit as demonstrated, for example, for cancer metastasis<sup>7,44,103</sup>. Finally, the decreased stiffness of fNPCs corresponds well with the comparatively low stiffness reported for brain tissue<sup>418</sup> and neural cells<sup>420</sup>.

The molecular and structural determinants underlying mechanical differences between iPSCs and fNPCs observed in this study remain to be determined in the future. Mechanical properties of cells are influenced by the organization of cytoskeletal networks, with actin cytoskeleton and its Rho-regulated contractility playing a prominent role<sup>31–33,155</sup>. Thus, evaluation of relative F-actin levels by confocal microscopy or flow cytometry assay, imaging of phospho-myosin, as well as evaluation of Rho activity using bulk pull-down assays<sup>421</sup> or fluorescence sensors<sup>422</sup> could provide first insights into potential origins of mechanical differences. Furthermore, differences in nuclear-to-cytoplasmic ratio and cytoplasmic mass density between NPCs and iPSCs could be tested. Further mechanistic insights could be acquired by evaluating activity of the transcriptional co-regulators YAP/TAZ. YAP and TAZ are known for their role in mechanotransduction and were shown to respond to cell shape and the changes in the actin cytoskeleton tension<sup>423</sup>. When activated, YAP and TAZ change their localization from cytoplasmic to nuclear<sup>424</sup>. YAP has been shown to play a role in rigidity-dependent differentiation of human iPSC towards the neural lineage<sup>425,426</sup> and in cell fate specification in the preimplantation stage mouse embryo<sup>131,427</sup>. On a global scale, RNA sequencing or proteomic analysis of iPSCs and fNPCs could be performed to screen for potential molecular targets involved in mechanical phenotype regulation. Of note, previously published microarray analysis of F-class cells versus iPSCs was used in the project aimed at identification of universal cell mechanics regulator presented in **Chapter 5**.

Cell stiffness is an inherent property, and as such could be used as a label-free marker of cell state to distinguish pluripotent from differentiated cells<sup>12</sup> (see also **Section 1.1.3**). Procedures currently used for derivation of human iPSCs are often inefficient and yield a heterogeneous populations of cells that include unreprogrammed source cells and reprogramming intermediates<sup>428</sup>. Thus, isolation of fully reprogrammed bona fide iPSCs is crucial for downstream differentiation and administration into patients. In turn, after the differentiation, it is important to exclude undifferentiated iPSCs from the therapeutic sample because of potential tumorigenicity of pluripotent cells<sup>429,430</sup>. Biochemical markers associated with pluripotency can be used for this purpose, however, most of them require either sacrifice of cells (e.g. alkaline phosphatase staining<sup>431</sup>) or introduction of a labeling agent (antibodies against surface markers such as SSEA1 in mice<sup>411</sup> or SSEA4 and TRA-1-60 in human<sup>428</sup>). In the light of our results, cell stiffness emerges as a marker for selecting fully reprogrammed, pluripotent cells or excluding incompletely differentiated cells from heterogeneous populations. Such cell enrichment/depletion could be achieved with the aid of mechanics-based cell sorters such as SSAW-based soRT-FDC<sup>313</sup> introduced in **Chapter 2**.

As introduced in **Section 1.2.4**, mechanical properties of cells, apart from being an indicator of cell state, can also play an active role in guiding developmental processes. For example, it has recently been shown that cell contractility drives the first lineage decision in the developing mouse embryo<sup>427</sup>. Additionally, the stiffness of individual cells contributes to the local microenvironment stiffness perceived by neighboring cells, and through that can influence the fate of cells<sup>432–435</sup>, or guide cell migration in the developing embryo<sup>139,140</sup>. Mechanical characterization of cells at different stages of embryonic development will aid in understanding of local mechanical landscapes in the embryo. In the future, with the aid of non-invasive techniques for measurement of cell and tissue mechanics such as Brillouin microscopy<sup>305</sup> and stem-cell-derived reconstitution models that recapitulate mammalian embryogenesis<sup>436–438</sup>, the cell-level findings obtained in the presented study could be verified *in situ* in the context of developing 3D structures.

Taken together, the findings presented in this chapter establish a defined mechanical phenotype associated with the state of pluripotency that is shared between ESCs and iPSCs, and could be used as a marker of the pluripotent cell state. With respect to NPCs, this phenotype appears stiff. Further studies covering differentiation towards other lineages *in vitro*, as well as *in situ* mechanical characterization of cells in embryos or reconstitution models would be advantageous for creating a complete mechanical landscape of murine stem cells during early development. In the long term, such efforts will deepen our understanding of the role of cell mechanics in cell fate commitment and embryogenesis.



### 4.3. Key conclusions

- fNPCs become progressively stiffer during reprogramming to pluripotency.
- Mechanical phenotype of iPSCs is comparable to that of ESCs, suggesting that it could be used as a marker of pluripotency.
- Alternative pluripotent cell state called F-class, maintained by exogenous expression of OSKM factors, is softer than ESC-like iPSCs.
- With the aid of SSEA1/CD24 surface marker staining, mechanical subpopulations of cells corresponding to differently advanced cells are revealed at intermediate reprogramming stages.
- Neural differentiation of iPSCs mechanically mirrors the reprogramming process, in that iPSCs become progressively softer and regain the phenotype of fNPCs.
- Ordering all characterized cell states from the most advanced developmentally fNPCs to the most pluripotent iPSCs/ESCs reveals that the more pluripotent the cells are, the stiffer their mechanical phenotype.

## 4.4. Materials and methods

### 4.4.1. Cell Culture

fNPCs and ESCs were a kind gift of Prof. Konstantinos Anastasiadis, TU Dresden. Tet-On system for dox-inducible expression of OSKM factors in fNPCs was established by Dr. Katrin Neuman<sup>439</sup>.

#### *fNPCs*

fNPCs were originally obtained from the telencephalon of E15.5 mouse embryos (strain C57BL/6J)<sup>439</sup> and expanded in NPC medium (Euromed-N (Biozol, Germany), 1× N2 supplement (Gibco, Thermo Fisher Scientific, MA, USA), 0.5× B27 supplement (Gibco), 2 mM L-glutamine, 10 ng ml<sup>-1</sup> EGF (Peprotech), 10 ng ml<sup>-1</sup> recombinant FGF2 (MPI-CBG, Dresden, Germany)) on culture-grade dishes coated with laminin (2 µg ml<sup>-1</sup>, Sigma Aldrich). Passaging was performed using accutase (Sigma Aldrich).

#### *ESCs*

ESCs were isolated from E3.5 blastocysts (strain C57BL/6J) according to previously established procedures<sup>439</sup> and cultured on 0.1% gelatin-coated dishes in FCS/LIF medium (DMEM+Glutamax (Gibco), 15% fetal calf serum (Pansera ES, PAN-Biotech), 100 µM β-mercaptoethanol (PAN-Biotech, Germany), 2 mM L-glutamine (Gibco), 1 mM sodium pyruvate (Gibco), 1x non-essential amino acids (Gibco), 15 ng ml<sup>-1</sup> recombinant LIF (MPI- CBG)) with or without a mixture of MEK inhibitor PD0325901 (1 µM) and GSK3 inhibitor CH99021 (3 µM) known as 2i. Subculturing was performed using 0.1% trypsin solution.

#### *EpiSCs*

EpiSCs were derived from ESCs according to previously published protocol<sup>440</sup> and cultured in N2B27 medium (50% DMEM/F12, 50% Neurobasal medium (Gibco), 0.5× B27 supplement (Gibco), 0.5× N2 supplement (Gibco), 2 mM L-glutamine (Gibco), 100 µM β-mercaptoethanol (PAN-Biotech)) supplemented with 12 ng ml<sup>-1</sup> recombinant FGF2 (MPI-CBG) and 30 ng ml<sup>-1</sup> Activin A (MPI-CBG) on dishes coated with fibronectin (10 µg ml<sup>-1</sup>, Merck Milipore, MA, USA). Passaging was performed using accutase (Sigma Aldrich).

### 4.4.2. Reprogramming and differentiation

#### *Reprogramming of fNPCs into iPSCs*

fNPCs with integrated Tet-On cassette for expression of OSKM factors (irtTA-neo PB-tetCMV-OSKM) were seeded on dishes coated with laminin at a density of 35–70x 10<sup>5</sup> per cm<sup>2</sup> in NPC medium with 1 µg ml<sup>-1</sup> of dox (Sigma Aldrich) to initiate induction of OSKM expression. The NPC medium was replaced with FCS/LIF medium two days after the beginning of reprogramming and refreshed daily. For stabilizing of iPSCs, a mixture of MEK inhibitor PD0325901 (1 µM) and the GSK3 inhibitor

CH99021 (3  $\mu$ M) known as 2i was supplemented to the medium on day 14. From day 17 on, dox was removed from the culture medium. For the reprogramming towards F-class, 2i was not added and dox was added to the culture medium continuously throughout the reprogramming process. The obtained iPSCs were cultured on gelatin-coated dishes.

#### *Neural differentiation of iPSCs*

For neural differentiation, iPSCs were seeded on 0.1% gelatin-coated dishes at a density of 5–10x 10<sup>5</sup> per cm<sup>2</sup> in FCS/LIF medium without 2i. After overnight incubation, to allow for cell adhesion, medium was exchanged to N2B27 and refreshed daily. From day 7 on, the culture was supplemented with 10 ng ml<sup>-1</sup> of EGF (Peprotech) and 10 ng ml<sup>-1</sup> recombinant FGF2 (MPI-CBG). Towards the end of differentiation (day 10 or 11), cells were detached using accutase and cultured over a few more passages in EGF/FGF2-supplemented N2B27 medium on gelatin-coated dishes.

### 4.4.3. Differential expression analysis and immunofluorescent staining

#### *Quantitative reverse transcription polymerase chain reaction (qRT-PCR)*

For the qRT-PCR analysis, total RNA was isolated using the Aurum Total RNA Mini Kit (Bio-Rad, CA, USA), with a DNase treatment on the column. For each qRT-PCR reaction 1  $\mu$ g of RNA was reverse transcribed using the High-Capacity cDNA Reverse Transcription Kit (Thermo Fisher Scientific). SYBR Green-based quantitative PCRs were run with the Absolute qPCR Mix (Thermo Fisher Scientific) on an Mx3000 qRT-PCR system (Stratagene, CA, USA). Measured transcript levels were normalized to *Tbp*. Samples were run in duplicates and three measurement replicates with samples originating from different passages were performed for each conditions. For primer sequences and lengths of obtained products see **Table 4.1**. The calculated fold change in expression corresponds to log<sub>2</sub> of the ratio of the expression levels in iPSCs to the expression levels in the reference stage (fNPCs).

**Table 4.1 | List of primers used for qRT-PCR analysis.**

gene name	sense primer (5'→3')	antisense primer (3'→5')	product length
<i>Ecad</i>	CGACCGGAAGTGACTCGAAA	TGTCCGCCAGCTTCTTGAAT	289 bp
<i>Ncad</i>	CCGAGGCCCGCTATTGTGTTA	CACCAGAAGCCTCCACAGAC	287 bp
<i>Nestin</i>	GCAGGAGAAGCAGGGTCT	AGGTGCTGGTCCCTCTGGT	228 bp
<i>Nanog</i>	GGAAGCAGAAGATGCGGACT	ATGCGTTCACCAGATAGCCC	291 bp
<i>Oct4* (endog.)</i>	TGGAAGCCCCACTTCACCACA	AGCATCCCCAGGGAGGGCTG	131 bp
<i>Sox1</i>	CCTTGCTAGAAGTTGCGGTC	TCACTCAGGGCTGAACTGTG	186 bp
<i>Vim</i>	GGATCAGCTACCAACGACA	AAGGTCAAGACGTGCCAGAG	178 bp
<i>Tbp</i>	CTTCCTGCCACAATGTCACAG	CCTTTCATGCTTGCTTCTCTG	118 bp

*Immunofluorescence staining*

For staining,  $50 \times 10^4$  cells per well were seeded in ibiTreat 8 well  $\mu$ -slides (ibidi, Germany), cultured for 1–2 days and fixed using 4% paraformaldehyde for 10 min. For permeabilization and blocking, cells were incubated in PBS with 0.3% Triton-X and 10% fetal calf serum for 30 min. Next, primary antibody staining—Nanog (1:200, RCAB002P-F, Reprocell, Japan), Sox2 (1:100, AB5603, Merck Millipore) and Pax6 (1:10, DSHB, TX, USA)—was performed overnight at 4°C in staining solution (0.3% Triton-X in PBS). Samples were washed several times with PBS and the secondary staining was performed using the staining solution containing Cy2-conjugated donkey secondary antibodies (1:500, Jackson ImmunoResearch, PA, USA), DAPI (1:5000, D1306, Molecular Probes, OR, USA), and Phalloidin-TRITC (1:500, P1951, Sigma Aldrich) for 30 min at room temperature. Imaging was performed on an inverted confocal laser scanning microscope (LSM700, Zeiss) using a Plan-Apochromat 20 $\times$ /0.8 air objective (Zeiss).

**4.4.4. Mechanical characterization of cells***RT-DC measurements*

Mechanical characterization of cells using RT-DC was performed at room temperature using 0.5% MC measurement buffer and 20  $\mu$ m chip according to procedures described in detail in **Chapter 2**. For plotting and further analysis, data were filtered for 50–500  $\mu$ m<sup>2</sup> cell area and 1.00–1.05 area ratio. Area ratio is defined as the ratio between the area enclosed by the convex hull of the contour and the area enclosed by the contour. Contour plots were generated using *Shape-Out 1.0.1* (available at <https://github.com/ZELLMECHANIK-DRESDEN/ShapeOut>). Young's modulus values were derived using lookup table from numerical simulations for an elastic solid<sup>317</sup> implemented in *Shape-Out 1.0.1*.

*RT-FDC measurements with fluorescence staining*

For simultaneous evaluation of surface marker expression and mechanical properties of single cells, an RT-FDC setup with integrated fluorescence detection was used<sup>312</sup>. Prior to loading into setup, detached cells were stained for 10 minutes with Anti-SSEA-1-APC (1:10, REA321, Miltenyi Biotec, Germany) and CD24-FITC (1:10, M1/69, Miltenyi Biotec) antibodies in a 0.3% BSA solution in PBS. Fluorescence was collected in channels 1 (excitation with 488 nm laser / emission band pass filter 525/50 nm) and channel 3 (excitation with 640 nm laser / emission band pass filter 700/75 nm). Peak maxima served as an estimate of fluorescence intensity and were used for gating and plotting.

*Atomic force microscopy (AFM)*

AFM indentation experiments were performed using the Nanowizard 1 and 4 setups (JPK Instruments, Germany). Tip-less silicone cantilevers with a force constant in the range 0.35–0.45 N m<sup>-1</sup> (Arrow™ TL1, Nanoworld, Switzerland) were equipped with a 5  $\mu$ m polystyrene beads (microParticles GmbH)

each and used as indenters. Cantilever calibration was performed with the thermal noise method. Measurements were performed in CO<sub>2</sub>-independent medium (Gibco) at a constant temperature of 37°C maintained using a petri dish heater (JPK Instruments). For measurements on rounded cells, cells were detached using 0.1% trypsin solution, placed onto a glass bottom petri dish (FD35100, World Precision Instruments, FL, USA) and allowed to settle onto the surface for approximately 10 minutes ahead of the measurements. For measurements of adherent cells, cells were plated on glass bottom petri dishes and allowed to adhere overnight. Indentation was performed roughly on the cell center with the extension speed of 5 μm s<sup>-1</sup> to a maximum force of 2 nN. Force–distance curves were converted into force–indentation curves and analyzed with the JPK data processing software (JPK Instruments) using Sneddon’s modification of the Hertz model for a spherical indenter<sup>442</sup>. The force-indentation curves were fitted to a maximum indentation of 1.5 μm and 0.5 Poisson ratio was assumed. For rounded cells, the obtained Young’s modulus values were corrected with (i) an effective probe radius for the case of contact between two spherical objects, and (ii) a simplified double contact model<sup>443</sup> accounting for compression arising from contact with the substrate at the bottom part of the cell. The obtained Young’s modulus values correspond to so-called effective/apparent values because some of the theoretical assumptions used for the implemented models are not fully satisfied in our setup; for example, we cannot assume that measured cells are fully homogenous and purely elastic.

#### *Statistical analysis*

For statistical analysis of multiple experiment replicates, linear mixed-effects models were implemented using the lme4-package in R (R Core Team, Austria). The model of choice included two fixed effects and one random effect. The fixed effects were attributed to the sample type and the experimental series; and the random effect was attributed to the measurement day. Both slope and intercept were set free for fitting. *p*-values were obtained by performing a likelihood ratio test comparing the model with a null model lacking the fixed effect attributed to the cell type. For statistical analysis of individual experiments, two-sided Wilcoxon rank sum test was implemented in MatLab (MATLAB R2020a, The MathWorks, MA, United States).

Chapter 5 is based on and contains materials adapted from the following preprint:

M. Urbanska\*, Y. Ge\*, M. Winzi, S. Abuhattum, M. Herbig, M. Kräter, N. Toepfner, J. Durgan, O. Florey, M. Dori, F. Calegari, F.-N. Lolo, M.A. del Pozo, A. Taubenberger, C.V. Cannistraci, and J. Guck (2021) **De novo identification of universal cell mechanics regulators**, *bioRxiv*, 2021.04.26.441418.

DOI: 10.1101/2021.04.26.441411

Own contributions: investigation (mechanical characterization of cells for carcinoma and iPSCs datasets, genetic perturbation experiments), project administration, data curation, formal analysis (analysis of all mechanical characterization data and support with computational analysis), visualization, writing – original draft preparation, writing – review and editing

\*equal contributions

## — Chapter 5 —

# Data-driven approach for *de novo* identification of cell mechanics regulators

Characterization of single-cell mechanical properties during cell state transitions, such as cell (de-)differentiation along neural lineage discussed in the previous chapter, brings valuable biophysical insights into cellular morphogenesis. However, to be able to thoroughly explore the impact of cell mechanics on physiological and pathological processes, it is necessary to not only characterize the mechanical properties of cells, but also to be able to control them<sup>294</sup>. Several structural elements of cells and regulatory pathways have been identified to contribute to mechanical properties of cells, with actomyosin cytoskeleton and its Rho-regulated contractility appearing as the most prominent players<sup>33</sup> (see **Section 1.3.1**). Targeting cytoskeletal structures when attempting to alter the mechanical properties of cells may, however, not be practical, as disruption of cytoskeleton can compromise overall cell integrity and function. Thus, it is desirable to identify novel targets that would enable subtle ways of intervening with cell stiffness.

Most of our knowledge about the molecular origins of mechanical properties of cells has been derived from chemical or genetic perturbations targeting structures known *a priori*. Identification of novel targets is a challenging task and can be approached by performing large-scale screening using RNA interference<sup>157,312,444</sup> or small-molecule compound libraries. Alternatively, a reverse-engineered mechanomics approach can be undertaken, in which omic profile changes accompanying alterations in mechanical phenotype are used for prediction of genes involved in the regulation of mechanical properties. The term mechanomics has, so far, been used in context of various studies related to the field of mechanobiology. For example, it was used to refer to changes in omics profiles in response to a mechanical stimuli such as shear flow, tensile stretch, or mechanical compression<sup>445–447</sup>, or to describe the entirety of the mechanical forces acting on or within cells<sup>448–452</sup>. Finally, mechanomics has also been used to address omics changes that accompany alterations of the mechanical properties of cells<sup>453,454</sup> — a context which is used in this study.

Within the framework of this project, we developed a system-level inference strategy that enables hypothesis-free identification of genes involved in the regulation of mechanical phenotype — an approach that we refer to as mechanomics. This approach relies on machine-learning based discriminative network analysis termed PC-corr<sup>453</sup> applied to transcriptomic signatures related to mechanical phenotype changes. First, the PC-corr results obtained for two datasets are overlaid to predict a network of target genes with putative roles in the regulation of mechanical phenotype. Next,

the identified genes are validated *in silico* on four further datasets. Finally, the ability of the top scoring gene to modify mechanical properties of cells is tested by following the effects of perturbing its expression. The computational approach for the identification of target genes was established by Dr. Yan Ge and Prof. Carlo Cannistraci (Biotec, TU Dresden). I supported the analysis, performed the mechanical characterization experiments and the experimental validation of the top scoring gene on cell mechanics.

## 5.1. Results

### 5.1.1. An overview of the mechanomics approach

The full pipeline of our mechanomics approach consists of the following step: data curation, target prediction, computational validation and experimental validation of the predicted targets (**Figure 5.1**).

In the data curation step, transcriptomic datasets encompassing two or more mechanically distinct cell states are collected (**Figure 5.1**). In the current implementation, six datasets originating from various mouse and human tissues, and encompassing processes from stem cell development to cancer progression, were collected (**Table 5.1**). RT-DC is employed as a method of choice for mechanical characterization of respective cell states. Due to its high throughput, RT-DC is perfectly suited for exploring a large variety of systems and states. Gene expression datasets, generated either by RNA sequencing (RNAseq) or microarray analysis, were retrieved from online databases (**Table 5.1**). In the target prediction step, selected transcriptomic datasets are used to identify a conserved network module of putative target genes involved in the regulation of cell mechanical phenotype (**Figure 5.1b**). To this end, an inference approach termed PC-corr<sup>453</sup> is implemented. PC-corr predicts a network of features that explain the sample segregation along the principal component (PC) associated with a phenotypic change. An overlay of PC-corr analysis performed separately on selected datasets (here two) is used to derive a conserved module of genes that are potentially involved in the regulation of cell mechanics. The ability of the obtained target genes to correctly classify soft and stiff cell states is next tested *in silico* on the validation datasets (**Figure 5.1c**) using the area under the curve of the receiver-operator characteristics (AUC-ROC)<sup>455</sup>. The best scoring targets are validated experimentally by monitoring mechanical phenotype changes upon their overexpression and downregulation in the cells of choice (**Figure 5.1d**).



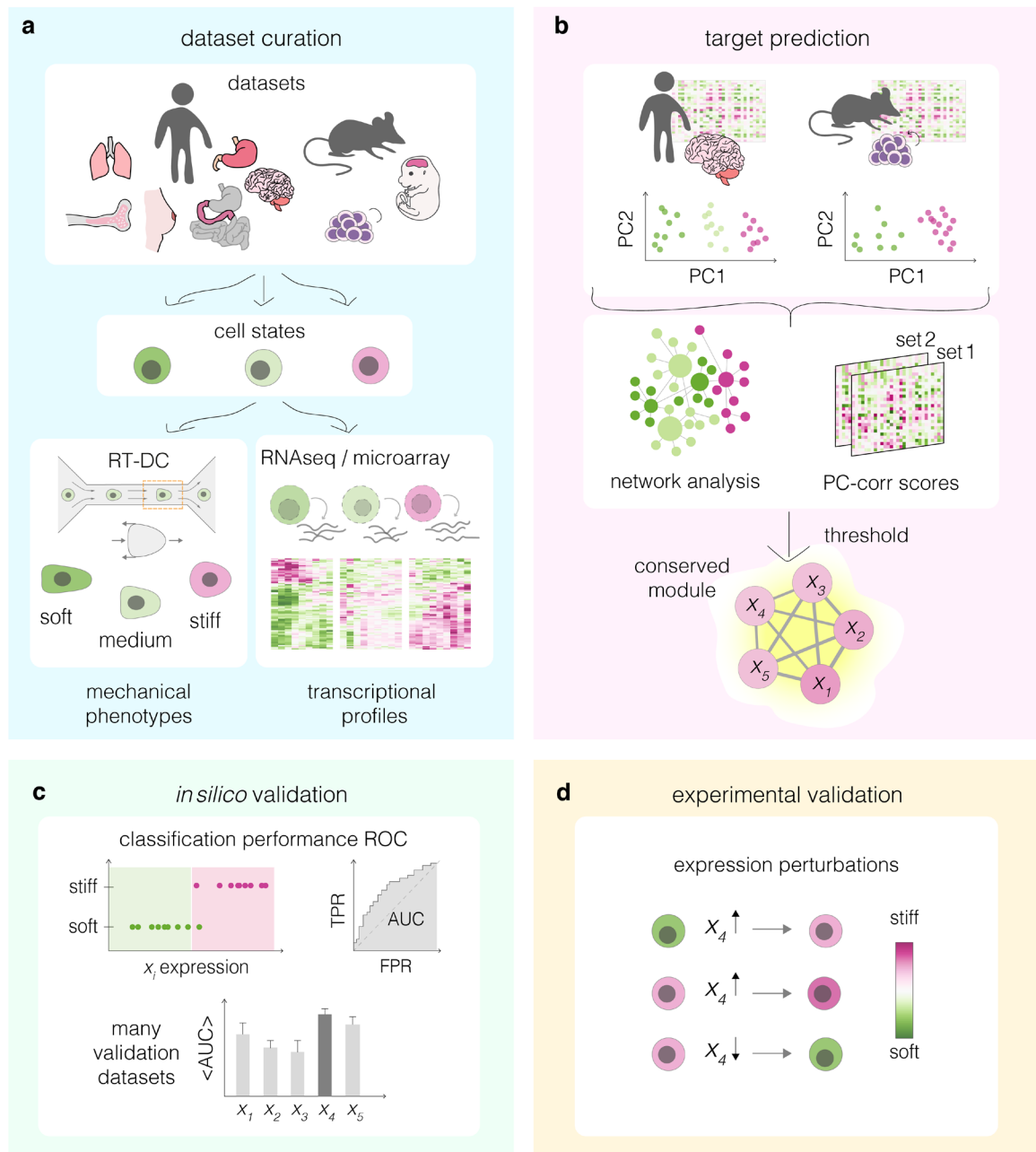


**Figure 5.1 | Overview of a mechanomics approach for *de novo* identification of genes involved in cell mechanics regulation.** **a**, Data curation. Datasets originating from different biological systems encompassing cell states with distinct mechanical phenotypes, as characterized by RT-DC, and associated transcriptomics profiles are collected. **b**, Target prediction. A subset of collected datasets is used to perform machine learning-based network analysis on transcriptomic data and identify conserved module of genes associated with cell mechanics changes. PC – principal component. **c**, *In silico* validation. The classification performance of individual genes from module identified in **b** is evaluated on remaining datasets. TPR – true positive rate, FPR – false positive rate, ROC – receiver operating characteristic, AUC – area under the curve. **d**, Experimental validation. Targets with highest classification performance *in silico* are verified experimentally in perturbation experiments. This figure is modified from Urbanska, Ge *et al.*<sup>456</sup>.

### 5.1.2. Model systems characterized by mechanical phenotype changes

To identify model systems that could be used for mechanomics analysis, we screened the projects ongoing in our group in search of cell transitions for which published transcriptomic data were available, and the concomitant mechanical phenotype changes were either already documented or implicated. A total of six datasets were curated (**Table 5.1**). The characterization of mechanical properties for all cell states in respective datasets was performed using RT-DC.

The first characterized dataset encompassed patient-derived glioblastoma cell lines cultured in conditions supporting different levels of activation of the STAT3-Ser/Hes3 signaling axis involved in cancer growth regulation<sup>457</sup>. As previously demonstrated, the glioblastoma cells are the stiffer, the lower the activation of STAT3-Ser/Hes3<sup>454</sup> (**Figure 5.2a**). The second system comprised small-cell and non-small-cell human carcinoma cell lines originating from three different tissues (intestine, lung, and stomach). Small-cell carcinomas have relatively small cell sizes, short doubling times and higher metastatic potential connected with poor clinical prognosis in patients<sup>458,459</sup>. Consistently across tissues, small cell-carcinoma cells had a lower Young's modulus compared to their non-small-cell counterparts (**Figure 5.2b**). In the third studied system, human hematopoietic stem and progenitor cells (HSPCs) isolated from mobilized peripheral blood showed a decrease in the Young's modulus upon treatment with a histone deacetylase inhibitor, valproic acid (VPA), that allows for extensive expansion of HSPCs *in vitro*<sup>460</sup> (**Figure 5.2c**). The fourth studied system included breast epithelium MCF10A cell lines bearing single-allele oncogenic mutations in the catalytic subunit alpha of the phosphatidylinositol-4,5-bisphosphate 3-kinase (PIK3CA)<sup>461</sup>. The studied mutations (E545K in exon 9 and H1047R in exon 20) lead to constitutive activation of PIK3CA and an aberrant triggering of the PI3K–AKT–mTOR signaling pathway that leads to growth factor-independent proliferation<sup>462,463</sup>. Both cell lines with PIK3CA mutation showed increased stiffness compared to wild type control (**Figure 5.2d**). The fifth system included two states of murine iPSCs; the fuzzy-colony forming state (F-class) and the bone-fide compact-colony forming state (C-class)<sup>378</sup> described in more detail in **Chapter 4**. C-class cells had higher Young's modulus than F-class cells (**Figure 5.2e**). Finally, we characterized three stages of developing neurons isolated from embryonic mouse brain<sup>464</sup>. The stiffness of the cells increased progressively with increasing neurogenic commitment; with differentiating progenitors (DPs) exhibiting a higher Young's modulus than proliferating progenitors (PPs) and newborn neurons (NNs) exhibiting the highest Young's modulus (**Figure 5.2f**). Area-deformation plots of RT-DC data used for Young's modulus extraction for all datasets are presented in **Supplementary Figure D.1**.

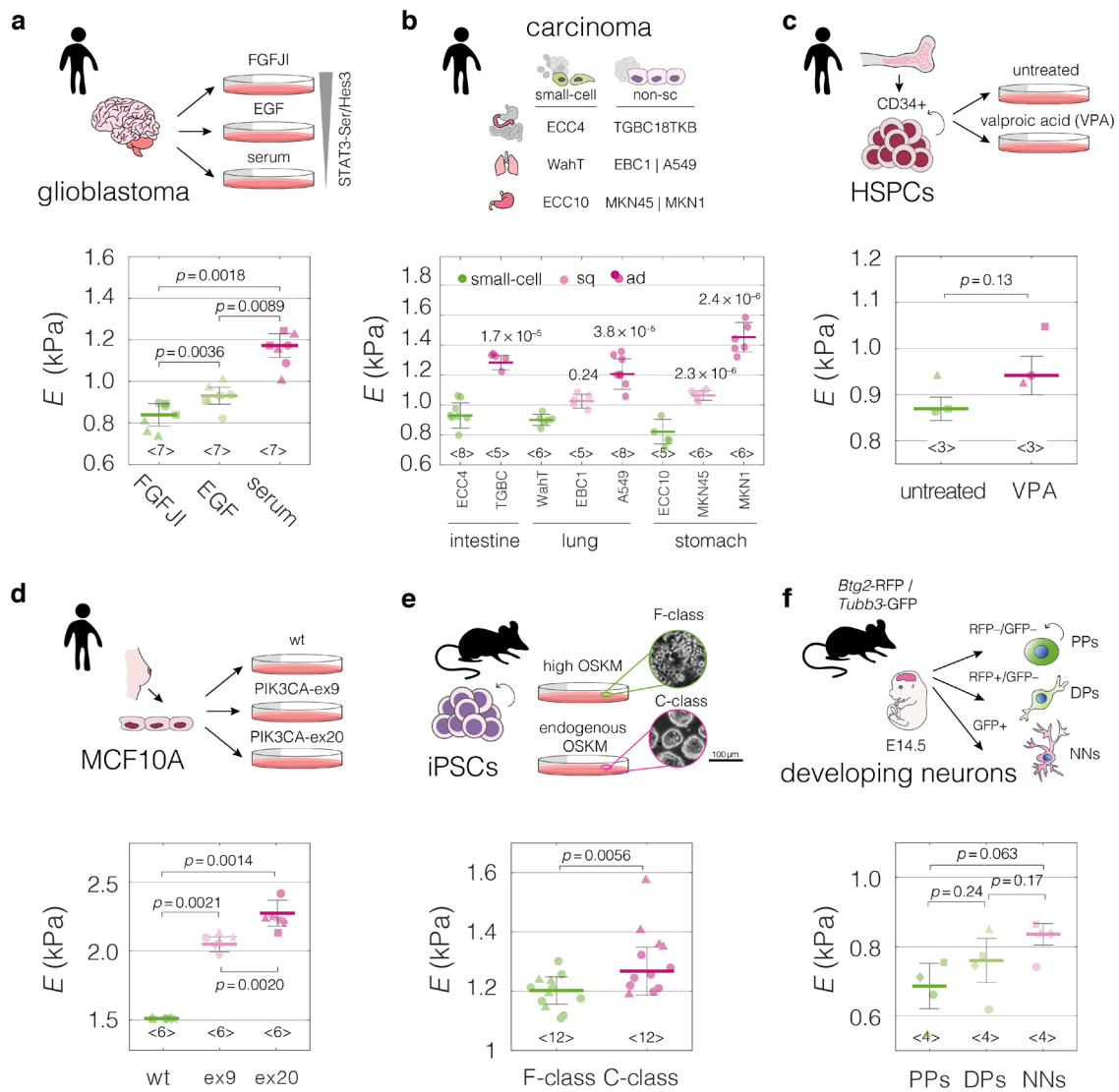


**Figure 5.2 | Mechanical characterization of divergent cell states in six systems used for the mechanomics study.** **a**, Human patient-derived glioblastoma cells with three distinct signaling states maintained by indicated culture conditions. **b**, Small-cell and non-small-cell (non-sc) human carcinoma cell types originating from intestine, lung, and stomach. Non-small cell carcinomas include squamous cell carcinomas (sq) and adenocarcinoma (ad). **c**, HSPCs mobilized from human bone marrow treated with valproic acid (VPA) or PBS as control. **d**, Human breast epithelium MCF10A cell lines bearing single-allele mutation in PIK3CA exon 9 (E545K) or exon 20 (H1047R), together with parental wild type (wt) as a control. **e**, F- and C-class murine iPSCs cultured in the presence or absence of doxycycline (dox) activating ectopic expression of OSKM factors. **f**, Developing neurons isolated from murine embryonic brains at three stages of neural commitment: proliferating progenitors (PPs), differentiating progenitors (DPs) and newborn neurons (NNs). Young's moduli,  $E$ , are derived from RT-DC measurements. In **a–f**, horizontal lines delineate medians with mean absolute deviation (MAD) as error, datapoints represent medians of individual replicates, numbers of replicates are indicated in the plots. Statistical analysis was performed using generalized linear mixed-effects model. Data in **a** and **e** were previously published in Urbanska *et al.*<sup>454</sup> (**Chapter 4**) and Poser *et al.*<sup>378</sup>, respectively. Data in **b** and **e** were acquired by myself; data in other panels were acquired by collaborators as outlined in **Materials and methods**. This figure is modified from Urbanska, Ge *et al.*<sup>456</sup>.

**Table 5.1 | Mechano-transcriptomic datasets used in this study.** P – prediction, V – validation, HT Seq – high-throughput RNA sequencing, CAGE – cap analysis gene expression. This table is adapted from Urbanska, Ge *et al.*<sup>456</sup>.

	general information			transcriptomic data				mechanics data		
	dataset name	used for	cell states	accession number	reference	technology	unique entries	total samples	method	reference
human	glioblastoma	P	FGFJI   EGF   serum	GEO: GSE77751	Poser <i>et al.</i> <sup>454</sup>	HT seq	39400	27	RT-DC	Poser <i>et al.</i> <sup>454</sup>
	carcinoma	V	small-cell   squamous   adeno *	DDBJ: DRA000991§	FANTOM consorptium <sup>465</sup>	CAGE	18821	8	RT-DC   AFM	this paper
	HSPCs	V	untreated   VPA-treated	GEO: GSE90552	Arulmozhivarman <i>et al.</i> <sup>460</sup>	HT seq	40101	6	RT-DC	this paper
	MCF10A	V	wt   PIK3CA mutation	GEO: GSE69822	Kiselev <i>et al.</i> <sup>466</sup>	HT seq	38508	6	RT-DC	this paper
mouse	iPSCs	P	F-class   C-class	GEO: GSE49940	Tonge <i>et al.</i> <sup>410</sup>	microarray	18118	28	RT-DC   AFM	Urbanska <i>et al.</i> <sup>378</sup>
	developing neurons	V	PPs   DPs   NNs	GEO: GSE51606	Apra <i>et al.</i> <sup>464</sup>	HT seq	21110	9	RT-DC	this paper

\*from 3 tissues: intestine, lung, stomach

§the data for samples of interest was extracted using TET tool from the FANTOM5 website <https://fantom.gsc.riken.jp/5/>

The six mechano-transcriptomic datasets collected for our study (**Table 5.1**) represent a diverse spectrum of systems that come from two different species (human and mouse), several tissues (brain, intestine, lung, stomach, bone marrow, breast, as well as embryonic tissue) and are associated with processes ranging from cancerogenic transformations to stem cell development. The high diversity of datasets is important for directing the analysis towards genes universally connected to the change in mechanical properties, rather than on genes specific for processes captured by individual datasets.

### 5.1.3. Discriminative network analysis on discovery datasets

After characterizing the mechanical phenotype of the cell states, we set out to identify genes associated with the mechanical phenotype changes across the different model systems. For this purpose, we applied a previously established method for inferring phenotype-associated network modules from omics datasets termed PC-Corr<sup>453</sup>. PC-corr was performed individually on two selected discovery datasets, and the results were combined to obtain a conserved module of genes.

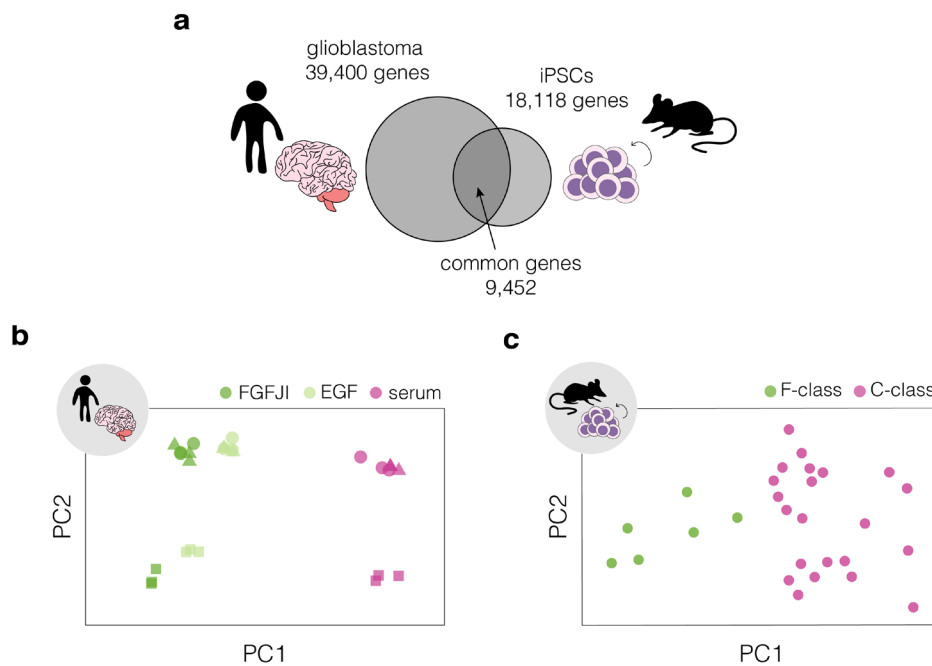


**Figure 5.3 | Separation of mechanically distinct cell states along PC axis in the discovery datasets.** a, Visualization of the intersection of glioblastoma and iPSC transcriptomes. Only the 9,452 intersecting genes were used for further analysis. b–c, PCA separation along two first principal components of the mechanically distinct cell states in the glioblastoma (b) and iPSC (c) datasets. This figure is modified from Urbanska, Ge *et al.*<sup>456</sup>.

For the network construction, we chose two datasets that originate from different species, concern unrelated biological processes, and have the highest number of samples included in the transcriptional analysis: human glioblastoma and murine iPSCs (**Table 5.1**). PC-corr analysis was performed on the discovery datasets individually using a subset of transcripts at which the two datasets intersect. First, the 9,452 unique genes from the intersection were used to perform PC analysis (PCA) (**Figure 5.3**).

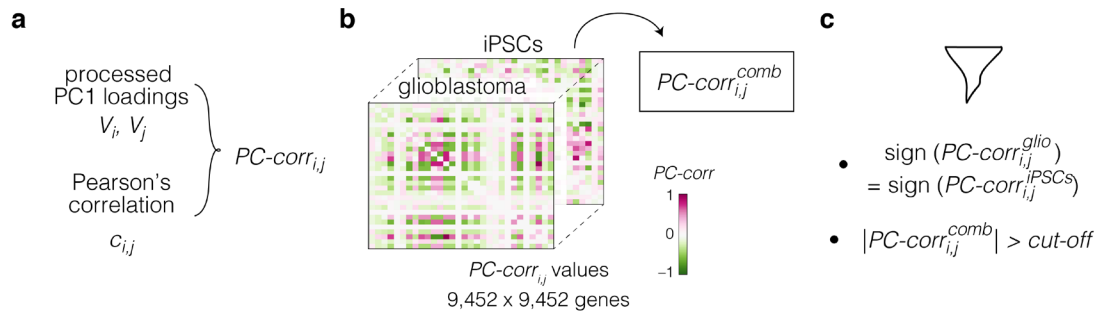


**Figure 5.4 | Schematic representation of the combined PC-corr analysis on two datasets.** **a**, Processed PC loadings from the component providing good separation of mechanical cell states (here PC1, see **Figure 5.3b,c**) are combined with Pearson's correlation to calculate  $PC-corr$  value for each pair of genes  $i, j$  for every dataset individually. **b**,  $PC-corr$  results obtained for the two datasets are integrated to obtain a combined value  $PC-corr_{i,j}^{comb}$ . **c**, Gene pairs that show same directionality of  $PC-corr$  value and for which the  $PC-corr_{i,j}^{comb}$  lays above specified cut-off are selected for network construction. This figure is modified from Urbanska, Ge *et al.*<sup>456</sup>.

Next, the PC loadings for the component showing good separation between the different cell states (PC1 for both of presented datasets, see **Figure 5.3b,c**) were normalized and scaled (see **Materials and methods**). The processed PC loadings,  $V$ , were then combined with Pearson's correlation coefficients,  $c$ , to obtain a  $PC-corr$  value for each pair of genes  $i, j$  for every  $n$ -th dataset according to the following formula<sup>453</sup>:

$$PC-corr_{i,j}^n = \text{sgn}(c_{i,j}^n) \min(|V_i^n|, |V_j^n|, |c_{i,j}^n|). \quad 5.1$$

The sign of the  $PC-corr$  value corresponds to the correlated or anti-correlated expression of genes  $i, j$ , and the magnitude of  $PC-corr$  conveys the combined information about the strength of the correlation and the contribution of the individual genes to the phenotype-based separation of samples.

To integrate the  $PC-corr$  results obtained for the discovery datasets, a combined  $PC-corr$  value,  $PC-corr_{i,j}^{comb}$ , was calculated either as a mean or as a minimum of the individual values. For  $n$  datasets:

$$PC-corr_{i,j}^{comb} = \begin{cases} \delta_{i,j} \frac{1}{N} \sum_{n=1}^N |PC-corr_{i,j}^n| \\ \delta_{i,j} \min(|PC-corr_{i,j}^1|, \dots, |PC-corr_{i,j}^n|) \end{cases}, \quad 5.2$$

where  $\delta_{i,j} \in \{-1, 1\}$  defines the sign of  $PC-corr_{i,j}^{comb}$ , and is equal to the mode of  $PC-corr_{i,j}$  signs over all individual datasets. For the implementation on two datasets, gene pairs with opposing  $PC-corr$  signs were masked by setting their  $PC-corr^{comb}$  values to zero. The schematic representation of the combined PC-corr analysis on two datasets is presented in **Figure 5.4**.

To elucidate the network of target genes, a cut-off was applied to the absolute value of  $PC-corr^{comb}$ . We explored several cut-off strategies in order to obtain a wide overview of the meaningful conserved network modules. By looking at  $PC-corr^{comb}$  calculated as mean and setting the threshold for its absolute value to 0.75, we obtained a network of 29 nodes connected by 30 edges (**Figure 5.5a**). The edges describe the connection between the genes in the network and their thickness is defined by the

$PC-corr^{comb}$  values (**Supplementary Table D.1**). The node colors reflect the strength of the contribution of individual genes to the separation of the different classes as described by the mean of the processed PC loadings  $V$ . The obtained network can be made more restrictive by using the minimum  $PC-corr^{comb}$  instead of the mean, or by changing the cut-off value. Using the  $PC-corr^{comb}$  calculated as minimum value (**Supplementary Table D.2**) and setting the cut-off value to 0.70, we obtained a network with 22 nodes connected by 29 edges (**Figure 5.5b**). Increasing the cut-off value to 0.75 resulted in a network of 9 genes connected by 12 edges (**Figure 5.5c**). The list of genes from the three networks presented in **Figure 5.5a–c**, together with their full names and processed PC loading values, is presented in **Supplementary Table D.3**.

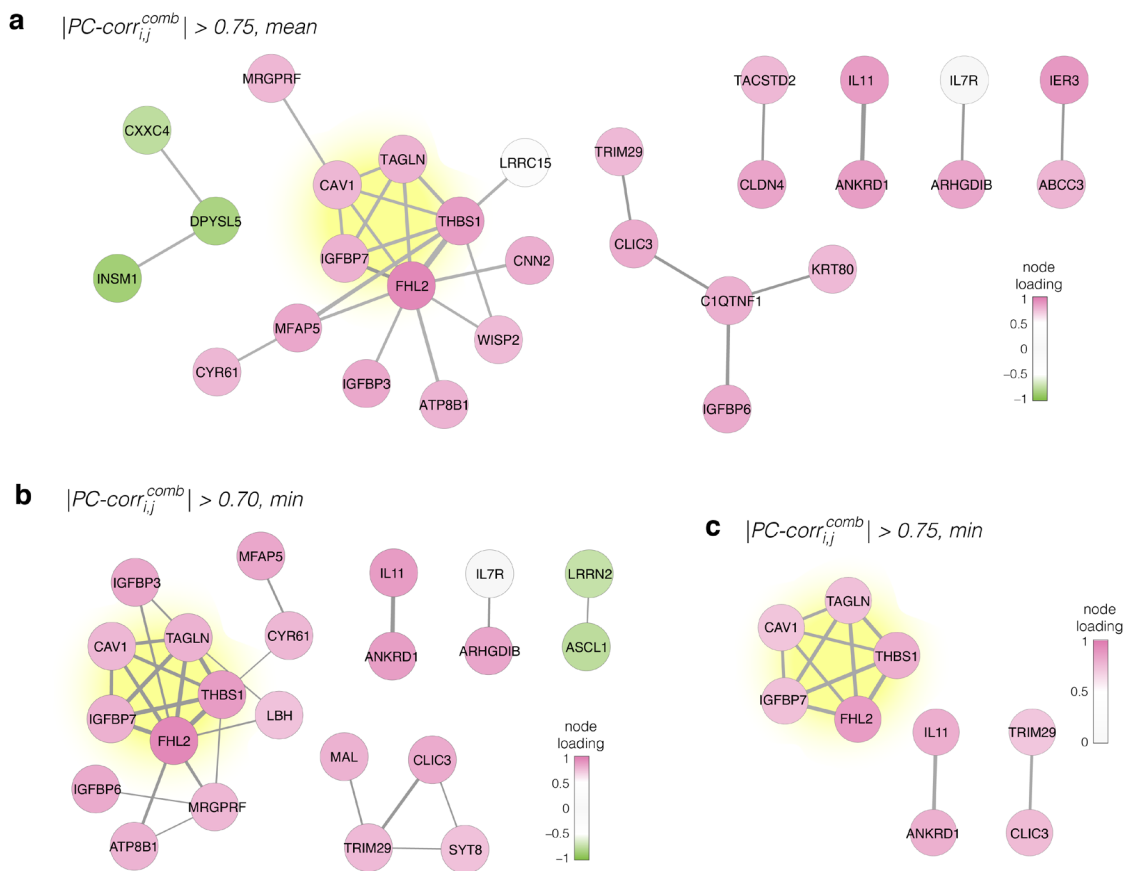


**Figure 5.5 | Identified networks of genes putatively involved in cell mechanics regulation.** a–c, Gene networks obtained by filtering gene pairs by  $|PC-corr^{comb}|$ . The presented networks were obtained by setting the cut-off value to 0.75, when calculating  $PC-corr^{comb}$  as mean (a), and to 0.70 (b) and 0.75 (c), when calculating  $PC-corr^{comb}$  as minimum value. The edge thicknesses represent the  $|PC-corr^{comb}|$  and the colors of the nodes represent the average processed PC loadings. This figure is modified from Urbanska, Ge *et al.*<sup>456</sup>.

To explore if the genes from obtained networks were related to specific biological process, we performed gene ontology (GO) enrichment analysis on the nodes of the network presented in **Figure 5.5a** (9 genes), as well as the union of all nodes presented in **Figure 5.5a–c** (34 genes). The top two significantly enriched terms in the 9-gene set were the negative regulation of transcription by polymerase II (GO: 000122) and negative regulation of endothelial cell proliferation (GO: 0001937)

(Figure 5.6). In the 34-gene set, apart from a broad term of signal transduction (GO: 0007165), the significantly enriched terms included negative regulation of transcription by polymerase II (GO: 000122), regulation of cell growth (GO: 0001558), and negative regulation of cell proliferation (GO: 0008285). These GO terms included predominantly genes with high expression in the stiff cell states. This suggests that transcriptional activity and growth/proliferation are downregulated in stiff compared to soft cells.

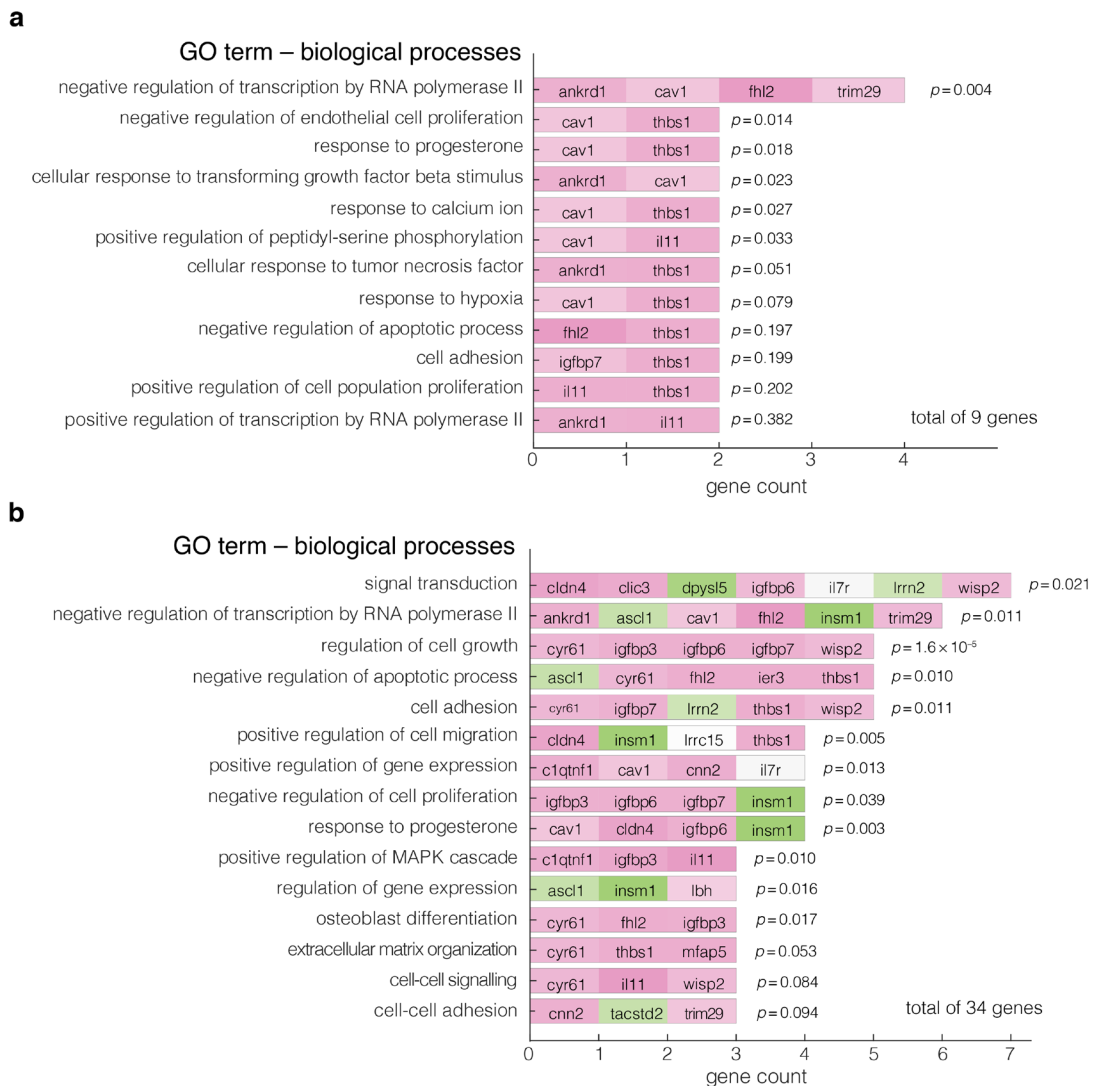


**Figure 5.6 | Gene ontology (GO) enrichment analysis of obtained target genes. a–b,** Enriched GO terms of biological processes are summarized for 9 genes corresponding to the results from Figure 5.5a (a) and 34 genes corresponding to all nodes presented in Figure 5.5a–c (b). The analysis was performed using DAVID 6.8 functional annotation tool online, with *Homo sapiens* as background dataset, ENSEMBL gene IDs as input, and focused on direct GO terms for biological processes. Color code of the blocks corresponds to the level of expression in stiff states with green corresponding to low expression and magenta corresponding to high expression. The reported *p*-values are the Fisher’s exact *p*-values obtained using a two tailed two sample *t*-test.



#### 5.1.4. Conserved functional network module comprises five genes

Regardless of the strategy chosen for the selection of gene pairs, a strongly interconnected module of 5 genes, including *CAV1*, *FHL2*, *IGFBP7*, *TAGLN*, and *THBS1* (**Table 5.2**, highlighted in yellow in **Figure 5.5a–c**), was present in the obtained networks. We focused on these five genes for further analysis.

**Table 5.2 | List of identified target genes comprising the conserved module.** HGNC – HUGO gene nomenclature committee (<https://www.genenames.org/>), MGI – mouse genome informatics (<http://www.informatics.jax.org/>).

symbol	gene description	HGNC ID	MGI ID
<i>CAV1</i>	caveolin-1	HGNC:1527	MGI:102709
<i>FHL2</i>	four and a half LIM domains 2	HGNC:3703	MGI:1338762
<i>IGFBP7</i>	insulin like growth factor binding protein 7	HGNC:5476	MGI:1352480
<i>TAGLN</i>	transgelin	HGNC:11553	MGI:106012
<i>THBS1</i>	thrombospondin 1	HGNC:11785	MGI:98737

Caveolin-1, *CAV1*, is a protein most prominently known for its role as a structural component of caveolae. Caveolae are small cup-shaped invaginations in the cell membrane that are involved in the mechanoprotective mechanism of buffering the plasma membrane tension<sup>209,210,467</sup>. Apart from membrane organization and membrane domain scaffolding, *CAV1* plays a role in an array of non-caveolar functions such as metabolic regulation or Rho-signalling<sup>210,468,469</sup>. The second identified target, four and a half LIM domains 2, *FHL2*, is a multifaceted LIM domain protein with many binding partners and a transcription factor activity<sup>470</sup>. *FHL2* has recently been shown to remain bound to actin filaments under high tension, and be shuttled to the nucleus when the cytoskeletal tension is low<sup>471,472</sup> — a property conserved among many LIM domain proteins<sup>472,473</sup>. The third target, Insulin-like growth factor binding protein 7, *IGFBP7*, is a secreted protein implicated in a variety of cancers<sup>474</sup>. It is involved in the regulation of processes such as cell proliferation, adhesion, and senescence<sup>474</sup>. Transgelin, *TGLN*, is an actin-binding protein known to be up-regulated by high cytoskeletal tension<sup>475</sup> and is also known to play a role in cancer<sup>476</sup>. Finally, thrombospondin 1, *THBS1*, is a matricellular, calcium-binding glycoprotein that mediates cell-cell and cell-matrix adhesions and has many regulatory functions<sup>477,478</sup>.

The identified target genes show clear differences in expression levels between the soft and stiff cell states in both discovery and validation datasets, and provide for fairly good clustering of the samples according to cell stiffnesses (**Figure 5.7**). Of note, the direction of changes in the expression levels between the soft and stiff cell states in the validation datasets was not always following the same

direction (Figure 5.7c–f, Supplementary Figure D.2). This suggests that the genes involved in cell mechanics regulation may have non-monotonic relationship with cell stiffness.

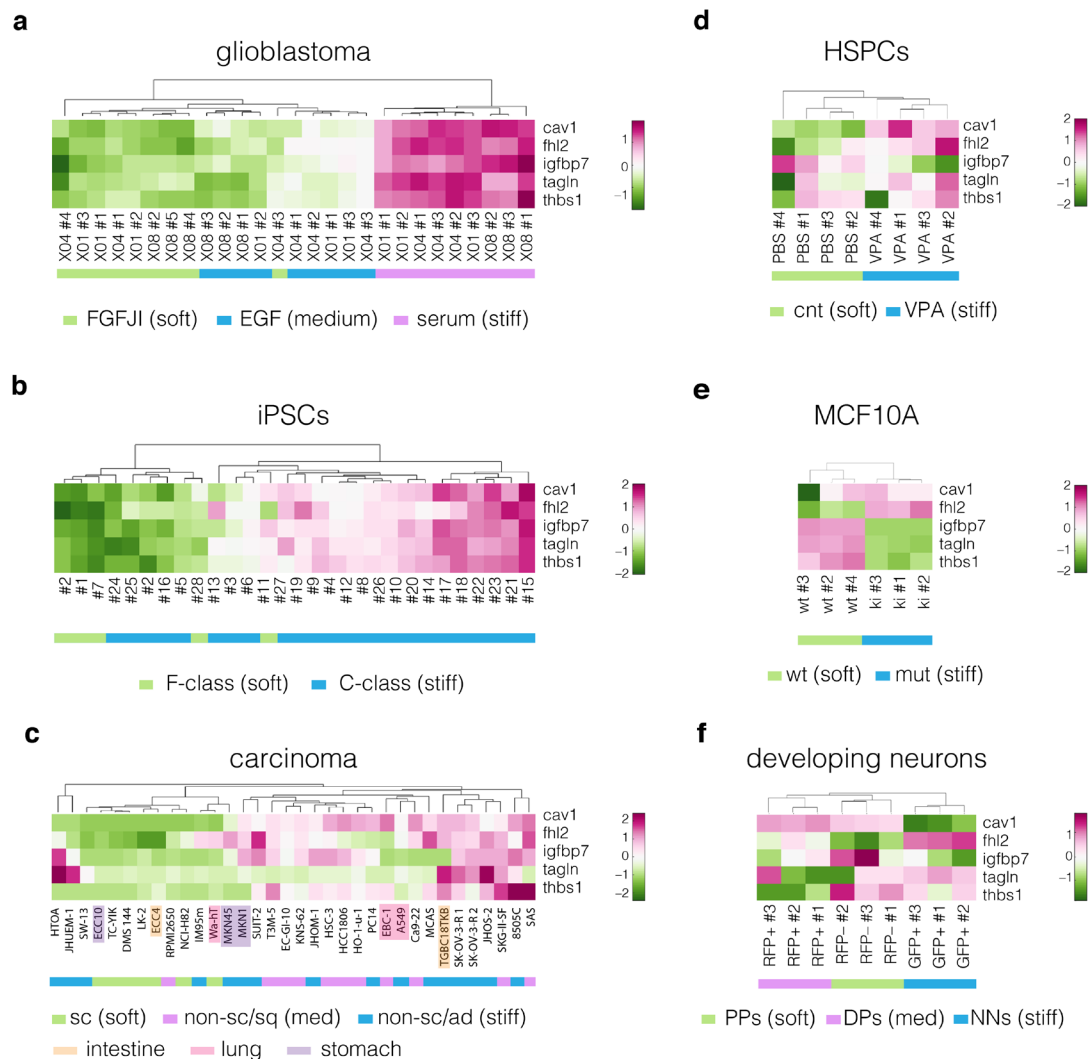


**Figure 5.7 | Expression of identified target genes in the discovery and validation datasets.** a–f, Unsupervised clustering heat maps of expression data from transcriptomic datasets for glioblastoma (a), iPSCs (b), carcinoma (c), HSPCs (d), MCF10A (e), and developing neurons (f). sc – small-cell carcinoma, non-sc – non-small-cell carcinoma, sq – squamous cell carcinoma, ad – adenocarcinoma, cnt – untreated control, VPA – valproic acid, wt – wild type, mut – mutant, PPs – proliferating progenitors, DPs – differentiating progenitors, NNs – newborn neurons. In c, all carcinoma cell lines available in the FANTOM5 dataset are included, the ones for which mechanical characterization was performed are highlighted with transparencies, color-coded for tissue of origin. This figure is modified from Urbanska, Ge *et al.*<sup>456</sup>.

### 5.1.5. *CAVI* performs best at classifying soft and stiff cell states in validation datasets

The four remaining datasets (carcinoma, HSPCs, MCF10A and developing neurons) were used to test the performance of the five identified genes in classifying the individual samples into soft or stiff phenotypes based on the transcription levels of individual genes. For this purpose, we implemented AUC–ROC analysis<sup>455</sup>.

**Table 5.3 | Results of *in silico* validation of the predicted targets using AUC-ROC.** The table contains values of AUC-ROC for target genes obtained for every soft-stiff cell state pair. The average of AUC-ROC values obtained for all validation systems is included in the last table row. sc – small cell carcinoma, sq – squamous cell carcinoma, adeno – adenocarcinoma, wt, wild type, cnt – untreated control, VPA – valproic acid, PPs – proliferating progenitors, DPs – differentiating progenitors, NNs – newborn neurons. This table is adapted from Urbanska, Ge *et al.*<sup>456</sup>.

dataset	state	<i>CAV1</i>	<i>FHL2</i>	<i>IGFBP7</i>	<i>TAGLN</i>	<i>THBS1</i>
carcinoma	sc vs sq	1	0.84	0.87	0.77	1
	sq vs adeno	0.84	0.61	0.51	0.72	0.61
	sc vs adeno	1	0.90	0.82	0.91	0.74
MCF10A	wt vs H1047R	0.78	1	1	1	1
HSPCs	cnt vs VPA	1	0.94	1	0.84	0.63
	PPs vs DPs	1	1	0.78	0.50	1
developing neurons	DPs vs NNs	1	1	0.78	0.67	1
	PPs vs NNs	1	1	0.89	1	1
mean		0.95	0.91	0.83	0.80	0.87

The ROC curve is a graphical plot that illustrates the classification ability of a binary classifier system. On the  $x$  axis of an ROC plot, the false positive rate (FPR) is represented, and on the  $y$  axis the true positive rate (TPR). We built ROC curves for every soft-stiff pair of cell states from individual datasets by swiping through different thresholds of the expression of a given gene and calculating the TPR and FPR for classifying the soft and stiff cell states based on these thresholds (**Supplementary Figure D.3**). We then used the area under the ROC curve (AUC-ROC) as a proxy for the performance of these one-feature classifiers. AUC-ROC takes values from 0 to 1, with 1 corresponding to a perfect classifier and 0.5 to a random classifier. The AUC-ROC values obtained for each gene from the conserved module in the respective validation datasets are summarized in **Table 5.3**. We found that *CAV1*, with an average AUC-ROC score of 0.95, was the best performing classifier. Thus, we set out to test experimentally if modifying the levels of *CAV1* in cells could elicit the predicted change in their mechanical phenotype.

In most of our datasets, the stiffer phenotypes were associated with high *CAV1* expression (**Figure 5.7**). Moreover, we characterized mouse embryonic fibroblasts isolated from *CAV1* knock out mice (*CAV1*KO) and observed that their stiffness is lower than that of the wild type cells (WT) (**Figure 5.8**). This led us to hypothesize that artificially decreasing the levels of *CAV1* causes cell softening, and conversely, increasing the level of *CAV1* causes increase in cell stiffness.

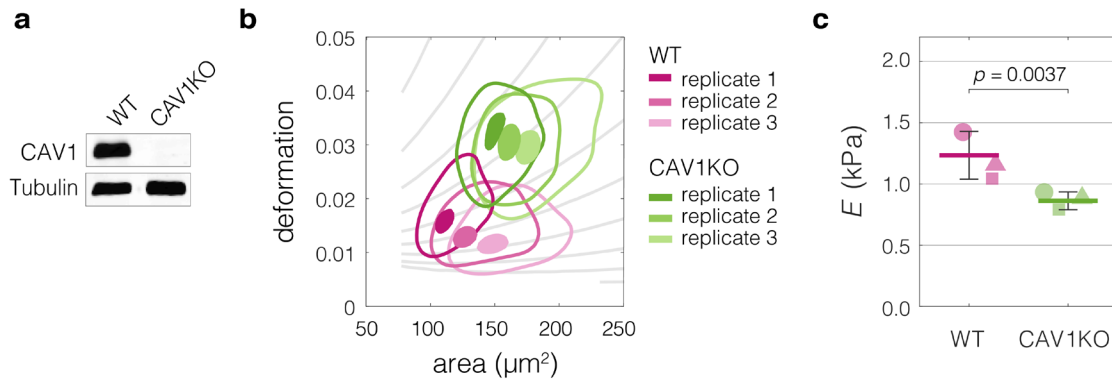


**Figure 5.8 | CAV1 knock-out mouse embryonic fibroblasts (CAV1KO) have lower stiffness compared to the wild type cells (WT).** **a**, Western blot analysis of CAV1 expression levels in CAV1KO compared to WT cells. **b**, Plots of area vs deformation for CAV1KO and WT cells characterized with RT-DC. Contour plots delineate 95% and 50% density areas (solid lines and filled area, respectively) of data from individual measurement replicates ( $n = 3$ ). The isoelasticity lines in the background (gray) indicate regions of the same Young's moduli. **c**, Young's modulus values estimated for WT and CAV1KO cells using area-deformation data in **b**. Horizontal lines delineate medians with mean absolute deviation (MAD) as error, datapoints represent medians of the individual replicates. Statistical analysis was performed using generalized linear mixed effects model. Data for this figure was acquired by Dr. Fidel-Nicolas Lolo from the group of Prof. Miguel Angel del Pozo (CNIC, Madrid, Spain). This figure is adapted from Urbanska, Ge *et al.*<sup>456</sup>.

### 5.1.6. Perturbing expression levels of CAV1 changes cells stiffness

To test whether modifying CAV1 expression has an impact on cell mechanical properties, we performed perturbation experiments in the cell lines representing two intestine carcinoma types: ECC4, the small-cell carcinoma with a comparably soft phenotype, and TGBC18TKB (TGBC), the adenocarcinoma with a comparatively stiff phenotype. First, we confirmed that TGBC cells have a higher level of CAV1 as compared to ECC4 on a protein level (**Figure 5.9a**) and that they are characterized by a stiffer phenotype, not only when measured with RT-DC (**Figure 5.2b**), but also AFM using both standard indentation experiments, as well as AFM microrheology (**Figure 5.9b–c**). The summary of Young's modulus values obtained with the different probing techniques for ECC4 and TGBC cell lines is presented in **Supplementary Table D.4** and in **Supplementary Figure D.4**.

Next, to decrease the levels of CAV1 in the TGBC cells, we performed knock-down experiments using two RNA interference (RNAi) systems, endoribonuclease-prepared siRNA (esiRNA) targeting three different parts of CAV1 transcript (esiCAV1-1, esiCAV1-2, and esiCAV1-3), and a pool of conventional siRNAs (CAV1-pool). All the RNAi approaches resulted in the decrease of the Young's modulus of TGBC cells as measured by RT-DC (**Figure 5.10a–b**, **Supplementary Figure D.5a–b**), the most prominent effect was observed using esiCAV1-1. We further confirmed that CAV1 knock-down with esiCAV1-1 resulted in decreased stiffness of TGBC cells using AFM indentation and AFM microrheology measurements (**Supplementary Figure D.6**).

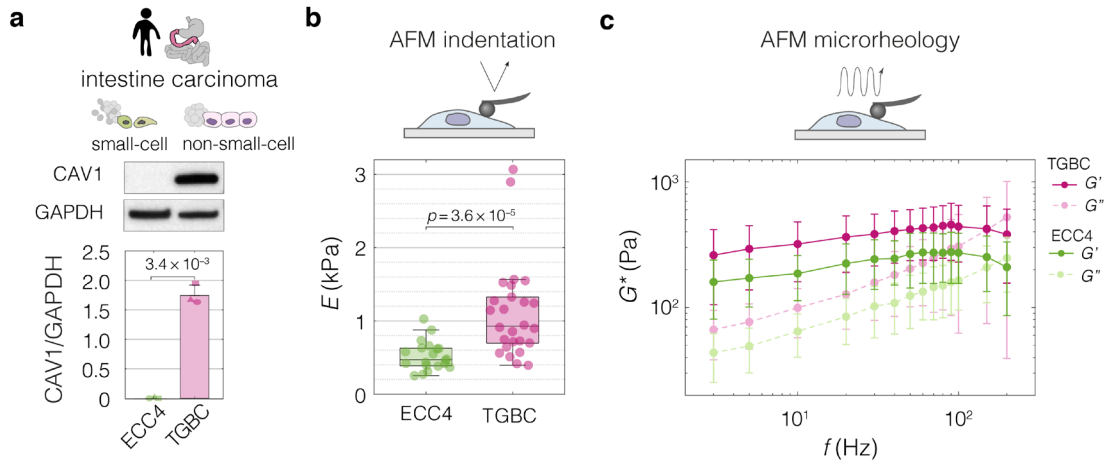


**Figure 5.9 | CAV1 expression and mechanical characterization with AFM of small-cell (ECC4) vs non-small-cell (TGBC) carcinoma cell lines from intestine.** **a**, ECC4 do not show detectable levels of CAV1, while TGBC have considerable basal CAV1 expression. For the Western blot analysis representative blots (top) as well as quantification (bottom,  $n = 3$ ) are shown. **b**, ECC4 show lower Young's moduli than TGBC in AFM indentation experiments. Box plots spread from 25<sup>th</sup> to 75<sup>th</sup> percentiles with a line at the median, whiskers span  $1.5 \times$  interquartile range (IQR), individual datapoints correspond to values obtained for individual cells (number of measured cells  $n = 20$  and  $26$  for ECC4 and TGBC, respectively). Statistical analysis was performed using two-sided two-sample  $t$ -test (**a**) or two-sided Wilcoxon rank sum test (**b**). **c**, ECC4 show storage and shear moduli lower than TGBC in AFM microrheology measurements. Datapoints correspond to means  $\pm$  standard deviation of all measurements at given oscillation frequencies ( $n = 18$  and  $27$  for each frequency for ECC4 and TGBC, respectively). Lines connecting datapoints serve as guides for the eye. This figure is modified from Urbanska, Ge *et al.*<sup>456</sup>.

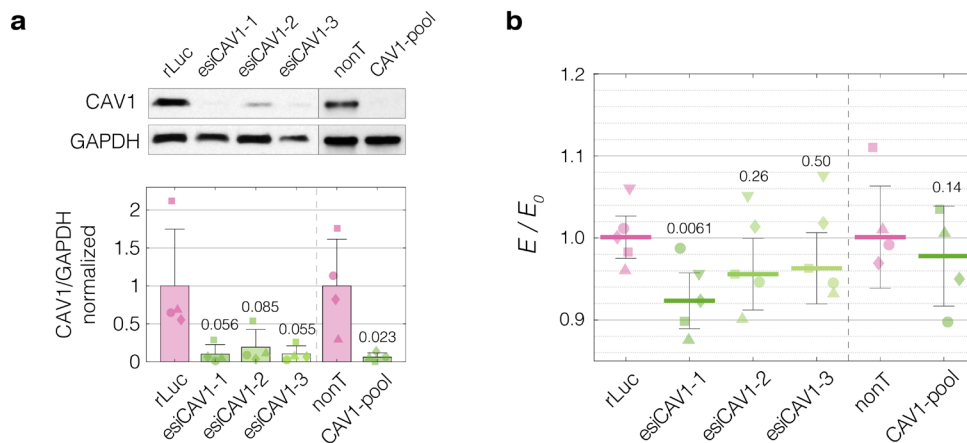


**Figure 5.10 | CAV1 downregulation in TGBC cells results in decreased cell stiffness.** **a**, Western blot analysis of CAV1 after knock-down in TGBC cells. Representative blot (top) as well as quantification (bottom,  $n = 4$ ) are shown. Bar plots show means  $\pm$  standard deviation. Statistical analysis was performed using two-sided two-sample  $t$ -tests. **b**, Young's modulus of TGBC cells upon CAV1 knock-down as measured by RT-DC, normalized to respective non-targeting controls ( $n = 5$  and  $4$  for set 1 and 2, respectively). Horizontal lines delineate medians with mean absolute deviation (MAD) as error, datapoints represent medians of the individual replicates. Statistical analysis was performed using generalized linear mixed-effects models. This figure is modified from Urbanska, Ge *et al.*<sup>456</sup>.

To investigate how CAV1 increase influences cell stiffness, we performed transient overexpression experiments of CAV1 with a dTomato reporter under independent ribosomal entry site, IRES, (CAV1iT) in both ECC4 and TGBC cell lines. At 72 hours post transfection, we observed elevated

levels of CAV1 in both cell lines on a protein level in bulk (**Figure 5.11a**). Since in the transient overexpression experiments not all of the cells are transfected, we leveraged the possibility to monitor the fluorescence of single cells in parallel with their mechanical phenotype offered by RT-FDC<sup>312</sup> and gated for the fluorescence-positive cells (T+, gate marked in magenta in **Figure 5.11b**). The fluorescence-positive cells in the CAV1-transfected sample, CAV1iT+, showed higher Young's moduli as compared to fluorescence-negative cells in both control sample (mock) and CAV1-transfected sample (CAV1iT-, internal control) (**Figure 5.11c, Supplementary Figure D.5c-d**). The effect was observed in ECC4 as well as TGBC cells, however, it was more pronounced in the TGBC cells, suggesting that the cells may be more responsive to the artificial increase in CAV1 levels when natively expressing a basal level of this protein.

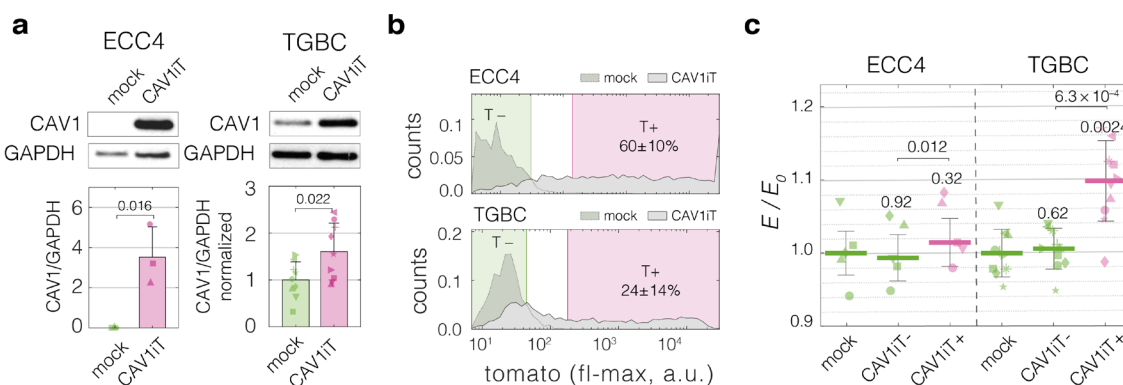


**Figure 5.11 | CAV1 overexpression in ECC4 and TGBC cell lines results in increased cell stiffness.** **a**, Western blot analysis of CAV1 after overexpression in ECC4 and TGBC cells. Representative blots (top) as well as quantification (bottom,  $n = 3$  and  $9$ , for ECC4 and TGBC, respectively) are shown. Bar plots show means  $\pm$  standard deviation. Statistical analysis was performed using two-sided two-sample *t*-tests. **b**, Gating for fluorescence positive and negative cells based on dTomato expression in ECC4 (top) and TGBC (bottom) cells. Fluorescence positive cells correspond to cells expressing CAV1-IRES-dTomato. **c**, Young's modulus of ECC4 and TGBC cells upon CAV1 overexpression as measured by RT-DC, normalized to mock controls ( $n = 5$  and  $9$  for ECC4 and TGBC, respectively). Horizontal lines delineate medians with mean absolute deviation (MAD) as error, datapoints represent medians of the individual replicates. Statistical analysis was performed using generalized linear mixed-effects models. This figure is modified from Urbanska, Ge *et al.*<sup>456</sup>.

Finally, we performed CAV1 perturbation experiments in a breast epithelial cell model of cancerous transformation, MCF10A-ER-Src cells, in which the Src proto-oncogene can be induced by treatment with tamoxifen (TAM). As previously shown, TAM addition triggers Src phosphorylation and cellular transformation<sup>479</sup>, which is associated with F-actin cytoskeletal changes and, after a transient stiffening, the acquisition of a soft phenotype evident at 36 hours post induction<sup>11</sup>. We inspected a previously published microarray dataset and determined that the expression of CAV1 diminishes over time after TAM treatment<sup>480</sup> (**Figure 5.12a**). We then showed that the decrease of CAV1 could be observed on protein level at 72 h post induction (**Figure 5.12b**), a timepoint at which the TAM-induced MCF10A-ER-Src cells show a significant decrease in cell stiffness as measured by AFM (Tavares *et al.*<sup>11</sup> and **Figure 5.12c**). Interestingly, RT-DC measurements showed an opposing trend, with induced cells appearing stiffer than uninduced ones at the 72-h timepoint (**Supplementary Figure D.7a**). We next

showed, using AFM, that decreasing the level of CAV1 by knock-down caused a decrease in stiffness of uninduced MCF10A-ER-Src cells similar to that caused by TAM induction (**Figure 5.12d**). We then performed an inverse experiment, in which we rescued the CAV1 levels in TAM-induced MCF10A-ER-Src cells by transient overexpression. Cells overexpressing CAV1 had increased stiffness, similar to that of uninduced cells (**Figure 5.12e**). Also when measured using RT-DC, CAV1 knock-down in MCF10A-ER-Src with the esiCAV1-1 construct resulted in cell softening (**Supplementary Figure D.7b**), while CAV1 overexpression caused an increase in cell stiffness for both EtOH control and TAM-induced cells (**Supplementary Figure D.7c**). Taken together, the results obtained with the intestine carcinoma cell lines and MCF10A-ER-Src cells show that CAV1 not only correlates with, but also is causative of mechanical phenotype change.

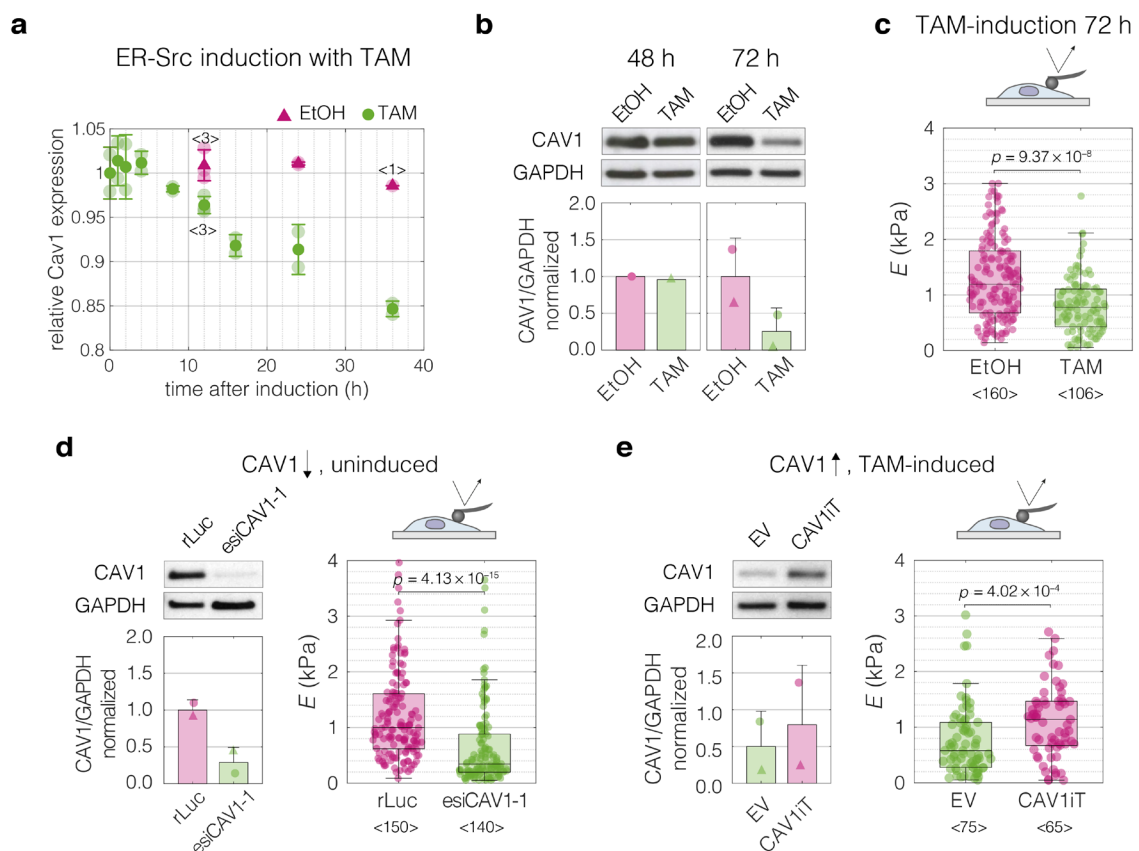


**Figure 5.12 | Perturbations of CAV1 levels in MCF10A-ER-Src cells result in cell stiffness changes. a**, Inducing transformation of MCF10A-ER-Src cells by tamoxifen (TAM) treatment, as opposed to vehicle control (ethanol, EtOH), causes a decrease of CAV1 expression over time, as captured by microarray analysis<sup>480</sup>. Datapoints with error bars represent means  $\pm$  standard deviation ( $n = 2$ , unless indicated otherwise). **b**, Western blot analysis shows the decrease of CAV1 at protein level 72 h post induction. **c**, MCF10A-ER-Src cells show decreased Young's moduli 72 h post TAM induction. **d**, CAV1 knock-down in uninduced MCF10A-ER-Src cells results in lowering of the Young's modulus. **e**, Overexpression of CAV1 in TAM-induced MCF10A-ER-Src cells causes increase in the Young's modulus and effectively reverts the softening caused by TAM induction (compare to panel c). Box plots in c–e spread from 25<sup>th</sup> to 75<sup>th</sup> percentiles with a line at the median, whiskers span  $1.5 \times$  interquartile range (IQR), individual datapoints correspond to values obtained for individual cells, the number of measured cells per conditions, pooled from  $n = 3$  independent experiments, is indicated below each box. Statistical analysis was performed using a two-sided Wilcoxon rank sum test. Data for this figure was acquired by Dr. Maria Winzi, the figure is adapted from Urbanska, *Ge et al.*<sup>456</sup>.

## 5.2. Discussion

Establishing ways of manipulating mechanical properties of cells is necessary to enable exploring their impact on cell and tissue function<sup>294</sup>. The increasing ease of screening for single-cell mechanical phenotypes thanks to the advent of high-throughput microfluidic methods such as RT-DC, together with growing availability of transcriptional profiles accompanying cell state transitions, offers an unprecedented opportunity for data-driven discovery of genes involved in the control of mechanical phenotype. Here we leveraged this opportunity and performed a discriminative network analysis of transcriptomic profiles associated with mechanical phenotype changes across different model systems. We elucidated a conserved module of five genes with putative roles in the regulation of cell mechanical phenotype, and evaluated the performance of the identified genes in classifying cells into soft and stiff states *in silico*. Finally, we demonstrated on the example of best performing gene, *CAV1*, that its experimental perturbations affect cellular stiffness in the predicted direction. The latter demonstrates that the level of *CAV1* not only correlates with, but also is causative of mechanical phenotype change.

The mechanomics approach presented here is a blueprint for hypothesis-free, data-driven strategy for the identification of cell mechanics regulators. Importantly, this approach enables integration of information from multiple datasets, what allows for focusing the analysis on genes that play a general role in cell mechanics regulation rather than on genes specific for the individual experimental models. Thanks to the combination of Pearson's correlation and the discriminative information included in the PC loadings, the PC-corr analysis does not only consider gene co-expression — as is the case for classical co-expression network analysis<sup>481,482</sup> — but also incorporates the relative relevance of each feature for discriminating between two or more conditions (in our case, the conditions representing soft and stiff mechanical phenotypes). Finally, PC-corr can be implemented on any type of omic data, including genomic, transcriptomic, proteomic and lipidomic profiles.

Surprisingly, we did not observe enrichment of GO terms related to actin cytoskeleton, actomyosin contractility, cell adhesion or cell migration — processes that are typically associated with cell mechanics — among the elucidated genes (**Figure 5.6**). However, closer literature research on individual targets let us establish some links connecting our targets with cell mechanics and cytoskeleton. To begin with, *CAV1*, in addition to its role in buffering plasma membrane tension<sup>209,467</sup>, is known to interact with Rho-signalling and actin-related regulatory processes<sup>210,468,469</sup>, and was shown to correlate with cell stiffness in Ras-transformed fibroblasts<sup>47</sup>. Additionally, *CAV1* was recently shown to modulate the activation of YAP in response to changes in stiffness of cell substrate<sup>483</sup> and in the mechanical stretch-induced mesothelial to mesenchymal transition<sup>484</sup>. YAP is an established transducer of not only various mechanical stimuli, but also of cell shape and the changes in the actin cytoskeleton tension<sup>423</sup>, the latter being an important determinant of cell stiffness. Conversely, YAP is an essential co-activator of *CAV1* expression<sup>485</sup>. In the extended gene networks (**Figure 5.5a–b**), we found three further genes that are identified (*CYR61*, *ANKRD1*)<sup>486,487</sup> or implicated (*THBS1*)<sup>423</sup> as transcriptional



targets of YAP. The next identified target, transgelin, TGLN (also known as SM22 $\alpha$ ) is an actin-binding protein, that stabilizes actin filaments and is positively correlated with cytoskeletal tension<sup>488</sup>. Transgelin is a member of the calponin protein family and one further member of this family, calponin 2, CNN2, is present among the genes identified with less stringent criteria (**Figure 5.5a–b, Supplementary Table D.3**). The expression of calponin 2, likewise, stabilizes actin filaments and is increased in cells with high cytoskeletal tension<sup>489,490</sup>. Finally, FHL2 is a transcriptional coactivator that is found, together with other LIM domain protein families such as zyxin and paxillin, to localize to actin filaments that are under stress<sup>471–473</sup>. When the cytoskeletal tension is low, FHL2 translocates to the nucleus, thus serving as a nuclear transducer of actomyosin contractility<sup>471</sup>.

The change in expression of the identified targets is correlated with mechanical properties across all datasets, but it does not always follow the same direction (**Figure 5.7c–f, Supplementary Figure D.2**). This non-monotonic relationship between gene expression and the mechanical phenotype change suggests that there may be local optima of expression. Furthermore, the effect of expression change on cell stiffness may be contextual and depend on the state of cells. This observation carries some parallels to the described roles of several of our target genes in cancer progression. For example, CAV1 has been implicated to both promote and suppress cancer progression in various tissues. It is proposed that the change in CAV1 expression may have different roles depending on the stage of cancer progression<sup>468,491,492</sup>. A similar ambiguity of their role in cancer progression was indicated for THBS1<sup>478</sup> and IGFBP7<sup>474</sup>. In the future, the dependence of observed mechanical change on starting protein levels as well as magnitude of deviation from starting levels need to be studied. It will be further important to consider the temporal dynamics of cell response to the change in expression of a given gene. Pushing the cell out of its equilibrium may cause the system to respond actively to counterbalance the induced change, which, in turn, may lead to oscillations in both the expression levels of manipulated protein and its effectors, as well as the mechanical properties of the cell.

CAV1 perturbations elicited consistent changes in mechanical phenotype in different cell lines. The downregulation of CAV1 by RNAi resulted in lowering of Young's modulus in MCF10A-ER-Src and TGBC cell lines consistently across RT-DC (TGBC, **Figure 5.10b**; MCF10A-ER-Src, **Supplementary Figure D.7b**) and AFM measurements (TGBC, **Supplementary Figure D.6**; MCF10A-ER-Src, **Figure 5.12d**). Also, the upregulation of CAV1 by transient overexpression resulted in the increase of Young's modulus in both RT-DC (TGBC, **Figure 5.11c**; MCF10A-ER-Src, **Supplementary Figure D.7c**) and AFM measurements (MCF10A-ER-Src, **Figure 5.12e**). Surprisingly, however, the 72-h induction of MCF10A-ER-Src cells with TAM, concomitant with a decrease in CAV1 levels (**Figure 5.12b**), resulted in lowering of Young's modulus as measured by AFM (**Figure 5.12c**), while increase of Young's modulus was observed with RT-DC (**Supplementary Figure D.7a**). This discrepancy may be caused by the detached vs substrate-adherent state in which cells are probed in RT-DC and AFM, respectively. Detaching cells from substrate triggers rearrangements in actin cytoskeleton that contribute to changes of the mechanical properties<sup>341,493</sup>. Additionally, previous AFM

measurement have revealed that substrate-adherent MCF10A-ER-Src undergo softening at 36 h post induction with TAM, while no softening was observed for MCF10A-ER-Src cells grown in 3D spheroids and dissociated into single cells for mechanical characterization, even after 72 h<sup>11</sup>. To resolve whether the substrate detachment contributes to measured differences, additional AFM measurements on rounded cells could be performed. Alternatively, the observed discrepancy could be caused by the different probing timescales of AFM (0.2 s) and RT-DC (1 ms), and resulting higher strain rates applied by RT-DC.

Mechanical properties of ECC4 and TGBC cell lines were compared across three methods operating at different timescales: RT-DC, AFM indentation and AFM microrheology (see **Figure 3.7** and **Table 3.4** for methods' comparison). In all three methods, TGBC had higher Young's modulus than ECC4 cells (see **Supplementary Table D.4** and **Supplementary Figure D.4**). The absolute Young's modulus values, however, differed between the methods: the values obtained from the RT-DC measurements were higher than for the AFM indentation, and the storage Young's moduli obtained from AFM microrheology were frequency-dependent and took values between those obtained with AFM indentation and RT-DC (**Supplementary Table D.4**). Overall, the Young's modulus values appeared to increase with the probing frequency across the methods (**Supplementary Figure D.4**). This corresponds well with previous reports of cell stiffening with increased probing rate observed both for AFM indentation<sup>23,24</sup> and in microrheology assays<sup>22,25-27</sup>.

Performing the mechanomics analysis on the level of transcriptome, as compared to other omic data, is advantageous and disadvantageous at the same time. The limitation of considering mRNA levels is that they do not necessarily reflect protein content in cells<sup>494</sup>. Furthermore, for many proteins it is not the absolute protein level that has a functional relevance, but rather the protein activation by, for example, phosphorylation or binding with co-activators, or its localization<sup>495,496</sup>. However, even though there are technologies that enable direct delivery of proteins into cells<sup>497</sup>, it is much more straightforward to modify mRNA levels using established genetic tool such as CRISPR-Cas technology or RNAi, especially for *in vivo* applications. Noteworthy, our analysis framework is readily applicable to other types of omics data, including proteomic, metabolomic, lipidomic, or glycomic data, the analysis of which would complement our study and provide different insights into the regulation of cell mechanics. Lipidomic data, for example, could reveal possible contributors to cell mechanics related to the composition of cell membrane.

The experimental verification of the four untested genes (*FHL2*, *IGFBP7*, *TAGLN*, and *THBS1*) from the conserved module remains to be explored in future studies. Since the implemented discriminative network analysis elucidates modules of highly interconnected genes, it would be further interesting to investigate the regulatory relationships among the genes from the identified module. This could be approached by monitoring the expression levels of all genes from the module when one of the genes is perturbed.

Data-driven approaches such as the one pioneered in this study will become more powerful with increasing availability of annotated datasets of mechanical characterization of cells. With the growing use of high-throughput cell mechanical characterization techniques, such as deformability cytometry methods, the establishment of a database for cell mechanics gains immediate relevance. In our group alone, within the timespan of five years since the RT-DC method was originally published<sup>21</sup>, we have accumulated over 100,000 individual mechanical characterization experiments, comprising roughly a billion of single cells measured. Once a vast number of mechanics datasets connected to omics profiles is available, it will be straightforward to develop a next generation artificial intelligence algorithm predicting cell stiffness from given omics profiles. Apart from analyzing divergent cell states, the search for mechanical regulators could be complemented by looking into omics data of cells from unimodal populations sorted by their mechanical properties — a pursuit that with the advent of high-throughput methods for mechanics-based sorting of cells, such as soRT-FDC<sup>313</sup> or passive filtration-based approaches<sup>498</sup>, becomes a realistic objective.

In sum, this work brings together machine learning-based discriminative network analysis and high-throughput mechanical phenotyping to establish a blueprint workflow for data-driven identification of novel targets involved in the regulation of cell mechanics. In the future, the identified targets will provide ways to tune the mechanical properties on demand and enable exploring the impact of mechanical properties on cellular functions *in vitro* and *in vivo*.

### 5.3. Key conclusions

- Mechanics is a system-level inference strategy for hypothesis-free identification of genes involved in the regulation of mechanical phenotype.
- Target identification is based on a discriminative network analysis method termed PC-corr that allows for association of cell mechanical states with large-scale transcriptomic datasets.
- By intersecting the discriminative networks inferred from two selected datasets, a conserved module of five genes (*CAV1*, *FHL2*, *IGFBP7*, *TAGLN*, and *THBS1*) with putative roles in the regulation of cell mechanics was identified.
- Among the identified targets, *CAV1* provides for the best classification of stiff and soft cell states in computational validation on four further datasets.
- Up- and down-regulation of *CAV1* expression induced changes in the mechanical phenotype in experimental validation.
- Thus, *CAV1* not only correlates with but is also causative of mechanical phenotype changes and can be used for adjusting mechanical properties of cells.

## 5.4. Materials and methods

### 5.4.1. Cell culture

#### *Glioblastoma cell lines*

The glioblastoma dataset contained three primary human brain tumour cell lines (X01, X04, and X08) in three distinct signalling states. The cells were cultured and characterized within a framework of a previous study<sup>454</sup>. The respective cell states were maintained by growth media containing either fetal bovine serum (serum), epidermal growth factor (EGF), or basic fibroblast growth factor combined with a JAK inhibitor (FGFJI). Cells were collected for mechanical characterization and RNA sequencing after 5-day exposure to the respective culture conditions<sup>454</sup>.

#### *Carcinoma cell lines*

Small-cell and non-small-cell carcinoma cell lines from intestine, stomach and lung were acquired from RIKEN BioResource Research Center, Japan (see **Table 5.4** for the list of cell lines and media). Cells were cultured in growth media supplemented with 5% (TGBC) or 10% (rest) heat-inactivated fetal bovine serum (10270106, Gibco, ThermoFisher Scientific, MA, USA) and 100 U ml<sup>-1</sup>/100 µg ml<sup>-1</sup> penicillin/streptavidin (15140122, Gibco), at 37°C and 5% CO<sub>2</sub>. Sub-culturing was performed using trypsin (25200072, Gibco). Cells were collected for mechanical characterization at 70% confluency. The RNAseq data was obtained from FANTOM5 consortium<sup>465</sup>.

**Table 5.4 | Carcinoma cell lines used in this study.** List of all carcinoma cell lines acquired from RIKEN institute used in this study, together with the catalogue number, tissue of origin, carcinoma type, growth medium specification, and passage number at purchase. non-sc – non small-cell, sq – squamous cell carcinoma, ad – adenocarcinoma.

cell line	cat no	tissue	type	medium (Gibco cat no)	serum	passage
ECC4	RCB0982	intestine	small-cell	RPMI1640 (11875093)	10%	7
TGBC18TKB	RCB1169	intestine	non-sc (ad)	DMEM (11885084)	5%	5
WA-hT	RCB2279	lung	small-cell	MEM (11095080)	10%	54
EBC-1	RCB1965	lung	non-sc (sq)	MEM (11095080)	10%	7
A549	RCB0098	lung	non-sc (ad)	DMEM (11885084)	10%	92
ECC10	RCB0983	stomach	small-cell	RPMI1640 (11875093)	10%	8
MKN45	RCB1001	stomach	non-sc (ad)	RPMI1640 (11875093)	10%	6
MKN1	RCB1003	stomach	non-sc (ad)	RPMI1640 (11875093)	10%	6

*MCF10A cell lines with PIK3CA mutations*

MCF10A cell lines with single-allele PIK3CA mutation E545K in exon 9 (ex9) or H1024R in exon 20 (ex20) were previously generated by homologous recombination by Horizon Discovery LTD, UK<sup>461</sup> and were kindly provided, together with an isogenic wild type (wt) control, by L.R. Stephens (Babraham Institute, Cambridge, UK). Cells used for mechanical characterization were prepared by Dr. Joanna Durgan and Dr. Oliver Florey (Babraham Institute, Cambridge, UK), and the mechanical characterization was performed by Dr. Nicole Toepfner (Universitätsklinikum Carl Gustav Carus Dresden). Cells were cultured in DMEM/F12 medium (31330038, Gibco) supplemented with 5% horse serum (PAA Laboratories), 10  $\mu\text{g ml}^{-1}$  insulin (I9278, Sigma Aldrich, MO, USA), 0.2  $\mu\text{g ml}^{-1}$  hydrocortisone (H0888, Sigma Aldrich), 0.1  $\mu\text{g ml}^{-1}$  cholera toxin (C8052, Sigma Aldrich), and 100 U  $\text{ml}^{-1}$ /100  $\mu\text{g ml}^{-1}$  penicillin/streptomycin (15140122, Gibco). The wt cells were additionally supplemented with 10 ng  $\text{ml}^{-1}$  EGF (E9644, Sigma Aldrich), while mutant cell lines were maintained without EGF. Sub-confluent cells were collected for mechanical characterization using trypsin (25200056, Gibco). Mechanical characterization was performed on two independent passages with three technical repetitions for each passage. The RNAseq data for ex20 and wt cells were retrieved from a previous study<sup>466</sup>, in which cells were cultured in a reduced medium (DMEM/F12 supplemented with 1% charcoal dextran treated fetal bovine serum, 0.2  $\mu\text{g ml}^{-1}$  hydrocortisone and 0.1  $\mu\text{g ml}^{-1}$  cholera toxin).

*CD34<sup>+</sup> hematopoietic stem and progenitor cells*

Hematopoietic stem and progenitor cells were prepared and measured by Dr. Martin Kräter. In brief, leukapheresis samples were obtained from G-CSF (granulocyte colony-stimulating factor) mobilized peripheral blood of healthy donors after informed consent (ethical approval no. EK221102004, EK47022007). CD34<sup>+</sup> cells were isolated via magnetic-activated cell sorting (MACS) and cultured *ex vivo* as described in detail elsewhere<sup>499</sup>. 1 mM VPA, or PBS as a control, were administered to CD34<sup>+</sup> cells after 24 h in culture. Cells were collected for mechanical characterization and RNA sequencing after 5-day exposure.

*Induced pluripotent stem cells*

F- and C-class iPSCs were derived through reprogramming of murine fetal neural progenitor cells with Tet-On system for doxycycline-inducible expression of OSKM factors as described in details in **Chapter 4**.

*Developing Neurons*

Developing neurons were isolated and prepared for analysis by Dr. Martina Dori, from the group of Prof. Federico Calegari (Center for Regenerative Therapies, TU Dresden), and the mechanical characterization was performed by Dr. Maik Herbig. Double-reporter mouse line *Btg2<sup>RFP</sup>/Tubb3<sup>GFP</sup>* was used to facilitate discrimination of proliferating progenitors (RFP<sup>-</sup>/GFP<sup>-</sup>), differentiating

progenitors (RFP+/GFP-), and newborn neurons (RFP+/GFP+). Lateral cortices dissected from E14.5 murine embryos were dissociated using a papain-based neural dissociation kit (Miltenyi Biotech, Germany) and the cell populations of interest were separated based on the RFP/GFP expression using FACS as described in detail elsewhere<sup>464</sup>. RNA sequencing was performed within a framework of a previous study<sup>464</sup>.

#### *Mouse embryonic fibroblasts*

Previously established, immortalized WT and CAV1KO mouse embryonic fibroblasts derived from WT and CAV1KO littermate C57BL/9 mice<sup>500</sup> were cultured and characterized by Dr. Fidel-Nicolas Lolo from the group of Prof. Miguel Angel del Pozo (CNIC, Madrid, Spain). Cells were cultured in DMEM medium (11960044, Gibco), supplemented with 10% fetal bovine serum (10270106, Gibco), 2 mM glutamine (25030081, Gibco), 100 U ml<sup>-1</sup>/100 µg ml<sup>-1</sup> penicillin/streptomycin (15070063, Gibco), at 37°C and 5% CO<sub>2</sub>. Sub-confluent cells were collected for mechanical measurements by trypsinization (25200056, Gibco).

#### *MCF10A ER-Src cell line*

The MCF10A ER-Src cells were a kind gift from K. Struhl (Harvard Medical School, MA, USA). ER-Src is a fusion of the v-Src (viral non-receptor tyrosine kinase) with the ligand-binding domain of the estrogen receptor, that can be induced by cell treatment with tamoxifen (TAM)<sup>479</sup>. Cell preparation and characterization were performed by Dr. Maria Winzi. Cells were grown at 37°C under 5% CO<sub>2</sub> in DMEM/F12 medium (11039047, Gibco), supplemented with 5% charcoal (C6241, Sigma-Aldrich)-stripped horse serum (16050122, Gibco), 20 ng ml<sup>-1</sup> EGF (AF-100-15, Peprotech), 10 mg ml<sup>-1</sup> insulin (I9278, Sigma-Aldrich), 0.5 mg ml<sup>-1</sup> hydrocortisone (H0888, Sigma Aldrich), 100 ng ml<sup>-1</sup> cholera toxin (C8052, Sigma Aldrich), and 100 U ml<sup>-1</sup>/100 µg ml<sup>-1</sup> penicillin/streptomycin (15070063, Gibco). To induce the Src expression cells were plated at 50% confluency, and after allowing to adhere for 24 h, treated with 1 µM 4OH-TAM (H7904, Sigma Aldrich) or with identical volume of ethanol as a control. Cells were characterized in adherent state using AFM at timepoints specified in the text.

### **5.4.2. Mechanical characterization of cells**

#### *Mechanical characterization of cells using RT-DC*

RT-DC measurements for mechanical characterization of cells were performed at room temperature according to procedures described in detail in **Chapter 2**. Young's modulus values were assigned to each cell based on its area and deformation under given experimental conditions (flow rate, channel size, viscosity of the medium, temperature) using a look-up table obtained through numerical simulations of an elastic solid<sup>317</sup> with the aid of *Shape-Out* (*Shape-Out 1.0.1*; Zellmechanik Dresden). Experimental details (channel sizes, flow rates, measurement buffers) and gates used for filtration in respective datasets are listed in **Table 5.5**.

**Table 5.5 | RT-DC measurement conditions for the individual datasets.** For each dataset experimental details of the measuring conditions are listed, including the widths of channel constriction ( $w_{channel}$ ), total flow rates ( $Q_{total}$ ), percentages of methylcellulose (MC) in the measurement buffer (buffer % MC), effective viscosity of the measurement buffer in the channel at the flowrate used ( $\eta_{eff}$ ), according to Herold<sup>318</sup>), as well as gates used for data filtering.

	measurement conditions				data filtering	
	$w_{channel}$ ( $\mu\text{m}$ )	$Q_{total}$ ( $\mu\text{l s}^{-1}$ )	buffer % MC	$\eta_{eff}$	area ( $\mu\text{m}^2$ )	area ratio
<b>glioblastoma</b>	30	0.16	0.5	5.4	50–600	1.0–1.05
<b>carcinoma</b>	30	0.16	0.5	5.4	60–600	1.0–1.05
<b>HSPCs</b>	20	0.06	0.6	6.3	50–175	1.0–1.08
<b>MCF10A PIK3CA</b>	20	0.04	0.5	5.7	75–320	1.0–1.05
<b>iPSCs</b>	20	0.04	0.5	5.7	50–500	1.0–1.05
<b>dev neurons</b>	20	0.04	0.5	5.7	25–300	1.0–1.05
<b>MEFs</b>	30	0.16	0.5	5.4	50–500	1.0–1.05
<b>MCF10A-ER-Src</b>	30	0.16	0.5	5.4	50–500	1.0–1.11

#### *Mechanical characterization of cells using AFM*

For AFM measurements, cells were seeded on glass bottom dishes (FluoroDish; FD35100, WPI, FL, USA) at least one day in advance. Mechanical characterization was performed on adherent cells in a sub-confluent culture in CO<sub>2</sub>-independent medium (18045054, Gibco) at 37°C (temperature was maintained by a petri dish heater, JPK Instruments, Germany). AFM measurements on TGBC and ECC4 cell lines were conducted on a *Nanowizard 4* (JPK Instruments). Tip-less cantilevers (PNP-TR-TL, nominal spring constant  $k = 0.08 \text{ N m}^{-1}$ , Nanoworld, Switzerland) decorated a polystyrene bead of 5- $\mu\text{m}$  diameter (PS-R-5.0, microParticles, Germany) each were used as the indenters. The cantilever spring constants were measured prior to each experiment using the thermal noise method implemented in the *JPK SPM* software (JPK Instruments). For each cell three indentation curves were recorded with a piezo extension speed of  $5 \mu\text{m s}^{-1}$  to a maximum set force of 2 nN. For the microrheology analysis, the cantilever was lowered using a piezo extension speed of  $5 \mu\text{m s}^{-1}$  until a force set point of 1 nN was reached, corresponding to an approximate indentation depth  $\delta_0$  of 1  $\mu\text{m}$ . The lowered cantilever was then oscillated by a sinusoidal motion of the piezo elements at an amplitude of 10 nm for a period of 10 cycles. The oscillations were performed sequentially at different frequencies in the range of 3–200 Hz. Indentation experiments on MCF10A ER-Src cells were conducted as described above, except different tip-less cantilevers (Arrow TL1, nominal spring constant  $k = 0.35\text{--}0.45 \text{ N m}^{-1}$ , Nanoworld) with a 5- $\mu\text{m}$  bead glued at the end were used as the indenter.

*AFM indentation data analysis*

Recorded force-distance curves were converted into force-indentation curves and fitted in JPK data processing software (*JPK DP*, JPK Instruments) using Sneddon's modification of the Hertz model for a spherical indenter<sup>442</sup>:

$$F = \frac{E}{1-\nu^2} \left( \frac{a^2+r^2}{2} \ln \frac{r+a}{r-a} - ar \right), \quad 5.3$$

with

$$\delta = \frac{a}{2} \ln \frac{r+a}{r-a}, \quad 5.4$$

where  $F$  denotes the indentation force,  $E$  the elastic modulus,  $\nu$  the Poisson's ratio,  $a$  the radius of the projected contact area formed between the sample and the indenter,  $r$  the radius of the indenter, and  $\delta$  the indentation depth. Poisson ratio was set to 0.5.

*AFM microrheology data analysis*

The force and indentation signals from oscillatory measurements were fitted using a sinusoidal function to extract the amplitude and phase angle of each signal. Data were analyzed analogously to the procedure described by Alcaraz *et al.*<sup>25</sup> but for a spherical not a pyramidal indenter. Briefly, the method relies on the linearization of the Hertz model for a spherical indenter due to small oscillations by using the first term of the Taylor expansion and subsequent transformation to the frequency domain:

$$F(\omega) = 2 \frac{E^*(\omega)}{(1-\nu^2)} \sqrt{r\delta_0} \delta(\omega), \quad 5.5$$

where  $F(\omega)$  and  $\delta(\omega)$  are the force and indentation signals in the frequency domain, respectively,  $E^*(\omega)$  is the complex Young's modulus,  $\nu$  is the Poisson's ratio assumed to be 0.5,  $r$  is the radius of the indenter and  $\omega$  is the angular frequency. The complex shear modulus  $G^*(\omega)$  can be written using  $G^*(\omega) = \frac{E^*(\omega)}{2(1+\nu)}$ <sup>501</sup>:

$$G^*(\omega) = G'(\omega) + iG''(\omega) = \frac{(1-\nu) F(\omega)}{4\sqrt{r\delta_0} \delta(\omega)}, \quad 5.6$$

where  $G'(\omega)$  is the storage modulus and  $G''(\omega)$  is the loss modulus. The ratio of the force  $F(\omega)$  and indentation  $\delta(\omega)$  is calculated from the measured amplitudes  $A^F(\omega)$  and  $A^\delta(\omega)$  and the phase shifts  $\theta^F(\omega)$  and  $\theta^\delta(\omega)$  of the oscillatory signals<sup>502</sup>:

$$\frac{F(\omega)}{\delta(\omega)} = \frac{A^F(\omega)}{A^\delta(\omega)} e^{i(\theta^F(\omega) - \theta^\delta(\omega))}, \quad 5.7$$

where the difference of the phase shifts  $(\theta^F(\omega) - \theta^\delta(\omega))$  is in the range of  $0^\circ$  (elastic solid) and  $90^\circ$  (viscous fluid). Furthermore, the hydrodynamic drag contribution on the cantilever oscillation was estimated and subtracted from the complex shear modulus as previously described<sup>503</sup>:



$$G^*(\omega) = \frac{(1 - \nu)}{4\sqrt{R\delta_0}} \left[ \frac{F(\omega)}{\delta(\omega)} - i\omega b(0) \right], \quad 5.8$$

where  $b(h)$  is the hydrodynamic drag coefficient function measured from non-contact oscillations of the cantilever at different distances  $h$  from the sample, and  $b(0)$  is the extrapolation to distance 0 from the sample. For PNP-TR-TL cantilevers, the hydrodynamic drag coefficient was estimated to be  $b(0) = 5.28 \mu\text{N s m}^{-1}$ .

### 5.4.3. Perturbation experiments

#### *CAV1 knock-down*

For RNAi experiments, cells were transfected using RNAiMax reagent (13778030, Thermo Fisher Scientific) and a reverse transfection protocol. Per transfection, 200 ng of esiRNA (Eupheria Biotech, Germany) or 300 ng of ON-TARGETplus siRNA (Dharmacon, CO, USA) and 2  $\mu\text{l}$  RNAiMax were prepared in OptiMEM (31985062, Gibco) according to the manufacturer's instructions and pipetted onto 12-well plates (see **Table 5.6** for list of siRNAs used). Cells in 1 ml of culture medium were plated on top of the transfection mix at a density allowing for sub-confluent growth within the experimental timeframe. 72 h post transfection, cells were collected for the mechanical characterization and Western blot analysis.

**Table 5.6 | siRNAs used in the CAV1 knock-down experiments.**

name	target	commercial name	cat no	vendor
rLuc	Renilla Luciferase	RLUC	RLUC	Eupheria Biotec
esiCAV1-1	human caveolin 1	hCAV1	HU-03125-1	Eupheria Biotec
esiCAV1-2	human caveolin 1	hCAV1, custom design	HU-03125-2	Eupheria Biotec
esiCAV1-3	human caveolin 1	hCAV1, custom design	HU-03125-3	Eupheria Biotec
nonT	non-targeting	ON-TARGETplus Non-targeting Pool	D-001810-10-05	Dharmacon
CAV1-pool	human caveolin 1	ON-TARGETplus Human CAV1 siRNA, SMARTPool	L-003467-00-0005	Dharmacon

#### *Plasmid for CAV1 overexpression*

The plasmid used for CAV1 overexpression was prepared in our group by Dr. Maria Winzi. The cDNA of *CAV1* was amplified by PCR, introducing NheI and XhoI restriction sites in the flanking regions. The PCR product was then cloned into the pCGIT destination vector (a kind gift from P. Serup, University of Copenhagen, Denmark) under the CAG promoter and with dTomato fluorescent marker under internal ribosomal entry site (IRES) downstream of CAV1.

*Transient CAV1 overexpression in ECC4 and TGBC cells*

ECC4 and TGBC cells were transiently transfected with the CAV1 overexpression plasmid by electroporation using Neon Transfection System (MPK5000, Thermo Fisher Scientific). Per transfection  $0.3 \times 10^6$  ECC4 cells, or  $0.2 \times 10^6$  TGBC cells were mixed with 1  $\mu$ g of plasmid DNA in PBS. Electroporation was conducted using 10  $\mu$ l Neon tips (MPK1096, Thermo Fisher Scientific) and a program of two pulses of 1050 V and 30 ms duration each. Electroporated cells were transferred to 500  $\mu$ l of fresh culture medium in a 24-well plate. The cells were collected for mechanical characterization and Western blot analysis 72 h post transfection. To identify fluorescent cells during mechanical characterization, the combined real-time fluorescence and deformability cytometry (RT-FDC)<sup>312</sup> setup was used, and the maximum intensity of the fluorescence signal from channel 2 (excitation 561 nm, 10% laser power; collection 700/75) was used for gating.

*Transient CAV1 overexpression in MCF10A-ER-src cells*

MCF10A-ER-src cells were transiently transfected with the CAV1 overexpressing plasmid using Effectene transfection reagent (301425, Qiagen). 24 h before transfection, cells were seeded on glass bottom dishes (35-mm; FluoroDish; FD35100, WPI, FL, USA) at a density of 20,000 cells per well. Transfection was performed according to the manufacturer's instruction using following reagent volumes per well: 75  $\mu$ l EC buffer, 0.6  $\mu$ g plasmid DNA, 4.8  $\mu$ l Enhancer and 6  $\mu$ l Effectene reagent. 24 h post transfection cells were induced with 1  $\mu$ M TAM. Mechanical analysis was performed after additional 72 h of culture.

*Western blotting*

For Western blot analysis of carcinoma and MCF10A-ER-Src cell lines, cell pellets were collected in parallel with mechanical measurements and lysed using ice-cold RIPA buffer (89900, ThermoFisher Scientific) supplemented with protease/phosphatase inhibitor cocktail (78441, ThermoFisher Scientific) and benzonase (E1014, Sigma Aldrich). The lysates were cleared at 4°C by 10-minute sonication followed by 10-minute centrifugation at 16,900 g. Obtained supernatants were mixed with Laemmli buffer (final concentration: 62.5 mM Tris-HCl (pH 6.8), 2% SDS, 10% glycerol, 5%  $\beta$ -mercaptoethanol, 0.01% bromophenol blue), boiled (5 min at 95°C), and separated by SDS-PAGE electrophoresis on 4–20% gradient gels (Mini-PROTEAN TGX Precast Gels; 4561093, Biorad, CA, USA) in MOPS SDS Running buffer (B0001, ThermoFisher Scientific). After transferring the proteins onto a PVDF membrane (Merck Millipore), the membranes were blocked in TBS-T (20 mM Tris, 137 mM NaCl, 0.1% Tween) containing 5% w/v skimmed milk powder (T145.1, Carl Roth, Germany) for 40 minutes. Next, membranes were incubated with the primary anti-Cav1 (1:1000; D46G3; #3267, Cell Signaling Technology, MA, USA) and anti-GAPDH (1:5000; ab9485, Abcam, UK) antibodies at 4°C overnight in 5% milk/TBS-T, washed, and incubated with anti-rabbit HRP-conjugated secondary antibody (1:4000; ab97069, Abcam). Chemiluminescence detection was performed using Pierce Enhanced Chemi-Luminescence (ECL) substrate (32109, ThermoFisher Scientific) and ECL films

(GE28-9068-37, Merck Millipore). Films were developed in an OptiMax X-ray film processor (KODAK, NY, USA). Quantitative analysis was performed on scanned films using the gel analysis tool in *ImageJ* version 2.0.0-rc-69/1.52p (<https://imagej.nih.gov/>). For western blot analysis of MEFs (performed by Dr. Fidel-Nicolas Lolo) the same anti-Cav1 antibody (1:1000; D46G3; #3267, Cell Signaling) was used, and anti-tubulin antibody (1:2000; DM1A; #3873, Cell Signaling) was used as a loading control. Goat anti-mouse 680 and goat anti-rabbit 800 (1:2000; A28183 and A32735, ThermoFisher Scientific) antibodies were used for secondary detection. Membranes were scanned with the Odyssey imaging system (LI-COR Biosciences, NE, USA).

#### 5.4.4. Computational analysis

##### *Transcriptomic datasets*

Transcriptomic datasets were retrieved from online databases (Gene Expression Omnibus, GEO and DNA Data Bank of Japan, DDBJ) with accession numbers listed in **Table 5.1**. Overview of experimental detail for RNA profiling procedures and data analysis in individual datasets is presented in **Supplementary Table D.5**. The IDs of samples used in respective categories in each dataset are listed in **Supplementary Table D.6**. In case of multiple entries for the same gene in a given transcriptomic dataset, the expression values were averaged, so that only one entry per gene and sample was available.

##### *PC-corr analysis*

PC-corr analysis procedure was established by and performed under guidelines of Dr. Yan Ge and Prof. Carlo Cannistraci from Biotec, TU Dresden. Before the analysis, glioblastoma and iPSC datasets were reduced to the common intersection (9,452 genes) and normalized by taking the log10 (glioblastoma) or zscore (iPSC). PC-corr was conducted individually on respective datasets as described by Ciucci *et al.*<sup>453</sup>. PCA was performed using *svd* function in *MATLAB* (R2020a, MathWorks, MA, USA) on normalized datasets. For the iPSC dataset, only samples classified as F- and C-class (6 and 22 samples, respectively; indicated in **Supplementary Table D.6**) were used for PCA, while the Pearson's correlation was computed across all 51 samples available in the dataset. For the glioblastoma dataset, all 27 samples were used throughout. For each dataset, the original PC loadings from the component providing good separation of sample categories (PC1 for both analyzed datasets) were normalized and scaled. The processing of the PC loadings is performed to adjust the distribution of the loadings to the range corresponding to that of Pearson's correlation values  $[-1,1]$ . The normalization was performed using a following previously function<sup>453</sup>:

$$V_i^* = \text{sgn}(V_i^0) \log_{10} \left( 1 + \frac{|V_i^0|}{\langle |V^0| \rangle} \right), \quad 5.9$$

where  $V_i^*$  denotes the normalized loading corresponding to the  $i$ -th feature,  $V_i^0$  the original loading corresponding to the  $i$ -th feature, and  $\langle |V^0| \rangle$  the average of all absolute loadings of the vector  $V^0$ .

After normalization, the loadings were scaled to fall on the interval  $[-1,1]$  using a custom function<sup>453</sup>:

$$V_i = \text{sgn}(V_i^*) \frac{|V_i^*| - \min(|V^*|)}{\max(|V^*|) - \min(|V^*|)}, \quad 5.10$$

where  $V_i$  denotes the processed loading corresponding to the  $i$ -th feature, and  $|V^*|$  the vector containing absolute values of all normalized loadings.

The *PC-corr* values for each pair of features were computed according to **Equation 5.1**. The PC-corr results of the glioblastoma and iPSC datasets were combined as described in the results section. Gene pairs showing different *PC-corr* signs were masked by setting the *PC-corr<sup>comb</sup>* to zero. The genes and edges for network construction were obtained via thresholding strategies described in the main text. The network was visualized using *cytoscape* (*cytoscape 3.8.0*; <https://cytoscape.org/>)<sup>504</sup>.

#### *Statistical analysis*

RT-DC datasets were compared using generalized linear mixed-effects models in *Shape-Out* (*Shape-Out 1.0.1*; Zellmechanik Dresden). AFM datasets were compared using two-sided Wilcoxon rank sum test in *MATLAB* (R2020a, MathWorks). Western blot results were compared using a two-sided two-sample *t*-test in *MATLAB* (R2020a, MathWorks).

#### *Data and code availability*

The transcriptomic data used in this study were obtained from public repositories under accession numbers listed in **Table 5.1**. The mechanical characterization data are deposited on figshare (<https://doi.org/10.6084/m9.figshare.c.5399826>). The MATLAB code for performing the PC-corr analysis was based on the code deposited alongside a previous publication<sup>453</sup>, accessible on GitHub [https://github.com/biomedical-cybernetics/PC-corr\\_net](https://github.com/biomedical-cybernetics/PC-corr_net).

## Conclusions and Outlook

This thesis consolidates single-cell mechanical phenotyping using microfluidic-based methods across timescales and cell state transitions. First, it presents recent developments of RT-DC, its transformation into a versatile image-based cell characterization and sorting platform, and its validation against two other deformability cytometry platforms operating at different timescales. Next, it leverages the high-throughput of RT-DC for population-wide tracking of mechanical phenotype changes in cell fate transitions on the example of (de-)differentiation along neural lineage. Finally, it introduces a systematic approach for hypothesis-free identification of molecular regulators of cell mechanics. In this section, I synthesize the main conclusions of the presented projects and highlight the most promising future research directions.

### **RT-DC is a versatile method for single-cell characterization and sorting**

Throughout this thesis, a breadth of cell types undergoing transitions connected to mechanical phenotype changes was characterized using RT-DC. Across the different chapters, I performed measurements of blood cells (**Chapter 2**), promyelocytic leukemia cell line (HL60; **Chapter 3**), multipotent (NPCs) and pluripotent (ESCs, EpiSCs, iPSCs) cell lines derived from mouse (**Chapter 4**), cancer cell lines originating from different human tissues (breast, intestine, stomach, lung, and brain; **Chapter 5**), as well as developing neurons isolated from mouse fetus (**Chapter 5**). The studied cell state transitions included models of physiological (e.g., cell differentiation; **Chapter 4**) and pathological (e.g., cancerous transformation; **Chapter 5**) processes, as well as externally-induced perturbations such as pharmacological treatments (LatB; **Chapter 3**), expression perturbations (CAV1; **Chapter 5**), or exposure to osmotic shocks (**Chapter 3**). Together, these projects encompass a comprehensive overview of the applicability of RT-DC for mechanical characterization of cells and demonstrate the versatility of the method.

I have further demonstrated, in two specific examples, the usefulness of parallel detection of fluorescence and cell mechanical properties offered by RT-FDC. First, I used SSEA1/CD24 surface marker staining to classify cells by their identity at intermediate stages of reprogramming from fNPCs to iPSCs (**Chapter 4**). Second, I used fluorescent protein marker co-expressed with CAV1 to identify successfully transfected cells in transient overexpression experiments (**Chapter 5**). Such classification based on marker expression is particularly useful when performing experiments with low transfection efficiency. The transfected cells can be identified based on their fluorescence signal directly during mechanical measurements, eliminating the need of pre-sorting.

The assessment of cell deformability in RT-DC is based on acquired images. These images are available for extraction of further parameters such as cell size, brightness, or aspect ratio in real-time during the experiment. The combination of two or more of these parameters can serve for efficient classification of cells in mixed populations, as illustrated on the example of the combination of deformation, size, and brightness for classification of blood cell types (Toepfner *et al.*<sup>5</sup> and **Sections 2.3.1** and **2.3.2**). Thanks to the recent addition of SSAW-based deflection mechanism, all of the extracted parameters can be utilized for active sorting of cells (**Section 2.2.2**). Furthermore, the images generated during RT-DC experiments can be used to train NNets to classify and sort cells. To explore this possibility, we demonstrated that neutrophils can be sorted from whole blood using a NNet trained on a dataset labelled for cell identity with surface markers (**Section 2.3.3**). The transfer of molecular specificity conferred in surface markers to image-based label-free cell sorting is not restricted to neutrophils and can be applied to any other cell type. Sorting of cells without the need for extrinsic labels is of particular value for downstream application of cells for regenerative medicine purposes.

### **Future of RT-DC will be driven by its integration with AI and its implementation for screening**

In every RT-DC measurement, thousands of events are captured within seconds, providing vast amounts of data that are perfectly suited for development of AI-based classification algorithms. Both, the parameters describing the cells<sup>314</sup>, as well as raw cell images<sup>313,315</sup> can be used to train AI-based algorithms to distinguish cell types of interest in heterogenous populations in a label-free manner. Furthermore, clustering of events based on the parameters derived from RT-DC — for example, with an aid of dimensionality reduction techniques such as UMAP<sup>505</sup> or t-SNE<sup>506</sup> — could lead to identification of new, previously unknown cell populations, for which surface markers are not available.

Apart from its use for the classification of cell types within samples, AI can also be employed for classification of samples originating from different conditions, for example to distinguish signatures of healthy and diseased patients, or to grade the severity of studied conditions<sup>10</sup>. With growing numbers of mechanical fingerprints attained with RT-DC from clinical studies, phenotyping cells from blood and other liquid as well as solid biopsies, such methods will become increasingly relevant. For successful implementation of the automated classification algorithms, it is important that the data is acquired in standardized way. Therefore, the conditions of the experiments should be carefully controlled for issues such as, for example, intensity of illumination or focus. Alternatively, the training datasets need to account for the potential sources of measurement variability.

With the rapid acquisition of data and short sample processing time, RT-DC is predestined to be applied for screening. In particular, genetic perturbations (RNAi<sup>343</sup>/CRISPR<sup>344</sup>) or FDA-approved small molecule libraries could be used to screen for regulators of mechanical properties of cells or of other morphological features. Furthermore, for all conditions in which mechanical phenotype changes

are associated with disease, RT-DC could serve as a screening platform for drug targets. Performing large-scale screens will be further facilitated by parallelization and automatization of sample handling that are being developed for a future generation of the device.

### **Measurement timescale affects outcomes of mechanical measurements**

The standardized comparative analysis of the three major microfluidics-based deformability cytometry classes (**Chapter 3**) showed that probing cells at high strain rates abolishes sensitivity to actin cytoskeleton disassembly. While all three tested methods detected osmotic shock-induced changes in cell deformability, the deformability increase upon drug-induced actin disassembly was detected by cDC and sDC operating at the timescales of 10 ms and 1 ms, respectively, but not by xDC operating at 10- $\mu$ s timescale. These results highlight the need of careful choice of probing method depending on the studied research question. To gain further insights into the contributions of various cell component to the measurements with different methods, this comparative study could be extended by targeting other cellular structures, such as the cell nucleus. Furthermore, elastic beads mimicking cells<sup>323,386</sup> could be used to study the range of the deformability responses obtained for beads with defined Young's moduli across the different platforms.

Apart from directly comparing three deformability cytometry methods operating at different timescales, this thesis also includes AFM-based measurements of cell stiffness that cover further timescales (in **Chapters 4 and 5**). While the deformability cytometry methods cover timescales from  $\mu$ s to ms, the AFM indentation was performed on a 0.2-s timescale and the cell probing in AFM oscillatory measurements was performed on the timescales of 5 ms (200 Hz)–0.5 s (3 Hz) (**Figure 3.7**). In general, the mechanical differences observed with AFM qualitatively confirm the results obtained with RT-DC. The absolute Young's modulus values, however, appeared to increase with the probing frequency across the methods (**Supplementary Table C.1, C.2, and D.4; Supplementary Figure D.4**), with RT-DC yielding the highest Young's moduli. While cell stiffening within increasing probing rate was reported for AFM indentation<sup>23,24</sup> and microrheology assays<sup>22,25–27</sup>, a cross-method analysis of this effect, such as the one reported here, could be performed on a larger scale in the future.

### **Changes in mechanical properties of cells accompany cell fate transitions and further studies on causality, in particular in the context of tissue, are required**

In the study of the developmental transitions along neural lineage (**Chapter 4**), I showed that fNPCs become progressively stiffer during reprogramming to pluripotency and that in the reverse process of neural differentiation iPSCs become softer and re-acquire the phenotype of fNPCs. Importantly, the phenotype of iPSCs corresponded to that of ESCs, the pluripotent cells established directly from mouse embryo. This suggests that the mechanical properties are inherent to the developmental stage of cells,

and thus could be used as a marker of pluripotency in regenerative medicine applications. Furthermore, the insights gained from this study can help to anticipate mechanical changes occurring during neural fate commitment *in vivo* and to speculate about the contribution of mechanical phenotype of cells to embryogenesis.

To understand whether the changes in mechanical properties that accompany cell fate transitions have a causative role in developmental progression, future perturbation studies are required. For this purpose, newly established regulators of cell mechanics, such as *CAV1* identified in the mechanomics approach presented in **Chapter 5**, could be used to interfere with mechanical properties of the cells. In *in vitro* studies, the tracking of cell fate changes upon perturbation of mechanical properties would shed light on the role of mechanical properties in establishing cell fate. To comprehensively tackle the influence of cell mechanics on development and morphogenesis, such perturbation studies could be further performed in a 3D context of developing tissue, for example in reconstitution systems mimicking embryogenesis<sup>436–438</sup>.

### **Regulators of cell mechanics identified with data-driven approaches will provide tools for tuning of mechanical properties in physiologically relevant contexts**

In **Chapter 5**, we established a method for *de novo* identification of cell mechanics regulators that we termed mechanomics. Using discriminative network analysis of transcriptomic data associated with mechanical phenotype changes, we identified a module of five putative cell mechanics regulators (*CAV1*, *FHL2*, *IGFBP7*, *TAGLN*, and *THBS1*) and showed that *CAV1* provides for the best classification of soft and stiff cell states *in silico*. We further showed in genetic perturbation experiments that *CAV1* is not only correlated with, but also causative of mechanical phenotype change, thus, it could potentially serve as a knob for tuning cell stiffness. Providing tools that enable tuning of cell mechanical properties is important for exploring physiological and pathological roles of cell mechanics. Importantly, the genetic targets identified in our study are, in principle, compatible with *in vivo* use, and could be perturbed with spatial and temporal control in context of a tissue using drug inducible expression systems (such as Tet-On<sup>507</sup>), cell type-specific promoters, or optogenetic activation.

The current implementation of the mechanomics approach constitutes a pilot study, that should be expanded in the future. With growing amount of available transcriptomic data and increasing popularity of mechanical characterization of cells, a much bigger database of mechanics-associated transcriptomes will likely be assembled and enable a next-generation analysis.



**Single-cell mechanical properties are only one piece of a puzzle**

In this thesis, I have focused on characterization of whole-cell mechanical properties of individual cells. Such single-cell mechanical phenotype can serve as a marker of cell state and carry functional consequences. However, in a living organism, cells do not exist in isolation, and mechanical properties of individual cells interplay with many other factors to guide physiological processes. For example, the migration and invasiveness of cancer cells is influenced not only by the mechanical phenotype of the cells themselves, but also by the mechanical properties of the microenvironment, the interactions with neighboring cells, and the ability of the cells to form adhesions<sup>37,508</sup>. Similar complexity of biophysical factors plays a role in cell migration and positioning during developmental progression<sup>142,143,509</sup>. Moreover, in many instances cellular functions are driven not by the static, whole-cell mechanical properties, but by their dynamic evolution over time or local heterogeneities<sup>30</sup>. Thus, for a comprehensive understanding of physiological and pathological processes, whole-cell mechanical properties need to be integrated with broader biophysical characterization of cells and their environment.



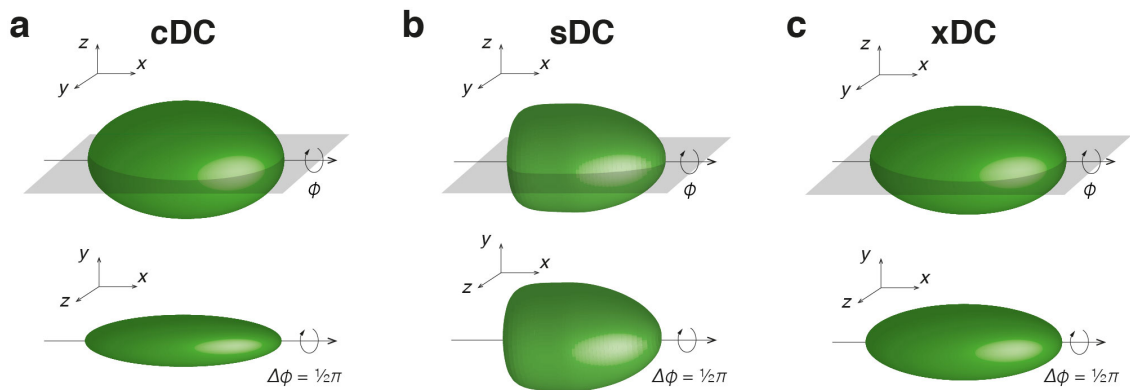
## — Appendix A —

# Estimation of stress and strain characteristic for the different DC methods

This Appendix is adapted with modifications from Urbanska, Muñoz *et al.*<sup>363</sup>.

### A.1. 3D geometry of deformed cells

Upon entering the microfluidic channel, initially spherical cells undergo a three-dimensional shape change resulting in a prolate ellipsoid in case of cDC and xDC or a bullet-like shape in case of sDC (**Supplementary Figure A.1**). Depending on the channel geometry, the resulting cell shape can be rotationally symmetric with respect to the angle  $\phi$  around the rotation axis  $x$  aligned with the longest shape dimension, or rotationally asymmetric.



**Supplementary Figure A.1 | The 3D shapes obtained during microfluidic deformation of spherical objects and their rotational views.** a–c, 3D projections of shapes obtained during cDC (a), sDC (b) and xDC (c) measurements presented from two rotational angles  $\phi$ . The  $xyz$ -directions are given for reference in the upper left corner of each image. The gray transparencies in the upper row indicate  $xy$ -plane. Reprinted from Urbanska, Muñoz *et al.*<sup>363</sup>.

In this work, we used cDC with  $6\ \mu\text{m}$  width and  $15\ \mu\text{m}$  height, what resulted in a deformation into a rotationally asymmetric ellipsoid (**Supplementary Figure A.1a**). sDC channels had a square cross-section of  $20\ \mu\text{m} \times 20\ \mu\text{m}$  resulting in a rotationally symmetric bullet-like shape (**Supplementary Figure A.1b**). xDC channels were  $60\ \mu\text{m}$  wide and  $30\ \mu\text{m}$  high, and the extensional flow caused the cells to compress in  $y$ , and extend in  $x$  and  $z$  in an asymmetric way. As a result, an ellipsoid that is not rotationally symmetric about the  $x$  axis is obtained (**Supplementary Figure A.1c**).

## A.2. Strain estimation

Strain  $\varepsilon$  induced in the cells can be defined as a deviation of the local cell radius  $r$  from the radius of an undeformed cell  $r_0$ , and can be calculated for all polar angles  $\theta$  and rotation angles  $\phi$ :

$$\varepsilon(\theta, \phi) = \frac{r(\theta, \phi) - r_0}{r_0}. \quad \text{A.1}$$

The local strains in  $xy$ -plane,  $\varepsilon_{xy}$ , and  $xz$ -plane,  $\varepsilon_{xz}$ , can be formalized as follows

$$\varepsilon_{xy}(\theta) = \varepsilon(\theta, 0), \quad \text{A.2}$$

$$\varepsilon_{xz}(\theta) = \varepsilon\left(\theta, \frac{\pi}{2}\right). \quad \text{A.3}$$

The maximum absolute strain experienced by the cell,  $\varepsilon_{\max}$ , is defined as

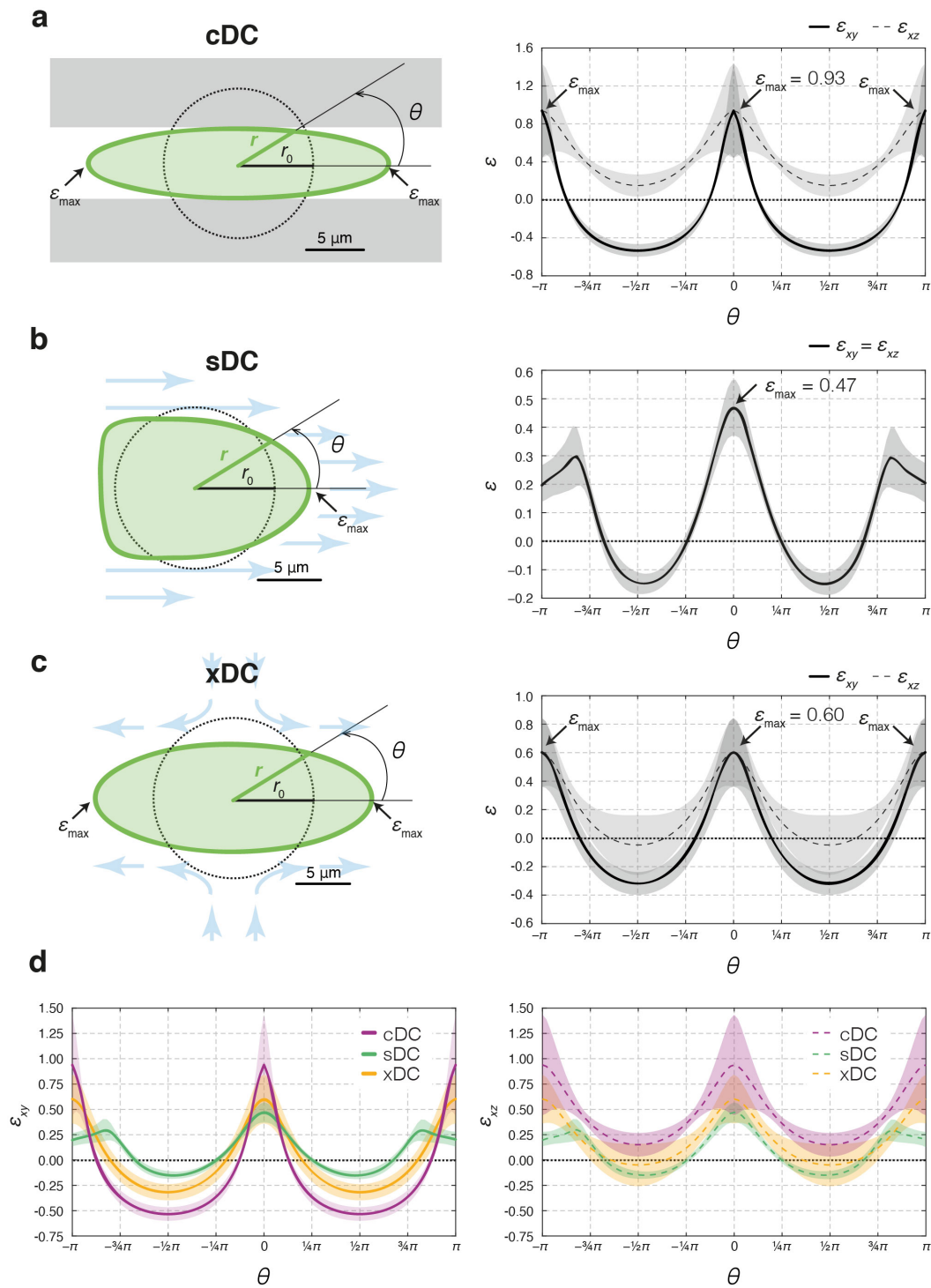
$$\varepsilon_{\max} = \max(|\varepsilon(\theta, \phi)|), \quad \text{A.4}$$

while the mean absolute strain,  $\bar{\varepsilon}$ , experienced over all polar angles  $\theta \in (-\pi, \pi)$  at every rotation angle  $\phi \in (-\pi, \pi)$  can be denoted as

$$\bar{\varepsilon} = \langle |\varepsilon(\theta, \phi)| \rangle. \quad \text{A.5}$$

For cDC,  $r_0$  is estimated for each cell from the measured cell volume as described in **Section 3.4.2**, and  $r(\theta, \phi)$  is calculated assuming volume conservation and a deformation into an ellipsoid with the maximum size in  $y$  and  $z$  determined by the width ( $6 \mu\text{m}$ ) and height ( $15 \mu\text{m}$ ) of the constriction, respectively. The graphical representation of the cell deformation in  $xy$ -plane together with the mean local strain estimates in  $xy$ - and in  $xz$ -planes are presented in **Supplementary Figure A.2a**. The maximum absolute strain,  $\varepsilon_{\max}$ , for an cDC measurement on untreated HL60 cells was located at the ellipse tip along the major axis and amounted to 92%, while the average absolute strain,  $\bar{\varepsilon}$ , amounted to 37%.

For sDC,  $r_0$  is estimated for each cell assuming a sphere of volume equivalent to the volume calculated by rotating a bullet-shaped contour of deformed cell around its symmetry axis.  $r(\theta, \phi)$  represents the distance of the fitted contour to the shape's center of mass. The graphical representation of the cell deformation in the imaging plane  $xy$  as well as mean local strain estimates  $\varepsilon_{xy}(\theta)$  and  $\varepsilon_{xz}(\theta)$  are presented in **Supplementary Figure A.2b**. The maximum absolute strain,  $\varepsilon_{\max}$ , for an sDC measurement on untreated HL60 cells is located at the tip of bullet-like shape and amounted to 47%, while the mean absolute strain,  $\bar{\varepsilon}$ , amounted to 17%.



**Supplementary Figure A.2 | Radial representation of local strain experienced by untreated HL60 cells during microfluidic deformation experiments. a–c**, A graphical representation of undeformed and deformed sphere cross-section in the  $xy$ -plane together with local strain estimate in  $xy$ - and  $xz$ -planes along the polar angle  $\theta$  for cDC (a), sDC (b), and xDC (c). **d**, An overlay of local strain in  $xy$ - (left-hand side) and  $xz$ -planes (right-hand side) for all three methods. For all plots, lines represent means over  $n = 1,428, 928, \text{ and } 6,157$  events for cDC, sDC and xDC, respectively, gathered in one representative experiment on untreated HL60 cells. Shaded areas represent standard deviations. Reprinted from Urbanska, Muñoz *et al.*<sup>363</sup>.

For xDC,  $r_0$  is specified for each cell based on the cell diameter estimated from images of undeformed cell, and  $r(\theta, \phi)$  is calculated assuming volume conservation and a deformation into an ellipsoid with the experimentally determined major and minor axes in the  $xy$ -plane ( $a$  and  $b$  in Figure 1c, respectively). The graphical representation of the cell deformation in the imaging plane  $xy$  as well as mean local strain estimates  $\varepsilon_{xy}(\theta)$  and  $\varepsilon_{xz}(\theta)$  are presented in **Supplementary Figure A.2c**. The maximum absolute strain,  $\varepsilon_{max}$ , for a xDC measurement on untreated HL60 cells was located at the ellipse tip along the major axis and amounted to 60%, while the mean absolute strain,  $\bar{\varepsilon}$ , amounted to 24%.

An overlay of  $\varepsilon_{xy}(\theta)$  and  $\varepsilon_{xz}(\theta)$  for all three methods is depicted in **Supplementary Figure A.2d**.

### A.3. Strain rate estimation

The strain rate is calculated for the individual methods according to the following formula:

$$\dot{\varepsilon} = \frac{d\varepsilon}{dt} = \frac{\bar{\varepsilon}}{\tau}, \quad \text{A.6}$$

where  $\bar{\varepsilon}$  is the mean absolute strain defined in **Equation A.5** and  $\tau$  is the characteristic timescale of the measurement, i.e., the time in which the cell is deformed.  $\tau$  amounts roughly to 10 ms for cDC, 1 ms for sDC, and 10  $\mu$ s for xDC.

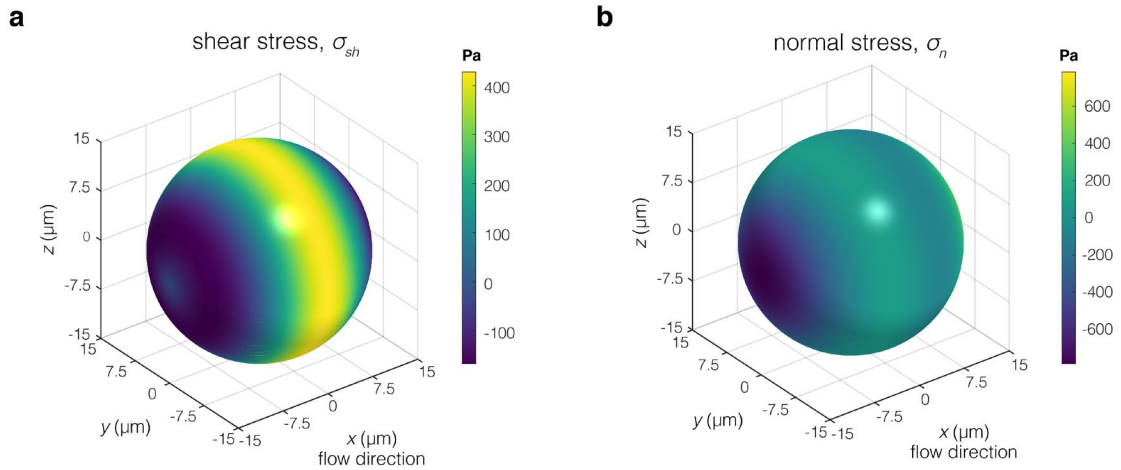
### A.4. Stress estimation

The maximum value of the stress applied to cells passing through the microconstriction in a cDC measurement corresponds to the total applied pressure differential in the system, which was set to 1 kPa. This stress is applied only if the cell tightly fills the entire cross-section of the constriction. In practice, the expected total applied stress is therefore close to, but below, 1 kPa.

In an sDC channel, two types of stresses are acting on a cell: shear stress,  $\sigma_{sh}$ , arising from the gradient of velocity across the channel width and acting tangentially to the cell surface, and normal stress,  $\sigma_n$ , which arises from pressure gradients and acts in the direction perpendicular to the cell surface. These stresses can be estimated analytically for a case of a channel with circular cross-section using a flow-field calculated with stream function approach as previously described<sup>298</sup>. The peak shear stress acting on the cell surface reaches 0.43 kPa, and the peak hydrodynamic pressure 0.78 kPa (see **Supplementary Figure A.3** for the distribution of the stress). Thus, the deformation-relevant peak stresses in sDC are on the order of 1 kPa.

In xDC, there are two type of forces acting on a cell at the cross-slot junction: the drag force and the shear force. The drag force is three order of magnitudes higher than the shear force and is estimated

to exceed  $1 \mu\text{N}^1$ . The corresponding stress acting on a cell with a diameter of  $15 \mu\text{m}$  would reach values exceeding  $5.7 \text{ kPa}$ .



**Supplementary Figure A.3 | Analytical estimation of surface stresses acting on an undeformed sphere passing through a circular channel approximating an sDC experiment. a–b,** A map of hydrodynamic shear stress (a) and normal stress (b) on a surface of a sphere of radius  $6.5 \mu\text{m}$  passing through a cylindrical channel with a diameter of  $20 \mu\text{m}$  at a flowrate of  $0.04 \mu\text{l s}^{-1}$  and medium viscosity of  $5.7 \text{ mPa s}$ , corresponding to the shear-adjusted viscosity of the used measurement buffer<sup>318</sup>. The estimation was performed using previously developed approach<sup>298</sup>. Reprinted from Urbanska, Muñoz *et al.*<sup>363</sup>.





— Appendix B —

Supplementary Material for Chapter 3

Supplementary Tables B.1 – B.2

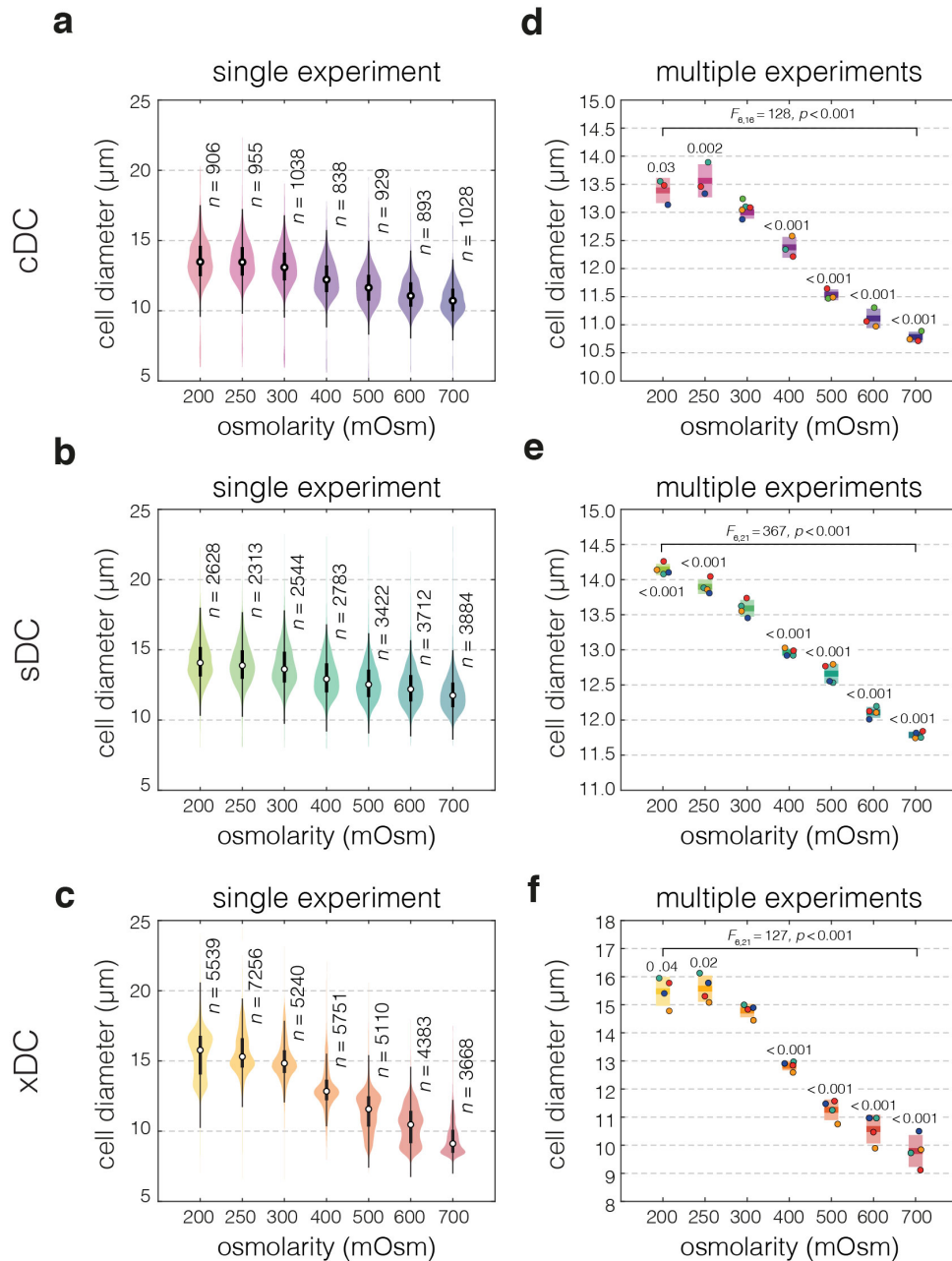
**Supplementary Table B.1 | Fit results for osmotic shock treatment.** The decay constants,  $\lambda$ , for the exponential curve fit to the relative deformability versus normalized osmolarity data for hyperosmotic shock. Fits were performed on medians from  $n = 3, 4,$  and  $4$  independent experiments, for cDC, sDC, and xDC, respectively. The fitted  $\lambda$  values are reported together with 95% confidence intervals, CI, and associated  $p$ -values from two-sided  $t$ -tests for this parameter.

	cDC	sDC	xDC
$\lambda$	1.206 95% CI [1.065, 1.366] $t(16) = 17.26$ $p = 9.14 \times 10^{-12}$	0.780 95% CI [0.695, 0.873] $t(19) = 18.14$ $p = 1.86 \times 10^{-13}$	0.397 95% CI [0.363, 0.433] $t(19) = 24.02$ $p = 1.12 \times 10^{-15}$

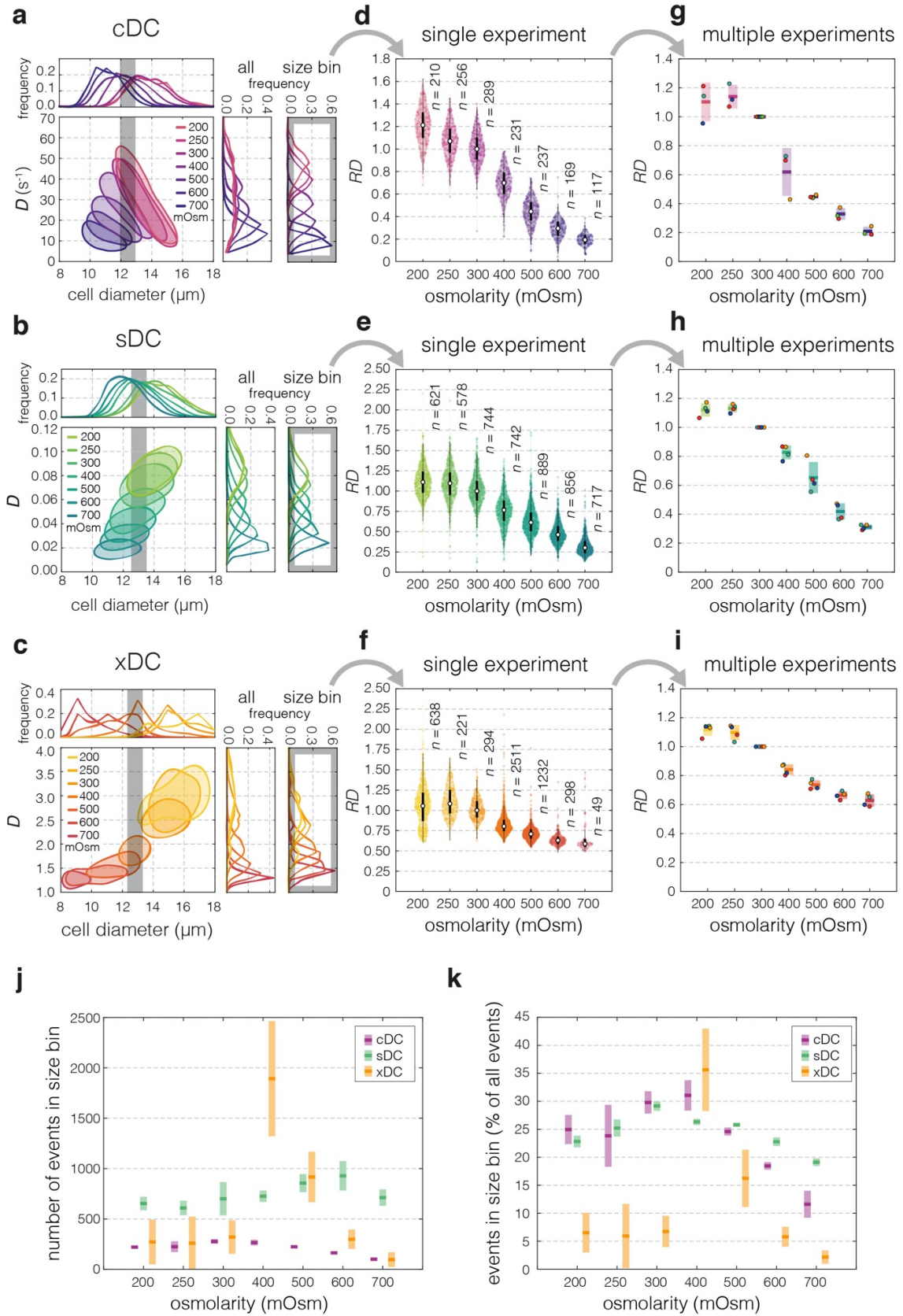
**Supplementary Table B.2 | Fit results for LatB treatment.** Fit parameters for the four-parameter log-logistic regression fit to the relative deformability versus LatB concentration data obtained with cDC, sDC, and xDC. Fits were performed on medians from  $n = 3, 5,$  and  $4$  independent experiments, for cDC, sDC, and xDC, respectively. The fitted values are reported together with 95% confidence intervals, CI, and associated  $p$ -values from two-sided  $t$ -tests for each parameter. This table is adapted from Urbanska, Muñoz *et al.*<sup>363</sup>.

	<b>cDC</b>	<b>sDC</b>	<b>xDC</b>
<b>b (slope)</b>	-4.47 ml ng <sup>-1</sup> 95% CI [-14.13, 5.18] $t(19) = -0.97$ $p = 0.34$	-2.06 ml ng <sup>-1</sup> 95% CI [-3.20, -0.94] $t(31) = -3.74$ $p = 7.57 \times 10^{-4}$	8.71 ml ng <sup>-1</sup> 95% CI [-72.57, 89.99] $t(24) = 0.22$ $p = 0.83$
<b>c (lower limit)</b>	1.04 95% CI [0.97, 1.10] $t(19) = 35.31$ $p < 2.20 \times 10^{-16}$	1.00 95% CI [0.95, 1.05] $t(31) = 38.13$ $p < 2.20 \times 10^{-16}$	0.96 95% CI [0.54, 1.38] $t(24) = 4.69$ $p = 9.03 \times 10^{-5}$
<b>d (upper limit)</b>	1.46 95% CI [1.38, 1.53] $t(19) = 39.71$ $p < 2.20 \times 10^{-16}$	1.52 95% CI [1.44, 1.60] $t(31) = 37.73$ $p < 2.20 \times 10^{-16}$	1.03 95% CI [1.00, 1.06] $t(24) = 77.72$ $p < 2.20 \times 10^{-16}$
<b>e (EC<sub>50</sub>)</b>	11.92 ng ml <sup>-1</sup> , 95% CI [6.82, 17.01] $t(19) = 4.90$ $p = 9.93 \times 10^{-5}$	14.85 ng ml <sup>-1</sup> , 95% CI [9.62, 20.07] $t(31) = 5.80$ $p < 2.20 \times 10^{-16}$	78.24 ng ml <sup>-1</sup> 95% CI [-273.0, 430] $t(24) = 0.46$ $p = 0.65$

## Supplementary Figures B.1 – B.9

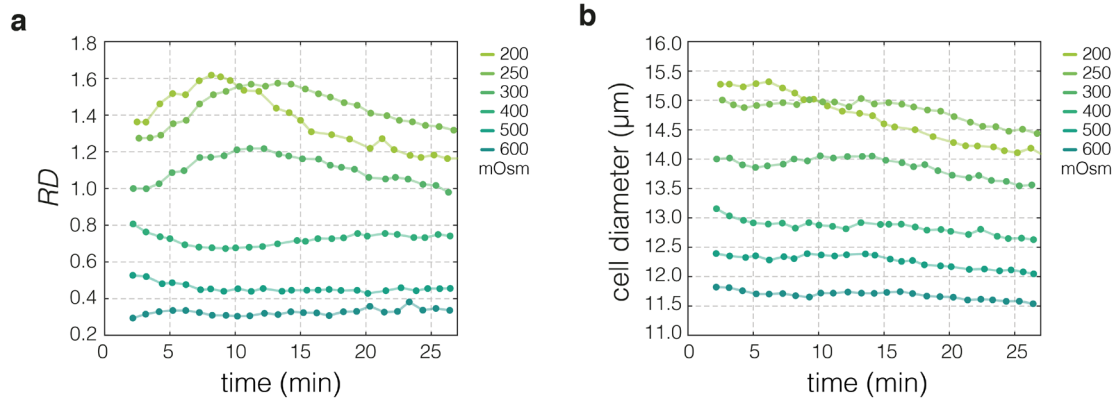


**Supplementary Figure B.1 | Diameter of HL60 cells upon exposure to altered osmolarity.** **a–c**, Violin plots of cell diameter in a representative cDC (**a**), sDC (**b**) and xDC (**c**) experiment. Black boxes extend from 25th to 75th percentiles, with a dot at the median, whiskers indicate  $1.5 \times \text{IQR}$ . **d–f**, Summary of median cell diameter values obtained in all experiment series with cDC (**d**), sDC (**e**) and xDC (**f**). Data points correspond to medians of individual experiments ( $n = 3, 4$  and  $4$ , for cDC, sDC and xDC, respectively). Conditions measured in the same experimental series are color-coded. Boxes span  $2 \times$  standard deviation with a line at the mean of all medians. In **d–f** statistical significance of overall differences among mean cell sizes at different osmolarities was tested using ANOVA and its result is shown on top of the horizontal line overarching all conditions. The  $p$ -values reported above each box come from comparison of the given treatment to the control condition (300 mOsm) obtained through post-hoc analysis using two-sided pairwise  $t$ -tests for multiple comparison with Benjamin-Hochberg  $p$ -value adjustment. Reprinted from Urbanska, Muñoz *et al.*<sup>363</sup>.

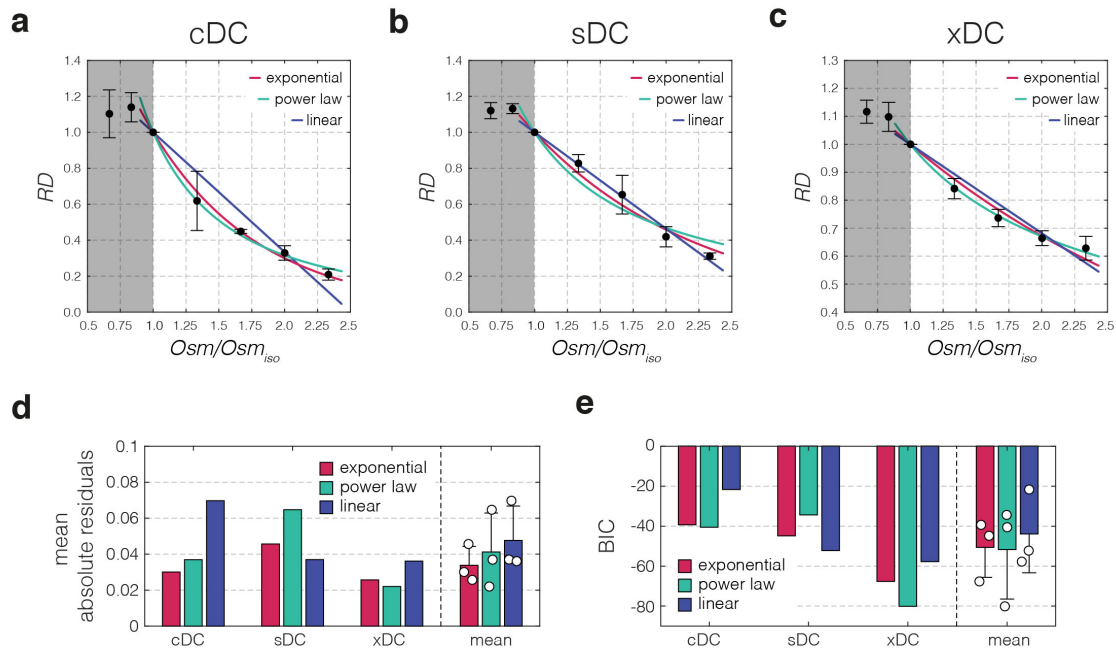


Supplementary Figure B.2 | Visualization of bin selection and data processing for osmolarity experiments. (cont.)

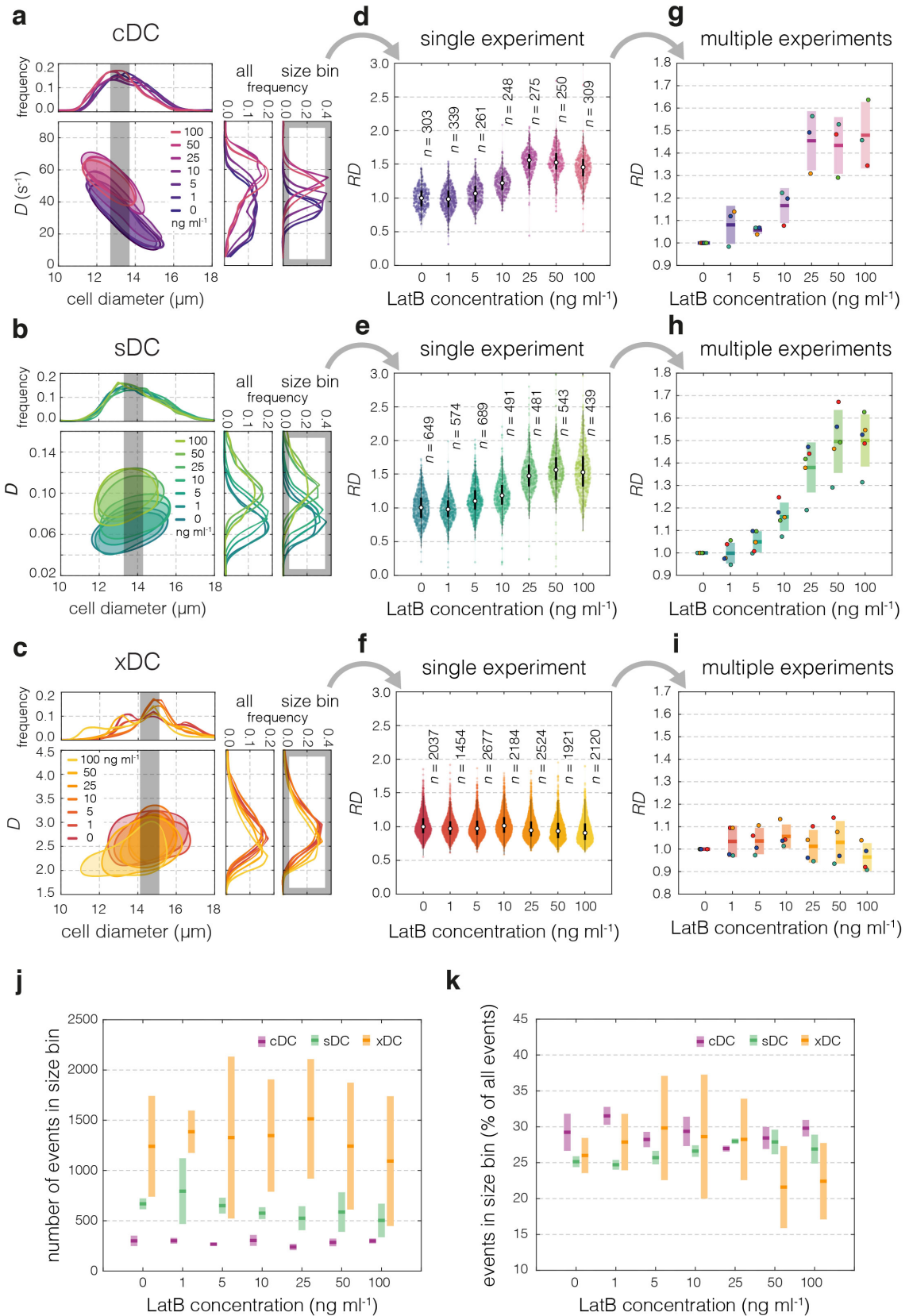
**a–c**, 50%-density contour plots of deformability vs cell diameter for an exemplary experiment on HL60 cells subjected to different osmolarity conditions. The contour plots are accompanied by deformability and cell diameter histograms for cDC (**a**), sDC (**b**), and xDC (**c**). The most represented 1- $\mu\text{m}$  wide diameter bins used for relative deformability,  $RD$ , calculations and the corresponding deformability histograms are outlined in grey. **d–f**, Jitter plots showing distribution of  $RD$  from cDC (**d**), sDC (**e**), and xDC (**f**) measurements for a single experiment. Boxes extend from 25th to 75th percentiles, with a dot at the median, whiskers indicate  $1.5 \times \text{IQR}$  and each data point corresponds to an individual cell. **g–i**, Summary of  $RD$  values obtained in all experimental series with cDC (**g**), sDC (**h**) and xDC (**i**). Data points correspond to medians of every experiment and conditions measured in same experimental series are color-coded. Boxes span  $2 \times$  standard deviation with a line at the mean of all medians. **(j)** Number of events in the selected 1- $\mu\text{m}$  wide diameter bin for each condition and method. **(k)** Events selected within the 1- $\mu\text{m}$  wide diameter as a percentage of all events measured. In **j** and **k**, the boxes span  $2 \times$  standard deviation with a line at the mean. In **g–k**, the statistics have been calculated for  $n = 3, 4$  and  $4$  independent measurement replicates, for cDC, sDC and xDC, respectively. Reprinted from Urbanska, Muñoz *et al.*<sup>363</sup>.



**Supplementary Figure B.3 | Time-resolved effect of osmotic shock on HL60 deformability and size as measured by sDC.** **a–c**, The changes in HL60 deformability,  $D$  (**a**), and cell diameter (**b**) over time after exposure to medium with altered osmolarity as measured by sDC. The experiments were performed in 30- $\mu\text{m}$  channels at a flowrate of  $0.16 \mu\text{l s}^{-1}$ . Data points represent medians of consecutive measurements taken at different times after the exposure to altered osmolarity medium. On average 3,000 events (and not less than 1,800) are analyzed for each data point. Reprinted from Urbanska, Muñoz *et al.*<sup>363</sup>.

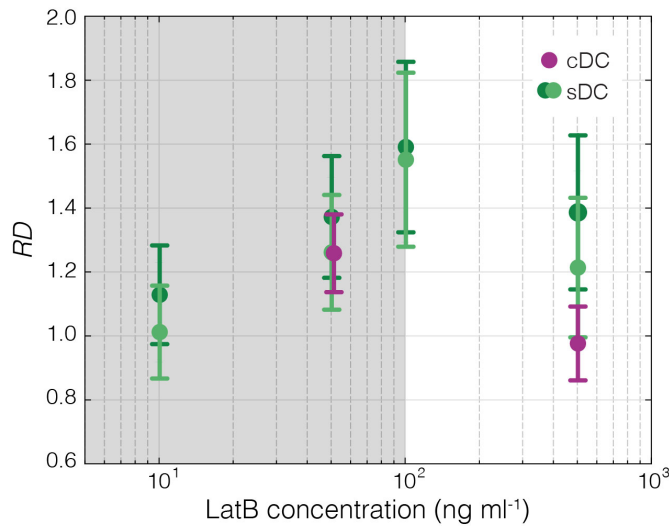


**Supplementary Figure B.4 | Fitting of the relation between osmolarity and relative deformability for hyperosmotic shock data.** **a-c**, Exponential (red), power law (green) and linear (blue) fits to relative deformability,  $RD$ , vs osmolarity data obtained with cDC (**a**), sDC (**b**) and xDC (**c**). Data points in **a-c** represent means of medians of multiple experimental replicates ( $n = 3, 4$ , and  $4$ , for cDC, sDC, and xDC, respectively), error bars represent standard deviation. **d-e**, Bar graphs of mean absolute residuals (**d**) and Bayesian information criterion (BIC) (**e**), that assess the quality of different fits. Values estimated for each method, as well as mean of values for all methods ( $n = 3$ ) for given fit function, are presented. The error bars on the mean plots represent standard deviation. Mean absolute residuals give an information on how much the values predicted by the fitted function deviate from the experimental data. Lower values of residuals indicate better agreement of experimental data with proposed function. In case of BIC, lower values indicate a better fit. Reprinted from Urbanska, Muñoz *et al.*<sup>363</sup>.



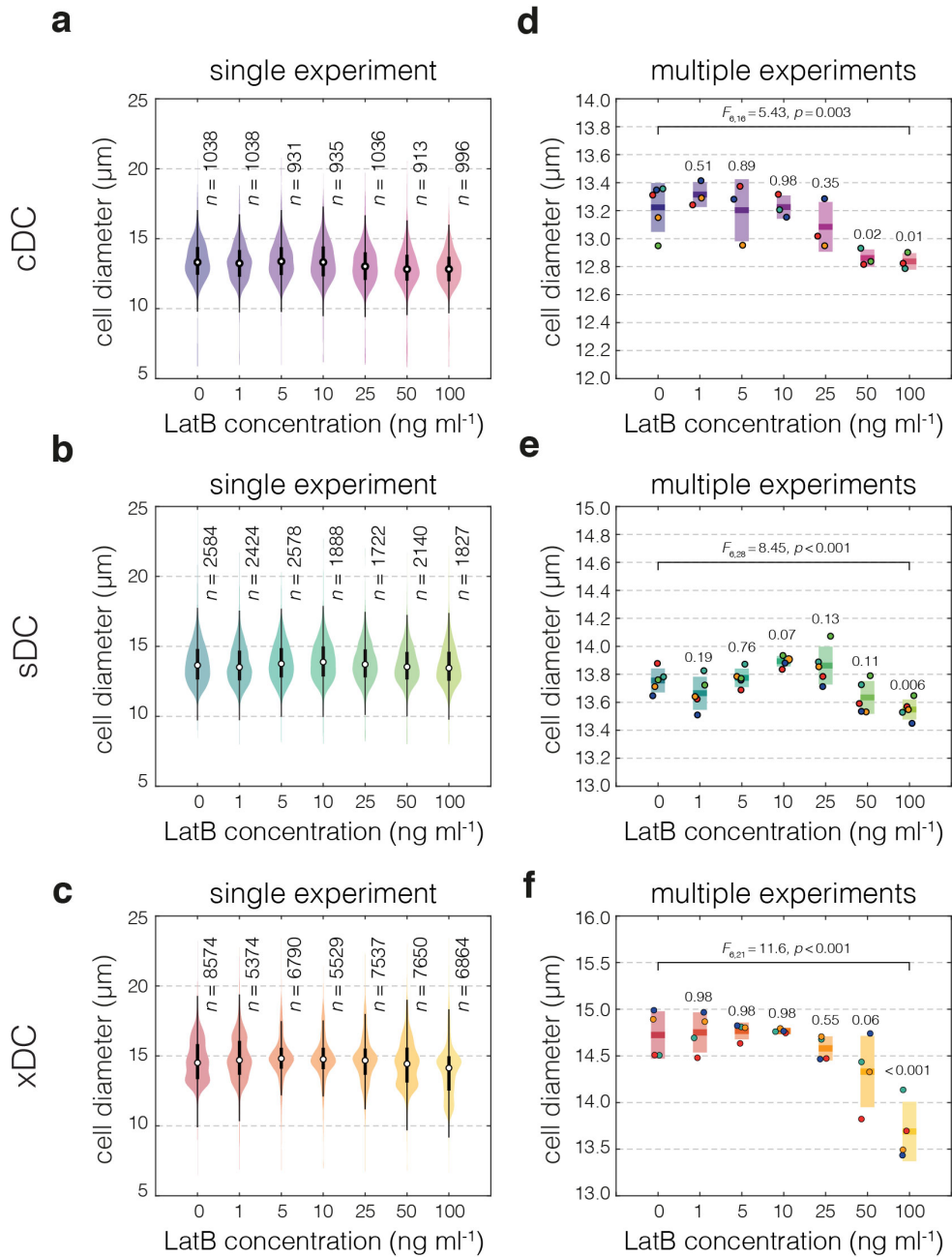
Supplementary Figure B.5 | Visualization of bin selection and data processing for LatB treatment experiments. (cont.)

**a–c**, 50%-density contour plots of deformability vs cell diameter for an exemplary experiment on HL60 cells treated with increasing concentration of LatB. The contour plots are accompanied by deformability and cell diameter histograms for cDC (**a**), sDC (**b**), and xDC (**c**). The most represented 1- $\mu\text{m}$  wide diameter bins used for relative deformability,  $RD$ , calculations and the corresponding deformability histograms are outlined in grey. **d–f**, Jitter plots showing distribution of  $RD$  from cDC (**d**), sDC (**e**), and xDC (**f**) measurements for a single experiment. Boxes extend from 25th to 75th percentiles, with a dot at the median, whiskers indicate  $1.5\times$  IQR and each data point corresponds to an individual cell. **g–i**, Summary of  $RD$  values obtained in all experimental series with cDC (**g**), sDC (**h**) and xDC (**i**). Data points correspond to medians of every experiment and conditions measured in the same experimental series are color-coded. Boxes span  $2\times$  standard deviation with a line at the mean of all medians. (**j**) Number of events in the selected 1- $\mu\text{m}$  wide diameter bin for each condition and method. (**k**) Events selected within the 1- $\mu\text{m}$  wide diameter as a percentage of all events measured. In (**j**) and (**k**) the boxes span  $2\times$  standard deviation with a line at the mean. In **g–k**, the statistics have been calculated for  $n = 3, 5$  and  $4$  independent measurement replicates, for cDC, sDC and xDC, respectively. Reprinted from Urbanska, Muñoz *et al.*<sup>363</sup>.



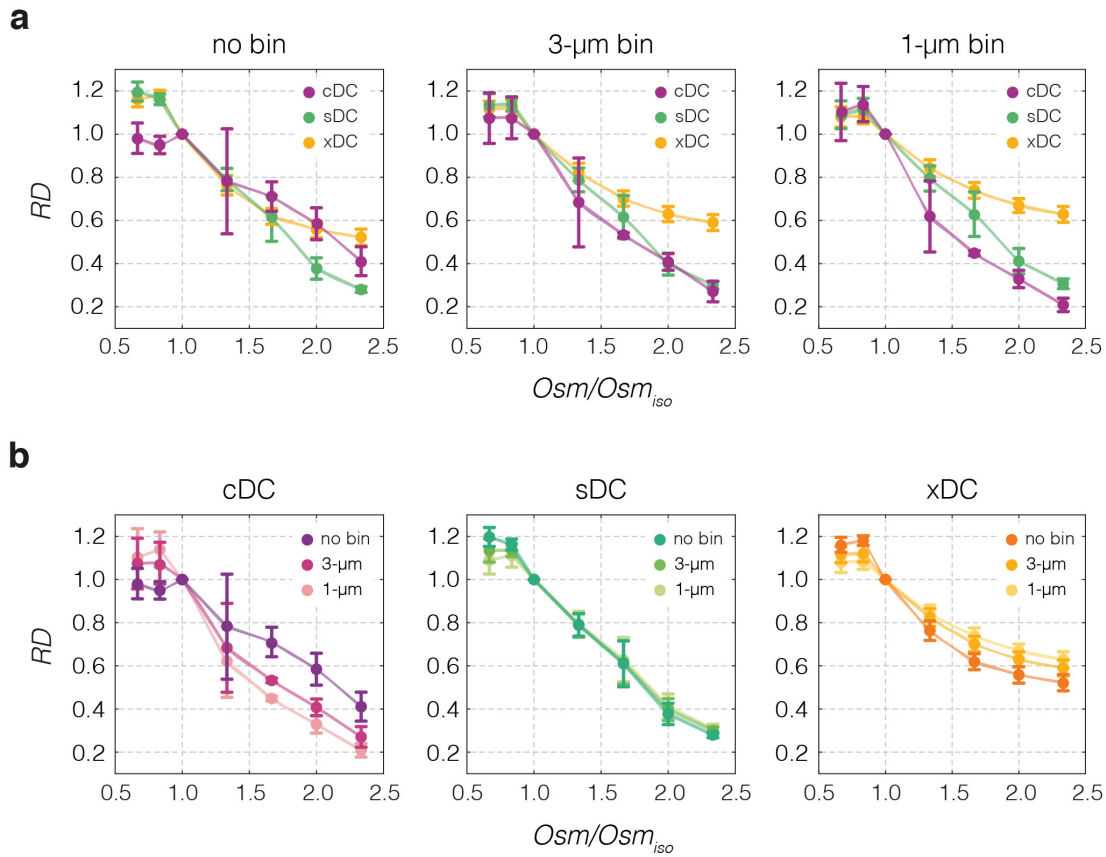
**Supplementary Figure B.6 | Response to high LatB concentrations measured with cDC and sDC.** The graph shows relative deformability,  $RD$ , as a function of LatB concentration. Dots represent medians of individual measurements. Error bars represent median absolute deviation. Bin-selected data was used. One measurement series was performed using cDC (purple, from left to right  $n = 296$  and  $271$  analyzed cells in the selected size bin per data point) and two measurement series were performed using sDC (bright and dark green, from left to right  $n = 656, 537, 420, 550$ , and  $n = 734, 615, 336, 541$  analyzed cells in the selected size bin, for bright and dark green data points, respectively). The concentration range used for main analysis is shaded in gray. Reprinted from Urbanska, Muñoz *et al.*<sup>363</sup>.



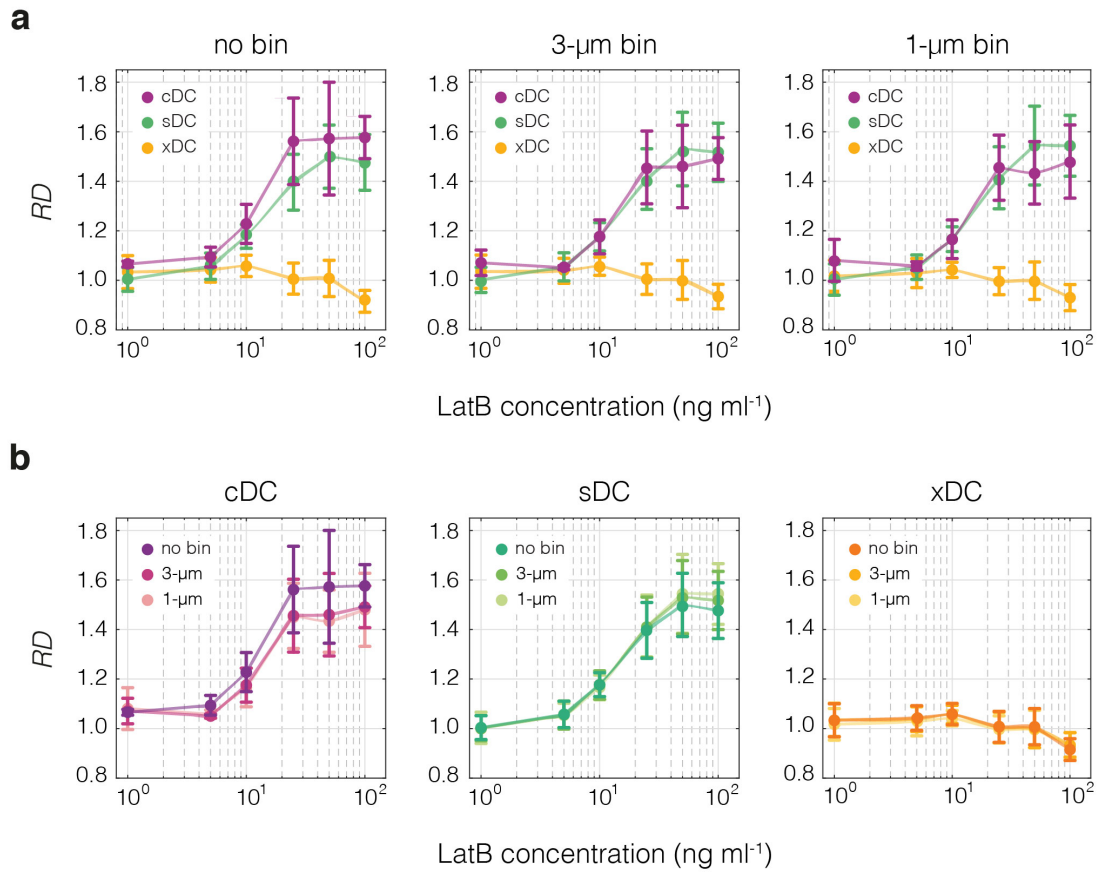


**Supplementary Figure B.7 | Diameter of HL60 cells treated with different concentrations of LatB.**

**a–c**, Violin plots of cell diameter in a single experiment as measured by cDC (**a**), sDC (**b**) and xDC (**c**). Black boxes extend from 25th to 75th percentiles, with a dot at the median, whiskers indicate  $1.5 \times \text{IQR}$ . **d–f**, Summary of median cell diameter values obtained in all experiment series with cDC (**d**), sDC (**e**) and xDC (**f**). Data points correspond to medians of individual experiments ( $n = 3, 5$  and  $4$ , for cDC, sDC and xDC, respectively). Conditions measured in same experimental series are color-coded. Boxes span  $2 \times$  standard deviation with a line at the mean of all medians. In **d–f** statistical significance of overall differences among mean cell sizes at different concentrations was tested using analysis of variance (ANOVA) and its result is shown on top of the horizontal line overarching all conditions. The  $p$ -values reported above each box come from comparison of the given treatment to the control condition obtained through post-hoc analysis using pairwise two-sided  $t$ -tests for multiple comparisons with Benjamin-Hochberg  $p$ -value adjustment. Reprinted from Urbanska, Muñoz *et al.*<sup>363</sup>.



**Supplementary Figure B.8 | The influence of size bin selection on relative deformability response to osmotic shock.** For all three methods  $RD$  was calculated for either all data, 3- $\mu$ m wide cell diameter bin or 1- $\mu$ m wide cell diameter bin. For the ease of comparison, the data is grouped based on binning strategy and all three methods are plotted together (**a**), or the data is grouped by method and all binning strategies are compared (**b**). The lines connect the data points representing means of medians from measurement replicates ( $n = 3, 4, \text{ and } 4$ , for cDC, sDC, and xDC, respectively). Error bars present the standard deviation of the medians. Reprinted from Urbanska, Muñoz *et al.*<sup>363</sup>.



**Supplementary Figure B.9 | The influence of size bin selection on relative deformability response to LatB treatment.** For all three methods  $RD$  was calculated for either all data, 3- $\mu m$  wide cell diameter bin or 1- $\mu m$  wide cell diameter bin. For the ease of comparison, the data is grouped based on binning strategy and all three methods are plotted together (a), or the data is grouped by method and all binning strategies are compared (b). The lines connect the data points representing means of medians from measurement replicates ( $n = 3, 5,$  and  $4,$  for cDC, sDC, and xDC, respectively). Error bars present the standard deviation of the medians. Reprinted from Urbanska, Muñoz *et al.*<sup>363</sup>.



— Appendix C —

Supplementary Material for Chapter 4

Supplementary Tables C.1 – C.2

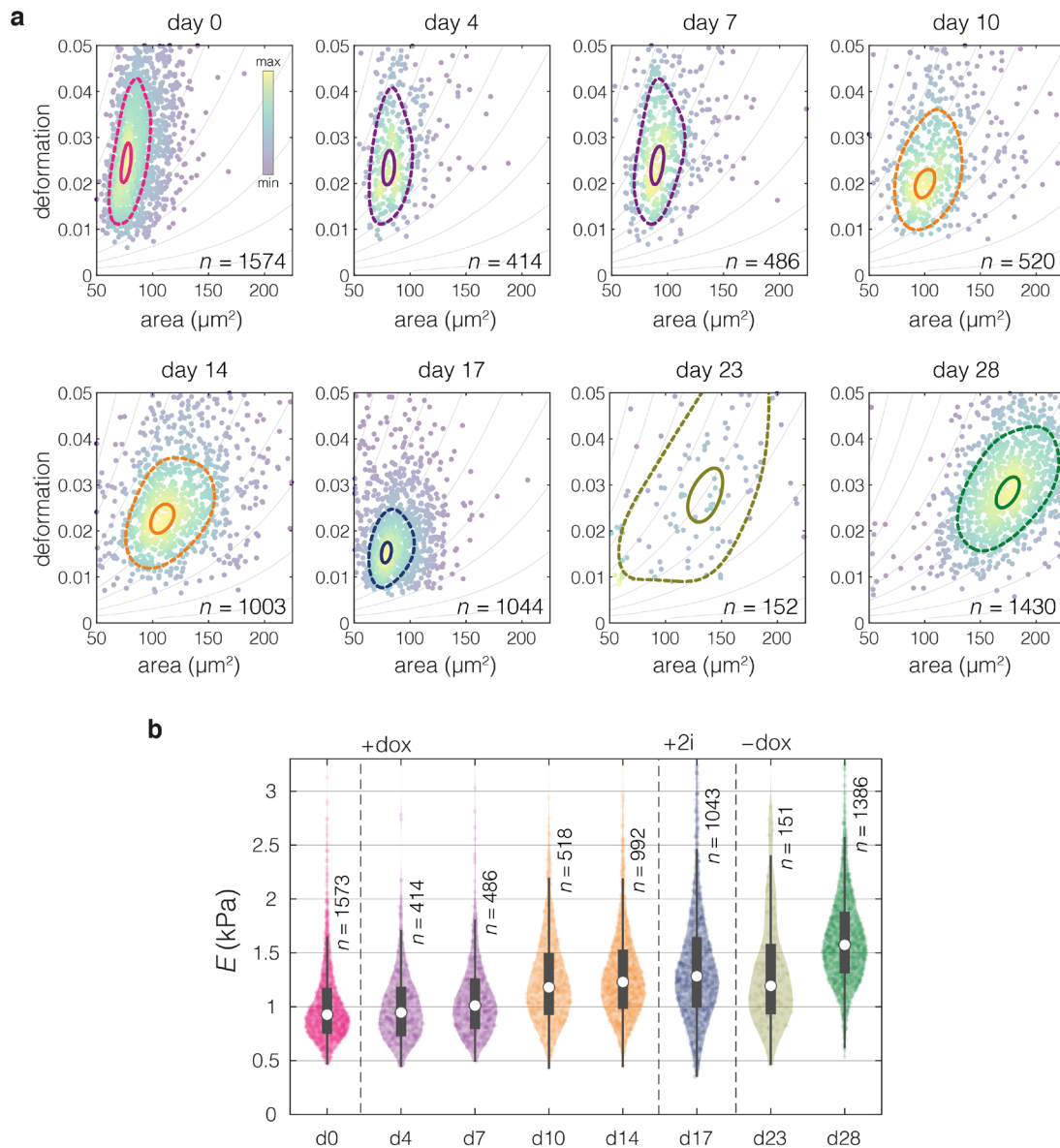
**Supplementary Table C.1 | Young’s moduli of fNPCs and iPSC measured in suspended, rounded and adherent state.** Young’s moduli of representative measurements performed with RT-DC and AFM in rounded as well as adherent state corresponding to plots in **Figure 4.5a–c**. The deformation timescales and mode of probing are indicated below method names.  $n$  – number of measured cells. MAD – mean absolute deviation of the median.

	<b>RT-DC</b>	<b>AFM indentation</b>	
	1 ms, whole-cell suspended	0.2 s, local indentation rounded	0.2 s, local indentation adherent
	$E$ (kPa)	$E$ (kPa)	$E$ (kPa)
	median $\pm$ MAD	median $\pm$ MAD	median $\pm$ MAD
<b>fNPCs</b>	$0.928 \pm 0.244$ ( $n = 1573$ )	$0.354 \pm 0.109$ ( $n = 51$ )	$0.163 \pm 0.075$ ( $n = 41$ )
<b>iPSCs</b>	$1.574 \pm 0.330$ ( $n = 1386$ )	$0.853 \pm 0.489$ ( $n = 57$ )	$0.872 \pm 0.599$ ( $n = 35$ )

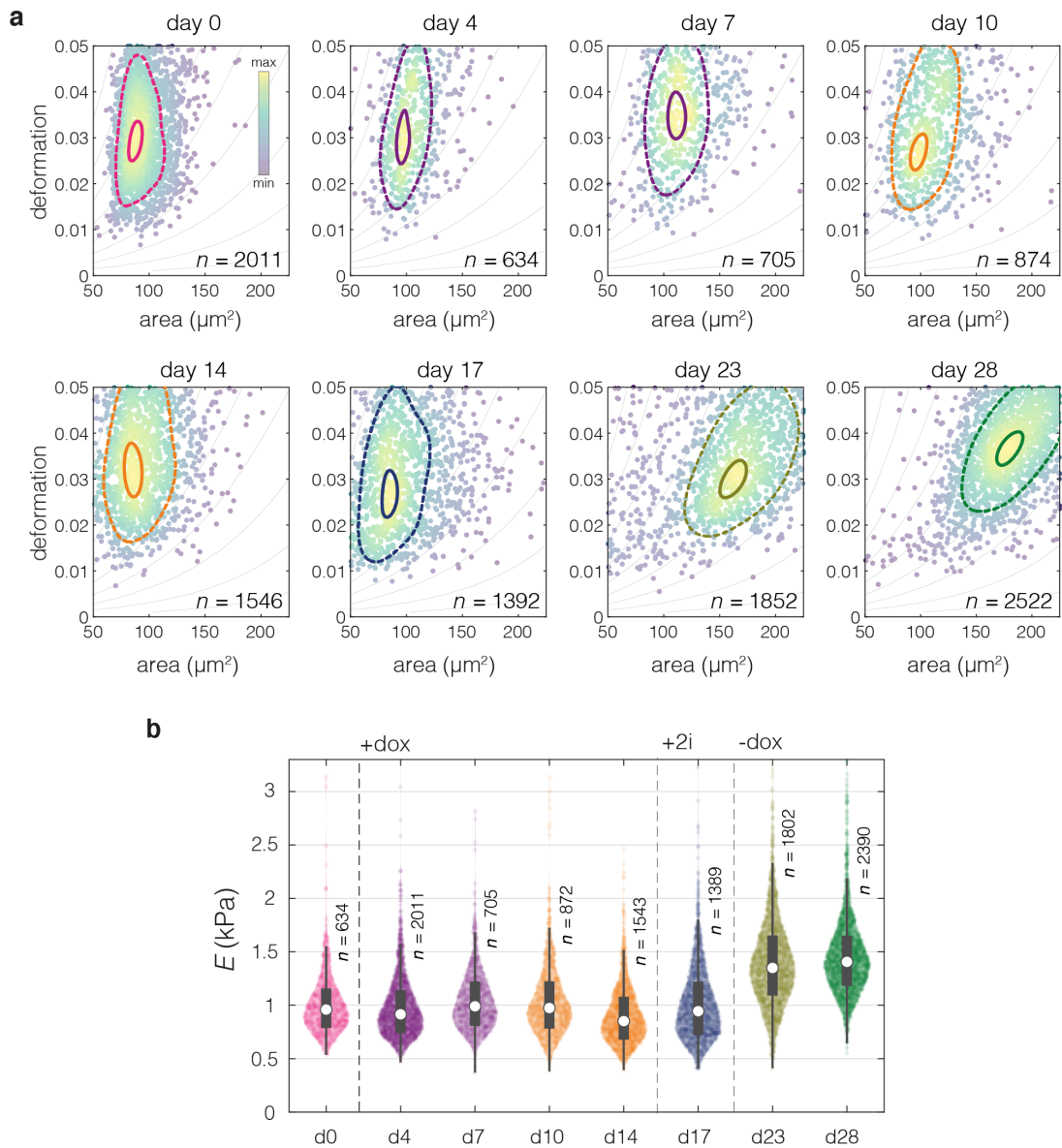
**Supplementary Table C.2 | Young’s moduli of three terminal reprogramming states measured across methods.** Young’s moduli of fNPCs, F-class cells and iPSCs as measured by RT-DC and AFM indentation on rounded cells. The deformation timescales and mode of probing are indicated below method names. The values correspond to data presented in **Supplementary Figure C.3b,d**.  $n$  – number of individual measurement replicates, mean was taken over medians from individual measurement replicates, SD – standard deviation.

	<b>RT-DC</b>	<b>AFM indentation</b>
	1 ms, whole-cell suspended	0.2 s, local indentation rounded
	$E$ (kPa)	$E$ (kPa)
	mean $\pm$ SD	mean $\pm$ SD
<b>fNPCs</b>	$0.885 \pm 0.075$ ( $n = 14$ )	$0.446 \pm 0.101$ ( $n = 3$ )
<b>F-class</b>	$1.208 \pm 0.062$ ( $n = 12$ )	$0.600 \pm 0.254$ ( $n = 6$ )
<b>iPSCs</b>	$1.381 \pm 0.115$ ( $n = 12$ )	$0.776 \pm 0.232$ ( $n = 5$ )

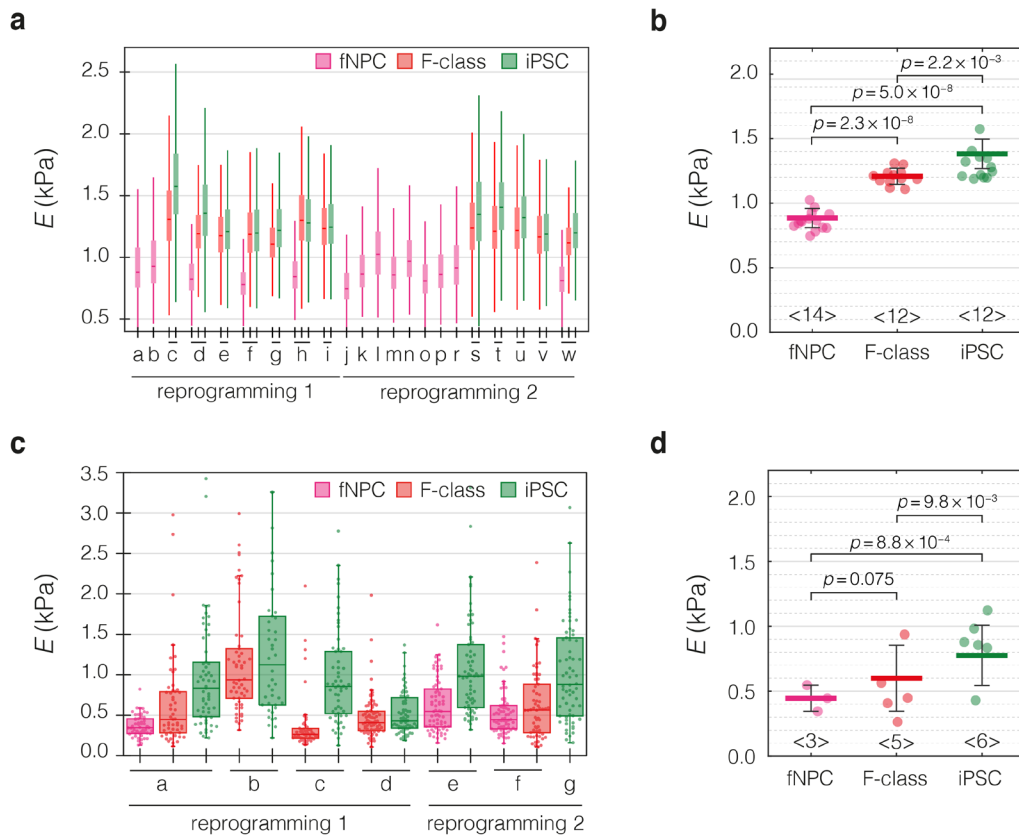
## Supplementary Figures C.1 – C.5



**Supplementary Figure C.1 | Transition of mechanical phenotype of fNPC during reprogramming towards pluripotency, replicate 1.** **a**, Deformation–area scatter plots of cell populations characterized by RT-DC at specified days within 28 days of reprogramming. Data points indicate individual cells. Color map indicates event density. Contours on top of scatter plots delineate 50% (dashed lines) and 95% (solid lines) densities. **b**, Violin plots of Young's moduli derived from RT-DC data in **a**. Data points represent individual cells. Boxes on top of the violins extend from 25th to 75th percentiles, with a dot at the median, whiskers indicate  $1.5 \times \text{IQR}$ . This figure is modified after Urbanska *et al.*<sup>378</sup>.

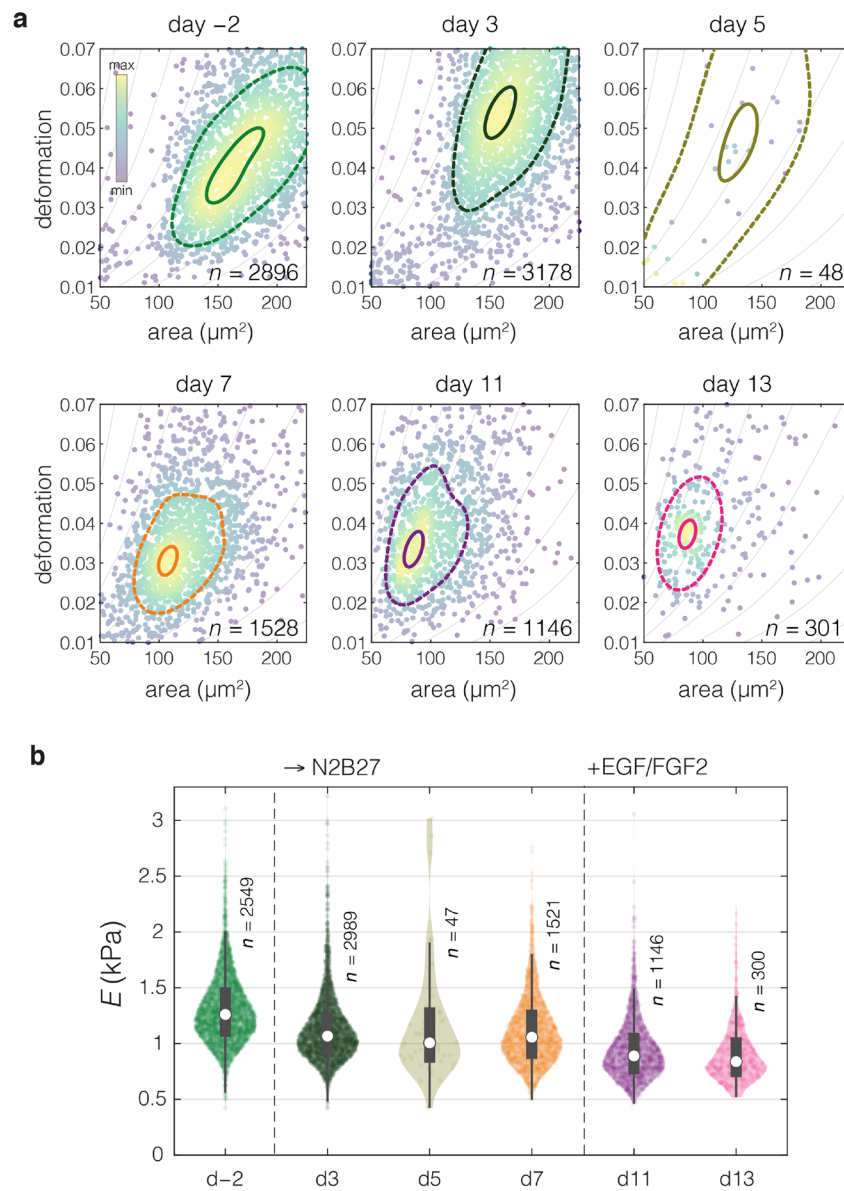


**Supplementary Figure C.2 | Transition of mechanical phenotype of fNPC during reprogramming towards pluripotency, replicate 2.** , Deformation–area scatter plots of cell populations characterized by RT-DC at specified days within 28 days of reprogramming. Data points indicate individual cells. Color map indicates event density. Contours on top of scatter plots delineate 50% (dashed lines) and 95% (solid lines) densities. **b**, Violin plots of Young's moduli derived from RT-DC data in **a**. Data points represent individual cells. Boxes on top of violins extend from 25th to 75th percentiles, with a dot at the median, whiskers indicate  $1.5 \times \text{IQR}$ . This figure is modified from Urbanska *et al.*<sup>378</sup>.

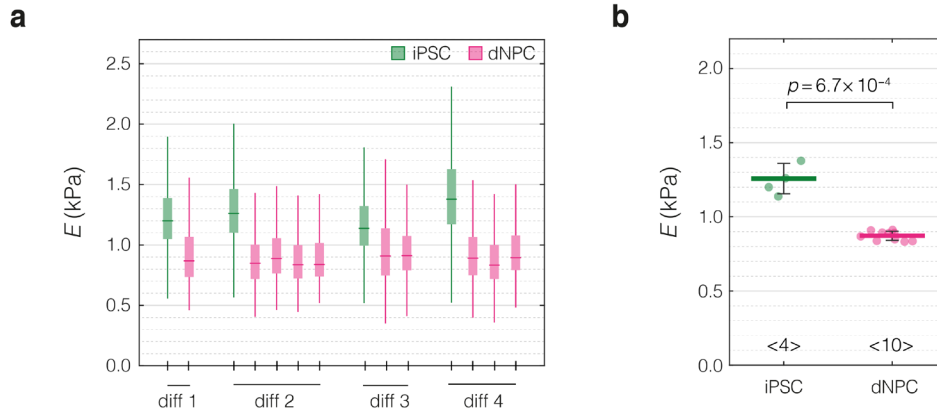


**Supplementary Figure C.3 | Cell stiffness at terminal reprogramming stages — summary of all replicates.** **a**, Distributions of Young's moduli derived from RT-DC measurement replicates of terminal reprogramming stages. Boxes represent individual measurements with  $n = 859\text{--}3413$  cells each; a–w indicate measurement days; reprogramming 1 and 2 indicate independent reprogramming experiments. **b**, Summary of median Young's moduli from RT-DC measurements. Data points represent medians of individual RT-DC measurements from panel **a**. **c**, Distributions of Young's moduli derived from AFM measurement replicates of terminal reprogramming stages. Boxes represent individual measurements with  $n = 42\text{--}80$  cells each; datapoints represent individual cells; a–g indicate measurement days; reprogramming 1 and 2 indicate independent reprogramming series. **d**, Summary of median Young's moduli from AFM measurements. Data points represent medians of individual RT-DC measurements from panel **c**. In **a** and **c**, boxes extend from 25th to 75th percentiles, with a line at the median. Whiskers span  $1.5 \times$  interquartile range (IQR). In **b** and **d**, horizontal lines delineate means with standard deviation (SD) as error, datapoints represent medians of the individual replicates, the numbers of replicates are indicated below each box. Statistical analysis performed using a linear mixed-effects model on all measurement replicates. This figure is modified after Urbanska *et al.*<sup>378</sup>.





**Supplementary Figure C.4 | Progression of iPSC stiffness during differentiation along the neural lineage.** **a**, Deformation–area scatter plots of cell populations characterized by RT-DC at specified timepoints of the differentiation. Data points indicate individual cells. Color map indicates event density. Contours on top of scatter plots delineate 50% (dashed lines) and 95% (solid lines) densities. **b**, Violin plots of Young's moduli derived from RT-DC data in **a**. Data points represent individual cells. Boxes on top of the violins extend from 25th to 75th percentiles, with a dot at the median, whiskers indicate  $1.5 \times \text{IQR}$ . This figure is modified after Urbanska *et al.*<sup>378</sup>.



**Supplementary Figure C.5 | Cell stiffness at terminal stages of neural differentiation — summary of all replicates.** **a**, Distributions of Young's moduli derived from RT-DC measurement replicates of terminal differentiation stages. Boxes represent individual measurements with  $n = 300\text{--}2776$  cells each and extend from 25th to 75th percentiles, with a line at the median; whiskers span  $1.5 \times$  interquartile range (IQR); diff 1 to 4 indicate independent differentiation series. **b**, Summary of median Young's moduli from RT-DC measurements. Horizontal lines delineate medians with mean absolute deviation (MAD) as error, datapoints represent medians of the individual replicates, the numbers of replicates are indicated at the bottom of each plot. Statistical analysis was performed using a linear mixed-effects model on all measurement replicates.

— Appendix D —  
Supplementary Material for Chapter 5

## Supplementary Tables D.1 – D.6

**Supplementary Table D.1 | Combined PC-corr values calculated as means of the two analysed sets.** The  $PC-corr_{i,j}^{comb}$  specify the values for network edges. Edges above a cut-off of 0.75 are displayed. The cut-off is indicated with a horizontal line at the bottom.

	node <i>i</i>	node <i>j</i>	edge, $PC-corr_{i,j}^{comb}$	
1	<i>FHL2</i>	<i>THBS1</i>	0.863	
2	<i>ANKRD1</i>	<i>IL11</i>	0.813	
3	<i>MFAP5</i>	<i>THBS1</i>	0.803	
4	<i>FHL2</i>	<i>IGFBP7</i>	0.788	
5	<i>IGFBP7</i>	<i>THBS1</i>	0.788	
6	<i>C1QTNF1</i>	<i>IGFBP6</i>	0.785	
7	<i>FHL2</i>	<i>TAGLN</i>	0.782	
8	<i>IGFBP7</i>	<i>TAGLN</i>	0.782	
9	<i>TAGLN</i>	<i>THBS1</i>	0.782	
10	<i>ATP8B1</i>	<i>FHL2</i>	0.780	
11	<i>CNN2</i>	<i>FHL2</i>	0.774	
12	<i>FHL2</i>	<i>MFAP5</i>	0.767	
13	<i>LRRC15</i>	<i>THBS1</i>	0.766	
14	<i>CAV1</i>	<i>FHL2</i>	0.765	
15	<i>CAV1</i>	<i>IGFBP7</i>	0.765	
16	<i>CAV1</i>	<i>TAGLN</i>	0.765	
17	<i>CAV1</i>	<i>THBS1</i>	0.765	
18	<i>C1QTNF1</i>	<i>CLIC3</i>	0.762	
19	<i>FHL2</i>	<i>IGFBP3</i>	0.758	
20	<i>DPYSL5</i>	<i>INSM1</i>	0.758	
21	<i>CLIC3</i>	<i>TRIM29</i>	0.756	
22	<i>C1QTNF1</i>	<i>KRT80</i>	0.756	
23	<i>FHL2</i>	<i>WISP2</i>	0.754	
24	<i>THBS1</i>	<i>WISP2</i>	0.754	
25	<i>CAV1</i>	<i>MRGPRF</i>	0.754	
26	<i>ARHGDIB</i>	<i>IL7R</i>	0.754	
27	<i>CXXC4</i>	<i>DPYSL5</i>	0.752	
28	<i>ABCC3</i>	<i>IER3</i>	0.752	
29	<i>CLDN4</i>	<i>TACSTD2</i>	0.751	
30	<i>CYR61</i>	<i>MFAP5</i>	0.751	↑ cut-off 0.75

**Supplementary Table D.2 | Combined PC-corr values calculated as minimum values of the two analysed sets.** The  $PC-corr_{i,j}^{comb}$  specify the values for network edges. Edges above a cut-off of 0.70 are displayed. Cut-offs 0.70 and 0.75 are marked with a horizontal line.

	node $i$	node $j$	edge, $PC-corr_{i,j}^{comb}$	
1	<i>FHL2</i>	<i>THBS1</i>	0.803	
2	<i>FHL2</i>	<i>IGFBP7</i>	0.785	
3	<i>IGFBP7</i>	<i>THBS1</i>	0.785	
4	<i>FHL2</i>	<i>TAGLN</i>	0.782	
5	<i>IGFBP7</i>	<i>TAGLN</i>	0.782	
6	<i>TAGLN</i>	<i>THBS1</i>	0.782	
7	<i>ANKRD1</i>	<i>IL11</i>	0.781	
8	<i>CAV1</i>	<i>FHL2</i>	0.759	
9	<i>CAV1</i>	<i>IGFBP7</i>	0.759	
10	<i>CAV1</i>	<i>TAGLN</i>	0.759	
11	<i>CAV1</i>	<i>THBS1</i>	0.759	
12	<i>CLIC3</i>	<i>TRIM29</i>	0.751	↑ cut-off 0.75
13	<i>ATP8B1</i>	<i>FHL2</i>	0.748	
14	<i>CAV1</i>	<i>MRGPRF</i>	0.736	
15	<i>FHL2</i>	<i>IGFBP3</i>	0.733	
16	<i>ARHGDIB</i>	<i>IL7R</i>	0.726	
17	<i>CYR61</i>	<i>MFAP5</i>	0.725	
18	<i>IGFBP3</i>	<i>TAGLN</i>	0.718	
19	<i>MAL</i>	<i>TRIM29</i>	0.718	
20	<i>FHL2</i>	<i>LBH</i>	0.717	
21	<i>FHL2</i>	<i>MRGPRF</i>	0.716	
22	<i>MRGPRF</i>	<i>THBS1</i>	0.709	
23	<i>CLIC3</i>	<i>SYT8</i>	0.709	
24	<i>LBH</i>	<i>TAGLN</i>	0.706	
25	<i>IGFBP6</i>	<i>MRGPRF</i>	0.705	
26	<i>ASCL1</i>	<i>LRRN2</i>	0.703	
27	<i>ATP8B1</i>	<i>MRGPRF</i>	0.702	
28	<i>SYT8</i>	<i>TRIM29</i>	0.701	
29	<i>CYR61</i>	<i>THBS1</i>	0.700	↑ cut-off 0.70

**Supplementary Table D.3 | List of target genes together with their processed PC loadings.**

	gene name	gene description	$V_i^1$	$V_i^2$	$\bar{V}$
1	<i>ABCC3</i>	ATP binding cassette subfamily C member 3	0.849	0.693	0.771
2	<i>ANKRD1</i>	ankyrin repeat domain 1	0.933	0.781	0.857
3	<i>ARHGDI3</i>	Rho GDP dissociation inhibitor beta	0.726	0.933	0.829
4	<i>ASCL1</i>	achaete-scute family bHLH transcription factor 1	-0.703	-0.813	-0.758
5	<i>ATP8B1</i>	ATPase phospholipid transporting 8B1	0.813	0.748	0.780
6	<i>C1QTNF1</i>	C1q and TNF related 1	0.895	0.697	0.796
7	<i>CAV1</i>	caveolin-1	0.772	0.759	0.765
8	<i>CLDN4</i>	claudin 4	0.754	0.919	0.836
9	<i>CLIC3</i>	chloride intracellular channel 3	0.827	0.794	0.810
10	<i>CNN2</i>	calponin 2	0.673	0.920	0.796
11	<i>CXXC4</i>	CXXC finger protein 4	-0.614	-0.891	-0.752
12	<i>CYR61</i>	cellular communication network factor 1	0.777	0.754	0.765
13	<i>DPYSL5</i>	dihydropyrimidinase like 5	-0.686	-0.970	-0.828
14	<i>FHL2</i>	four and a half LIM domains 2	0.951	0.927	0.939
15	<i>IER3</i>	immediate early response 3	0.841	0.918	0.879
16	<i>IGFBP3</i>	insulin like growth factor binding protein 3	0.733	0.904	0.819
17	<i>IGFBP6</i>	insulin like growth factor binding protein 6	0.879	0.749	0.814
18	<i>IGFBP7</i>	insulin like growth factor binding protein 7	0.790	0.785	0.788
19	<i>IL11</i>	interleukin 11	0.845	0.880	0.862
20	<i>IL7R</i>	interleukin 7 receptor	0.788	-0.786	0.001
21	<i>INSM1</i>	INSM transcriptional repressor 1	-0.739	-0.979	-0.859
22	<i>KRT80</i>	keratin 80	0.872	0.639	0.756
23	<i>LBH</i>	LBH regulator of WNT signaling pathway	0.731	0.717	0.724
24	<i>LRRC15</i>	leucine rich repeat containing 15	0.916	-0.617	0.149
25	<i>LRRN2</i>	leucine rich repeat neuronal 2	-0.721	-0.733	-0.727
26	<i>MAL</i>	mal, T cell differentiation protein	0.724	0.841	0.782
27	<i>MFAP5</i>	microfibril associated protein 5	0.921	0.725	0.823
28	<i>MRGPRF</i>	MAS related GPR family member F	0.775	0.751	0.763
29	<i>SYT8</i>	synaptotagmin 8	0.746	0.709	0.727
30	<i>TACSTD2</i>	tumor associated calcium signal transducer 2	0.689	0.833	0.761
31	<i>TAGLN</i>	transgelin	0.782	0.782	0.782
32	<i>THBS1</i>	thrombospondin 1	0.922	0.803	0.863
33	<i>TRIM29</i>	tripartite motif containing 29	0.751	0.760	0.756
34	<i>WISP2</i>	cellular communication network factor 5	0.834	0.674	0.754

**Supplementary Table D.4 | Comparison of Young's modulus values obtained for ECC4 and TGBC cell lines across different methods.** Young's moduli derived from RT-DC as well as AFM indentation and microrheology measurements. The deformation timescales and mode of probing are indicated below method names. AFM indentation and microrheology were performed on adherent cells. For AFM microrheology, storage Young's moduli  $E'$  were obtained from storage shear moduli ( $G'$ ) according to **Equation 1.7**, assuming a Poisson's ratio of 0.5. In RT-DC,  $E$  is calculated as median over the medians from  $n$  measurement replicates; in AFM,  $E$  is calculated as median/mean of  $n$  measured cells. MAD – mean absolute deviation, SD – standard deviation.

	<b>RT-DC</b>	<b>AFM microrheology</b>		<b>AFM indentation</b>
	1 ms, whole-cell	5 ms (200 Hz), local	0.3 s (3 Hz), local	0.2 s, local
	$E$ (kPa)	$E'$ (kPa)	$E'$ (kPa)	$E$ (kPa)
	median $\pm$ MAD	mean $\pm$ SD	mean $\pm$ SD	median $\pm$ MAD
<b>ECC4</b>	$0.928 \pm 0.058^*$ ( $n = 8$ )	$0.628 \pm 0.370^\#$ ( $n = 18$ )	$0.479 \pm 0.237^\#$ ( $n = 18$ )	$0.470 \pm 0.153^\dagger$ ( $n = 20$ )
<b>TGBC</b>	$1.325 \pm 0.028^*$ ( $n = 5$ )	$1.145 \pm 0.677^\#$ ( $n = 27$ )	$0.782 \pm 0.467^\#$ ( $n = 27$ )	$0.905 \pm 0.401^\dagger$ ( $n = 26$ )

data correspond to: \* Figure 5.2b; # Figure 5.9c; † Figure 5.9b.

**Supplementary Table D.5 | Summary of details regarding transcriptomic profiling of the datasets used in this study.**

	glioblastoma	carcinoma	HSPCs	MCF10A	iPSCs	developing neurons
accession no	GEO: GSE77751	DDBJ: DRA000991	GEO: GSE90552	GEO: GSE69822	GEO: GSE49940	GEO: GSE51606
technology	HT seq	CAGE	HT seq	HT seq	microarray	HT seq
instrument	Illumina HiSeq 2500	Helicos HeliScope	Illumina HiSeq 2500	Illumina HiSeq 2500	Illumina BeadArray Reader*	Illumina HiSeq 2000
platform ID	GPL16791	GPL14761	GPL16791	GPL16791	GPL6885	GPL13112
sequencing depth	26–35 million single-end reads per sample	4 million mapped tags per sample	27–56 million fragments per pooled libraries	31 million single-end reads per library	N/A	30-40 million reads per sample
RNA isolation	total RNA, High Pure RNA Isolation Kit (Roche)	total RNA, miRNeasy Kit (Qiagen)	total RNA, trizol isolation	total RNA, RNeasy Kit (Qiagen)	total RNA, RNeasy Kit (Qiagen)	polyA RNA, $\mu$ MACS™ mRNA Isolation Kit (Miltenyi)
library preparation	Ultra Directional RNA Library Prep (NEB)	HeliScopeCAGE <sup>510</sup>	TruSeq RNA Sample Prep Kit (Illumina)	TruSeq RNA Sample Prep Kit (Illumina)	labelling with biotin	custom protocol
alignment	to GRCh38 GSNAP (v 2014-12-17)	to GRCh37 Delve	to GRCh38 GSNAP (v 2015-12-31)	to GRCh37 TopHat (v 2.0.10)	BeadStudio (v 3.2)	to MGSCv37 BWA (v 0.5.9)
counting	featureCounts (v 1.4.6)	decomposition peak identification (DPI) <sup>465,§</sup>	featureCounts (v 1.5.0)	HTSeq (v 0.6.1) <sup>†</sup>	BeadStudio (v 3.2)	BEDtools (v 2.11)
normalization	size factor normalization (DESeq2 v 1.6.2)	TPM - tags per milion (edgeR)	size factor normalization (DESeq2 v 1.10.1)	RPKM (DESeq2 v 1.4.5)	log2-scaling, qnt (Lumi)	size factor normalization (DESeq v 1.8.1)

\*with mouseRef-8 v2 expression BeadChips (Illumina),

§available at <https://github.com/hkawaji/dpi1/>,

†available at <http://www-huber.embl.de/users/anders/HTSeq/doc/count.html>

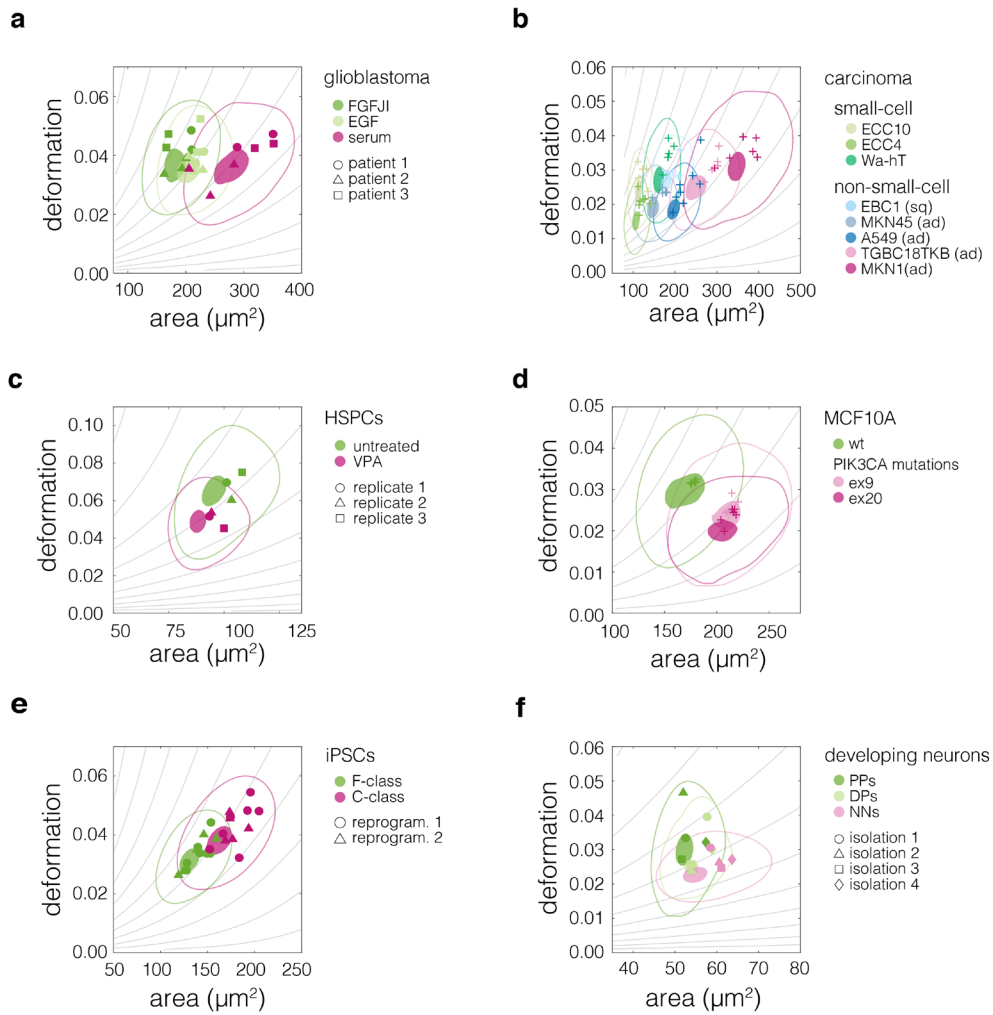


**Supplementary Table D.6 | List of sample IDs assigned to the different cell states in the respective transcriptomic datasets.** sc – small-cell, sq – squamous cell, adeno – adenocarcinoma.

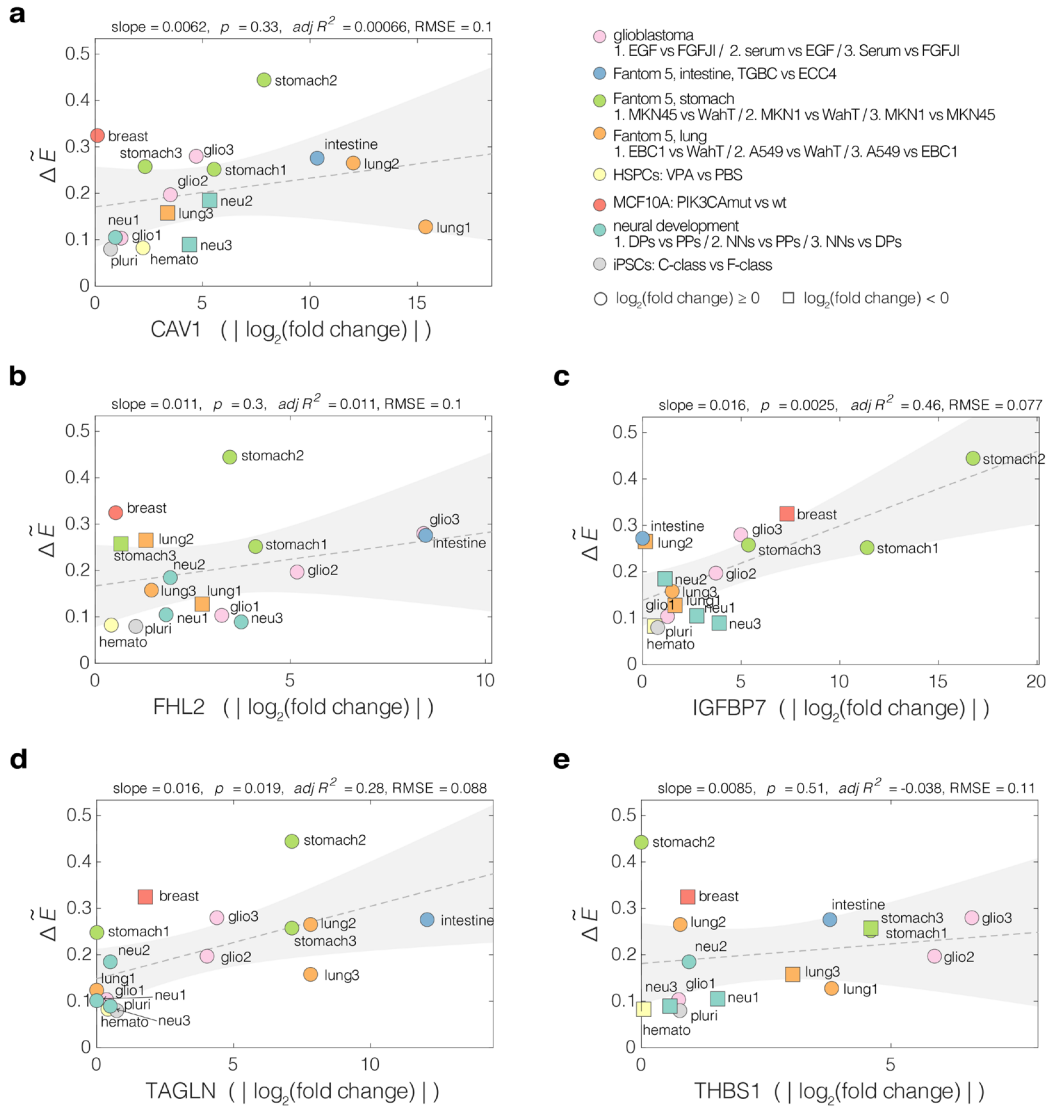
accession number	cell state	sample IDs
glioblastoma GSE77751	FGFJI (soft)	GSM2058533   GSM2058534   GSM2058535   GSM2058542   GSM2058543   GSM2058544   GSM2058551   GSM2058552   GSM2058553
	EGF medium)	GSM2058530   GSM2058531   GSM2058532   GSM2058539   GSM2058540   GSM2058541   GSM2058548   GSM2058549   GSM2058550
	serum (stiff)	GSM2058536   GSM2058537   GSM2058538   GSM2058545   GSM2058546   GSM2058547   GSM2058554   GSM2058555   GSM2058556
carcinoma DRA000991	sc (soft)	10589   10610*   10841   10541   10842   10562 <sup>§</sup>   10609 <sup>§</sup>
	sq (medium)	10717   10760   10692   10434   10550   10545   10544   10463   10486 <sup>§</sup>
	adeno (stiff)	10796   10643   10614*   10612   10499 <sup>§</sup>   10408   10648   10784   10437   10417 <sup>§</sup>   10639   11843   11841   10693   10797
HSPCs GSE90552	VPA (soft)	GSM2406738   GSM2406739   GSM2406740   GSM2406741
	PBS (stiff)	GSM2406734   GSM2406735   GSM2406736   GSM2406737
MCF10A GSE69822	WT (soft)	GSM1709515   GSM1709516   GSM1709517
	H1047R (stiff)	GSM1709572   GSM1709573   GSM1709574
iPSCs GSE49940	F-class (soft)	GSM1544134   GSM1544135   GSM1544139   GSM1544140   GSM1544146   GSM1544160
	C-class (stiff)	GSM1544136   GSM1544137   GSM1544138   GSM1544141   GSM1544142   GSM1544143   GSM1544144   GSM1544145   GSM1544147   GSM1544148   GSM1544149   GSM1544150   GSM1544151   GSM1544152   GSM1544153   GSM1544154   GSM1544155   GSM1544156   GSM1544157   GSM1544158   GSM1544159   GSM1544161
developing neurons GSE51606	PPs (soft)	GSM1249110   GSM1249113   GSM1249116
	DPs (medium)	GSM1249111   GSM1249114   GSM1249117
	NNs (stiff)	GSM1249112   GSM1249115   GSM1249118

\*stomach, <sup>§</sup>lung, <sup>§</sup>intestine

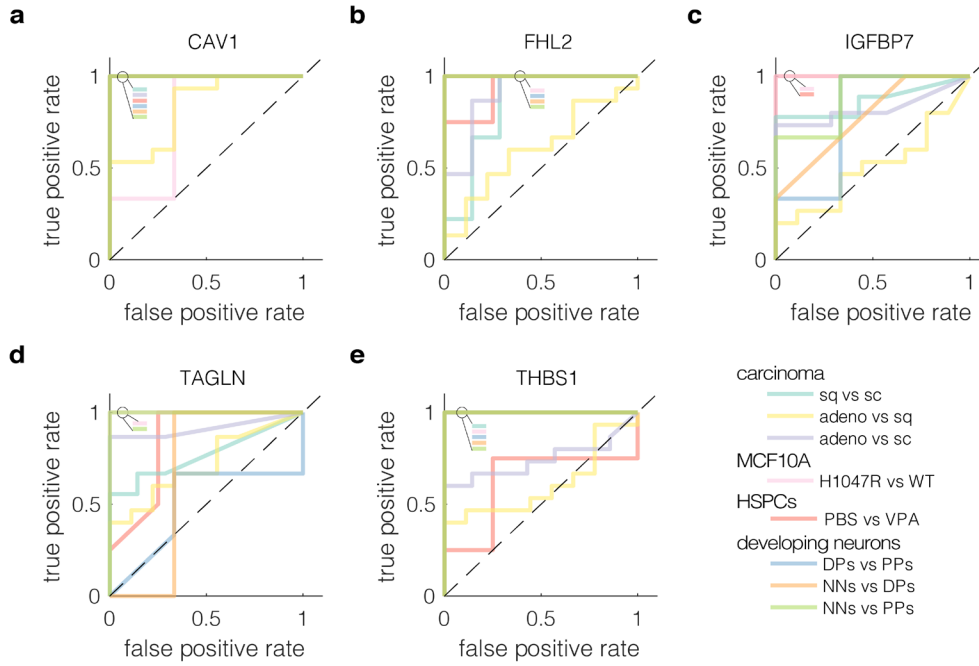
## Supplementary Figures D.1 – D.7



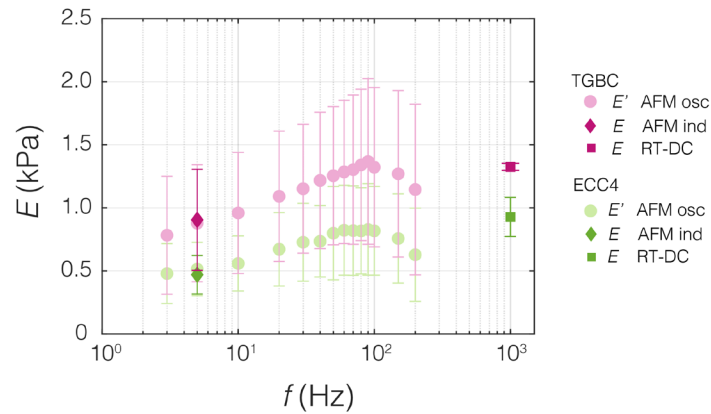
**Supplementary Figure D.1 | Plots of area vs deformation for different cell states in characterized systems.** Panels correspond to the following systems: **a**, glioblastoma, **b**, carcinoma, **c**, human stem and progenitor cells (HSPCs), **d**, non-tumorigenic breast epithelia MCF10A, **e**, induced pluripotent stem cells (iPSCs), and **f**, developing neurons. 95%- and 50% density contours of data pooled from all measurements of given cell state are indicated by shaded areas and continuous lines, respectively. Datapoints indicate medians of individual measurements. The isoelasticity lines in the background (gray) indicate regions of the same Young's moduli. DDs – differentiating progenitors, DPs – differentiating progenitors, NNs – newborn neurons.



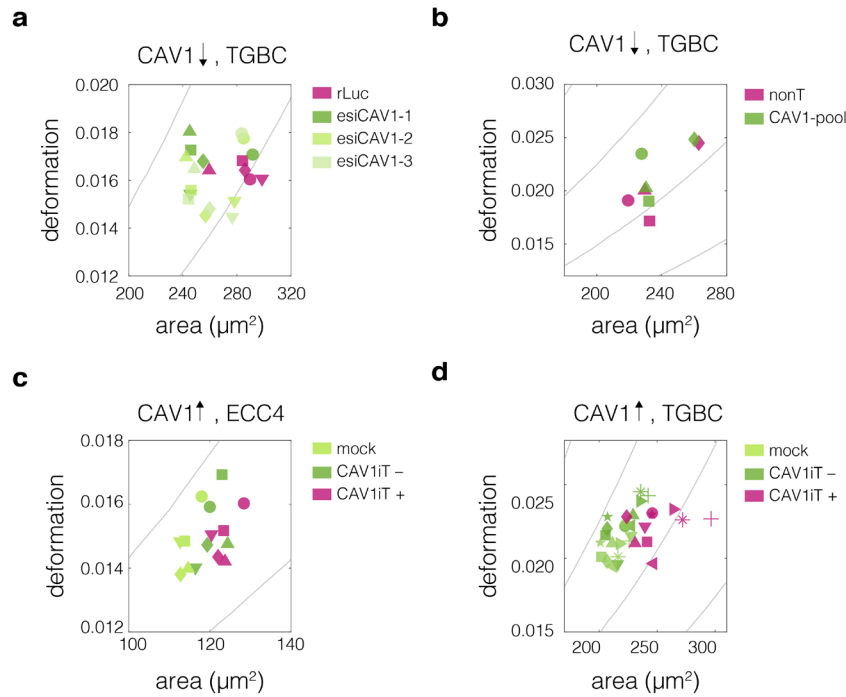
**Supplementary Figure D.2 | Relation between the magnitude of Young's modulus change and the absolute change in the expression levels of target genes. a–e,** Plots of normalized change in Young's modulus  $\Delta\tilde{E}$  versus absolute value of change in expression for the target genes from conserved module: CAV1 (a), FHL2 (b), IGFBP7 (c), TAGLN (d) THBS1 (e). Every soft-stiff state pair from the respective datasets is presented as an individual point.  $\Delta\tilde{E} = \frac{E_{stiff} - E_{soft}}{E_{stiff}}$ , where  $E_{stiff}$  and  $E_{soft}$  correspond to the Young's moduli (mean of all measurements) of the stiff and soft states within the given pairs, respectively. The dashed lines correspond to linear fits to data, with gray-shaded areas representing 95% confidence intervals.



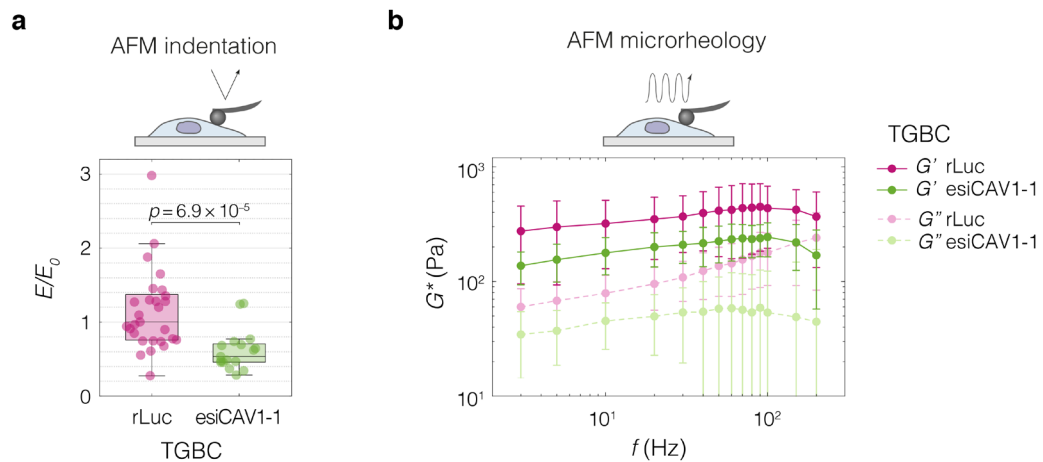
**Supplementary Figure D.3 | ROC curves characterizing classification performance of the five genes from the conserved module.** a–e, True positive rate was plotted against the false positive rate at different classification thresholds for each soft-stiff phenotype pair from the validation datasets for: CAV1 (a), FHL2 (b), IGFBP7 (c), TAGLN (d), and THBS1 (e). The insets in the upper left corners of the plot show the colors of all overlying curves with AUC = 1. The ROC curves were constructed using *perfcurve* function in *MATLAB* (R2020a, MathWorks). sc – small cell carcinoma, sq – squamous cell carcinoma, adeno – adenocarcinoma, wt, wild type, cnt – control, VPA – valproic acid, PPs – proliferating progenitors, DPs – differentiating progenitors, NNs – newborn neurons.



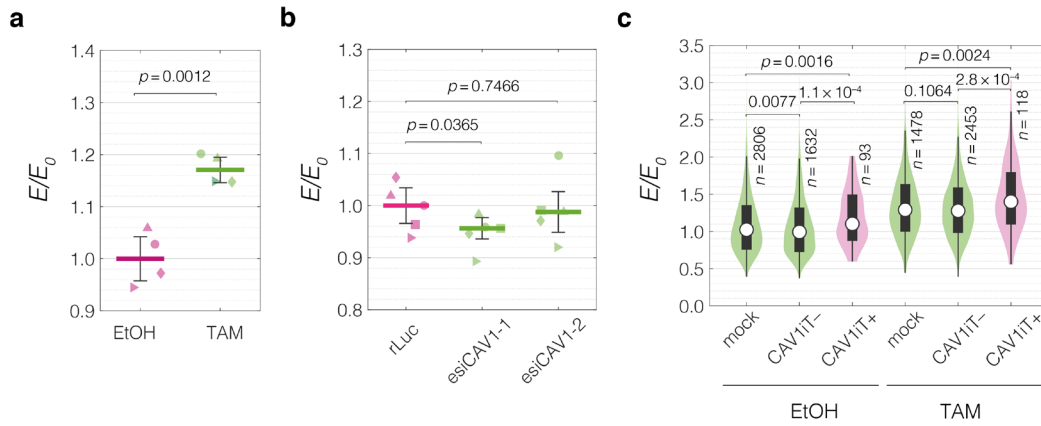
**Supplementary Figure D.4 | Young's moduli of ECC4 and TGBC cell lines across methods.** Young's moduli derived from RT-DC as well as AFM indentation and microrheology measurements plotted against probing frequency. For AFM microrheology, storage Young's moduli  $E'$  were obtained from storage shear moduli ( $G'$ ) according to **Equation 1.7**, assuming a Poisson's ratio of 0.5. For AFM microrheology, datapoints correspond to means  $\pm$  SD of individual cells (number of measured cells  $n = 18$  and  $27$  for each frequency for ECC4 and TGBC, respectively; data corresponds to **Figure 5.9c**). For AFM indentation, datapoints correspond to medians  $\pm$  MAD (number of measured cells  $n = 20$  and  $26$  for ECC4 and TGBC, respectively; data corresponds to **Figure 5.9b**). For RT-DC, datapoints correspond to medians  $\pm$  MAD (number of measurement replicates  $n = 8$  and  $5$  for ECC4 and TGBC, respectively; data corresponds to **Figure 5.2b**).



**Supplementary Figure D.5 | Plots of area vs deformation from RT DC measurements of cells with perturbed CAV1 levels.** **a–b**, CAV1 knock-down in TGBC cells using esiRNA (**a**) and ONTarget siRNA (**b**), **c–d**, transient CAV1 overexpression in ECC4 cells (**c**) and TGBC cells (**d**). Datapoints indicate medians of individual measurement replicates. The isoelasticity lines in the background (gray) indicate regions of same mechanical properties.



**Supplementary Figure D.6 | TGBC cells show decreased stiffness upon CAV1 knock-down as measured by AFM.** **a**, After CAV1 knock-down (esiCAV1-1), the TGBC cells show lower Young's moduli than control cells transfected with non-targeting esiRNA (rLuc). Box plots spread from 25<sup>th</sup> to 75<sup>th</sup> percentiles with a line at the median, whiskers span  $1.5 \times$  interquartile range (IQR), individual datapoints correspond to values obtained for individual cells (number of measured cells  $n = 29$  and  $17$  for rLuc and esiCAV1-1 conditions, respectively). Statistical analysis was performed using two sample two-sided Wilcoxon rank sum test. **b**, After CAV1 knock-down (esiCAV1-1), the TGBC cells show storage and shear modulus lower than the control cells (rLuc) in AFM microrheology measurements. Datapoints correspond to means  $\pm$  standard deviation of all measurements at given oscillation frequencies ( $n = 32$  and  $18$  for each frequency for rLuc and esiCAV1-1 conditions, respectively). Lines connecting datapoints serve as guides for the eye.



**Supplementary Figure D.7 | RT-DC measurements of CAV1 perturbations in MCF10A-Er-Src.**

**a**, MCF10A-ER-Src cells show increased Young's moduli 72 h post TAM induction as measured by RT-DC. Values normalized to EtOH control. **b**, CAV1 knock-down in uninduced MCF10A-ER-Src cells results in lowering of the Young's modulus as measured by RT-DC. Values normalized to rLuc control. **c**, Overexpression of CAV1 in both EtOH-treated (uninduced) and TAM-induced MCF10A-ER-Src cells causes increase in the Young's. All values are normalized to mock EtOH sample. CAViT- and CAViT+ indicate negative and positive cells from CAViT-transfected sample filtered based on maximum fluorescence intensity. In **a** and **b**, horizontal lines delineate medians with mean absolute deviation (MAD) as error, datapoints represent medians of the individual replicates ( $n = 4$  and  $5$  for **a** and **b**, respectively). In **c**, boxes on top of violins extend from 25th to 75th percentiles, with a dot at the median, whiskers indicate  $1.5 \times$  IQR, data originates from one replicate, number of cells analyzed for each condition is indicated in the plot. All experiments were performed using  $30 \mu\text{m}$  channels and a flow rate of  $0.16 \mu\text{l s}^{-1}$ , filtering for area (50-500) and area ratio (1.0-1.1) was applied. Statistical analysis was performed using generalized linear mixed-effects models (**a** and **b**) or a two-sided Wilcoxon rank sum test (**c**).

# List of Figures

Figure 1.1   Mechanical phenotype as a marker of cell state transitions.....	5
Figure 1.2   Circulation through microvasculature requires blood cells to deform. ....	9
Figure 1.3   Stages of cancer metastasis.....	10
Figure 1.4   Migration of neutrophils and macrophages to bacterial infection site. ....	11
Figure 1.5   An overview of early development of a mouse embryo. ....	12
Figure 1.6   Epithelial and mesenchymal cell phenotype in gastrulating mouse embryo.....	13
Figure 1.7   Schematic diagram of an animal cell.....	14
Figure 1.8   The three major types of cytoskeletal networks. ....	15
Figure 1.9   Actin cortex underlies the plasma membrane and determines the mechanical properties of the cell surface. ....	16
Figure 1.10   The contractility of the actin cytoskeleton is regulated by RhoA signalling pathway.....	16
Figure 1.11   Nucleus is interconnected with the cytoskeletal networks. ....	17
Figure 1.12   Septin cytoskeleton assembly and localization within cells. ....	18
Figure 1.13   Cells maintain membrane reservoirs in topological superstructures.....	20
Figure 1.14   Response of purely elastic and purely viscous mechanical elements to stress. ....	23
Figure 1.15   Two- and three-element spring-dashpot models of viscoelastic materials. ....	24
Figure 1.16   Springpot as a versatile viscoelastic element. ....	25
Figure 1.17   Two common modes of mechanical loading and the related elastic moduli.....	26
Figure 1.18   Dynamic response of a viscoelastic material to a sinusoidal probing signal.....	28
Figure 1.19   An overview of selected methods for the measurements of single-cell mechanical properties. ....	30
Figure 1.20   AFM-based indentation experiment.....	31
Figure 2.1   Operation principle of RT-DC for mechanical characterization of cells.....	38
Figure 2.2   Layout of the RT-DC chip.....	39
Figure 2.3   Determination of Young's modulus from RT-DC data.....	40
Figure 2.4   RT-DC setup with fluorescence measurement functionality. ....	41
Figure 2.5   Examples of fluorescence-based gating of RT-FDC data. ....	42
Figure 2.6   Operation principle of sorting real-time fluorescence and deformability cytometry (soRT-FDC).....	44
Figure 2.7   Overview of the microfluidic chip used for sorting.....	45
Figure 2.8   Fluorescence and feature-based sorting of beads with soRT-FDC. ....	47
Figure 2.9   Feature-based sorting of cells with soRT-FDC.....	48
Figure 2.10   Deformation-assisted discrimination of three major cell types in blood samples.....	49
Figure 2.11   Deformation-assisted sorting for three major blood cell types. ....	50
Figure 2.12   Brightness-based neutrophils sorting from RBC-depleted blood. ....	51
Figure 2.13   NNet-based sorting of neutrophils from RBC-depleted blood.....	53
Figure 2.14   Setting focus for the RT-DC measurements. ....	62
Figure 2.15   An example of RT-DC data filtering using area and area ratio. ....	64
Figure 2.16   Graphical representation of the area ratio parameter.....	65

---

Figure 3.1   Representatives of the three deformability cytometry classes used in this study.....	69
Figure 3.2   Schematic representation of the osmotic shock assay.....	71
Figure 3.3   Effects of osmolarity changes on cell deformability.....	72
Figure 3.4   Schematic representation of the actin disassembly assay.....	73
Figure 3.5   Effects of LatB-induced disassembly of actin cytoskeleton on cell deformability. ....	74
Figure 3.6   Increasing the flow rate in sDC impacts the magnitude of deformability response to LatB treatment.....	75
Figure 3.7   Comparison of timescales used in deformability cytometry and AFM-based probing techniques implemented in this thesis. ....	80
Figure 4.1   Stem cell model of developmental transition from neural precursor cells to pluripotent stem cells. ....	88
Figure 4.2   fNPCs become progressively stiffer during reprogramming to pluripotency. ....	89
Figure 4.3   Expression signature of neural and pluripotency markers confirms successful reprogramming. ....	90
Figure 4.4   Mechanical phenotype of iPSCs is equivalent to that of ESCs.....	90
Figure 4.5   iPSCs are stiffer than fNPCs in RT-DC measurements as well as in AFM measurements on rounded and adherent cells.....	91
Figure 4.6   F-class cells are more compliant than transgene-independent iPSCs.....	92
Figure 4.7   The evolution of CD24/SSEA1 expression during fNPC reprogramming towards two pluripotency routes. ....	94
Figure 4.8   CD24/SSEA1-based gating reveals mechanical subpopulations on reprogramming day 23. ....	95
Figure 4.9   iPSCs become progressively softer during differentiation towards neural lineage. ....	96
Figure 4.10   The differentiated NPCs lose Nanog, maintain Sox2, and acquire Pax6 expression.....	97
Figure 4.11   Mechanical phenotype along the neural progenitors-pluripotency axis. ....	97
Figure 5.1   Overview of a mechanomics approach for <i>de novo</i> identification of genes involved in cell mechanics regulation. ....	109
Figure 5.2   Mechanical characterization of divergent cell states in six systems used for the mechanomics study. ....	111
Figure 5.3   Separation of mechanically distinct cell states along PC axis in the discovery datasets. ....	113
Figure 5.4   Schematic representation of the combined PC-corr analysis on two datasets.....	114
Figure 5.5   Identified networks of genes putatively involved in cell mechanics regulation. ....	115
Figure 5.6   Gene ontology (GO) enrichment analysis of obtained target genes.....	116
Figure 5.7   Expression of identified target genes in the discovery and validation datasets. ....	118
Figure 5.8   CAV1 knock-out mouse embryonic fibroblasts (CAV1KO) have lower stiffness compared to the wild type cells (WT). ....	120
Figure 5.9   CAV1 expression and mechanical characterization with AFM of small-cell (ECC4) vs non-small-cell (TGBC) carcinoma cell lines from intestine. ....	121
Figure 5.10   CAV1 downregulation in TGBC cells results in decreased cell stiffness.....	121
Figure 5.11   CAV1 overexpression in ECC4 and TGBC cell lines results in increased cell stiffness. ....	122
Figure 5.12   Perturbations of CAV1 levels in MCF10A-ER-Src cells result in cell stiffness changes. ....	123



---

Supplementary Figure A.1   The 3D shapes obtained during microfluidic deformation of spherical objects and their rotational views.....	143
Supplementary Figure A.2   Radial representation of local strain experienced by untreated HL60 cells during microfluidic deformation experiments.....	145
Supplementary Figure A.3   Analytical estimation of surface stresses acting on an undeformed sphere passing through a circular channel approximating an sDC experiment. ....	147
Supplementary Figure B.1   Diameter of HL60 cells upon exposure to altered osmolarity. ....	151
Supplementary Figure B.2   Visualization of bin selection and data processing for osmolarity experiments. ....	152
Supplementary Figure B.3   Time-resolved effect of osmotic shock on HL60 deformability and size as measured by sDC. ....	153
Supplementary Figure B.4   Fitting of the relation between osmolarity and relative deformability for hyperosmotic shock data.....	154
Supplementary Figure B.5   Visualization of bin selection and data processing for LatB treatment experiments. ....	155
Supplementary Figure B.6   Response to high LatB concentrations measured with cDC and sDC. ....	156
Supplementary Figure B.7   Diameter of HL60 cells treated with different concentrations of LatB.....	157
Supplementary Figure B.8   The influence of size bin selection on relative deformability response to osmotic shock. ....	158
Supplementary Figure B.9   The influence of size bin selection on relative deformability response to LatB treatment.....	159
Supplementary Figure C.1   Transition of mechanical phenotype of fNPC during reprogramming towards pluripotency, replicate 1. ....	162
Supplementary Figure C.2   Transition of mechanical phenotype of fNPC during reprogramming towards pluripotency, replicate 2. ....	163
Supplementary Figure C.3   Cell stiffness at terminal reprogramming stages — summary of all replicates. ....	164
Supplementary Figure C.4   Progression of iPSC stiffness during differentiation along the neural lineage. ....	165
Supplementary Figure C.5   Cell stiffness at terminal stages of neural differentiation — summary of all replicates. ....	166
Supplementary Figure D.1   Plots of area vs deformation for different cell states in characterized systems. ....	174
Supplementary Figure D.2   Relation between the magnitude of Young’s modulus change and the absolute change in the expression levels of target genes.....	175
Supplementary Figure D.3   ROC curves characterizing classification performance of the five genes from the conserved module.....	176
Supplementary Figure D.4   Young’s moduli of ECC4 and TGBC cell lines across methods.....	176
Supplementary Figure D.5   Plots of area vs deformation from RT DC measurements of cells with perturbed CAV1 levels. ....	177
Supplementary Figure D.6   TGBC cells show decreased stiffness upon CAV1 knock-down as measured by AFM. ....	177
Supplementary Figure D.7   RT-DC measurements of CAV1 perturbations in MCF10A-Er-Src.....	178

## List of Tables

Table 1.1   Summary of methods for single-cell mechanical characterization.....	29
Table 2.1   Features analysed in real-time during RT DC measurement. ....	46
Table 2.2   Consumables necessary for setting up an RT-DC experiment. ....	59
Table 2.3   Flow rates used for the RT-DC measurements with 0.5% MC medium. ....	61
Table 2.4   Flow rates used for the RT-DC measurements with 0.6% MC medium. ....	62
Table 2.5   Additional features available during post-processing in <i>Shape-Out</i> . ....	63
Table 3.1   Characteristic operation parameters of cDC, sDC, and xDC. ....	70
Table 3.2   Ranges of response to LatB treatment at different flowrates in sDC. ....	76
Table 3.3   Demonstrated applications of the different deformability cytometry classes.....	78
Table 3.4   Characteristic operation parameters of AFM as compared to RT-DC.....	80
Table 3.5   Summary of mass and molar concentrations of LatB.....	83
Table 4.1   List of primers used for qRT-PCR analysis. ....	103
Table 5.1   Mechano-transcriptomic datasets used in this study.....	112
Table 5.2   List of identified target genes comprising the conserved module. ....	117
Table 5.3   Results of <i>in silico</i> validation of the predicted targets using AUC-ROC.....	119
Table 5.4   Carcinoma cell lines used in this study. ....	128
Table 5.5   RT-DC measurement conditions for the individual datasets. ....	131
Table 5.6   siRNAs used in the CAV1 knock-down experiments. ....	133
Supplementary Table B.1   Fit results for osmotic shock treatment. ....	149
Supplementary Table B.2   Fit results for LatB treatment. ....	150
Supplementary Table C.1   Young's moduli of fNPCs and iPSC measured in suspended, rounded and adherent state. ....	161
Supplementary Table C.2   Young's moduli of three terminal reprogramming states measured across methods. ....	161
Supplementary Table D.1   Combined PC-corr values calculated as means of the two analysed sets. ....	168
Supplementary Table D.2   Combined PC-corr values calculated as minimum values of the two analysed sets. ....	169
Supplementary Table D.3   List of target genes together with their processed PC loadings. ....	170
Supplementary Table D.4   Comparison of Young's modulus values obtained for ECC4 and TGBC cell lines across different methods. ....	171
Supplementary Table D.5   Summary of details regarding transcriptomic profiling of the datasets used in this study.....	172
Supplementary Table D.6   List of sample IDs assigned to the different cell states in the respective transcriptomic datasets. ....	173

## List of Abbreviations

1D	one-dimensional
2D	two-dimensional
3D	three-dimensional
AFM	atomic force microscopy
AI	artificial intelligence
ANOVA	analysis of variance
APC	allophycocyanin
ATP	adenosine triphosphate
AUC-ROC	area under the curve of receiver operating characteristics
<i>Btg2</i>	BTG family member 2
CAGE	cap analysis of gene expression
Cas	CRISPR associated protein
CAV1	caveolin-1
CAV1KO	caveolin-1 knock-out
CD	cluster of differentiation
cDC	constriction-based deformability cytometry
CI	confidence interval
CMOS	complementary metal–oxide–semiconductor
COVID19	coronavirus disease 2019
CRISPR	clustered regularly interspaced short palindrome repeats
DC	deformability cytometry
dNPCs	differentiated neural progenitor cells
dox	doxycycline
DPs	differentiating progenitors
EB1	end-binding protein 1
EC50	half maximal effective concentration
EDTA	ethylenediaminetetraacetic acid
EGF	epidermal growth factor
EpiSCs	epiblast stem cells
ER	ligand-binding domain of the estrogen receptor
ERM	ezrin, moesin, radixin
ESCs	embryonic stem cells
FACS	fluorescence-activated cell sorting
FEP	fluorinated ethylene propylene
FGF	fibroblast growth factor
FGFJI	fibroblast growth factor combined with a JAK inhibitor
fNPCs	fetal neural progenitor cells
FPR	false positive rate
fps	frames per second
fr	flow rate

G-CSF	granulocyte colony-stimulating factor
GDP	guanosine diphosphate
GEO	Gene Expression Omnibus
GFP	green fluorescent protein
GO	gene ontology
GSK3 $\alpha/\beta$	glycogen synthase kinase 3 $\alpha/\beta$
GTP	guanosine triphosphate
HSPCs	human stem and progenitor cells
IDTs	interdigital transducers
INM	inner nuclear membrane
iPSCs	induced pluripotent stem cells
IQR	interquartile range
IRES	independent ribosomal entry site
LatB	Latrunculin B
LED	laser emitting diode
LINC	linker of the nucleoskeleton and cytoskeleton
MACS	magnetic-activated cell sorting
MAD	mean absolute deviation
MAP2	microtubule-associated protein 2
MAPs	microtubule-associated proteins
MB	measurment buffer
MC	methylcellulose
MCAK	mitotic centromere-associated kinesin
MEK1/2	mitogen-activated protein kinase 1/2
MLC	myosin light chain
MLCK	myosin light chain kinase
MLCP	myosin light chain phosphatase
MLP	multilayer perceptron
MTOCs	microtubule organization centers
MVA	maximum validation accuracy
NNets	neural networks
NNs	newborn neurons
ONM	outer nuclear membrane
PAAm	polyacrylamide
PB	PiggyBac
PBS	phosphate-buffered saline
PC	prinicipal component
PCA	principal component analysis
PDMS	polydimethylsiloxane
PEG	polyethylene glycol
PIK3CA	phosphatidylinositol-4,5-bisphosphate 3-kinase catalytic subunit alpha

---

PLL	poly-L-lysine
PMMA	poly(methyl methacrylate)
PPs	proliferating (neural) progenitors
qRT-PCR	quantitative real-time polymerase chain reaction
RBCs	red blood cells
RFP	red fluorescent protein
RhoA	Ras homolog family member A
RNA	ribonucleic acid
RNAi	RNA interference
RNAseq	RNA sequencing
ROCK	Rho-protein kinase
ROI	region of interest
RT-DC	real-time deformability cytometry
RT-FDC	real-time fluorescence and deformability cytometry
rtTA	reverse tetracycline-controlled transactivator
sDC	shear flow deformability cytometry
siRNA	short interfering RNA
SLF	standard linear fluid
SLS	standard linear solid
SMR	suspended microchannel resonator
soRT-FDC	sorting real-time fluorescence and deformability cytometry
Src	Src proto-oncogene, non-receptor tyrosine kinase
SSAW	standing surface acoustic waves
SSEA1	stage-specific embryonic antigen-1
TAM	tamoxifen
TAZ	WW domain containing transcription regulator 1; co-activator of YAP
tet	tetracycline
TPR	true positive rate
t-SNE	t-distributed stochastic neighbour embedding
<i>Tubb3</i>	tubulin beta 3
UMAP	uniform manifold approximation and projection
VPA	valproic acid
WBCs	white blood cells
WT	wild type
xDC	extensional flow deformability cytometry
YAP	yes-associated protein 1



## List of Symbols

$A$	area
$a$	contact radius
$A^D$	indentation amplitude
$A^F$	force amplitude
$d$	diameter
$D$	deformability
$E$	Young's modulus
$E^*$	complex Young's modulus
$f$	resonance frequency
$F$	$F$ -test statistic
$F_n$	normal force
$F_r$	acoustic radiation force
$F_{sh}$	shear force
$G$	shear modulus
$G^*$	complex shear modulus
$G'$	storage shear modulus
$G''$	loss shear modulus
$k$	spring constant
$L$	length
$L_p$	persistence length
$Osm$	osmolarity
$P$	perimeter
$p_0$	acoustic pressure
$r$	radius
$RD$	relative deformability
$Re$	Reynolds number
$t$	time
$V$	processed PC loading
$v$	flow velocity
$V^*$	normalized PC loading
$V_0$	original PC loading
$V_p$	particle volume
$\beta$	power-law exponent (Chapter 1); acoustic compressibility (Chapter 2)
$\Gamma$	gamma function
$\gamma$	shear strain
$\delta$	indentation depth
$\varepsilon$	strain
$\dot{\varepsilon}$	strain rate

$\eta$	viscosity
$\theta$	phase shift (Chapter 1 and 5); polar angle (Appendix A)
$\lambda$	acoustic wavelength (Chapter 2); decay constant (Chapter 3)
$\nu$	Poisson's ratio
$\rho$	density
$\sigma$	stress
$\sigma_n$	normal stress
$\sigma_{sh}$	shear stress
$\tau$	retardation time (Chapter 1); timescale of deformation (Chapter 3)
$v$	velocity of sound
$\phi$	acoustic contrast factor (Chapter 2); angle of rotation (Appendix A)
$\omega$	angular frequency



## References

1. Gossett, D. R. *et al.* Hydrodynamic stretching of single cells for large population mechanical phenotyping. *PNAS* **109**, 7630–7635 (2012).
2. Ekpenyong, A. E. *et al.* Viscoelastic Properties of Differentiating Blood Cells Are Fate- and Function-Dependent. *PLoS One* **7**, e45237 (2012).
3. Rosenbluth, M. J., Lam, W. A. & Fletcher, D. A. Analyzing cell mechanics in hematologic diseases with microfluidic biophysical flow cytometry. *Lab Chip* **8**, 1062–1070 (2008).
4. Bufi, N. *et al.* Human primary immune cells exhibit distinct mechanical properties that are modified by inflammation. *Biophys. J.* **108**, 2181–2190 (2015).
5. Toepfner, N. *et al.* Detection of human disease conditions by single-cell morpho-rheological phenotyping of blood. *Elife* **7**, e29213 (2018).
6. Bashant, K. R. *et al.* Real-time deformability cytometry reveals sequential contraction and expansion during neutrophil priming. *J. Leukoc. Biol.* **105**, 1143–1153 (2019).
7. Guck, J. *et al.* Optical deformability as an inherent cell marker for testing malignant transformation and metastatic competence. *Biophys. J.* **88**, 3689–3698 (2005).
8. Swaminathan, V. *et al.* Mechanical Stiffness grades metastatic potential in patient tumor cells and in cancer cell lines. *Cancer Res.* **71**, 5075–5080 (2011).
9. Byun, S. *et al.* Characterizing deformability and surface friction of cancer cells. *Proc. Natl. Acad. Sci. U. S. A.* **110**, 7580–5 (2013).
10. Tse, H. T. K. *et al.* Quantitative diagnosis of malignant pleural effusions by single-cell mechanophenotyping. *Sci. Transl. Med.* **5**, 212ra163 (2013).
11. Tavares, S. *et al.* Actin stress fiber organization promotes cell stiffening and proliferation of pre-invasive breast cancer cells. *Nat. Commun.* **8**, 1–18 (2017).
12. Di Carlo, D. A Mechanical Biomarker of Cell State in Medicine. *J. Lab. Autom.* **17**, 32–42 (2012).
13. Guck, J. & Chilvers, E. R. Mechanics meets medicine. *Sci. Transl. Med.* **5**, 3–6 (2013).
14. Nematbakhsh, Y. & Lim, C. T. Cell biomechanics and its applications in human disease diagnosis. *Acta Mech. Sin.* **31**, 268–273 (2015).
15. Milo, R. & Phillips, R. How big is a human cell? in *Cell biology by the numbers* 14–17 (2015).
16. Prass, M., Jacobson, K., Mogilner, A. & Radmacher, M. Direct measurement of the lamellipodial protrusive force in a migrating cell. *J. Cell Biol.* **174**, 767–772 (2006).
17. Armistead, F. J. *et al.* Cells under stress: an inertial-shear microfluidic determination of cell behavior. *Biophys. J.* **116**, 1127–1135 (2019).
18. Hochmuth, R. M. Micropipette aspiration of living cells. *J. Biomech.* **33**, 15–22 (2000).
19. Radmacher, M. Studying the Mechanics of Cellular Processes by Atomic Force Microscopy. *Methods Cell Biol.* **83**, 347–372 (2007).
20. Darling, E. M. & Di Carlo, D. High-Throughput Assessment of Cellular Mechanical Properties. *Annu. Rev. Biomed. Eng.* **17**, 35–62 (2015).
21. Otto, O. *et al.* Real-time deformability cytometry: on-the-fly cell mechanical phenotyping. *Nat. Methods* **12**, 199–202 (2015).
22. Fabry, B. *et al.* Scaling the microrheology of living cells. *Phys. Rev. Lett.* **87**, 1–4 (2001).
23. Li, Q. S., Lee, G. Y. H., Ong, C. N. & Lim, C. T. AFM indentation study of breast cancer cells. *Biochem. Biophys. Res. Commun.* **374**, 609–613 (2008).
24. Zhou, Z. L., Ngan, A. H. W., Tang, B. & Wang, A. X. Reliable measurement of elastic modulus of cells by nanoindentation in an atomic force microscope. *J. Mech. Behav. Biomed. Mater.* **8**, 134–142 (2012).
25. Alcaraz, J. *et al.* Microrheology of human lung epithelial cells measured by atomic force microscopy.

- Biophys. J.* **84**, 2071–2079 (2003).
26. Massiera, G., Van Citters, K. M., Biancaniello, P. L. & Crocker, J. C. Mechanics of single cells: Rheology, time dependence, and fluctuations. *Biophys. J.* **93**, 3703–3713 (2007).
  27. Rigato, A., Miyagi, A., Scheuring, S. & Rico, F. High-frequency microrheology reveals cytoskeleton dynamics in living cells. *Nat. Phys.* **13**, 771–775 (2017).
  28. Tietze, S. *et al.* Spheroid Culture of Mesenchymal Stromal Cells Results in Morphorheological Properties Appropriate for Improved Microcirculation. *Adv. Sci.* **6**, 1802104 (2019).
  29. Gensbittel, V. *et al.* Mechanical Adaptability of Tumor Cells in Metastasis. *Dev. Cell* **56**, 164–179 (2021).
  30. Collinet, C. & Lecuit, T. Programmed and self-organized flow of information during morphogenesis. *Nat. Rev. Mol. Cell Biol.* **22**, 245–265 (2021).
  31. Fletcher, D. A. & Mullins, R. D. Cell mechanics and the cytoskeleton. *Nature* **463**, 485–492 (2010).
  32. Salbreux, G., Charras, G. & Paluch, E. Actin cortex mechanics and cellular morphogenesis. *Trends Cell Biol.* **22**, 536–545 (2012).
  33. Kelkar, M., Bohec, P. & Charras, G. Mechanics of the cellular actin cortex: From signalling to shape change. *Curr. Opin. Cell Biol.* **66**, 69–78 (2020).
  34. Lim, C. T. & Li, A. Mechanopathology of red blood cell diseases — Why mechanics matters. *Theor. Appl. Mech. Lett.* **1**, 014000 (2011).
  35. Tomaiuolo, G. Biomechanical properties of red blood cells in health and disease towards microfluidics. *Biomicrofluidics* **8**, (2014).
  36. Kumar, S. & Weaver, V. M. Mechanics, malignancy, and metastasis: The force journey of a tumor cell. *Cancer Metastasis Rev.* **28**, 113–127 (2009).
  37. Chaudhuri, P. K., Low, B. C. & Lim, C. T. Mechanobiology of Tumor Growth. *Chem. Rev.* **118**, 6499–6515 (2018).
  38. Levental, K. R. *et al.* Matrix Crosslinking Forces Tumor Progression by Enhancing Integrin Signaling. *Cell* **139**, 891–906 (2009).
  39. Suresh, S. Biomechanics and biophysics of cancer cells. *Acta Biomater.* **3**, 413–438 (2007).
  40. Alibert, C., Goud, B. & Manneville, J.-B. Are cancer cells really softer than normal cells? *Biol. cell* **109**, 167–189 (2017).
  41. Suresh, S. *et al.* Connections between single-cell biomechanics and human disease states: Gastrointestinal cancer and malaria. *Acta Biomater.* **1**, 15–30 (2005).
  42. Wottawah, F. *et al.* Optical rheology of biological cells. *Phys. Rev. Lett.* **94**, 1–4 (2005).
  43. Efremov, Y. M. *et al.* Mechanical properties of fibroblasts depend on level of cancer transformation. *Biochim. Biophys. Acta - Mol. Cell Res.* **1843**, 1013–1019 (2014).
  44. Xu, W. *et al.* Cell stiffness is a biomarker of the metastatic potential of ovarian cancer cells. *PLoS One* **7**, e46609 (2012).
  45. Lekka, M. *et al.* Cancer cell recognition - Mechanical phenotype. *Micron* **43**, 1259–1266 (2012).
  46. Cross, S. E., Jin, Y.-S., Rao, J. & Gimzewski, J. K. Nanomechanical analysis of cells from cancer patients. *Nat. Nanotechnol.* **2**, 780–783 (2007).
  47. Lin, H.-H. *et al.* Mechanical phenotype of cancer cells: cell softening and loss of stiffness sensing. *Oncotarget* **6**, 20946 (2015).
  48. Nyberg, K. D. *et al.* Predicting cancer cell invasion by single-cell physical phenotyping. *Integr. Biol.* **10**, 218–231 (2018).
  49. Remmerbach, T. W. *et al.* Oral cancer diagnosis by mechanical phenotyping. *Cancer Res.* **69**, 1728–1732 (2009).
  50. Rosenbluth, M. J., Lam, W. A. & Fletcher, D. A. Force microscopy of nonadherent cells: A comparison of leukemia cell deformability. *Biophys. J.* **90**, 2994–3003 (2006).

51. Lautenschläger, F. *et al.* The regulatory role of cell mechanics for migration of differentiating myeloid cells. *PNAS* **106**, 15696–15701 (2009).
52. Zheng, Y. *et al.* Decreased deformability of lymphocytes in chronic lymphocytic leukemia. *Sci. Rep.* **5**, 1–5 (2015).
53. Mayadas, T. N., Cullere, X. & Lowell, C. A. The multifaceted functions of neutrophils. *Annu. Rev. Pathol. Mech. Dis.* **9**, 181–218 (2014).
54. Worthen, G. S., Schwab, B., Elson, E. L. & Downey, G. P. Mechanics of stimulated neutrophils: Cell stiffening induces retention in capillaries. *Science* **245**, 183–186 (1989).
55. Roca-Cusachs, P. *et al.* Rheology of passive and adhesion-activated neutrophils probed by atomic force microscopy. *Biophys. J.* **91**, 3508–3518 (2006).
56. Pai, A., Sundd, P. & Tees, D. F. J. In situ microrheological determination of neutrophil stiffening following adhesion in a model capillary. *Ann. Biomed. Eng.* **36**, 596–603 (2008).
57. Ekpenyong, A. E. *et al.* Mechanical deformation induces depolarization of neutrophils. *Sci. Adv.* **3**, 1–12 (2017).
58. Denk, S. *et al.* Complement C5a-Induced Changes in Neutrophil Morphology During Inflammation. *Scand. J. Immunol.* **86**, 143–155 (2017).
59. Crawford, K. *et al.* Rapid Biophysical Analysis of Host Immune Cell Variations Associated with Sepsis. *Am. J. Respir. Crit. Care Med.* **198**, 280–282 (2018).
60. Kubánková, M. *et al.* Physical phenotype of blood cells is altered in COVID-19. *Biophys. J.* (2021) doi:10.1016/j.bpj.2021.05.025.
61. Walther, A. *et al.* Depressive disorders are associated with disease-specific increased peripheral blood cell deformation: A cross-sectional case-control study. *medRxiv* 1–32 (2021) doi:10.1101/2021.07.01.21259846v1.
62. Starodubtseva, M. N. *et al.* Nano- and microscale mechanical properties of erythrocytes in hereditary spherocytosis. *J. Biomech.* **83**, 1–8 (2019).
63. Brandão, M. M. *et al.* Optical tweezers for measuring red blood cell elasticity: Application to the study of drug response in sickle cell disease. *Eur. J. Haematol.* **70**, 207–211 (2003).
64. Zheng, Y. *et al.* Mechanical differences of sickle cell trait (SCT) and normal red blood cells. *Lab Chip* **15**, 3138–3146 (2015).
65. Byun, H. S. *et al.* Optical measurement of biomechanical properties of individual erythrocytes from a sickle cell patient. *Acta Biomater.* **8**, 4130–4138 (2012).
66. Maciaszek, J. L., Andemariam, B. & Lykotrafitis, G. Microelasticity of red blood cells in sickle cell disease. *J. Strain Anal. Eng. Des.* **46**, 368–379 (2011).
67. Hosseini, S. M. & Feng, J. J. How malaria parasites reduce the deformability of infected red blood cells. *Biophys. J.* **103**, 1–10 (2012).
68. Guo, Q., Reiling, S. J., Rohrbach, P. & Ma, H. Microfluidic biomechanical assay for red blood cells parasitized by *Plasmodium falciparum*. *Lab Chip* **12**, 1143–1150 (2012).
69. Koch, M. *et al.* *Plasmodium falciparum* erythrocyte-binding antigen 175 triggers a biophysical change in the red blood cell that facilitates invasion. *PNAS* **114**, 4225–4230 (2017).
70. Pillarisetti, A. *et al.* Mechanical phenotyping of mouse embryonic stem cells: increase in stiffness with differentiation. *Cell. Reprogram.* **13**, 371–380 (2011).
71. Boraas, L. C., Guidry, J. B., Pineda, E. T. & Ahsan, T. Cytoskeletal expression and remodeling in pluripotent stem cells. *PLoS One* **11**, 1–16 (2016).
72. Mao, X., Gavara, N. & Song, G. Nuclear Mechanics and Stem Cell Differentiation. *Stem Cell Rev. Reports* **11**, 804–812 (2015).
73. Chowdhury, F. *et al.* Material properties of the cell dictate stress-induced spreading and differentiation in embryonic stem cells. *Nat. Mater.* **9**, 82–88 (2010).

74. Tan, Y. *et al.* Probing the mechanobiological properties of human embryonic stem cells in cardiac differentiation by optical tweezers. *J. Biomech.* **45**, 123–8 (2012).
75. Ofek, G. *et al.* Mechanical characterization of differentiated human embryonic stem cells. *J. Biomech. Eng.* **131**, 061011 (2009).
76. Chen, Q. *et al.* AFM studies of cellular mechanics during osteogenic differentiation of human amniotic fluid-derived stem cells. *Anal. Sci.* **26**, 1033–7 (2010).
77. Yu, H. *et al.* Mechanical behavior of human mesenchymal stem cells during adipogenic and osteogenic differentiation. *Biochem. Biophys. Res. Commun.* **393**, 150–155 (2010).
78. Bongiorno, T. *et al.* Mechanical stiffness as an improved single-cell indicator of osteoblastic human mesenchymal stem cell differentiation. *J. Biomech.* **47**, 2197–2204 (2014).
79. González-Cruz, R. D., Fonseca, V. C. & Darling, E. M. Cellular mechanical properties reflect the differentiation potential of adipose-derived mesenchymal stem cells. *Proc. Natl. Acad. Sci. U. S. A.* **109**, (2012).
80. Jacobi, A. *et al.* Analysis of biomechanical properties of hematopoietic stem and progenitor cells using real-time fluorescence and deformability cytometry. *Methods Mol. Biol.* **2017**, 135–148 (2019).
81. Xavier, M. *et al.* Mechanical phenotyping of primary human skeletal stem cells in heterogeneous populations by real-time deformability cytometry. *Integr. Biol.* **8**, 616–623 (2016).
82. Popel, A. S. & Johnson, P. C. Microcirculation and Hemorheology. *Annu. Rev. Fluid Mech.* **37**, 43–69 (2005).
83. Dupire, J., Puech, P. H., Helfer, E. & Viallat, A. Mechanical adaptation of monocytes in model lung capillary networks. *Proc. Natl. Acad. Sci. U. S. A.* **117**, 14798–14804 (2020).
84. Lipowsky, H. H. Microvascular rheology and hemodynamics. *Microcirculation* **12**, 5–15 (2005).
85. Shelby, J. P., White, J., Ganesan, K., Rathod, P. K. & Chiu, D. T. A microfluidic model for single-cell capillary obstruction by Plasmodium falciparum-infected erythrocytes. *Proc. Natl. Acad. Sci. U. S. A.* **100**, 14618–14622 (2003).
86. Herricks, T., Antia, M. & Rathod, P. K. Deformability limits of Plasmodium falciparum-infected red blood cells. *Cell. Microbiol.* **11**, 1340–1353 (2009).
87. Dondorp, A. M., Kager, P. A., Vreeken, J. & White, N. J. Abnormal blood flow and red blood cell deformability in severe malaria. *Parasitol. Today* **16**, 272 (2000).
88. Franklin Bunn, H. Pathogenesis and treatment of sickle cell disease. *N. Engl. J. Med.* **337**, 762–769 (1997).
89. Lichtman, M. A. Rheology of leukocytes, leukocyte suspensions, and blood in leukemia. Possible relationship to clinical manifestations. *J. Clin. Invest.* **52**, 350–358 (1973).
90. Lam, W. A., Rosenbluth, M. J. & Fletcher, D. A. Increased leukaemia cell stiffness is associated with symptoms of leucostasis in paediatric acute lymphoblastic leukaemia. *Br. J. Haematol.* **142**, 497–501 (2008).
91. Lam, W. A., Rosenbluth, M. J. & Fletcher, D. A. Chemotherapy exposure increases leukemia cell stiffness. *Blood* **109**, 3505–3508 (2007).
92. Preira, P. *et al.* Microfluidic tools to investigate pathologies in the blood microcirculation. *Int. J. Nanotechnol.* **9**, 529–547 (2012).
93. Preira, P. *et al.* The leukocyte-stiffening property of plasma in early acute respiratory distress syndrome (ARDS) revealed by a microfluidic single-cell study: The role of cytokines and protection with antibodies. *Crit. Care* **20**, 1–11 (2016).
94. Nishino, M. *et al.* Serial changes in leukocyte deformability and whole blood rheology in patients with sepsis or trauma. *J. Trauma - Inj. Infect. Crit. Care* **59**, 1425–1431 (2005).
95. Yoshida, K., Kondo, R., Wang, Q. & Doerschuk, C. M. Neutrophil cytoskeletal rearrangements during capillary sequestration in bacterial pneumonia in rats. *Am. J. Respir. Crit. Care Med.* **174**, 689–698 (2006).
96. Mahla, R. S. Stem cells applications in regenerative medicine and disease therapeutics. *Int. J. Cell Biol.* **2016**, (2016).

97. Watanabe, T. *et al.* Decrease in circulating hematopoietic progenitor cells by trapping in the pulmonary circulation. *Cytotherapy* **3**, 461–466 (2001).
98. Schrepfer, S. *et al.* Stem Cell Transplantation: The Lung Barrier. *Transplant. Proc.* **39**, 573–576 (2007).
99. Eggenhofer, E. *et al.* Mesenchymal stem cells are short-lived and do not migrate beyond the lungs after intravenous infusion. *Front. Immunol.* **3**, 1–8 (2012).
100. Erkers, T. *et al.* Treatment of severe chronic graft-versus-host disease with decidual stromal cells and tracing with 111indium radiolabeling. *Stem Cells Dev.* **24**, 253–263 (2015).
101. Steeg, P. S. Targeting metastasis. *Nat. Rev. Cancer* **16**, 201–218 (2016).
102. Wirtz, D. Particle-tracking microrheology of living cells: Principles and applications. *Annu. Rev. Biophys.* **38**, 301–326 (2009).
103. Liu, Z. *et al.* Cancer cells display increased migration and deformability in pace with metastatic progression. *FASEB J.* **34**, 9307–9315 (2020).
104. Ribatti, D., Tamma, R. & Annese, T. Epithelial-Mesenchymal Transition in Cancer: A Historical Overview. *Transl. Oncol.* **13**, 100773 (2020).
105. Chen, Y. Q. *et al.* Epithelial-mesenchymal transition softens head and neck cancer cells to facilitate migration in 3D environments. *J. Cell. Mol. Med.* **22**, 3837–3846 (2018).
106. Han, Y. L. *et al.* Cell swelling, softening and invasion in a three-dimensional breast cancer model. *Nat. Phys.* **16**, 101–108 (2020).
107. Higgins, G. *et al.* Decreased cell stiffness facilitates cell detachment and cell migration from breast cancer spheroids in 3D collagen matrices of different rigidity. *bioRxiv* 2021.01.21.427639 (2021).
108. Rianna, C., Radmacher, M. & Kumar, S. Direct evidence that tumor cells soften when navigating confined spaces. *Mol. Biol. Cell* **31**, 1726–1734 (2020).
109. Hosseini, K., Taubenberger, A., Werner, C. & Fischer-Friedrich, E. EMT-Induced Cell-Mechanical Changes Enhance Mitotic Rounding Strength. *Adv. Sci.* **7**, 1–12 (2020).
110. Chen, J. *et al.* Efficient extravasation of tumor-repopulating cells depends on cell deformability. *Sci. Rep.* **6**, 1–13 (2016).
111. Friedl, P., Wolf, K. & Lammerding, J. Nuclear mechanics during cell migration. *Curr. Opin. Cell Biol.* **23**, 55–64 (2011).
112. Wolf, K. *et al.* Physical limits of cell migration: Control by ECM space and nuclear deformation and tuning by proteolysis and traction force. *J. Cell Biol.* **201**, 1069–1084 (2013).
113. Harada, T. *et al.* Nuclear lamin stiffness is a barrier to 3D migration, but softness can limit survival. *J. Cell Biol.* **204**, 669–682 (2014).
114. Surcel, A. *et al.* Targeting mechanoresponsive proteins in pancreatic cancer: 4-hydroxyacetophenone blocks dissemination and invasion by activating MYH14. *Cancer Res.* **79**, 4665–4678 (2019).
115. Parajón, E., Surcel, A. & Robinson, D. N. The mechanobiome: A goldmine for cancer therapeutics. *Am. J. Physiol. - Cell Physiol.* **320**, C306–C323 (2021).
116. Wirtz, D., Konstantopoulos, K. & Searson, P. C. The physics of cancer: The role of physical interactions and mechanical forces in metastasis. *Nat. Rev. Cancer* **11**, 512–522 (2011).
117. Luster, A. D., Alon, R. & von Andrian, U. H. Immune cell migration in inflammation: Present and future therapeutic targets. *Nat. Immunol.* **6**, 1182–1190 (2005).
118. Vestweber, D. How leukocytes cross the vascular endothelium. *Nat. Rev. Immunol.* **15**, 692–704 (2015).
119. Prame Kumar, K., Nicholls, A. J. & Wong, C. H. Y. Partners in crime: neutrophils and monocytes/macrophages in inflammation and disease. *Cell Tissue Res.* **371**, 551–565 (2018).
120. Schnoor, M., Vadillo, E. & Guerrero-Fonseca, I. M. The extravasation cascade revisited from a neutrophil perspective. *Curr. Opin. Physiol.* **19**, 119–128 (2021).
121. Shi, C. & Pamer, E. G. Monocyte recruitment during infection and inflammation. *Nat. Rev. Immunol.* **11**,

- 762–774 (2011).
122. Hallows, K. R., Packman, C. H. & Knauf, P. A. Acute cell volume changes in anisotonic media affect F-actin content of HL-60 cells. *Am. J. Physiol.* **261**, C1154–61 (1991).
  123. Anderson, G. J., Roswit, W. T., Holtzman, M. J., Hogg, J. C. & Van Eeden, S. F. Effect of mechanical deformation of neutrophils on their CD18/ICAM-1-dependent adhesion. *J. Appl. Physiol.* **91**, 1084–1090 (2001).
  124. Steffen, S. *et al.* Toll-Like Receptor-Mediated Upregulation of CXCL16 in Psoriasis Orchestrates Neutrophil Activation. *J. Invest. Dermatol.* **138**, 344–354 (2018).
  125. Bashant, K. R. *et al.* The mechanics of myeloid cells. *Biol. Cell* **112**, 103–112 (2020).
  126. Davidson, P. M., Denais, C., Bakshi, M. C. & Lammerding, J. Nuclear deformability constitutes a rate-limiting step during cell migration in 3-D environments. *Cell. Mol. Bioeng.* **7**, 293–306 (2014).
  127. Yap, B. & Kamm, R. D. Mechanical deformation of neutrophils into narrow channels induces pseudopod projection and changes in biomechanical properties. *J. Appl. Physiol.* **98**, 1930–1939 (2005).
  128. Patel, N. R. *et al.* Cell Elasticity Determines Macrophage Function. *PLoS One* **7**, 1–10 (2012).
  129. Maître, J. L., Niwayama, R., Turlier, H., Nedelec, F. & Hiiragi, T. Pulsatile cell-autonomous contractility drives compaction in the mouse embryo. *Nat. Cell Biol.* **17**, 849–855 (2015).
  130. Samarage, C. R. *et al.* Cortical Tension Allocates the First Inner Cells of the Mammalian Embryo. *Dev. Cell* **34**, 435–447 (2015).
  131. Nishioka, N. *et al.* The Hippo Signaling Pathway Components Lats and Yap Pattern Tead4 Activity to Distinguish Mouse Trophoblast from Inner Cell Mass. *Dev. Cell* **16**, 398–410 (2009).
  132. Hirate, Y. *et al.* Polarity-dependent distribution of angiominin localizes hippo signaling in preimplantation embryos. *Curr. Biol.* **23**, 1181–1194 (2013).
  133. Hirate, Y. *et al.* Par-aPKC-dependent and -independent mechanisms cooperatively control cell polarity, Hippo signaling, and cell positioning in 16-cell stage mouse embryos. *Dev. Growth Differ.* **57**, 544–556 (2015).
  134. Bergert, M. *et al.* Cell Surface Mechanics Gate Embryonic Stem Cell Differentiation. *Cell Stem Cell* **28**, 209–216.e4 (2021).
  135. De Belly, H. *et al.* Membrane Tension Gates ERK-Mediated Regulation of Pluripotent Cell Fate. *Cell Stem Cell* **28**, 273–284.e6 (2021).
  136. Takaoka, K. & Hamada, H. Cell fate decisions and axis determination in the early mouse embryo. *Development* **139**, 3–14 (2012).
  137. Ernst, A. Mechanical phenotyping of embryonic stem cell derived germ layers. (Bachelor Thesis, Technische Universität Dresden, 2016).
  138. Krieg, M. *et al.* Tensile forces govern germ-layer organization in zebrafish. *Nat. Cell Biol.* **10**, 429–436 (2008).
  139. Barriga, E. H., Franze, K., Charras, G. & Mayor, R. Tissue stiffening coordinates morphogenesis by triggering collective cell migration in vivo. *Nature* **554**, 523–527 (2018).
  140. Thompson, A. J. *et al.* Rapid changes in tissue mechanics regulate cell behaviour in the developing embryonic brain. *Elife* **8**, 1–18 (2019).
  141. Ferrer-Vaquer, A., Viotti, M. & Hadjantonakis, A.-K. Transitions between epithelial and mesenchymal states and the morphogenesis of the early mouse embryo. *Cell Adh. Migr.* **4**, 447–457 (2010).
  142. Mammoto, T. & Ingber, D. E. Mechanical control of tissue and organ development. *Development* **137**, 1407–20 (2010).
  143. Lecuit, T., Lenne, P. F. & Munro, E. Force generation, transmission, and integration during cell and tissue morphogenesis. *Annu. Rev. Cell Dev. Biol.* **27**, 157–184 (2011).
  144. Pollard, T. D. & Earnshaw, W. C. General Principles of Cellular Organization. in *Cell Biology* 1–16 (Saunders, 2002).

145. Ellis, R. J. Macromolecular crowding: Obvious but underappreciated. *Trends Biochem. Sci.* **26**, 597–604 (2001).
146. Animal Cell. *Wikimedia Commons*  
[https://upload.wikimedia.org/wikipedia/commons/1/11/Animal\\_Cell.svg](https://upload.wikimedia.org/wikipedia/commons/1/11/Animal_Cell.svg) (2021).
147. McGuffee, S. R. & Elcock, A. H. Diffusion, crowding & protein stability in a dynamic molecular model of the bacterial cytoplasm. *PLoS Comput. Biol.* **6**, (2010).
148. Herrmann, H., Strelkov, S. V., Burkhard, P. & Aebi, U. Intermediate filaments: Primary determinants of cell architecture and plasticity. *J. Clin. Invest.* **119**, 1772–1783 (2009).
149. Gittes, F., Mickey, B., Nettleton, J. & Howard, J. Flexural rigidity of microtubules and actin filaments measured from thermal fluctuations in shape. *J. Cell Biol.* **120**, 923–934 (1993).
150. Isambert, H. *et al.* Flexibility of actin filaments derived from thermal fluctuations. Effect of bound nucleotide, phalloidin, and muscle regulatory proteins. *J. Biol. Chem.* **270**, 11437–11444 (1995).
151. Steinmetz, M. O., Goldie, K. N. & Aebi, U. A correlative analysis of actin filament assembly, structure, and dynamics. *J. Cell Biol.* **138**, 559–574 (1997).
152. Van Mameren, J., Vermeulen, K. C., Gittes, F. & Schmidt, C. F. Leveraging single protein polymers to measure flexural rigidity. *J. Phys. Chem. B* **113**, 3837–3844 (2009).
153. Pegoraro, A. F., Janmey, P. & Weitz, D. A. Mechanical properties of the cytoskeleton and cells. *Cold Spring Harb. Perspect. Biol.* **9**, (2017).
154. Tojkander, S., Gateva, G. & Lappalainen, P. Actin stress fibers - Assembly, dynamics and biological roles. *J. Cell Sci.* **125**, 1855–1864 (2012).
155. Chugh, P. & Paluch, E. K. The actin cortex at a glance. *J. Cell Sci.* **131**, 1–9 (2018).
156. Koenderink, G. H. & Paluch, E. K. Architecture shapes contractility in actomyosin networks. *Curr. Opin. Cell Biol.* **50**, 79–85 (2018).
157. Chugh, P. *et al.* Actin cortex architecture regulates cell surface tension. *Nat. Cell Biol.* **19**, 689–697 (2017).
158. Riento, K. & Ridley, A. J. Rocks: Multifunctional kinases in cell behaviour. *Nat. Rev. Mol. Cell Biol.* **4**, 446–456 (2003).
159. Hall, A. Rho GTPases and the control of cell behaviour. *Biochem. Soc. Trans.* **33**, 891–895 (2005).
160. Mücke, N. *et al.* Assessing the Flexibility of Intermediate Filaments by Atomic Force Microscopy. *J. Mol. Biol.* **335**, 1241–1250 (2004).
161. Wagner, O. I. *et al.* Softness, strength and self-repair in intermediate filament networks. *Exp. Cell Res.* **313**, 2228–2235 (2007).
162. Patteson, A. E. *et al.* Vimentin protects cells against nuclear rupture and DNA damage during migration. *J. Cell Biol.* **218**, 4079–4092 (2019).
163. Gruenbaum, Y., Margalit, A., Goldman, R. D., Shumaker, D. K. & Wilson, K. L. The nuclear lamina comes of age. *Nat. Rev. Mol. Cell Biol.* **6**, 21–31 (2005).
164. Starr, D. A. & Fridolfsson, H. N. Interactions between nuclei and the cytoskeleton are mediated by SUN-KASH nuclear-envelope bridges. *Annu. Rev. Cell Dev. Biol.* **26**, 421–444 (2010).
165. Starr, D. A. KASH and SUN proteins. *Curr. Biol.* **21**, R414–R415 (2011).
166. Kirby, T. J. & Lammerding, J. Emerging views of the nucleus as a cellular mechanosensor. *Nat. Cell Biol.* **20**, 373–381 (2018).
167. Mitchison, T. & Kirschner, M. Dynamic instability of microtubule growth. *Nature* **312**, (1984).
168. Goodson, H. V & Jonasson, E. M. Microtubules and Microtubule-Associated Proteins. *Cold Spring Harb Perspect Biol* 10:a022608 (2018).
169. Bodakuntla, S., Jijumon, A. S., Villablanca, C., Gonzalez-Billault, C. & Janke, C. Microtubule-Associated Proteins: Structuring the Cytoskeleton. *Trends Cell Biol.* **29**, 804–819 (2019).
170. Brangwynne, C. P. *et al.* Microtubules can bear enhanced compressive loads in living cells because of

- lateral reinforcement. *J. Cell Biol.* **173**, 733–741 (2006).
171. Mostowy, S. & Cossart, P. Septins: The fourth component of the cytoskeleton. *Nat. Rev. Mol. Cell Biol.* **13**, 183–194 (2012).
172. Spiliotis, E. T. & Nakos, K. Cellular functions of actin- and microtubule-associated septins. *Curr. Biol.* **31**, R651–R666 (2021).
173. Mavrakakis, M. *et al.* Septins promote F-actin ring formation by crosslinking actin filaments into curved bundles. *Nat. Cell Biol.* **16**, 322–334 (2014).
174. Caudron, F. & Barral, Y. Septins and the Lateral Compartmentalization of Eukaryotic Membranes. *Dev. Cell* **16**, 493–506 (2009).
175. Gilden, J. K., Peck, S., Chen, Y. C. M. & Krummel, M. F. The septin cytoskeleton facilitates membrane retraction during motility and blebbing. *J. Cell Biol.* **196**, 103–114 (2012).
176. Gilden, J. & Krummel, M. F. Control of cortical rigidity by the cytoskeleton: Emerging roles for septins. *Cytoskeleton* **67**, 477–486 (2010).
177. Petersen, N., McConnaughey, W. B. & Elson, E. L. Dependence of locally measured cellular deformability on position on the cell, temperature, and cytochalasin B. **79**, 5327–5331 (1982).
178. Wakatsuki, T., Schwab, B., Thompson, N. C. & Elson, E. L. Effects of cytochalasin D and latrunculin B on mechanical properties of cells. *J. Cell Sci.* **114**, 1025–1036 (2001).
179. Golfier, S. *et al.* High-throughput cell mechanical phenotyping for label-free titration assays of cytoskeletal modifications. *Cytoskeleton* **74**, 283–296 (2017).
180. Nyberg, K. D. *et al.* Quantitative Deformability Cytometry: Rapid, Calibrated Measurements of Cell Mechanical Properties. *Biophys. J.* **113**, 1574–1584 (2017).
181. Guillou, L. *et al.* Measuring Cell Viscoelastic Properties Using a Microfluidic Extensional Flow Device. *Biophys. J.* **111**, 2039–2050 (2016).
182. Martens, J. C. & Radmacher, M. Softening of the actin cytoskeleton by inhibition of myosin II. *Pflügers Arch. Eur. J. Physiol.* **456**, 95–100 (2008).
183. Tinevez, J. Y. *et al.* Role of cortical tension in bleb growth. *Proc. Natl. Acad. Sci. U. S. A.* **106**, 18581–18586 (2009).
184. Fischer-Friedrich, E. *et al.* Rheology of the Active Cell Cortex in Mitosis. *Biophys. J.* **111**, 589–600 (2016).
185. Wittmann, T., Dema, A. & van Haren, J. Lights, cytoskeleton, action: Optogenetic control of cell dynamics. *Curr. Opin. Cell Biol.* **66**, 1–10 (2020).
186. Valon, L., Marín-Llauradó, A., Wyatt, T., Charras, G. & Trepat, X. Optogenetic control of cellular forces and mechanotransduction. *Nat. Commun.* **8**, (2017).
187. Hennig, K. *et al.* Stick-slip dynamics of cell adhesion triggers spontaneous symmetry breaking and directional migration of mesenchymal cells on one-dimensional lines. *Sci. Adv.* **6**, 1–13 (2020).
188. Oakes, P. W. *et al.* Optogenetic control of RhoA reveals zyxin-mediated elasticity of stress fibres. *Nat. Commun.* **8**, (2017).
189. Wagner, E. & Glotzer, M. Local RhoA activation induces cytokinetic furrows independent of spindle position and cell cycle stage. *J. Cell Biol.* **213**, 641–649 (2016).
190. Izquierdo, E., Quinkler, T. & De Renzis, S. Guided morphogenesis through optogenetic activation of Rho signalling during early Drosophila embryogenesis. *Nat. Commun.* **9**, 1–13 (2018).
191. Cavanaugh, K. E., Staddon, M. F., Munro, E., Banerjee, S. & Gardel, M. L. RhoA Mediates Epithelial Cell Shape Changes via Mechanosensitive Endocytosis. *Dev. Cell* **52**, 152–166.e5 (2020).
192. Wang, N. & Stamenović, D. Contribution of intermediate filaments to cell stiffness, stiffening, and growth. *Am. J. Physiol. - Cell Physiol.* **279**, 188–194 (2000).
193. Guo, M. *et al.* The role of vimentin intermediate filaments in cortical and cytoplasmic mechanics. *Biophys. J.* **105**, 1562–1568 (2013).



194. Mendez, M. G., Restle, D. & Janmey, P. A. Vimentin enhances cell elastic behavior and protects against compressive stress. *Biophys. J.* **107**, 314–323 (2014).
195. Stankevicius, L. D. C. *et al.* Vimentin provides the mechanical resilience required for amoeboid migration and protection of the nucleus. *bioRxiv* (2019) doi:10.1101/720946.
196. Janmey, P. A., Euteneuer, U., Traub, P. & Schliwa, M. Viscoelastic properties of vimentin compared with other filamentous biopolymer networks. *J. Cell Biol.* **113**, 155–160 (1991).
197. Charrier, E. E. & Janmey, P. A. Mechanical Properties of Intermediate Filament Proteins. *Methods Enzymol.* **568**, 35–57 (2016).
198. Kubitschke, H. *et al.* Actin and microtubule networks contribute differently to cell response for small and large strains. *New J. Phys.* **19**, (2017).
199. Chang, Y. C., Nalbant, P., Birkenfeld, J., Chang, Z. F. & Bokoch, G. M. GEF-H1 couples nocodazole-induced microtubule disassembly to cell contractility via RhoA. *Mol. Biol. Cell* **19**, 2147–2153 (2008).
200. Mostowy, S. *et al.* A role for septins in the interaction between the *Listeria monocytogenes* invasion protein InlB and the Met receptor. *Biophys. J.* **100**, 1949–1959 (2011).
201. Chang, L. & Goldman, R. D. Intermediate filaments mediate cytoskeletal crosstalk. *Nat. Rev. Mol. Cell Biol.* **5**, 601–613 (2004).
202. Dogterom, M. & Koenderink, G. H. Actin–microtubule crosstalk in cell biology. *Nat. Rev. Mol. Cell Biol.* **20**, 38–54 (2019).
203. Watson, H. Biological membranes. *Essays Biochem.* **59**, 43–70 (2015).
204. Hamill, O. P. & Martinac, B. Molecular basis of mechanotransduction in living cells. *Physiol. Rev.* **81**, 685–740 (2001).
205. Sens, P. & Plastino, J. Membrane tension and cytoskeleton organization in cell motility. *J. Phys. Condens. Matter* **27**, (2015).
206. Gauthier, N. C., Masters, T. A. & Sheetz, M. P. Mechanical feedback between membrane tension and dynamics. *Trends Cell Biol.* **22**, 527–535 (2012).
207. Le Roux, A. L., Quiroga, X., Walani, N., Arroyo, M. & Roca-Cusachs, P. The plasma membrane as a mechanochemical transducer. *Philos. Trans. R. Soc. B Biol. Sci.* **374**, (2019).
208. Groulx, N., Boudreault, F., Orlov, S. N. & Grygorczyk, R. Membrane reserves and hypotonic cell swelling. *J. Membr. Biol.* **214**, 43–56 (2006).
209. Sinha, B. *et al.* Cells respond to mechanical stress by rapid disassembly of caveolae. *Cell* **144**, 402–413 (2011).
210. Parton, R. G. & Del Pozo, M. A. Caveolae as plasma membrane sensors, protectors and organizers. *Nat. Rev. Mol. Cell Biol.* **14**, 98–112 (2013).
211. Echarri, A. & Del Pozo, M. A. Caveolae - mechanosensitive membrane invaginations linked to actin filaments. *J. Cell Sci.* **128**, 2747–2758 (2015).
212. Diz-Muñoz, A., Weiner, O. D. & Fletcher, D. A. In pursuit of the mechanics that shape cell surfaces. *Nat. Phys.* **14**, 648–652 (2018).
213. Clark, A. G., Wartlick, O., Salbreux, G. & Paluch, E. K. Stresses at the cell surface during animal cell morphogenesis. *Curr. Biol.* **24**, R484–R494 (2014).
214. Morone, N. *et al.* Three-dimensional reconstruction of the membrane skeleton at the plasma membrane interface by electron tomography. *J. Cell Biol.* **174**, 851–862 (2006).
215. Escolano, J. C. *et al.* Compliant Substrates Enhance Macrophage Cytokine Release and NLRP3 Inflammasome Formation During Their Pro-Inflammatory Response. *Front. Cell Dev. Biol.* **9**, 1–14 (2021).
216. Guilak, F. Compression-induced changes in the shape and volume of the chondrocyte nucleus. in *Journal of Biomechanics* vol. 28 1529–1541 (1995).
217. Caille, N., Thoumine, O., Tardy, Y. & Meister, J. J. Contribution of the nucleus to the mechanical properties of endothelial cells. *J. Biomech.* **35**, 177–187 (2002).

218. Guilak, F., Tedrow, J. R. & Burgkart, R. Viscoelastic properties of the cell nucleus. *Biochem. Biophys. Res. Commun.* **269**, 781–786 (2000).
219. Sugitate, T., Kihara, T., Liu, X. Y. & Miyake, J. Mechanical role of the nucleus in a cell in terms of elastic modulus. *Curr. Appl. Phys.* **9**, e291–e293 (2009).
220. Reynolds, N. H. *et al.* On the role of the actin cytoskeleton and nucleus in the biomechanical response of spread cells. *Biomaterials* **35**, 4015–4025 (2014).
221. Wang, X. *et al.* Mechanical stability of the cell nucleus - roles played by the cytoskeleton in nuclear deformation and strain recovery. *J. Cell Sci.* **131**, (2018).
222. Efremov, Y. M., Kotova, S. L., Akovantseva, A. A. & Timashev, P. S. Nanomechanical properties of enucleated cells: Contribution of the nucleus to the passive cell mechanics. *J. Nanobiotechnology* **18**, 1–11 (2020).
223. Broers, J. L. V. *et al.* Decreased mechanical stiffness in LMNA-/- cells is caused by defective nucleocyto-skeletal integrity: Implications for the development of laminopathies. *Hum. Mol. Genet.* **13**, 2567–2580 (2004).
224. Lammerding, J. *et al.* Lamin A / C deficiency causes Tema Grupo defective nuclear mechanics and mechanotransduction. *J. Clin. Invest.* **113**, 370–378 (2004).
225. Lee, J. S. H. *et al.* Nuclear lamin A/C deficiency induces defects in cell mechanics, polarization, and migration. *Biophys. J.* **93**, 2542–52 (2007).
226. Hanson, J. N., Rodriguez, B. J., Nemanich, R. J. & Gruverman, a. Fabrication of metallic nanowires on a ferroelectric template via photochemical reaction. *Nanotechnology* **17**, 4946–4949 (2006).
227. Chalut, K. J. *et al.* Chromatin decondensation and nuclear softening accompany Nanog downregulation in embryonic stem cells. *Biophys. J.* **103**, 2060–2070 (2012).
228. Guilak, F., Erickson, G. R. & Ting-Beall, H. P. The effects of osmotic stress on the viscoelastic and physical properties of articular chondrocytes. *Biophys. J.* **82**, 720–727 (2002).
229. Steltenkamp, S., Rommel, C., Wegener, J. & Janshoff, A. Membrane stiffness of animal cells challenged by osmotic stress. *Small* **2**, 1016–1020 (2006).
230. Zhou, E. H. *et al.* Universal behavior of the osmotically compressed cell and its analogy to the colloidal glass transition. *PNAS* **106**, 10632–10637 (2009).
231. Moendarbary, E. *et al.* The cytoplasm of living cells behaves as a poroelastic material. *Nat. Mater.* **12**, 253–261 (2013).
232. Guo, M. *et al.* Cell volume change through water efflux impacts cell stiffness and stem cell fate. *PNAS* **c**, 201705179 (2017).
233. Delarue, M. *et al.* mTORC1 Controls Phase Separation and the Biophysical Properties of the Cytoplasm by Tuning Crowding. *Cell* **174**, 338–349.e20 (2018).
234. Janmey, P. A., Georges, P. C. & Hvidt, S. Basic Rheology for Biologists. *Methods Cell Biol.* **83**, 3–27 (2007).
235. Roylance, D. *Engineering Viscoelasticity*. (Massachusetts Institute of Technology, 2001).
236. Lakes, R. Introduction: Phenomena. in *Viscoelastic Materials* 1–13 (Cambridge University Press, 2009). doi:10.1017/CBO9780511626722.002.
237. Olsson, R. & Båth, M. Analogy between elastic and electric systems. *Phys. Earth Planet. Inter.* **10**, 1–11 (1975).
238. Roeder, R. K. Mechanical characterization of biomaterials. in *Characterization of biomaterials* 49–104 (Elsevier, 2013).
239. Kelly, P. A. 10. Viscoelasticity. *Solid mechanics part I: An introduction to solid mechanics* 283–342 (2013).
240. AA Kulkarni, R Srivastava, B. B. Vibration Transmissibility Based Identification of Soft Viscoelastic Systems. *ISSS Natl. Conf. MEMS Smart Mater. Struct. Syst.* 1–7 (2015).
241. Bonfanti, A., Kaplan, J. L., Charras, G. & Kabla, A. Fractional viscoelastic models for power-law materials. *Soft Matter* **16**, 6002–6020 (2020).

- 
242. Kollmannsberger, P. & Fabry, B. Linear and Nonlinear Rheology of Living Cells. *Annu. Rev. Mater. Res.* **41**, 75–97 (2011).
243. Di Paola, M., Pirrotta, A. & Valenza, A. Visco-elastic behavior through fractional calculus: An easier method for best fitting experimental results. *Mech. Mater.* **43**, 799–806 (2011).
244. Bonfanti, A., Fouchard, J., Khalilgharibi, N., Charras, G. & Kabla, A. A unified rheological model for cells and cellularised materials. *R. Soc. Open Sci.* **7**, 190920 (2019).
245. Kasza, K. E. *et al.* The cell as a material. *Curr. Opin. Cell Biol.* **19**, 101–107 (2007).
246. Hao, Y. *et al.* Mechanical properties of single cells: Measurement methods and applications. *Biotechnol. Adv.* **45**, 107648 (2020).
247. Zhang, J., Nou, X. A., Kim, H. & Scarcelli, G. Brillouin flow cytometry for label-free mechanical phenotyping of the nucleus. *Lab Chip* **17**, 663–670 (2017).
248. Mitchison, J. M. & Swann, M. M. The Mechanical Properties of the Cell Surface : I. The Cell Elastimeter. *J. Exp. Biol.* **31**, 443–460 (1954).
249. Mitchison, B. Y. J. M. & Swann, M. M. The Mechanical Properties of the cell Surface: II. The Unfertilized Sea-Urchin Egg. *J. Exp. Biol.* **31**, 461–472 (1954).
250. Cole, K. S. Surface forces of the arbacia egg. *J. Cell. Comparative Physiol.* **1**, 1–9 (1932).
251. Hiramoto, Y. Mechanical properties of sea urchin eggs. I. Surface force and elastic modulus of the cell membrane. *Exp. Cell Res.* **32**, 59–75 (1963).
252. Hiramoto, Y. Mechanical properties of sea urchin eggs. II. Changes in mechanical properties from fertilization to cleavage. *Exp. Cell Res.* **32**, 76–89 (1963).
253. Yoneda, M. The Compression Method for Determining the Surface Force. *Methods Cell Biol.* **27**, 421–434 (1986).
254. McConnaughey, W. B. & Petersen, N. O. Cell poker: An apparatus for stress-strain measurements on living cells. *Rev. Sci. Instrum.* **51**, 575–580 (1980).
255. Daily, B., Elson, E. L. & Zahalak, G. I. Cell poking. Determination of the elastic area compressibility modulus of the erythrocyte membrane. *Biophys. J.* **45**, 671–682 (1984).
256. Zahalak, G. I., McConnaughey, W. B. & Elson, E. L. Determination of cellular mechanical properties by cell poking, with an application to leukocytes. *J. Biomech. Eng.* **112**, 283–294 (1990).
257. Radmacher, M., Tillmann, R. W., Fritz, M. & Gaub, H. E. From molecules to cells: Imaging soft samples with the atomic force microscope. *Science* **257**, 1900–1905 (1992).
258. Radmacher, M. Measuring the elastic properties of biological samples with the AFM. *IEEE Eng. Med. Biol. Mag.* **16**, 47–57 (1997).
259. Hertz, H. Ueber die Berührung fester elastischer Körper. *J. für die Reine und Angew. Math.* **1882**, 156–171 (1882).
260. Darling, E. M., Zauscher, S. & Guilak, F. Viscoelastic properties of zonal articular chondrocytes measured by atomic force microscopy. *Osteoarthr. Cartil.* **14**, 571–579 (2006).
261. Stewart, M. P. *et al.* Wedged AFM-cantilevers for parallel plate cell mechanics. *Methods* **60**, 186–194 (2013).
262. Thoumine, O. & Ott, A. Time scale dependent viscoelastic and contractile regimes in fibroblasts probed by microplate manipulation. *J. Cell Sci.* **110**, 2109–2116 (1997).
263. Desprat, N., Richert, A., Simeon, J. & Asnacios, A. Creep function of a single living cell. *Biophys. J.* **88**, 2224–2233 (2005).
264. Desprat, N., Guiroy, A. & Asnacios, A. Microplates-based rheometer for a single living cell. *Rev. Sci. Instrum.* **77**, (2006).
265. Gardel, M. L., Valentine, M. T. & Weitz, D. A. Microrheology. in *Microscale Diagnostic Techniques* (ed. Breuer, K. S.) 1–49 (Springer Berlin Heidelberg, 2005). doi:10.1007/3-540-26449-3\_1.
266. Mason, T. G., Ganesan, K., Van Zanten, J. H., Wirtz, D. & Kuo, S. C. Particle tracking microrheology

- of complex fluids. *Phys. Rev. Lett.* **79**, 3282–3285 (1997).
267. Valberg, P. A. Magnetometry of ingested particles in pulmonary macrophages. *Science* **224**, 513–516 (1984).
268. Crick, F. H. C. & Hughes, A. F. W. The physical properties of cytoplasm. *Exp. Cell Res.* **1**, 37–80 (1950).
269. Bausch, A. R., Möller, W. & Sackmann, E. Measurement of local viscoelasticity and forces in living cells by magnetic tweezers. *Biophys. J.* **76**, 573–579 (1999).
270. Wang, N., Butler, J. P. & Ingber, D. E. Mechanotransduction across the cell surface and through the cytoskeleton. *Science* **260**, 1124–1127 (1993).
271. Maksym, G. N. *et al.* Mechanical properties of cultured human airway smooth muscle cells from 0.05 to 0.4 Hz. *J. Appl. Physiol.* **89**, 1619–1632 (2000).
272. Yanai, M. *et al.* Intracellular elasticity and viscosity in the body, leading, and trailing regions of locomoting neutrophils. *Am. J. Physiol. - Cell Physiol.* **277**, (1999).
273. Wei, M.-T. *et al.* A comparative study of living cell micromechanical properties by oscillatory optical tweezers. *Opt. Express* **16**, 8594 (2008).
274. Ayala, Y. A. *et al.* Rheological properties of cells measured by optical tweezers. *BMC Biophys.* **9**, 1–11 (2016).
275. Sorkin, R. *et al.* Probing cellular mechanics with acoustic force spectroscopy. *Mol. Biol. Cell* **29**, 2005–2011 (2018).
276. Nguyen, A., Brandt, M., Muenker, T. M. & Betz, T. Multi-oscillation microrheology via acoustic force spectroscopy enables frequency-dependent measurements on endothelial cells at high-throughput. *Lab Chip* **21**, 1929–1947 (2021).
277. Ashkin, A. Acceleration and trapping of particles by radiation pressure. *Phys. Rev. Lett.* **24**, 156 (1970).
278. Ashkin, A., Dziedzic, J. M., Bjorkholm, J. E. & Chu, S. Observation of a single-beam gradient force optical trap for dielectric particles. *Opt. Lett.* **11**, 288–290 (1986).
279. Zhang, H. & Liu, K. K. Optical tweezers for single cells. *J. R. Soc. Interface* **5**, 671–690 (2008).
280. Favre-Bulle, I. A., Stilgoe, A. B., Scott, E. K. & Rubinsztein-Dunlop, H. Optical trapping in vivo: Theory, practice, and applications. *Nanophotonics* **8**, 1023–1040 (2019).
281. Bustamante, C. J., Chemla, Y. R., Liu, S. & Wang, M. D. Optical tweezers in single-molecule biophysics. *Nat. Rev. Methods Prim.* **1**, (2021).
282. Bertseva, E. *et al.* Optical trapping microrheology in cultured human cells. *Eur. Phys. J. E* **35**, (2012).
283. Hénon, S., Lenormand, G., Richert, A. & Gallet, F. A new determination of the shear modulus of the human erythrocyte membrane using optical tweezers. *Biophys. J.* **76**, 1145–1151 (1999).
284. Dao, M., Lim, C. T. & Suresh, S. Mechanics of the human red blood cell deformed by optical tweezers. *J. Mech. Phys. Solids* **51**, 2259–2280 (2003).
285. Lim, C. T., Dao, M., Suresh, S., Sow, C. H. & Chew, K. T. Large deformation of living cells using laser traps. *Acta Mater.* **52**, 1837–1845 (2004).
286. Mills, J. P., Qie, L., Dao, M., Lim, C. T. & Suresh, S. Nonlinear elastic and viscoelastic deformation of the human red blood cell with optical tweezers. *Mech. Chem. Biosyst.* **1**, 169–180 (2004).
287. Yoon, Y.-Z., Kotar, J., Yoon, G. & Cicuta, P. The nonlinear mechanical response of the red blood cell. *Phys. Biol.* **5**, 36007 (2008).
288. Guck, J., Ananthakrishnan, R., Moon, T. J., Cunningham, C. C. & Käs, J. Optical deformability of soft biological dielectrics. *Phys. Rev. Lett.* **84**, 5451–4 (2000).
289. Guck, J. *et al.* The optical stretcher: a novel laser tool to micromanipulate cells. *Biophys. J.* **81**, 767–784 (2001).
290. Matthews, H. K. *et al.* Changes in Ect2 Localization Couple Actomyosin-Dependent Cell Shape Changes to Mitotic Progression. *Dev. Cell* **23**, 371–383 (2012).

- 
291. Chan, C. J. *et al.* Myosin II Activity Softens Cells in Suspension. *Biophys. J.* **108**, 1856–1869 (2015).
292. Lincoln, B. *et al.* Deformability-based flow cytometry. *Cytom. Part A* **59**, 203–209 (2004).
293. Faigle, C. *et al.* A monolithic glass chip for active single-cell sorting based on mechanical phenotyping. *Lab Chip* **15**, 1267–1275 (2015).
294. Guck, J. Some thoughts on the future of cell mechanics. *Biophys. Rev.* **11**, 667–670 (2019).
295. Lange, J. R. *et al.* Microconstriction Arrays for High-Throughput Quantitative Measurements of Cell Mechanical Properties. *Biophys. J.* **109**, 26–34 (2015).
296. Adamo, A. *et al.* Microfluidics-based assessment of cell deformability. *Anal. Chem.* **84**, 6438–6443 (2012).
297. Zhou, Y. *et al.* Characterizing Deformability and Electrical Impedance of Cancer Cells in a Microfluidic Device. *Anal. Chem.* **90**, 912–919 (2018).
298. Mietke, A. *et al.* Extracting Cell Stiffness from Real-Time Deformability Cytometry: Theory and Experiment. *Biophys. J.* **109**, 2023–2036 (2015).
299. Di Carlo, D. Inertial microfluidics. *Lab Chip* **9**, 3038 (2009).
300. Deng, Y. *et al.* Inertial Microfluidic Cell Stretcher (iMCS): Fully Automated, High-Throughput, and Near Real-Time Cell Mechanotyping. *Small* **13**, (2017).
301. Liang, M. *et al.* Single-cell stretching in viscoelastic fluids with electronically triggered imaging for cellular mechanical phenotyping. *Anal. Chem.* **93**, 4567–4575 (2021).
302. Prevedel, R., Diz-Muñoz, A., Ruocco, G. & Antonacci, G. Brillouin microscopy: an emerging tool for mechanobiology. *Nat. Methods* **16**, 969–977 (2019).
303. Kennedy, B. F., Wijesinghe, P. & Sampson, D. D. The emergence of optical elastography in biomedicine. *Nat. Photonics* **11**, 215–221 (2017).
304. Scarcelli, G. & Yun, S. H. Confocal Brillouin microscopy for three-dimensional mechanical imaging. *Nat. Photonics* **2**, 39–43 (2008).
305. Scarcelli, G. *et al.* Noncontact three-dimensional mapping of intracellular hydromechanical properties by Brillouin microscopy. *Nat. Methods* **12**, 1132–1134 (2015).
306. Schlübler, R. *et al.* Mechanical Mapping of Spinal Cord Growth and Repair in Living Zebrafish Larvae by Brillouin Imaging. *Biophys. J.* **115**, 911–923 (2018).
307. Bevilacqua, C., Sánchez-Iranzo, H., Richter, D., Diz-Muñoz, A. & Prevedel, R. Imaging mechanical properties of sub-micron ECM in live zebrafish using Brillouin microscopy. *Biomed. Opt. Express* **10**, 1420 (2019).
308. Hildebrand, J. A. & Rugar, D. Measurement of cellular elastic properties by acoustic microscopy. *J. Microsc.* **134**, 245–260 (1984).
309. Kundu, T., Bereiter-Hahn, J. & Hillmann, K. Measuring elastic properties of cells by evaluation of scanning acoustic microscopy V(Z) values using simplex algorithm. *Biophys. J.* **59**, 1194–1207 (1991).
310. Lüers, H., Hillmann, K., Litniewski, J. & Bereiter-Hahn, J. Acoustic microscopy of cultured cells - Distribution of forces and cytoskeletal elements. *Cell Biophys.* **18**, 279–293 (1991).
311. Wu, P. H. *et al.* A comparison of methods to assess cell mechanical properties. *Nat. Methods* **15**, 491–498 (2018).
312. Rosendahl, P. *et al.* Real-time fluorescence and deformability cytometry. *Nat. Methods* **15**, 355 (2018).
313. Nawaz, A. A. A. *et al.* Intelligent image-based deformation-assisted cell sorting with molecular specificity. *Nat. Methods* **17**, 595–599 (2020).
314. Ge, Y. *et al.* Cell Mechanics Based Computational Classification of Red Blood Cells Via Machine Intelligence Applied to Morpho-Rheological Markers. *IEEE/ACM Trans. Comput. Biol. Bioinforma.* **5963**, 1–1 (2019).
315. Kräter, M. *et al.* AIDeveloper: Deep Learning Image Classification in Life Science and Beyond. *Adv. Sci.* **8**, 1–12 (2021).

316. Urbanska, M., Rosendahl, P., Kräter, M. & Guck, J. High-throughput single-cell mechanical phenotyping with real-time deformability cytometry. *Methods Cell Biol.* **147**, (2018).
317. Mokbel, M. *et al.* Numerical Simulation of Real-Time Deformability Cytometry To Extract Cell Mechanical Properties. *ACS Biomater. Sci. Eng.* **3**, 2962–2973 (2017).
318. Herold, C. Mapping of Deformation to Apparent Young’s Modulus in Real-Time Deformability Cytometry. *arXiv* arXiv:1704.00572 (2017).
319. Shapiro, H. M. *Practical Flow Cytometry*. (John Wiley & Sons, Inc., 2003). doi:10.1002/0471722731.
320. Gustafson, M. P. *et al.* A method for identification and analysis of non-overlapping myeloid immunophenotypes in humans. *PLoS One* **10**, e0121546 (2015).
321. Ding, X. *et al.* Surface acoustic wave microfluidics. *Lab Chip* **13**, 3626–49 (2013).
322. Di Carlo, D., Irimia, D., Tompkins, R. G. & Toner, M. Continuous inertial focusing, ordering, and separation of particles in microchannels. *Proc. Natl. Acad. Sci. U. S. A.* **104**, 18892–18897 (2007).
323. Girardo, S. *et al.* Standardized microgel beads as elastic cell mechanical probes. *J. Mater. Chem. B* **6**, 6245–6261 (2018).
324. Hartono, D. *et al.* On-chip measurements of cell compressibility via acoustic radiation. *Lab Chip* **11**, 4072–4080 (2011).
325. 3.6. Cellular Differentiation. *Anatomy and Physiology*. Openstax <https://openstax.org/books/anatomy-and-physiology/pages/3-6-cellular-differentiation> (2019).
326. Creative Commons Attribution 4.0 International License. <https://creativecommons.org/licenses/by/4.0/>.
327. Das, D., Ghosh, M., Chakraborty, C., Maiti, A. K. & Pal, M. Probabilistic prediction of malaria using morphological and textural information. in *2011 international conference on image information processing* 1–6 (IEEE, 2011). doi:10.1109/ICIIP.2011.6108879.
328. Linder, N. *et al.* A malaria diagnostic tool based on computer vision screening and visualization of Plasmodium falciparum candidate areas in digitized blood smears. *PLoS One* **9**, e104855 (2014).
329. Adjed, F., Faye, I., Ababsa, F., Gardezi, S. J. & Dass, S. C. Classification of skin cancer images using local binary pattern and SVM classifier. in *AIP Conference Proceedings* vol. 1787 080006 (2016).
330. Hamilton, N. A., Pantelic, R. S., Hanson, K. & Teasdale, R. D. Fast automated cell phenotype image classification. *BMC Bioinformatics* **8**, 110 (2007).
331. Herbig, M. Real-time image-based cell identification. (Doctoral dissertation, Technische Universität Dresden, 2020).
332. Handgretinger, R. *et al.* Isolation and transplantation of autologous peripheral CD34+ progenitor cells highly purified by magnetic-activated cell sorting. *Bone Marrow Transplant.* **21**, 987–993 (1998).
333. Stamm, C. *et al.* Autologous bone-marrow stem-cell transplantation for myocardial regeneration. *Lancet* **361**, 45–46 (2003).
334. Bartsch, U. *et al.* Retinal cells integrate into the outer nuclear layer and differentiate into mature photoreceptors after subretinal transplantation into adult mice. *Exp. Eye Res.* **86**, 691–700 (2008).
335. Gagliardi, G. *et al.* Characterization and Transplantation of CD73-Positive Photoreceptors Isolated from Human iPSC-Derived Retinal Organoids. *Stem Cell Reports* **11**, 665–680 (2018).
336. Fregin, B. *et al.* High-throughput single-cell rheology in complex samples by dynamic real-time deformability cytometry. *Nat. Commun.* **10**, 1–11 (2019).
337. Wittwer, L., Reichel, F. & Aland, S. Numerical simulation of deformability cytometry-transport of a biological cell through a microfluidic channel. *submitted* 1–31 (2021).
338. Tassieri, M. *et al.* i-Rheo: Measuring the materials’ linear viscoelastic properties “in a step”! . *J. Rheol.* (N. Y. N. Y). **60**, 649–660 (2016).
339. Chim, Y. H. *et al.* A one-step procedure to probe the viscoelastic properties of cells by Atomic Force Microscopy. *Sci. Rep.* **8**, 1–12 (2018).

340. Rivas-Barbosa, R., Escobedo-Sánchez, M. A., Tassieri, M. & Laurati, M. I-Rheo: Determining the linear viscoelastic moduli of colloidal dispersions from step-stress measurements. *Phys. Chem. Chem. Phys.* **22**, 3839–3848 (2020).
341. Maloney, J. M. *et al.* Mesenchymal stem cell mechanics from the attached to the suspended state. *Biophys. J.* **99**, 2479–2487 (2010).
342. Scheuermann, S. *et al.* TissueGrinder, a novel technology for rapid generation of patient-derived single cell suspensions from solid tumors by mechanical tissue dissociation. *bioRxiv* (2021) doi:10.1101/2021.06.08.447529.
343. Echeverri, C. J. & Perrimon, N. High-throughput RNAi screening in cultured cells: A user's guide. *Nat. Rev. Genet.* **7**, 373–384 (2006).
344. Shalem, O., Sanjana, N. E. & Zhang, F. High-throughput functional genomics using CRISPR-Cas9. *Nat. Rev. Genet.* **16**, 299–311 (2015).
345. Beech, J. P., Holm, S. H., Adolfsson, K. & Tegenfeldt, J. O. Sorting cells by size, shape and deformability. *Lab Chip* **12**, 1048–1051 (2012).
346. Holmes, D. *et al.* Separation of blood cells with differing deformability using deterministic lateral displacement. *Interface Focus* **4**, 20140011 (2014).
347. Di Carlo, D., Edd, J. F., Irimia, D., Tompkins, R. G. & Toner, M. Equilibrium separation and filtration of particles using differential inertial focusing. *Anal. Chem.* **80**, 2204–2211 (2008).
348. Ding, X. *et al.* Cell separation using tilted-angle standing surface acoustic waves. *Proc. Natl. Acad. Sci. U. S. A.* **111**, 12992–12997 (2014).
349. Augustsson, P., Karlsen, J. T., Su, H. W., Bruus, H. & Voldman, J. Iso-acoustic focusing of cells for size-insensitive acousto-mechanical phenotyping. *Nat. Commun.* **7**, 1–9 (2016).
350. Preira, P. *et al.* Passive circulating cell sorting by deformability using a microfluidic gradual filter. *Lab Chip* **13**, 161–170 (2013).
351. Wang, G. *et al.* Microfluidic cellular enrichment and separation through differences in viscoelastic deformation. *Lab Chip* **15**, 532–540 (2015).
352. Luo, S. *et al.* Machine-Learning-Assisted Intelligent Imaging Flow Cytometry: A Review. *Adv. Intell. Syst.* **2100073**, 2100073 (2021).
353. Blasi, T. *et al.* Label-free cell cycle analysis for high-throughput imaging flow cytometry. *Nat. Commun.* **7**, (2016).
354. Nitta, N. *et al.* Intelligent Image-Activated Cell Sorting. *Cell* **175**, 266–276.e13 (2018).
355. Hiramatsu, K. *et al.* High-throughput label-free molecular fingerprinting flow cytometry. *Sci. Adv.* **5**, 1–9 (2019).
356. Suzuki, Y. *et al.* Label-free chemical imaging flow cytometry by high-speed multicolor stimulated Raman scattering. *Proc. Natl. Acad. Sci. U. S. A.* **116**, 15842–15848 (2019).
357. Min, J. *et al.* Quantitative phase imaging of cells in a flow cytometry arrangement utilizing Michelson interferometer-based off-axis digital holographic microscopy. *J. Biophotonics* **12**, 1–10 (2019).
358. Zhang, J., Fiore, A., Yun, S. H., Kim, H. & Scarcelli, G. Line-scanning Brillouin microscopy for rapid non-invasive mechanical imaging. *Sci. Rep.* **6**, 1–8 (2016).
359. Herbig, M. *et al.* Real-time Deformability Cytometry: Label-free functional characterization of cells. in *Flow Cytometry Protocols* (eds. Hawley, R. & Hawley, T.) (Humana Press, 2017). doi:10.1007/978-1-4939-7346-0.
360. Silverthorn, D. U. & Johnson, B. R. Human physiology an integrated approach. (2013).
361. Herbig, M., Mietke, A., Müller, P. & Otto, O. Statistics for real-time deformability cytometry: Clustering, dimensionality reduction, and significance testing. *Biomicrofluidics* **12**, (2018).
362. Bates, D., Mächler, M., Bolker, B. & Walker, S. Fitting Linear Mixed-Effects Models using lme4. *J. Stat. Softw.* **67**, (2015).

363. Urbanska, M. *et al.* A comparison of microfluidic methods for high-throughput cell deformability measurements. *Nat. Methods* **17**, 587–593 (2020).
364. Hoffmann, E. K., Lambert, I. H. & Pedersen, S. F. Physiology of cell volume regulation in vertebrates. *Physiol. Rev.* **89**, 193–277 (2009).
365. Spector, I., Shorlet, N. R., Blasberger, D. & Kashman, Y. Latrunculins - novel marine macrolides that disrupt microfilament organization and affect cell growth: I. Comparison with cytochalasin D. *Cell Motil. Cytoskeleton* **13**, 127–144 (1989).
366. Morton, W. M., Ayscough, K. R. & McLaughlin, P. J. Latrunculin alters the actin-monomer subunit interface to prevent polymerization. *Nat. Cell Biol.* **2**, 376–378 (2000).
367. Ritz, C., Baty, F., Streibig, J. C. & Gerhard, D. Dose-response analysis using R. *PLoS One* **10**, 1–13 (2015).
368. Finan, J. D. & Guilak, F. The effects of osmotic stress on the structure and function of the cell nucleus. *J. Cell. Biochem.* **109**, 460–467 (2010).
369. Finan, J. D., Chalut, K. J., Wax, A. & Guilak, F. Nonlinear osmotic properties of the cell nucleus. *Ann. Biomed. Eng.* **37**, 477–491 (2009).
370. Maruyama, K., Kaibara, M. & Fukada, E. Rheology of F-actin I. Network of F-actin in solution. *Biochim. Biophys. Acta - Protein Struct.* **371**, 20–29 (1974).
371. Burg, T. P. *et al.* Weighing of biomolecules, single cells and single nanoparticles in fluid. *Nature* **446**, 1066–1069 (2007).
372. Byun, S., Hecht, V. C. & Manalis, S. R. Characterizing Cellular Biophysical Responses to Stress by Relating Density, Deformability, and Size. *Biophys. J.* **109**, 1565–1573 (2015).
373. Rowat, A. C. *et al.* Nuclear envelope composition determines the ability of neutrophil-type cells to passage through micron-scale constrictions. *J. Biol. Chem.* **288**, 8610–8618 (2013).
374. Shaw Bagnall, J. *et al.* Deformability of Tumor Cells versus Blood Cells. *Sci. Rep.* **5**, 18542 (2016).
375. Kwan, J. M., Guo, Q., Kyliuk-Price, D. L., Ma, H. & Scott, M. D. Microfluidic analysis of cellular deformability of normal and oxidatively damaged red blood cells. *Am. J. Hematol.* **88**, 682–689 (2013).
376. Shaw Bagnall, J. *et al.* Deformability-based cell selection with downstream immunofluorescence analysis. *Integr. Biol.* **8**, 654–664 (2016).
377. Ahmmed, S. M. *et al.* Multi-sample deformability cytometry of cancer cells. *APL Bioeng.* **2**, 032002 (2018).
378. Urbanska, M. *et al.* Single-cell mechanical phenotype is an intrinsic marker of reprogramming and differentiation along the mouse neural lineage. *Development* **144**, 4313–4321 (2017).
379. Kräter, M. *et al.* Cell-derived Bone marrow-mimetics induce erythroid lineage commitment of hematopoietic stem and progenitor cells ex-vivo. *Matters* **3**, e201709000004 (2017).
380. Munder, M. C. *et al.* A pH-driven transition of the cytoplasm from a fluid- to a solid-like state promotes entry into dormancy. *Elife* **5**, (2016).
381. Kräter, M. *et al.* Alterations in Cell Mechanics by Actin Cytoskeletal Changes Correlate with Strain-Specific Rubella Virus Phenotypes for Cell Migration and Induction of Apoptosis. *Cells* **7**, 136 (2018).
382. Masaeli, M. *et al.* Multiparameter mechanical and morphometric screening of cells. *Sci. Rep.* **6**, 37863 (2016).
383. Lin, J. *et al.* High-throughput physical phenotyping of cell differentiation. *Microsystems Nanoeng.* **3**, 17013 (2017).
384. Cha, S. *et al.* Cell Stretching Measurement Utilizing Viscoelastic Particle Focusing. *Anal. Chem.* **84**, 10471–10477 (2012).
385. Toth, K. F. *et al.* Trichostatin A-induced histone acetylation causes decondensation of interphase chromatin. *J Cell Sci* **117**, 4277–4287 (2004).
386. Labriola, N. R., Mathiowitz, E. & Darling, E. M. Fabricating polyacrylamide microbeads by inverse emulsification to mimic the size and elasticity of living cells. *Biomater. Sci.* **5**, 41–45 (2017).



- 
387. Charrier, E. E., Pogoda, K., Wells, R. G. & Janmey, P. A. Control of cell morphology and differentiation by substrates with independently tunable elasticity and viscous dissipation. *Nat. Commun.* **9**, 1–13 (2018).
388. Cermak, N. *et al.* High-throughput measurement of single-cell growth rates using serial microfluidic mass sensor arrays. *Nat. Biotechnol.* **34**, 1052–1059 (2016).
389. Lee, J. *et al.* Suspended microchannel resonators with piezoresistive sensors. *Lab Chip* **11**, 645–651 (2011).
390. Motulsky, H. & Christopoulos, A. Comparing models using the extra sum-of-squares F test. in *Fitting models to biological data using linear and nonlinear regression: a practical guide to curve fitting*, 138–142 (Oxford University Press, 2004).
391. Abdi, H. The Bonferroni and Šidák Corrections for Multiple Comparisons. in *Encyclopedia of Measurement and Statistics* (ed. Salkind, N.) 103–107 (Sage, 2007).
392. Chan, C. J., Heisenberg, C. P. & Hiiragi, T. Coordination of Morphogenesis and Cell-Fate Specification in Development. *Curr. Biol.* **27**, R1024–R1035 (2017).
393. White, M. D., Zenker, J., Bissiere, S. & Plachta, N. Instructions for Assembling the Early Mammalian Embryo. *Dev. Cell* **45**, 667–679 (2018).
394. Shahbazi, M. N. Mechanisms of human embryo development: From cell fate to tissue shape and back. *Dev.* **147**, (2020).
395. Hanna, J. H., Saha, K. & Jaenisch, R. Pluripotency and cellular reprogramming: Facts, hypotheses, unresolved issues. *Cell* **143**, 508–525 (2010).
396. Weinberger, L., Ayyash, M., Novershtern, N. & Hanna, J. H. Dynamic stem cell states: Naive to primed pluripotency in rodents and humans. *Nat. Rev. Mol. Cell Biol.* **17**, 155–169 (2016).
397. Nichols, J. & Smith, A. Pluripotency in the embryo and in culture. *Cold Spring Harb. Perspect. Biol.* **4**, 1–14 (2012).
398. Takahashi, K. & Yamanaka, S. Induction of Pluripotent Stem Cells from Mouse Embryonic and Adult Fibroblast Cultures by Defined Factors. *Cell* **126**, 663–676 (2006).
399. Li, R. *et al.* A mesenchymal-to-epithelial transition initiates and is required for the nuclear reprogramming of mouse fibroblasts. *Cell Stem Cell* **7**, 51–63 (2010).
400. Samavarchi-Tehrani, P. *et al.* Functional genomics reveals a BMP-Driven mesenchymal-to-Epithelial transition in the initiation of somatic cell reprogramming. *Cell Stem Cell* **7**, 64–77 (2010).
401. Buganim, Y. *et al.* Single-cell expression analyses during cellular reprogramming reveal an early stochastic and a late hierarchic phase. *Cell* **150**, 1209–1222 (2012).
402. Polo, J. M. *et al.* A molecular roadmap of reprogramming somatic cells into iPS cells. *Cell* **151**, 1617–1632 (2012).
403. Hussein, S. M. I. *et al.* Genome-wide characterization of the routes to pluripotency. *Nature* **516**, 198–206 (2014).
404. Cacchiarelli, D. *et al.* Integrative Analyses of Human Reprogramming Reveal Dynamic Nature of Induced Pluripotency. *Cell* **162**, 412–424 (2015).
405. Maherali, N. *et al.* Directly reprogrammed fibroblasts show global epigenetic remodeling and widespread tissue contribution. *Cell Stem Cell* **1**, 55–70 (2007).
406. Lee, D.-S. *et al.* An epigenomic roadmap to induced pluripotency reveals DNA methylation as a reprogramming modulator. *Nat. Commun.* **5**, 5619 (2014).
407. Sakurai, K. *et al.* Kinome-wide functional analysis highlights the role of cytoskeletal remodeling in somatic cell reprogramming. *Cell Stem Cell* **14**, 523–534 (2014).
408. Ying, Q.-L. *et al.* The ground state of embryonic stem cell self-renewal. *Nature* **453**, 519–523 (2008).
409. Silva, J. *et al.* Promotion of reprogramming to ground state pluripotency by signal inhibition. *PLoS Biol.* **6**, 2237–2247 (2008).
410. Tonge, P. D. *et al.* Divergent reprogramming routes lead to alternative stem-cell states. *Nature* **516**, 192–197 (2014).

411. Brambrink, T. *et al.* Sequential Expression of Pluripotency Markers during Direct Reprogramming of Mouse Somatic Cells. *Cell Stem Cell* **2**, 151–159 (2008).
412. Shakiba, N. *et al.* CD24 tracks divergent pluripotent states in mouse and human cells. *Nat. Commun.* **6**, 7329 (2015).
413. Ying, Q.-L., Stavridis, M., Griffiths, D., Li, M. & Smith, A. Conversion of embryonic stem cells into neuroectodermal precursors in adherent monoculture. *Nat. Biotechnol.* **21**, 183–186 (2003).
414. Heisenberg, C. P. & Bellaïche, Y. Forces in tissue morphogenesis and patterning. *Cell* **153**, 948–962 (2013).
415. Stooke-Vaughan, G. A. & Campàs, O. Physical control of tissue morphogenesis across scales. *Curr. Opin. Genet. Dev.* **51**, 111–119 (2018).
416. Hannezo, E. & Heisenberg, C. P. Mechanochemical Feedback Loops in Development and Disease. *Cell* **178**, 12–25 (2019).
417. Pajerowski, J. D., Dahl, K. N., Zhong, F. L., Sammak, P. J. & Discher, D. E. Physical plasticity of the nucleus in stem cell differentiation. *Proc. Natl. Acad. Sci. U. S. A.* **104**, 15619–15624 (2007).
418. Handorf, A. M., Zhou, Y., Halanski, M. a & Li, W.-J. Tissue stiffness dictates development, homeostasis, and disease progression. *Organogenesis* **11**, 1–15 (2015).
419. Darling, E. M., Topel, M., Zauscher, S., Vail, T. P. & Guilak, F. Viscoelastic properties of human mesenchymally-derived stem cells and primary osteoblasts, chondrocytes, and adipocytes. *J. Biomech.* **41**, 454–464 (2008).
420. Lu, Y.-B. *et al.* Viscoelastic properties of individual glial cells and neurons in the CNS. *PNAS* **103**, 17759–17764 (2006).
421. Pellegrin, S. & Mellor, H. Rho GTPase activation assays. *Curr. Protoc. Cell Biol.* 1–19 (2008) doi:10.1002/0471143030.cb1408s38.
422. Pertz, O., Hodgson, L., Klemke, R. L. & Hahn, K. M. Spatiotemporal dynamics of RhoA activity in migrating cells. *Nature* **440**, 1069–1072 (2006).
423. Dupont, S. *et al.* Role of YAP/TAZ in mechanotransduction. *Nature* **474**, 179–184 (2011).
424. Panciera, T., Azzolin, L., Cordenonsi, M. & Piccolo, S. Mechanobiology of YAP and TAZ in physiology and disease. *Nat. Rev. Mol. Cell Biol.* (2017) doi:10.1038/nrm.2017.87.
425. Musah, S. *et al.* Substratum-induced differentiation of human pluripotent stem cells reveals the coactivator YAP is a potent regulator of neuronal specification. *PNAS* **111**, 13805–13810 (2014).
426. Sun, Y. *et al.* Hippo/YAP-mediated rigidity-dependent motor neuron differentiation of human pluripotent stem cells. *Nat. Mater.* **13**, 599–604 (2014).
427. Maître, J.-L. *et al.* Asymmetric division of contractile domains couples cell positioning and fate specification. *Nature* **536**, 344–348 (2016).
428. Bharathan, S. P. *et al.* Systematic evaluation of markers used for the identification of human induced pluripotent stem cells. *Biol. Open* **6**, 100–108 (2017).
429. Knoepfler, P. S. Deconstructing stem cell tumorigenicity: A roadmap to safe regenerative medicine. *Stem Cells* **27**, 1050–1056 (2009).
430. Yamanaka, S. Pluripotent Stem Cell-Based Cell Therapy—Promise and Challenges. *Cell Stem Cell* **27**, 523–531 (2020).
431. Singh, U. *et al.* Novel Live Alkaline Phosphatase Substrate for Identification of Pluripotent Stem Cells. *Stem Cell Rev. Reports* **8**, 1021–1029 (2012).
432. Guilak, F. *et al.* Control of Stem Cell Fate by Physical Interactions with the Extracellular Matrix. *Cell Stem Cell* **5**, 17–26 (2009).
433. Yim, E. K. & Sheetz, M. P. Force-dependent cell signaling in stem cell differentiation. *Stem Cell Res. Ther.* **3**, 41 (2012).
434. Engler, A. J., Sen, S., Sweeney, H. L. & Discher, D. E. Matrix Elasticity Directs Stem Cell Lineage

- Specification. *Cell* **126**, 677–689 (2006).
435. Przybyla, L., Lakins, J. N. & Weaver, V. M. Tissue Mechanics Orchestrate Wnt-Dependent Human Embryonic Stem Cell Differentiation. *Cell Stem Cell* **19**, 462–475 (2016).
436. Fu, J., Warmflash, A. & Lutolf, M. P. Stem-cell-based embryo models for fundamental research and translation. *Nat. Mater.* **20**, 132–144 (2021).
437. Baillie-Benson, P., Moris, N. & Martinez Arias, A. Pluripotent stem cell models of early mammalian development. *Curr. Opin. Cell Biol.* **66**, 89–96 (2020).
438. Shahbazi, M. N., Siggia, E. D. & Zernicka-Goetz, M. Self-organization of stem cells into embryos: A window on early mammalian development. *Science* **364**, 948–951 (2019).
439. Neumann, K. H3K4 methyltransferases Mll1 and Mll2 have distinct roles and cooperate in neural differentiation and reprogramming. *PbD thesis* (Technische Universität Dresden, Dresden, Germany, 2014).
440. Guo, G. *et al.* Klf4 reverts developmentally programmed restriction of ground state pluripotency. *Development* **136**, 1063–1069 (2009).
441. Rosendahl, P. *et al.* Real-time fluorescence and deformability cytometry — flow cytometry goes mechanics. *Nat. Methods*.
442. Sneddon, I. N. The relation between load and penetration in the axisymmetric boussinesq problem for a punch of arbitrary profile. *Int. J. Eng. Sci.* **3**, 47–57 (1965).
443. Glaubitz, M. *et al.* A novel contact model for AFM indentation experiments on soft spherical cell-like particles. *Soft Matter* **10**, 6732–6741 (2014).
444. Toyoda, Y. *et al.* Genome-scale single-cell mechanical phenotyping reveals disease-related genes involved in mitotic rounding. *Nat. Commun.* **8**, 1–10 (2017).
445. Wang, J., Lü, D., Mao, D. & Long, M. Mechanomics: An emerging field between biology and biomechanics. *Protein Cell* **5**, 518–531 (2014).
446. Putra, V. D. L. *et al.* Mechanomics Approaches to Understand Cell Behavior in Context of Tissue Neogenesis, During Prenatal Development and Postnatal Healing. *Front. Cell Dev. Biol.* **7**, 1–8 (2020).
447. Zhang, F. *et al.* Mechanomics analysis of hESCs under combined mechanical shear, stretch, and compression. *Biomech. Model. Mechanobiol.* (2020) doi:10.1007/s10237-020-01378-5.
448. Lang, M. Lighting up the mechanome. *Front. Eng. Reports leading-edge Eng. from 2007 Symp.* (2008).
449. Van Loon, J. J. W. A. Mechanomics and physicomics in gravisensing. *Microgravity Sci. Technol.* **21**, 159–167 (2009).
450. Song, M. J. *et al.* Mapping the mechanome of live stem cells using a novel method to measure local strain fields in situ at the fluid-cell interface. *PLoS One* **7**, 1–12 (2012).
451. Song, M. J., Dean, D. & Knothe Tate, M. L. Mechanical modulation of nascent stem cell lineage commitment in tissue engineering scaffolds. *Biomaterials* **34**, 5766–5775 (2013).
452. Wang, H. *et al.* Mechanomics Biomarker for Cancer Cells Unidenti fi able through Morphology and Elastic Modulus. (2021) doi:10.1021/acs.nanolett.1c00003.
453. Ciucci, S. *et al.* Enlightening discriminative network functional modules behind principal component analysis separation in differential-omic science studies. *Sci. Rep.* **7**, 1–24 (2017).
454. Poser, S. W. *et al.* Controlling distinct signaling states in cultured cancer cells provides a new platform for drug discovery. *FASEB J.* **33**, 9235–9249 (2019).
455. Hanley, J. A. & McNeil, B. J. The meaning and use of the area under a receiver operating characteristic (ROC) curve. *Radiology* **143**, 29–36 (1982).
456. Urbanska, M. *et al.* De novo identification of universal cell mechanics regulators. *bioRxiv* 2021.04.26.441418 (2021) doi:10.1101/2021.04.26.441418.
457. Poser, S. W., Park, D. M. & Androutsellis-Theotokis, A. The STAT3-Ser/Hes3 signaling axis: An emerging regulator of endogenous regeneration and cancer growth. *Front. Physiol.* **4**, 273 (2013).

458. Brenner, B., Tang, L. H., Klimstra, D. S. & Kelsen, D. P. Small-cell carcinomas of the gastrointestinal tract: A review. *J. Clin. Oncol.* **22**, 2730–2739 (2004).
459. Kalemkerian, G. P. *et al.* Small cell lung cancer: Clinical practice guidelines in oncology. *JNCCN J. Natl. Compr. Cancer Netw.* **11**, 78–98 (2013).
460. Arulmozhivarman, G. *et al.* Zebrafish In-Vivo Screening for Compounds Amplifying Hematopoietic Stem and Progenitor Cells: - Preclinical Validation in Human CD34+ Stem and Progenitor Cells. *Sci. Rep.* **7**, 1–15 (2017).
461. Juvin, V. *et al.* Signaling via Class IA Phosphoinositide 3-Kinases (PI3K) in Human, Breast-Derived Cell Lines. *PLoS One* **8**, (2013).
462. Bader, A. G., Kang, S. & Vogt, P. K. Cancer-specific mutations in PIK3CA are oncogenic in vivo. *Proc. Natl. Acad. Sci. U. S. A.* **103**, 1475–1479 (2006).
463. Kang, S., Bader, A. G. & Vogt, P. K. Phosphatidylinositol 3-kinase mutations identified in human cancer are oncogenic. *Proc. Natl. Acad. Sci. U. S. A.* **102**, 802–807 (2005).
464. Aprea, J. *et al.* Transcriptome sequencing during mouse brain development identifies long non-coding RNAs functionally involved in neurogenic commitment. *EMBO J.* **32**, 3145–3160 (2013).
465. Forrest, A. R. R. *et al.* A promoter-level mammalian expression atlas. *Nature* **507**, 462–470 (2014).
466. Kiselev, V. Y. *et al.* Perturbations of PIP3 signalling trigger a global remodelling of mRNA landscape and reveal a transcriptional feedback loop. *Nucleic Acids Res.* **43**, 9663–9679 (2015).
467. Lolo, F.-N. *et al.* Continuous membrane tension buffering by caveolin-1 invaginations switch to discontinuous caveolae flattening by PTRF. *submitted*.
468. Raudenska, M., Gumulec, J., Balvan, J. & Masarik, M. Caveolin-1 in oncogenic metabolic symbiosis. *Int. J. Cancer* **147**, 1793–1807 (2020).
469. Pol, A., Morales-Paytuví, F., Bosch, M. & Parton, R. G. Non-caveolar caveolins - Duties outside the caves. *J. Cell Sci.* **133**, (2020).
470. Johannessen, M., Møler, S., Hansen, T., Moens, U. & Van Ghelue, M. The multifunctional roles of the four-and-a-half-LIM only protein FHL2. *Cell. Mol. Life Sci.* **63**, 268–284 (2006).
471. Nakazawa, N., Sathe, A. R., Shivashankar, G. V. & Sheetz, M. P. Matrix mechanics controls FHL2 movement to the nucleus to activate p21 expression. *Proc. Natl. Acad. Sci. U. S. A.* **113**, E6813–E6822 (2016).
472. Sun, X. *et al.* Mechanosensing through Direct Binding of Tensed F-Actin by LIM Domains. *Dev. Cell* (2020) doi:10.1016/j.devcel.2020.09.022.
473. Winkelman, J. D., Anderson, C. A., Suarez, C., Kovar, D. R. & Gardel, M. L. Evolutionarily diverse LIM domain-containing proteins bind stressed actin filaments through a conserved mechanism. *Proc. Natl. Acad. Sci. U. S. A.* **117**, 25532–25542 (2020).
474. Jin, L., Shen, F., Weinfeld, M. & Sergi, C. Insulin Growth Factor Binding Protein 7 (IGFBP7)-Related Cancer and IGFBP3 and IGFBP7 Crosstalk. *Front. Oncol.* **10**, 1–14 (2020).
475. Liu, R., Hossain, M. M., Chen, X. & Jin, J. P. Mechanoregulation of SM22 $\alpha$ /Transgelin. *Biochemistry* **56**, 5526–5538 (2017).
476. Dvorakova, M., Nenutil, R. & Bouchal, P. Transgelins, cytoskeletal proteins implicated in different aspects of cancer development. *Expert Rev. Proteomics* **11**, 149–165 (2014).
477. Adams, J. C. & Lawler, J. The thrombospondins. *Cold Spring Harb. Perspect. Biol.* **3**, 1–29 (2011).
478. Huang, T., Sun, L., Yuan, X. & Qiu, H. Thrombospondin-1 is a multifaceted player in tumor progression. *Oncotarget* **8**, 84546–84558 (2017).
479. Hirsch, H. A., Iliopoulos, D., Tsiichlis, P. N. & Struhl, K. Metformin selectively targets cancer stem cells, and acts together with chemotherapy to block tumor growth and prolong remission. *Cancer Res.* **69**, 7507–7511 (2009).
480. Hirsch, H. A. *et al.* A Transcriptional Signature and Common Gene Networks Link Cancer with Lipid Metabolism and Diverse Human Diseases. *Cancer Cell* **17**, 348–361 (2010).

- 
481. Zhang, B. & Horvath, S. A General Framework for Weighted Gene Co- Expression Network Analysis A General Framework for Weighted Gene Co-Expression Network Analysis. *Stat. Appl. Genet. Mol. Biol.* **4**, Article17 (2005).
482. J., R., A.K., D. & W., Z. A general co-expression network-based approach to gene expression analysis: Comparison and applications. *BMC Syst. Biol.* **4**, (2010).
483. Moreno-Vicente, R. *et al.* Caveolin-1 Modulates Mechanotransduction Responses to Substrate Stiffness through Actin-Dependent Control of YAP. *Cell Rep.* **25**, 1622-1635.e6 (2018).
484. Strippoli, R. *et al.* Caveolin1 and YAP drive mechanically induced mesothelial to mesenchymal transition and fibrosis. *Cell Death Dis.* **11**, 1–19 (2020).
485. Rausch, V. *et al.* The Hippo Pathway Regulates Caveolae Expression and Mediates Flow Response via Caveolae. *Curr. Biol.* **29**, 242-255.e6 (2019).
486. Stein, C. *et al.* YAP1 Exerts Its Transcriptional Control via TEAD-Mediated Activation of Enhancers. *PLoS Genet.* **11**, 1–28 (2015).
487. Zhao, B. *et al.* TEAD mediates YAP-dependent gene induction and growth control. *Genes Dev.* **22**, 1962–1971 (2008).
488. Jiang, W. R. *et al.* Mechanoregulation of h2-calponin gene expression and the role of notch signaling. *J. Biol. Chem.* **289**, 1617–1628 (2014).
489. Hossain, M. M., Smith, P. G., Wu, K. & Jin, J. P. Cytoskeletal tension regulates both expression and degradation of h2-calponin in lung alveolar cells. *Biochemistry* **45**, 15670–15683 (2006).
490. Hossain, M. M., Crish, J. F., Eckert, R. L., Lin, J. J. C. & Jin, J. P. H2-Calponin Is Regulated By Mechanical Tension and Modifies the Function of Actin Cytoskeleton. *J. Biol. Chem.* **280**, 42442–42453 (2005).
491. Goetz, J. G., Lajoie, P., Wiseman, S. M. & Nabi, I. R. Caveolin-1 in tumor progression: The good, the bad and the ugly. *Cancer Metastasis Rev.* **27**, 715–735 (2008).
492. Wang, Z. *et al.* Caveolin-1, a stress-related oncotarget, in drug resistance. *Oncotarget* **6**, 37135–37150 (2015).
493. Ali Haghparast, S. M., Kihara, T. & Miyake, J. Distinct mechanical behavior of HEK293 cells in adherent and suspended states. *PeerJ* **2015**, 1–13 (2015).
494. Vogel, C. & Marcotte, E. M. Insights into the regulation of protein abundance from proteomic and transcriptomic analyses. *Nat. Rev. Genet.* **13**, 227–232 (2012).
495. Petsko, G. A. & Ringe, D. Control of protein function. *Protein structure and function* 86–126 (2004).
496. Lee, M. J. & Yaffe, M. B. Protein regulation in signal transduction. *Cold Spring Harb. Perspect. Biol.* **8**, 1–20 (2016).
497. Chau, C., Actis, P. & Hewitt, E. Methods for protein delivery into cells: From current approaches to future perspectives. *Biochem. Soc. Trans.* **48**, 357–365 (2020).
498. Lv, J. *et al.* Cell softness regulates tumorigenicity and stemness of cancer cells. 1–14 (2020) doi:10.15252/emj.2020106123.
499. Arulmozhivarman, G. *et al.* In Vivo Chemical Screen in Zebrafish Embryos Identifies Regulators of Hematopoiesis Using a Semiautomated Imaging Assay. *J. Biomol. Screen.* 1087057116644163 (2016) doi:10.1177/1087057116644163.
500. Razani, B. *et al.* Caveolin-1 Null Mice Are Viable but Show Evidence of Hyperproliferative and Vascular Abnormalities. *J. Biol. Chem.* **276**, 38121–38138 (2001).
501. Landau, L. D., Lifshitz, E. M., Sykes, J. B., Reid, W. H. & Dill, E. H. Theory of Elasticity: Vol. 7 of Course of Theoretical Physics. *Phys. Today* **13**, 44–46 (2009).
502. Rother, J., Nöding, H., Mey, I. & Janshoff, A. Atomic force microscopy-based microrheology reveals significant differences in the viscoelastic response between malignant and benign cell lines. *Open Biol.* (2014) doi:10.1098/rsob.140046.
503. Alcaraz, J. *et al.* Correction of microrheological measurements of soft samples with atomic force microscopy for the hydrodynamic drag on the cantilever. *Langmuir* (2002) doi:10.1021/la0110850.

504. Shannon, P. *et al.* Cytoscape: A Software Environment for Integrated Models of Biomolecular Interaction Networks. 2498–2504 (2003) doi:10.1101/gr.1239303.metabolite.
505. McInnes, L., Healy, J. & Melville, J. Umap: Uniform manifold approximation and projection for dimension reduction. *arXiv Prepr. arXiv1802.03426* (2018).
506. Van der Maaten, L. & Hinton, G. Visualizing data using t-SNE. *J. Mach. Learn. Res.* **9**, (2008).
507. T. Das, A., Tenenbaum, L. & Berkhout, B. Tet-On Systems For Doxycycline-inducible Gene Expression. *Curr. Gene Ther.* **16**, 156–167 (2016).
508. Kai, F. B., Laklai, H. & Weaver, V. M. Force Matters: Biomechanical Regulation of Cell Invasion and Migration in Disease. *Trends Cell Biol.* **26**, 486–497 (2016).
509. Vining, K. H. & Mooney, D. J. Mechanical forces direct stem cell behaviour in development and regeneration. *Nat. Rev. Mol. Cell Biol.* **18**, 728–742 (2017).
510. Itoh, M. *et al.* Automated workflow for preparation of cDNA for cap analysis of gene expression on a single molecule sequencer. *PLoS One* **7**, (2012).

## Acknowledgements

I would like to express my deepest gratitude to all the people that supported and accompanied me during the process of completing my doctoral degree. Pursuing a PhD is a rocky road of personal and professional growth and, I dare say, no one has gone through it unchanged. I would like to thank each and every one of you for the continuous support, guidance and intellectual exchange, but most importantly, for inspiring me to become a better scientist and a better person.

First and foremost, I would like to thank my supervisor, Prof. **Jochen Guck**, for making this work possible and for all the insightful scientific feedback that shaped the projects. I am very grateful for the opportunity to work in your group, for all the interactions we had and for the amount of scientific freedom that you gave me. Thank you for believing in me and for every word of encouragement. You are rock solid and it really inspires me how calmly you deal with adversities. I would also like to thank you for introducing me to many diplomatic(-o) aspects of the scientific endeavor.

I would like to also thank my further TAC committee members: Prof. **Konstantinos Anastasiadis**, Prof. **Frank Buchholz** and Prof. **Stephan Grill**. I have benefited greatly from discussing with you and hearing your feedback. I will particularly cherish the memory of a special advice from Stephan to “do less (experiments) and think more” — painful but priceless. I would also like to express my gratitude to Prof. **Timo Betz** and Prof. **Stephan Grill** for agreeing to review this thesis.

I would like to acknowledge the great support that I have received from several senior scientists in the group. First, my big thanks go to Prof. (yes, you have gone a long way!) **Oliver Otto**. Your support and kindness were beyond helpful. I would like to particularly thank you for helping me organize my work during the early stages of my PhD, and for involving me in several collaborative projects. Next, I would like to thank **Maria Winzi** for teaching me a great deal about molecular biology and stem cell biology, for sharing with me not only all her reagents and protocols, but also her smile and contagious positive attitude. It was an absolute honor to share the office with you! I would like to further thank **Anna Taubenberger** for introducing me to AFM and supporting my projects. Even more importantly, Anna, I would like to thank you for being a role-model! You are a truly open mind and one of a few people that I know who can truly synthesize knowledge from the fields of biology, physics and engineering. I would like to express my deepest gratitude to **Angela Jacobi** for the most special support that I can imagine. You were my inspiration, my advocate, and throughout the years you became a dear friend.

I would like to acknowledge all of the support from further Guck group members, the interactions with you have always been very fruitful and your help was instrumental for conducting my research. I would like to thank **Philipp Rosendahl** for the countless times you explained to me the technical details related to RT-(F)DC and helped me adjust hardware on the setup, as well as for sharing the offline tracking software. **Ahsan Nawaz** for bringing in the sorting technology, making the SSAW behave, and for all interactions we

had when finalizing the sorting manuscript. I would like to further acknowledge everyone who contributed to the sorting project, especially **Martin Nötzel** who was instrumental for software implementation and **Maik Herbig** who developed the AI analysis. Maik, you have also been around for much more than the sorting project — thank you for your continuous support, help with RT-DC measurements, statistical analysis, and many useful discussions. **Felix Reichel**, thank you for being a great team player, for all the discussions we had and for your willingness to help. Big thanks go to **Paul Müller** for developing and maintaining the *Shape-Out* analysis software and for the readiness to implement suggestions, fix bugs, and discuss technical aspects of evaluating RT-DC data. I would also like to acknowledge the support from **Christoph Herold** and **Daniel Klaue** from Zellmechanik Dresden GmbH — thank you for your helping hand with the setup, sharing protocols for production of methylcellulose buffer, as well as codes and graphical materials. **Nicole Töpfer** – thank you for all the interactions and input when preparing the manuscripts. I would like to collectively thank all further members of the microfluidics subgroup that never failed to provide support and constructive criticism: **Martin Kräter**, **Katarzyna Plak**, **Markéta Kubánková**, **Despina Soteriou**, and many others that participated in the microfluidic meetings throughout the years. Big thanks go further to **Salvatore Girardo** and **Ruchi Goswami** that supported all the cleanroom work and the bead production from the side of Microstructure Facility. I want to extend my thanks to all the student assistants who produced the innumerable RT-DC chips that were used in this thesis: **Felix Reichel**, **Sebastian Hammer**, and **Alejandro Rivera Prieto**. Beyond the microfluidic gang, I would like to particularly thank **Shada Abuhattum** for her support with AFM measurements and countless inspiring scientific discussions. It was always a pleasure to interact with you! **Timon Beck** and **Raimund Schlüßler** – thank you for your companionship and readiness to answer all my silly questions. **Kyoohyun Kim** — for all scientific discussions; **Isabel Richter** and **Christine Schweitzer** — for your technical support and making the lab run on the organizational level. **Heike Neumann**, **Till Kirst**, **Stefanie Dünkel**, **Claudia Schwäger**, as well as **Ruth Hans** – for your assistance with administrative issues. At this point, I would also like to collectively thank all the current and past members of the Guck Group for creating a stimulating and respectful professional environment.

Furthermore, I would like to express my gratitude to all external collaborators, without whom many of the projects presented in this thesis would not have been possible. First, I would like to acknowledge the contributions of Prof. **Konstantinos Anastasiadis** and **Katrin Neumann** (Biotec, TU Dresden) to the cell fate transition project. Thank you for providing me with the stem cell systems, sharing all the know-how of the stem cell culture, as well as for all your support with handling the project. Next, my thanks go to Prof. **Dino Di Carlo** and **Hector Muñoz** (UCLA), as well as Prof. **Scott Manalis** and **Josephine Shaw Bagnall** (MIT), for the collaboration on the comparison project. I am especially grateful to Hector — thanks to you, I picked up many useful coding tricks in MATLAB and R, learned a lot about color-proofing of figures and did my first steps on Git – thank you for all of that! To Prof. **Carlo Cannistraci** and **Yan Ge** (Biotec, TU Dresden) for the collaboration on the mechanomics project. In particular, thank you Yan for executing the original implementation of the analysis, sharing all the resources and answering all my questions. Carlo,



thank you for your passionate and enthusiastic support. To Prof. **Aurélien Roux** and **Chloe Roffay** (University of Geneva) for involving me in their osmotic shock project. I have learned a lot through discussions with you. To Prof. **Franziska Lautenschläger** and **Luiza Da Cunha Stankevics** (Saarland University) for involving me in the mechanical characterization of vimentin knock-out dendritic cells. To Prof. **Miguel Ángel del Pozo**, **Miguel Sánchez Álvarez** and **Fidel-Nicolás Lolo** (CNIC, Madrid) for sharing the expertise on the biology of caveolin. My thanks go also to the other contributors to the mechanomics project: Prof. **Federico Calegari** and **Martina Dori** (CRTD, TU Dresden), as well as **Joanne Durgan** and **Oliver Florey** (Babraham Institute, Cambridge).

I would also like to name a couple of people who gave me particularly strong support in finalizing the writing of this thesis: **Elke**, **Anna**, **Angela**, **Agata Nyga**, **JC**, **Shada**, **Felix**, **Benedikt**, **Maik**, **Timon**, **Raimund**, **Despina**, and **Lucas** — thank you for your help with structuring, for all the proof-reading, and especially for your encouragement and mental support.

Now that I got all the official acknowledgements out of the way, let me tell you again Guckies how much fun it was to be around you all these years. For the sake of space, I cannot share all the specific aspects of what I am grateful for, but I would like to mention a few. I would like to thank **Martin** and **Gela** for encouraging me to speak German and giving me a nickname that I will always fondly remember; **Martin** — for introducing me, together with **Maik**, to *Sterni*, having the beer hours on zoom during the pandemic and for being a partner in crime when opening a wine bottle with a syringe; **Gela** — thank you for all the chats, coffees, and absolutely everything you did with and for me; **JC** — for sharing all your *jamón* and tortillas with us and bringing in the good vibe and some loud shouts into the lab; **Shada** — for being an inspiring woman and always having an open ear and an open door for me, and also for giving me the reason to visit Israel; **Isabel** — for all the funny stories, warm chats and making me realize that there is another meaning of *Dosenöffner*; **Kasia** — for bringing in some Polish spirit, frying *faworki* together and many good times in and outside of the lab; **Markéta** — for all the chats, letting me crush on your couch, making me have my first cross-country skiing experience and being such an open, lovely creature.

Coming closer to the end, I would like to thank all my friends from far and near that have not been directly involved in my scientific work but kept me sane during the last years, especially: **Rebecca Pradet**, **Ewa Kania**, **Denise Nittel**, **Aleksandra Spiegel**, **Agata Rakszewska**, **Agata Szuba**, **Aleksandra Gołoś-Wójcicka**, **Natalia Ike**. My thanks go also to all my volleyball and tennis companions — you gave me the much-needed breaks to go from my head into my body. I would like to thank **Celina Love** and **Lucia Rotheray** for introducing me to Lise Meitner Gesellschaft. I would also like to deeply thank **Georg Krainer** for all his support and companionship. Thank you for being an inspiration and an immediate mentor in so many ways. Thank you for all the great times, countless deep conversations about science and life, the feeling of home, for always believing in me, and for many hikes and skiing trips in the Alps.

Last but not least, my heartfelt thanks go to my family. To my **parents** for supporting me in whichever steps I take and for making me believe that I can become anything I want. To my (not anymore annoying but still a little crazy) **sister**, I know I can count on you no matter what and this is very special. And to my **big brother**, for being there for me.



## **Erklärung entsprechend §5.5 der Promotionsordnung**

Hiermit versichere ich, dass ich die vorliegende Arbeit ohne unzulässige Hilfe Dritter und ohne Benutzung anderer als der angegebenen Hilfsmittel angefertigt habe; die aus fremden Quellen direkt oder indirekt übernommenen Gedanken sind als solche kenntlich gemacht. Die Arbeit wurde bisher weder im Inland noch im Ausland in gleicher oder ähnlicher Form einer anderen Prüfungsbehörde vorgelegt. Diese Dissertation wurde am Biotechnologischen Zentrum der Technischen Universität Dresden unter der wissenschaftlichen Betreuung von Prof. Dr. Jochen Guck angefertigt.

Meine Person betreffend erkläre ich hiermit, dass keine früheren erfolglosen Promotionsverfahren stattgefunden haben.

Ich erkenne die Promotionsordnung der Fakultät für Mathematik und Naturwissenschaften, Technische Universität Dresden an.

*Marta Urbańska*

Dresden, den 12.10.2021